# UNIVERSITA' DEGLI STUDI DI VERONA

*DEPARTMENT OF*

*Neurosciences, Biomedicine and Movement Sciences*

*GRADUATE SCHOOL OF*

*Natural Sciences and Engineering*

*DOCTORAL PROGRAM IN*

*Nanosciences and Advanced Technologies*

XXXV Cycle

TITLE OF THE DOCTORAL THESIS

## THE AGING OF SKELETAL MUSCLE: MORPHOLOGICAL EXPERIMENTAL APPROACHES

S.S.D. BIO/16

Coordinator:     Prof. Adolfo SPEGHINI

               Signature _____

Tutor:     Prof. Carlo ZANCANARO

               Signature _____

Doctoral Student: Maria Assunta LACAVALLA

Signature _____

"You can't connect the dots looking forward; you can only connect them looking backwards.

So, you have to trust that the dots will somehow connect in your future."

S. Jobs

# ACKNOWLEDGMENTS

# SOMMARIO

La sarcopenia è una condizione patologica che interessa il muscolo scheletrico ed è caratterizzata dalla graduale perdita di massa, forza e funzione muscolare. Questa condizione è strettamente legata all'avanzamento dell'età e le conseguenze legate ad essa hanno un forte impatto sulla qualità della vita del paziente oltre a determinare significative conseguenze a livello socioeconomico. Ad oggi, le cause relative all'insorgenza della patologia rimangono ancora poco chiare. Diversi studi hanno dimostrato che la sarcopenia ha una natura multifattoriale. Tra le modificazioni legate alla patologia vi sono un alterato turnover proteico, una deregolazione della struttura cromatinica e l'instabilità genomica dell'rDNA. Durante l'invecchiamento, anche la matrice extracellulare muscolare (ECM) subisce modificazioni strutturali e di composizione in grado di influenzare negativamente le interazioni cellula-matrice, il potere rigenerativo delle cellule staminali muscolari (cellule satellite) e la rigidità del tessuto muscolare. Pertanto, in questo lavoro di tesi è stato approfondito sia il coinvolgimento del myonucleo nel processo di invecchiamento del muscolo scheletrico sia i cambiamenti della matrice extracellulare del muscolo scheletrico. A tal scopo, sono stati utilizzati due diversi approcci metodologici. Nel primo caso, le reazioni di immunocitochimica e le osservazioni al microscopio elettronico effettuate sul muscolo retto femorale di topi vecchi di (28 mesi) e (19 mesi) hanno rivelato differenze età-dipendenti nella distribuzione e nella densità di alcuni fattori molecolari coinvolti nel processing dell'mRNA. Nel secondo studio, le valutazioni morfologiche e morfometriche (eseguite mediante microscopia elettronica e a fluorescenza) combinate ad un approccio proteomico, hanno mostrato una maggiore quantità di diverse componenti della matrice extracellulare nel muscolo gastrocnemio di topi vecchi (24 mesi) messi a confronto con topi adulti (12 mesi). Tali risultati suggeriscono che il rimodellamento della matrice extracellulare muscolare in invecchiamento può ostacolare l'interazione cellula-matrice e modificare la sua organizzazione strutturale.

Una volta individuate tali alterazioni, abbiamo esplorato due strategie potenzialmente in grado di contrastare la patologia: l'esercizio fisico come

approccio non farmacologico e la nanotecnologia, considerata come strumento idoneo all'intervento farmacologico.

I dati preliminari ottenuti dalle osservazioni eseguite al microscopio elettronico e a fluorescenza hanno dimostrato che, in topi vecchi (24 mesi), l'esercizio fisico potrebbe limitare/prevenire le alterazioni età-dipendenti sia della miofibra muscolare (a livello cellulare e sub-cellulare) sia dell'organizzazione strutturale della matrice extracellulare del muscolo.

Infine, è stato condotto uno studio pilota per testare l'idoneità delle nanoparticelle a base di fosfolipidi (etosomi e transetosomi) come carrier per la molecola vitamina D3, in quanto il suo apporto sembra essere legato al miglioramento della funzionalità muscolare negli anziani. In prima analisi, è stata valutata la biocompatibilità delle NPs in tre diverse linee cellulari rappresentative del tessuto epiteliale, connettivo e muscolare. Successivamente sono state eseguite osservazioni in campo chiaro, fluorescenza e microscopia elettronica a trasmissione per studiarne l'internalizzazione, il destino intracellulare e le potenziali alterazioni a livello subcellulare. I nostri risultati preliminari forniscono una solida base sperimentale per testare tali NPs anche *in vivo* al fine di proporre in futuro la somministrazione transdermica della vitamina D come nuova strategia per contrastare le patologie legate all'età del tessuto muscolare.

Infine, durante il periodo di ricerca all'estero, ho collaborato alla messa a punto di un sistema di co-coltura cellulare *in vitro* contenente macrofagi primari e cellule muscolari murine, precedentemente trattate con etoposide (una molecola in grado di indurre danni al DNA). Successivamente, sono stati adottati due diversi approcci metodologici: le cellule muscolari sono state sottoposte ad un'analisi di espressione genica (mediante la tecnica di real-time RT-qPCR), al fine di determinare se la presenza o meno dei macrofagi influisse sulla funzionalità intrinseca delle cellule muscolari; in un secondo momento, è stata eseguita una reazione di immunofluorescenza sulle cellule muscolari per studiare la capacità dei macrofagi di contrastare il danno al DNA. Lo scopo di questa indagine preliminare è stato quello di investigare, sfruttando un sistema di co-coltura *in vitro*, il cross talk tra macrofagi e cellule muscolari in condizioni di danno al DNA.

# ABSTRACT

Nowadays, sarcopenia is recognised as condition characterized by the gradual loss of muscle mass, strength, and function. This condition mainly affects older people, and its adverse outcomes strongly impact patient's quality of life with significant socio-economic consequences. Currently, a single cause for sarcopenia has not been discovered. Experimental evidence showed that sarcopenia has a multifactorial nature, involving several contributing factors such as altered protein turnover, chromatin dysregulation and rDNA genome instability. Moreover, in age-dependent sarcopenia, muscle extracellular matrix (ECM) undergoes alterations in architecture and composition, which negatively influence cell-matrix interactions, the regenerative power of satellite cells and muscle tissue stiffness. The research project of my doctorate was to further investigate on myonuclear involvement in skeletal muscle aging as well as age-related changes in muscle ECM. In this purpose, two different methodological approaches were used. First, ultrastructural immunocytochemistry revealed age-related differences in the distribution and density of some molecular factors involved in RNA pathways between old (28 months) mice and their late adult counterpart (19 months). Second, morphological and morphometrical evaluation (performed by fluorescent and transmission electron microscopy) combined with proteomic approach showed higher amount of several muscle ECM components in old (24 months) compared to adult mice (12 months), suggesting that muscle ECM remodelling may hinder muscle cell-matrix interplay as well as its structural organization. Once age-related muscular dysfunctions had been identified, we investigated two strategies potentially able to counteract sarcopenia: physical exercise (as a non-pharmacological approach) and nanotechnology (considered as a suitable tool for pharmacological intervention).

Preliminary data based on morphometrical and morphological evaluations performed at transmission and fluorescence microscopy showed that in old (24 months) trained mice physical activity limit/prevent age-related modifications of myofiber (at cellular and sub-cellular level) as well as muscle ECM organization. Further, a pilot study tested the suitability of phospholipid-based nanoparticles (NPs: ethosomes, transethosomes) as nanocarriers to deliver vitamin D3, based on

evidence suggesting that vitamin D supplementation may improve muscle functionality in elderly. We have evaluated NPs biocompatibility in three different cell line representative of epithelial, connective and muscle tissue. Then, observation at bright-field, fluorescence and transmission electron microscopy were performed to assess NPs internalization, intracellular fate and the potentially associated subcellular alteration. Our preliminary results set the stage for *in vivo* investigations aimed at testing vitamin D transdermal administration as a novel strategy to address age-related muscular disease.

Finally, during my research period abroad I collaborated in setting up an *in vitro* co-culture system containing primary macrophages and murine myoblast cells which were previously exposed to etoposide (a drug able to induce DNA damage). Muscle cells were investigated by real-time PCR, to determine whether myoblast gain or lose their intrinsic function in presence of DNA damage and in presence or absence of macrophages. Lastly, immunofluorescence investigations were carried out in muscle cells to investigate the ability of macrophages to counteract DNA damage. The purpose of this preliminary investigation was to describe *in vitro* the crosstalk between macrophages and muscle cells under DNA damage condition.

# TABLE OF CONTENTS

# *INTRODUCTION*

# INTRODUCTION

## 1. Sarcopenia

### 1.1. State of the art

Sarcopenia is defined as age-related musculoskeletal disorder characterized by a progressive loss of muscle mass, strength, and functionality [1]. During aging, the skeletal muscle mass declines annually by ~0.1%–0.5%, with a dramatic acceleration post age 65 [2]. Although this phenomenon mainly affects older population (a prevalence range of 5–13% in people 60–70 years of age, and 11–50% in people >80 years [3]), it is now recognised to start from 40 years [4]. Sarcopenia contributes to a lower quality of life since is associated with an increased risk of falls and fractures, mobility disorders, cardiac and respiratory impairment, hospitalization, and death [5], producing significant implications in global healthcare services.

Over the years, research groups around the world have been tried to develop different diagnostic criteria and an unequivocal explanation of sarcopenia. Three decades later from the first definition by Rosenberg [6], sarcopenia has been formally recognised as a muscle disorder in the International Classification of Disease with its ICD-10-MC diagnostic code [7]. Moreover in 2018, the European Working Group on Sarcopenia in Older People (EWGSOP2) reviewed and extended the definition of sarcopenia in order to better diagnose, characterize and cure the adverse outcomes of the pathology [4]. Nowadays, the efforts of community science are still aimed at understanding the mechanisms that regulate age-related changes of skeletal muscle in order to improve the interventional strategies and relieve health care system [8].

Despite numerous studies, a single pathogenic cause for sarcopenia has not yet been settled in. In clinical practice is defined "primary sarcopenia" (or age related) when no other cause than aging itself is detected; if different factors contribute other than or in addition to the process of aging, sarcopenia is considered "secondary" [4].

In this case, sarcopenia is defined as a complex geriatric syndrome because of its multifactorial pathogenesis. Several mechanisms are proposed to be involved in the development of sarcopenia *e.g.*, neuromuscular degeneration [9], chronic inflammation [10], alterations in hormone levels and insulin sensitivity [11], altered immune-system regulation [12]. Moreover, sarcopenia can develop because of inadequate intake of energy or protein and behaviour/lifestyle factors [13] (Figure 1).

The core structural features of sarcopenia that contribute to reduction in muscle mass may include a depletion in the number of muscle fibres and a shortening of them [14]. Furthermore, it has been observed that muscle loss could be determined by impaired balance between protein synthesis and breakdown [15]. At the cellular and subcellular levels, sarcopenia is associated also with muscle mitochondria loss and dysfunction, mitochondrial DNA mutations and an increase in mitochondrial reactive oxygen species (ROS) emission [16]. Aging of skeletal muscle is accompanied by modifications also at nuclear levels with chromatin defects, malfunctioning in DNA damage repair system [17], and alterations in RNA transcription/maturation machinery [18]. Another potential mechanism mainly involved in the reduction of skeletal muscle mass converged on the loss in number and function of satellite cells that contribute to failure of aged muscle regeneration [19] (Figure 1).
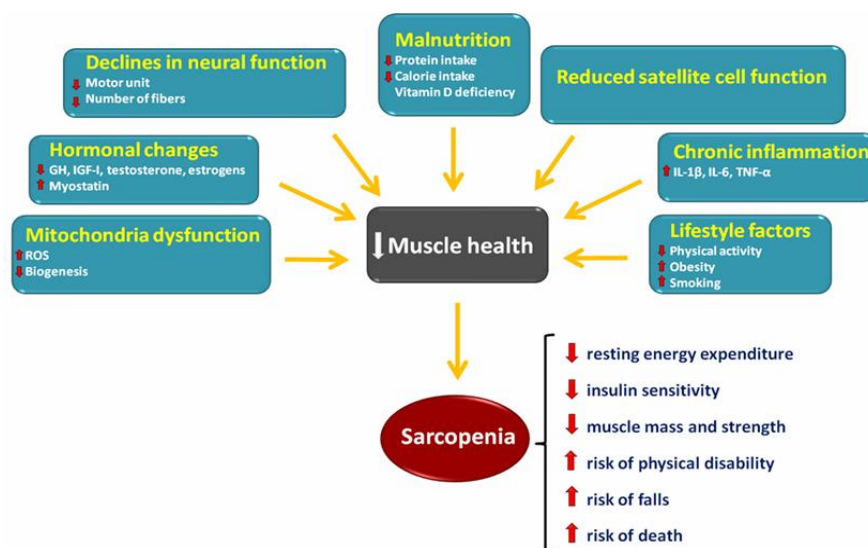


Figure 1: Schematic representation of the core structural features contributing to the onset sarcopenia and its adverse outcomes [20].

Despite the difficulties to define this condition, the recent understanding of the multifactorial causes correlated to sarcopenia have allowed the investigation of diverse therapeutic approaches, although only some of them are effective in treating and preventing sarcopenia and its correlated adverse outcomes. However, promising alternative therapeutic strategies are nowadays under investigation.

## 1.2. Age-related changes in skeletal muscle

### 1.2.1. Skeletal muscle fibre types

The loss in muscle mass and strength during aging can be directed by specific changes in fibre number, size, and typology. The myosin heavy chains (MHC) isoforms expression determines myofibers types and thus, their function in response to neural excitement [8]. The muscle fibres can be classified as oxidative slow-twitch fibres (type I); glycolytic fast-twitch fibres (type II) in rodent, which are equivalent to type IIX fibres (glycolytic fast-twitch) in human [21, 22]. Each muscle has type I to type II myofiber ratio. Type I are preferentially rich in mitochondria and myoglobin that make them reddish in colour. Oxidative phosphorylation generated by mitochondria is predominant mechanism for energy production in this myofibers, making them suitable for sustain aerobic exercise [23]. On the contrary, type II B and IIX produce more force in comparison with type I myofibers, because of the largest cross-sectional area (CSA) and highest contractile velocity. Moreover, these fibres contain less mitochondria; in particular the primary source of ATP in type II B myofibers is generated by glycolysis of glycogen [23, 24]. Many reports have demonstrated that aging is accompanied with fibre-type shift from type II to type I determining a progressive decrease mainly of type II B fibre number and size [25, 26]. A failed cycle of denervation of type II fibres with a consequent reinnervation with axons from type I motor unit is one of the mechanisms mainly investigated during aging muscle. Consequently, the percentage of type I fibres tends to increase when compared to type II fibres which are progressively lost with a decrease of both CSA and cellular components responsible of power generation [23]. It has been reported that neuromuscular degeneration, defined as the progressive loss of motoneurons with consequent muscle fibres atrophy, may be implicated in this process [13, 27].

Moreover, it seems likely that fibre type transition precede loss of motoneurons and that the muscle atrophy arises only in very advanced stages of aging, triggering a more aggressive decrease in muscle mass and strength [28]. Since the loss of muscle mass due to fibre type shift affects more severely hindlimb than forelimbs muscles in mammals this phenomenon have a stronger impact on elderly health. Thus, decreased muscle power may complicate daily actions such as rising from a chair or climbing steps [23, 29, 30].

### 1.2.2. Mitochondria

Several cellular and molecular mechanisms are contributors to the aetiology of age-related muscle wasting. Mitochondria play pivotal role in several functions within the cell, including energy production, regulation of calcium homeostasis, apoptosis, senescence, and redox regulation [31, 32]. Efficient skeletal muscle bioenergetics rely on mitochondria, and mitochondrial dysfunction is recognized in literature as one of the major "hallmark of aging" [33], contributing to altered skeletal muscle mass and strength.

Over the last years, many studies provided evidence of mitochondrial dysfunctions comparing skeletal muscle of old and young animals or humans (reviewed in [34]). Mitochondrial functional and qualitative decline have been related to an increased accumulation of mtDNA mutations in muscle fibres mostly affected by sarcopenia [35]. The latter event produces errors in the synthesis of electron transport chain components, that leads to defective ATP production and ROS generation (reviewed in [31]). Studies using muscle transcriptomes also revealed a reduced expression in genes involved in regulation of mitochondria biogenesis and homeostasis [36]. The diminished mitochondrial capacity typically observed during aging together with fewer functional mitochondria, leads to a lower capacity of force production. Interestingly, the process of mitophagy which guarantees the maintenance of functional mitochondria eliminating the damaged ones, seems to reduce during aging [37]. These findings may extend previous studies reporting an increase in mitochondrial number in muscle cells of aged mice [38], supporting the decreased turnover with a consequent accumulation of dysfunctional mitochondria observed during aging [39].

Mitochondria can be distinguished basing on their localization within the skeletal muscle: subsarcolemmal mitochondria (SS) more globular in size, are placed below the sarcolemma of muscle fibre, often close to myonuclei and blood vessels [40]. SS mitochondria are identified as the place where biochemical exchanges between blood and myofibers occur [41, 42]. Intermyofibrillar mitochondria (IMF), characterized by elongated shape, dwell between the myofibrils [40], and are the site where biochemical pathways related to contraction occur [41]. Structural mitochondrial abnormalities are observed in skeletal muscles of old mice: ultrastructural morphological evaluation [37] have shown that both SS and IMF mitochondria have larger size and longer cristae. It has been largely hypothesised that these morphological alterations could be related to unbalanced fission/fusion processes as well as activity of shaping proteins [43].

Moreover, the age-related lipids accumulation in skeletal muscles [44, 45] could promote a higher consume of fatty acids as the energy source for respiration, thus inducing enlargement of mitochondria and expansion of their cristae [46, 47]. Furthermore, the activation of apoptosis process due to mitochondrial dysfunction may further impairs skeletal muscle strength and mass in aging [48]. Nevertheless, the actual knowledge about changes of mitochondrial dynamic, function and structure involved in development of sarcopenia need to be clarified.

### 1.2.3. Muscle protein turnover and RNA pathway

Skeletal muscle operates as the major reservoir of body proteins and amino acids which are used for energy production as well as protein synthesis. As in all mammalian tissues, a dynamic balance between the synthesis and the degradation pathways regulates the levels of specific proteins. In particular, protein turnover in skeletal muscle is regulated by nutritional, hormonal and mechanical factors [49, 50]. Progression toward muscle wasting during aging may involve the alterations in skeletal muscle protein turnover, whereby rates of proteins breakdown chronically may exceed their synthesis [51], leading to the loss of muscle mass. Few studies performed on skeletal muscle of human subjects have shown evidence of aging-related decline in protein synthesis pathways that contribute to sarcopenia [52]. In addition, according to research carried out both in humans [52] and rodents

[53], an enhanced muscle proteolysis may contribute to the loss of muscle mass in sarcopenia. However, the age-associated alterations of protein turnover can include changes in genome integrity, gene expression [54] and translation and post-translational modifications of proteins [55]. Functional changes in mRNA-processing machinery have been described in several age-related diseases (reviewed in [56]) supporting the idea that the alterations of gene expression pathways do not only imply mutations but may be also related to changes in the transcription and/or splicing of pre-mRNAs. The steps of processing, maturation and cytoplasmic export of mRNA take place in the following nuclear ribonucleoprotein (RNP-) containing structures: perichromatin fibrils (PFs) are the *in situ* counterpart of nascent mRNA (reviewed in [57]) and the site of early splicing [58]; interchromatin granules (IG), recognizable as clusters in interchromatin space, are sites of storage of mRNA transcription/maturation factors [59]; perichromatin granules (PG) that act as intranuclear and nucleus-to-cytoplasm transport of already spliced mRNA [57].

It has been observed that both myonuclei of skeletal myofibers of old rats [60] and satellite cells of the same old muscle [61], have smaller size, an increased proportion of heterochromatin and a lower amount of DNA/RNA hybrid molecules, phosphorylated form of RNA polymerase II (RNA pol II) and splicing factors, supporting the idea of age-related alteration in RNA transcription and maturation pathways. Moreover, during aging myonuclei also showed an increased amount of polyadenylated tails (*i.e.*, markers of mature RNA) and cleavage factors, as well as of PFs an PGs in interchromatin space, highlighting the mRNA processing and transport impairment during aging [60-62]. Changes in the distribution and density of key nuclear factors involved in maintaining chromatin stability, processing and transport of mRNA have been investigated also in subnuclear compartments (e.g., heterochromatin areas, interchromatin space and nucleolus) of rectus femoris muscle of old mice [18]. Immunocytochemical reactions showed a reduction of nuclear actin in all subnuclear compartments described above in old mice; since nuclear actin acts as motor protein and regulator of RNA transcription, its lower amount supports the impairment of mRNA transcription in muscle aging. Interestingly, either the pre-ribosome biogenesis and its export to cytoplasm is

found to be affected during aging, as demonstrated by lower amount of 5-methyl cytosine (5-mC, an epigenetic regulator of gene transcription) nuclear actin and ribonuclease A (RNase A, an RNA degrading enzyme) in nucleoli of the same sample. These findings extent the age-related protein turnover dysregulation, further supporting the concept of nuclear involvement during aging.

### *1.2.4. Satellite cells*

Satellite cells (SCs) are muscle adult stem cells which resides in specialized niches located below the basal lamina and adjacent to the sarcolemma of myofibers [63]. In homeostatic muscle, SCs are normally present in a reversible state of quiescence. However, in response to external stimuli, such as degenerative muscle disease, muscle injury, physical exercise, SCs exit the cell cycle and produce a population of committed progenitors that can either differentiate, in order to generate new myofibers and repair the damaged ones or return to quiescence and replenish the SCs pool (reviewed in [64]). The functional decline and the lower amount of SCs are typically associated to aging leading to the loss of muscle regenerative capacity. Indeed, studies performed on muscles of old humans and animals showed a lower content of satellite cells when compared to the younger counterparts (reviewed in [19]).

Over the last years it has been proposed that the exhaustion of regenerative potential may arise from SCs niche, systemic and SCs themselves alterations. These modifications could drive some SCs enter into a senescence state at advanced age (reviewed in[64]).

Among the intrinsic factors (Figure 2), age-related alterations of numerous signalling pathways are known to intensify the myogenic differentiation of SCs enhancing the exhaustion of their pool [65] and the loss of quiescence state [66]. Moreover, many other cell-intrinsic signs of aging affect SCs such as epigenetic alterations, altered metabolic and autophagic process, mitochondrial dysfunctions, loss of genomic integrity and increased state of senescence [33, 67].

The long-lasting persistence of stem cells in the organism makes them prone to the exposure to genotoxic assaults from both endogenous and exogenous sources,

resulting in a potential accumulation of DNA damage that guides to stem cell functional decline [68]. Studies carried out on aged satellite cells, revealed increased levels of nuclear foci staining for the phosphorylated form of the variant histone H2AX (γH2AX)[69], a marker of DNA double strand-breaks[70]. Furthermore, epigenetic modification founded in satellite cells of over 28 months old mice may determine the transition from quiescence to pre-senescence state of SCs [71]; since senescence is often coupled with DNA damage, this could support the idea of DNA damage occurrence in satellite cells during aging [72]. Additionally, genetic manipulation of genes involved in DNA Damage Response (DDR) leads to various muscle stem cell defects that mirror aging phenotypes [72].
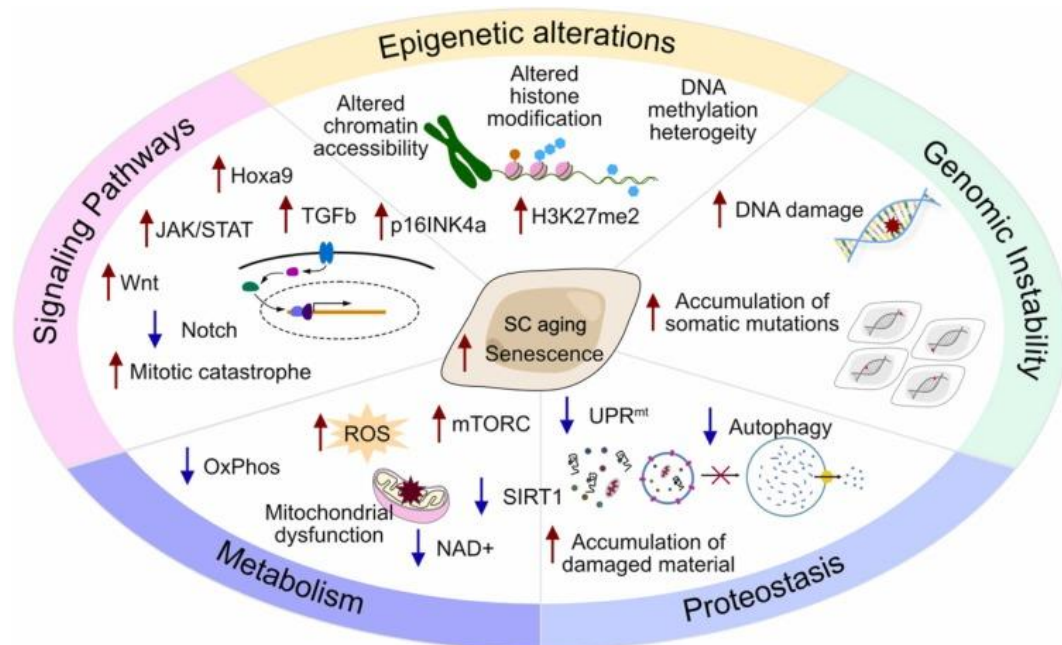


Figure 2: Schematic representation of SCs intrinsic age-related changes [64].

Extracellular signals, as well, can influence quiescence, proliferation, multipotency and differentiation of SCs. Aging of systemic environment, for example, may alter the normal functions of SCs. Interestingly, heterochronic parabiosis experiment shed light on some specific blood factors that play a role in SCs regenerative mechanism. Indeed, by joining the circulatory system of aged and young mice, the regenerative capacity of muscle in old mice was improved [73, 74], supporting the idea that aging of tissue milieu may contribute to satellite cells decline.

Moreover, extracellular signals may arrive also from the local environment namely, satellite cells niche [75]. SCs niche can be defined as a complex of somatic and

stromal cells (*e.g.,* myofibers, fibro-adipogenic progenitors (FAPs), immune and endothelial cells), tissue and muscular extracellular matrix that directly interact or are close to the SCs, contributing to maintain the functionality of SCs [63, 64]. The SCs niche physiologically modify muscle stem cell function by secreting growth factors, cytokines as well as remodelling the muscular extracellular matrix (ECM). During aging, altered signalling of transforming growth factor (TGF)-beta and delta-driven Notch together with lower levels of fibroblast growth factor 2 (FGF2), are found in aged muscle, leading to imbalance between SC activation and differentiation. Moreover, lower amount of some muscular ECM components is found to cooperate to the loss of regenerative capacity in SCs of old skeletal muscle (reviewed in [64]).

Among the niches cellular constituents, immune cells and in particular macrophages, increase their number and stimulate satellite cells functions in case of muscle injury [76]. Indeed, macrophages not only clear the damaged areas by phagocyting tissue debris, but also sustain the regenerative myogenesis producing several factors such as Tumor Necrosis Factor-α (Tnf-α), [77] Interleukin-6 (IL-6), Interleukin-1 beta (IL-1β) [78] which stimulate the SCs proliferation and influence the intrinsic capabilities of muscle cells, suggesting an active interplay between macrophages and muscle resident cells involved in the repair process [79]. During aging and under regenerative stress, there can be defective recruitment of myeloid cells and deficiencies in their function that affect the muscle regeneration process.

Based on the emerging knowledges on the intrinsic and environmental impairment of SCs, different potential therapeutic strategies are still under investigation in order to counteract the aging of skeletal muscle stem cells.

## 1.3. Muscle extracellular matrix

The muscular extracellular matrix (ECM) is involved in muscle development, in proliferation and differentiation of both satellite cells and muscle fibres, representing the structural support for blood vessels, and nerves. This plays also a role in the transmission of contractile forces [80] and muscle tissue repair process [81]. The muscular ECM consists of three distinct and interconnected layers: the epimysium, that wraps the entire muscle tissue; the perimysium, that surrounds each

bundle of muscle fibres and the endomysium, the connective tissue that covers each muscle cells (reviewed in [82]). The ECM of skeletal muscle appears as a complex meshwork of collagenous and non-collagenous glycoproteins such as laminin, tenascin and fibronectin, glycosaminoglycans and proteoglycans. In addition, there are components with the role of receptors and regulators (e.g., integrin) and matrix metalloproteinase (MMP). Taken together, the molecules contained in ECM are important for maintaining the physiological activities of skeletal muscle [82].

During aging, skeletal muscle ECM undergoes structural and functional remodelling. It has been shown that ECM is the microenvironment that support the migration, adhesion, proliferation, and differentiation of satellite cells. Age-related alteration of some cell signalling pathways (e.g. upregulation of Wnt/beta catenin and TGF beta) determine a fibrogenic conversion of both satellite cells and myoblasts that contribute to muscle fibrosis, one of the hallmarks of muscular aging, dystrophies and severe muscle injuries (reviewed in [83]). Moreover, the excessive accumulation of ECM components seems to be correlated with epigenetic alterations of ECM genes, a phenomenon that provokes their up regulation with a consequent deregulation of myogenic differentiation capabilities of SCs [84]. It is to be noted that in literature the data about age-related changes of muscular ECM are very heterogeneous. Indeed, proteomic and morphological analyses performed on gastrocnemius muscle of old mice revealed that the amount of fibrillar collagens, such as collagen type I and III, did not change with aging [85]. Nevertheless, transcriptomic analysis of aged skeletal muscle, revealed a down regulation of collagen type I and type III genes [86], while it has been observed an increased collagen type I and III content in aged long-lived animals (reviewed in [87]). The different results obtained may be explained by the type of muscle used for the analysis, processing and/or techniques applied in each experiment. The age associated increase of ECM components might also be explained by an altered degradation process rather than synthesis or by a combination of both processes [86, 87].

Studies performed on skeletal muscle of aged mice showed that the altered composition of ECM may affect its mechanical and structural features. Since muscular ECM seemed to be related to increased stiffness during aging [87, 88],

different studies suggest a correlation between the altered deposition of ECM macromolecules, increased advanced glycation end-products (AGE) and muscle stiffness [89].

Accordingly, it has been reported that the fibrillar collagen bundles (predominantly made of type I collagen) of perimysium layer of old mice showed a more loosely, linear, and larger organized structure in comparison with the adult counterpart [85]. Interestingly, in the same animals, higher levels of proteoglycans (such as lumican, byglican and asporin) are found in old skeletal muscle by using a proteomic approach. Proteoglycans are important component of ECM and these work as connector with collagen components regulating collagen fibrillogenesis as well as collagen fibril size and the space between single collagen fibrils. As result, in old vs. adult mice, single collagen fibrils showed increased distance between each other, despite the higher level of proteoglycans seemed to not affect the collagen fibril size. These data, together with a lower collagen fibre "tortuosity" [90] and the highest amount of glycation crosslinking observed in aged skeletal muscle [91], support the hypothesis of interposition of ECM components between collagen fibrils leading to increased muscle stiffness typically observed during aging.

Beyond the three layers that constitute the muscular ECM, the basement membrane can be identified as a supramolecular ECM structure [82] mainly composed of collagens type IV, laminin, glycoproteins and proteoglycans interconnected to each other in order to form an integrated structure [92]. Collagen type VI is not properly known as basal lamina molecules but dwells in the neighbourhood of that playing a role as anchoring component of basement membrane [82]. Moreover, type VI collagen is a key component of SCs niche, regulating the physiological function of skeletal muscle. In aging muscle, either the function or architecture of basement membrane could be compromised by different factors. The age-related increased amount of collagen type VI [85] and collagen type IV found in old animals [85] [93] may affect their structural role in basement membrane. Moreover, the accumulation of basal membrane proteins, such as collagen type IV, showed to affect the SCs behaviour supporting the hypothesis of satellite cells reduction during aging [87, 94]. Laminin is a glycoprotein which can promote the proliferation, differentiation, and adhesion of muscle cells. The age-related increase

of laminin found in old animals may contribute not only to the increase of basement membrane thickness [85], but also may alter the capability of muscular ECM as reservoir of growth factors and cytokines needful for myogenic conversion of SCs [95]. Finally, the basement membrane alteration with aging showed to have a negative impact on muscle regeneration capability through deficient support for muscle fibres and disorganized scaffold orientation [96].

## 1.4. Immune system

Under minor or severe regenerative stress (*e.g.,* strains, physical exercise, trauma, or degenerative muscle disease), both SCs and cells that make up their niche are involved in a coordinate sequence of events to repair injured muscle. Among others, immune cells and in particular macrophages, play a critical role in SCs regeneration responses: after injury these increase in number, remove tissue debris as well as influence SCs function and the milieu of the activated niche [97] [98]. The first to infiltrate the injury site are neutrophils that promote the recruitment and differentiation of macrophages into pro-inflammatory phenotype which stimulate SCs activation and proliferation (reviewed in [99]). Afterwards, macrophages undergo to pro-repair transition in order to stimulate myogenic differentiation and reparative process. Thus, muscle regeneration can be defined successful when the differentiation of macrophages in the two phenotypes take place in the correct time course ([100] [101]). Recent findings demonstrate that age-related dysfunction of myeloid cells is characterized by a defective recruitment of macrophages in the site of muscle injury [97] and by an altered transition between inflammatory/pro-reparative profiles during muscle injury response as in old animals [97] than humans (reviewed in [102]).

Different *in vitro* studies reported that some of the age-related changes in macrophages can occur independently of the muscle environment. For example, primary human myoblasts cultured in conditioned media obtained from macrophages derived from blood monocytes of old human [103] and myoblast cultured in conditional media obtained from macrophages derived from bone marrow cells (BMCs) of old mice [104], showed in both condition an impaired proliferation capacity when compared to myoblasts treated with conditioned media

of macrophages obtained from young counterpart. In addition, the myoblasts treated with media from old mice BMDMs expressed a lower amount of MyoD (myoblast determination protein 1) and myogenin (MGN) - two factors involved in myotube differentiation - suggesting that age-related macrophage progenitors' impairment affect both proliferation and differentiation process of myogenic cells [104]. Furthermore, through a bone marrow cells transplantation from an old mice donor into young mice it has been showed that SCs of young mice were reduced in number with a tendency to fibrogenic conversion [104].

Immune cells can influence muscle regeneration by releasing several cytokines, chemokines (reviewed in [64, 98]) and growth factors. However, many of those may display defective age-related signalling pathway as well as altered expression levels. For example, Tumor necrosis factor α (TNF-α), interleukin-6 (IL-6) and interleukin-1β (IL-1β) are pro-inflammatory cytokines released by macrophages, satellite cells and myofibers during the regeneration process of injured skeletal muscle. TNF-alpha and IL-6 positively affect SCs proliferation after muscle injury; IL-1 β, acts by recruiting immune cells to the site of injury and influencing the intrinsic capabilities of myoblasts. Indeed, following skeletal muscle injury, IL-1 β is highly expressed by muscle cells, neutrophils and macrophages recruited around the injured area, promoting the proliferation of primary muscle cells [78]. It has been reported that at advanced age the levels of IL-1, IL-6 and TNF-α from mononuclear cells increase contributing to muscle wasting and dysregulation of SCs normal function (reviewed in [98] [102]).

## 1.5. Physical exercise: a gold standard treatment

Physical inactivity in elderly can lead to onset of sarcopenia since it promotes the loss of muscle mass and strength. Moreover, this condition is associated with increased mobility limitation and poor quality of life [1]. Several studies proposed physical exercise as one of the best non-pharmacologic approaches to slow down the musculoskeletal system decline (Figure 3) and several clinical condition commonly related to aging such as osteoporosis, osteoarthritis, heart disease, diabetes, and depression [23].
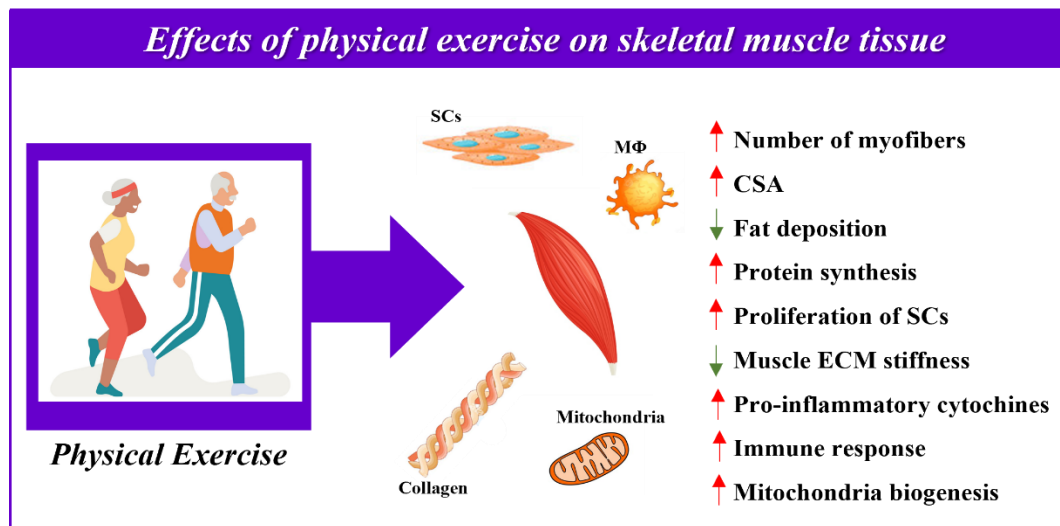
Figure 3: Potential effects of physical exercise on skeletal muscle tissue and its environment.

A balanced physical training seems to counteract the decline in muscle mass and strength during aging [105] by increasing both the number and the cross-sectional area of skeletal muscle fibres (reviewed in [23, 61]) and preventing muscle fat deposition [106]. In terms of beneficial effects on age-related cellular changes, physical exercise increases the amount of transcription factors and binding proteins involved in the formation of new muscle fibres and in the transcription of mitochondrial genes [105].

Physical exercise can determine micro-muscle injuries that promotes the activation of satellite cells from their quiescence state, although the mechanisms underneath this event are still largely unknown. Studies performed on skeletal muscle of old rodents, showed that physical training may increase the number of satellite cells, promote their functionality [107] (e.g., activation, proliferation, migration and differentiation) and remodels SCs microenvironment, thus improving the regeneration capability of skeletal muscle (reviewed in [99]). Moreover, an ultrastructural cytochemical investigation of skeletal muscle reports the beneficial effects of physical exercise on transcriptional and post-transcriptional events in both myonuclei and SCs nuclei of old animals [61, 107]. Physical training seems to restore adulthood features in terms of myonuclear components involved in mRNA transcription, splicing and nucleus to cytoplasm transport. On the other hand, in SCs nuclei the effect of physical exercise seemed to be limited to the reactivation

of factors linked to  transcriptional and splicing process without increasing RNA production [61].

Another fundamental effect of physical exercise is that it may reorganize the structure of extracellular matrix, for example, reducing its stiffness in muscle of old animals [108] and/or promoting collagen turnover (reviewed in [87]). Moreover, physical activity may mitigate the inflammatory state, one of the typical hallmarks of muscle aging. Some authors suggested that exercise may influence the levels of expression of some pro-inflammatory cytokines such as IL-6 and TNF-α promoting, as result, a more efficient muscle regeneration process with the activation of SCs [109].

Little is still known about the potential consequences of exercise on the immune system. Recent findings on trained old human subject showed higher levels of anti-inflammatory cytokine mRNA that is involved in regulating the transition of macrophages from pro-inflammatory to pro-reparative phenotype [109]. However, whether physical training affect the shift of macrophages remains still unknown [102].

Although one of the best interventional approaches to counteract age-related wasting of skeletal muscle is an appropriate exercise program, patients with severe sarcopenia cannot endure this kind of treatment. Pharmaceuticals named "exercise mimetics" or "exercise in a pill" are proposed as replacement pharmacological therapy to treat these population of patients, since these molecules may activate some of the signalling pathway promoted by exercise (reviewed in [8]). However additional studies are required.

## 1.6. Nutritional treatment

Behavioural lifestyles, such as scarce physical activity and malnutrition, represent contributing factors to sarcopenia. In elderly persons energy and nutrient consumption are frequently reduced, a geriatric condition known as "anorexia of aging" [110]. Since energy intake declines by half between 20 and 80 years, affecting especially frail [111] and/or sarcopenic people [112], nutritional interventions have been proposed as a non-pharmacological approach to reverse

sarcopenia [13]. For example, increased protein and essential amino acids intake in a dietary program may influence muscle mass and function in elderly patients [113] stimulating muscle protein synthesis [114]. Deficiency of vitamin D influences muscle mass and function [115]. Considering its role in myogenesis, muscle metabolism and tropism, the decline of Vitamin D may be related to sarcopenia [114]. However, an adequate dietary supplementation of vitamin D in elderly can increase muscle strength and improve some cellular mechanism (e.g, protein synthesis, mitochondrial function) [116, 117]. Notwithstanding vitamin D intake shows beneficial effects in reducing its age-related deficiency, preliminary *in vitro* studies have proposed that vitamin D integration trough topical application increases muscular function, especially in the case of people suffering from vitamin D deficit related to aging [118].

Nowadays, other nutritional supplementations (summarized in [13]) are proposed as strategies to improve muscle performance. However, no remarkable consequences of nutritional addition alone on muscle mass and muscle strength have been conclusively-demonstrated [119]. Currently, many trials and studies are in progress to address both exercise and nutritional interventions for sarcopenic patients [120].

# 2. Methodological approaches

## 2.1. In vivo and in vitro experimental models of muscle aging and sarcopenia

### 2.1.1. Mouse models

Experimental animals, such as mice, are widely used as suitable models to study human pathologies [121] for different good reasons:

- High gene homology with humans [122].
- Similarities in organs, tissues, cell biology and their mechanisms of functioning (reviewed in [123]).
- Mouse models get many diseases resembling to that of humans [124]; moreover, modern technologies allow their genetic manipulation in order to mimic the human pathologies [125].
- The relative low cost of mice and the opportunity to use a larger sample size in pre-clinical research, makes them one of the best candidate in experimental studies (reviewed in [126]).
- The use of mouse models improves the aetiology accuracy of human diseases, recapitulating their typical features (reviewed in [123]).

Regarding sarcopenia, different model organisms such as rodents, *Drosophila*, *Caenorhabditis elegans* and zebrafish, were proposed as valid candidates to study the biological and molecular mechanisms of sarcopenia as well as its relative interventions [127]. However, in several studies related to sarcopenia, mouse models have been chosen as suitable to investigation. Indeed, since the aging progress takes a long period to develop in humans, the use of mouse models and the rapid developing of their musculoskeletal system make study of sarcopenia cost effective taking place in a shorter time [128, 129]. Furthermore, the homology relationship between elderly and aged mice under a biological point of view, represents an advantage to deeper understanding age-related dysfunctions [130]. Finally, the choice of mouse models enables to overcome the ethical problem associated with human studies [123].

Numerous mouse models are currently used in experimental research of sarcopenia: aged mouse models; genetically engineered models; muscle atrophy induction models (*e.g.* Hindlimb suspension; Denervation model; Immobilization) [126].

- *Aged mouse models*

Since the aging process is recognised as one of the triggers of sarcopenia, aged mouse models are frequently used for aging related sarcopenia studies. When the selected form of aging is natural, 18 months old or older mice (22-, 24-, 27-months old mice; reviewed in [123]) are indicated in literature as valid aging mouse models. Moreover, different studies in which these models have been used, evaluated the presence of sarcopenia  according to some parameters strictly linked to disease, such as lower grip strength, exercise endurance, muscle mass [131], cross-sectional area  and some cellular age-related dysfunctions [132]. However, natural senescent models are time consuming and maybe not cost effective; thus, nowadays mice strains with accelerated aging are preferred in laboratory research (e.g. high fatty diet aging models, senescence accelerated mouse (SAM) (reviewed in [133]).

- *Genetically engineered mouse models*

Over the past years, the use of genetically modified mouse models increased in the study of muscle aging and sarcopenia. Indeed, a plethora of engineered animal models (e.g. knock-out mice, gene overexpression mouse models, mtDNA mutant mice; classified and reviewed in [123, 134]) are described in scientific literature as a valid tool to better understand altered molecular and biochemical pathways involved in the onset of sarcopenia as well as evaluate potential therapeutic strategies. However, among the disadvantages, mice genetic manipulation may exacerbate some features of sarcopenia that are not found under normal aging state. Moreover, it is possible to use mice with genetic knockouts to study a single altered pathway at time, thus limiting comprehensive knowledge of disease [133].

- *Muscle atrophy induction models*

Hindlimb suspension, denervation and immobilization have been designed as methods to induce and study muscle atrophy either in rat or mouse models [133]. Each of these models may mimic respectively the lack of physical exercise (hindlimb suspension) [135], neuro-muscular degeneration process (denervation) [13, 123] and muscle disuse related to bedridden patients (immobilization) [136], thus their use can be easily extended to investigation of age-related muscle deficiencies and sarcopenia. Although these methods seem to be faster and simpler for experimental purpose, the ethical concern may impose some limitations for using muscle atrophy induction models.

The choice of specific animal models must satisfy some criteria in line with the aim of research. Although similarities in aging process between human and mice allow the use of mouse models as suitable tools to study age-related disease such as sarcopenia, there are significant differences that must not be ignored (e.g, immune system functioning, anatomy, physiology, and shorter lifespan [137]). Moreover mice exhibit a lower muscle mass reduction and higher regenerative power [138] during aging. The composition of skeletal muscle changes between the two species, since mice muscles are mainly composed of fast type II fibres in comparison with humans [21]. Taken together, this variability needs to be considered especially in translational studies from mice to human. Furthermore, the set-up of unequivocal methods for evaluations of sarcopenia in mouse models may reduce the variability of results reported in literature [137].

## 2.1.2. In vitro models

The improvement of socio-economic condition determined increasing lifetime as well as the world-wide number of elderly [139]. As result, a great interest on age related skeletal muscle changes grew during the last years. This implied the setting up of experimental models able to recapitulate biological and molecular pathways of sarcopenia and to act as valid systems to test some therapeutic strategies [29]. Although *in vivo* experiments are frequently used in the study of human pathologies, such as sarcopenia, the recent regulations aimed at reducing animal

experimentations [140, 141]. In this perspective, *in vitro* systems have been developed as suitable alternative tools in biomedical research. Moreover, *in vitro* models are frequently selected compared to laboratory animals for different valid reason:

- Several biological and molecular processes are evaluated in standardized and controlled conditions without interferences of physiological reactions in a living body;
- Reproducibility of experiments and the use of lower number of replicates;
- Cost and time efficiency.

Among cell culture models used for investigation of aging of skeletal muscle and sarcopenia, there are: *i)* rat skeletal muscle L6 cells [142]; *ii)* C2C12, murine myoblast cell line.

C2C12 is an immortalized murine cell line able to proliferate. Cells fuse together to form myotubes under appropriate culture condition [143]. Because of their intrinsic capabilities, these cells became a well-established model both of skeletal muscle cell biology [144] and myoblasts differentiation processes [145]. C2C12 are derived from satellite cells (SCs) which are skeletal muscle stem progenitors able to proliferate and differentiate in adult muscle after activating stimuli [146]: thus, C2C12 are able to recapitulate satellite cells *in vitro* [147]. Among other advantages: C2C12 may be easily used for specific genes transfection in order to reproduce and study different pathologies [148, 149]; they can be used in co-culture system with more than two cell populations such as neural cells [150], to induce neuromuscular junction formation or fibroblasts and macrophages [151] to study myoblasts migration and proliferation; moreover, electro-pulse stimulation may be applied to C2C12 cells to investigate the muscle contraction process and mimic physical exercise *in vitro* [144]. The use of immortalized cell line allows the investigation of cellular and molecular mechanisms contributing to sarcopenia at time. For this purpose, C2C12 can be treated with several molecules (e.g., $H_2O_2$, sphingophospholipid, inflammatory cytokines and dexamethasone; reviewed in [133]) which induce some of pathological modifications related to sarcopenia.

Beside the use of C2C12 cell line, primary myoblasts cell lines derived from both murine and human skeletal muscle are proposed as valid approaches to study skeletal muscle development and regeneration in normal and age-related pathological condition [71, 152, 153]. Although their isolation and culture procedures are still challenging, it is assumed that they may retain some intrinsic features of tissues of origin [153]; moreover, the use of primary skeletal muscle cells derived from samples of different ages allows a better investigation of some alterations linked to sarcopenia [133]. Additionally, these cells represent an efficient tool used in pre-clinical research to investigate the beneficial effects of some therapeutical treatments designed to enhance the regenerative power of SCs during aging [154, 155].

Finally, another promising device able to reproduce *in vitro* part of cellular organization and environmental interaction of skeletal muscle *in vivo*, is the single myofiber explant culture technique. It might be applied for sarcopenia and muscle age-related disease research [156].

## 2.2. Ultrastructure and immunocytochemistry

Sarcopenia is recognised as musculoskeletal disease characterized by the progressive decline of muscle mass and strength during aging that led to loss of function and diminished quality of life [1]. The study of biological processes implicated in its pathogenesis is complicated by the multifactorial nature of sarcopenia, the long duration of aging process (especially in humans), the extended variability among individuals and species, the use of different experimental approaches [29]. Thus, scientific efforts based on state of the art pre-clinical and clinical investigations are necessary to deeper understand age-related muscle changes. In order to extend the knowledge on age-related muscle alteration and investigate on the role of physical activity as therapeutic strategy to manage skeletal muscle aging, the methodological approaches adopted in the first part of this thesis exploited electron microscopy alone or combined with histochemical and proteomic techniques on *ex-vivo* samples:

> ➢ Ultrastructural immunocytochemistry reactions were performed in myonuclei of rectus femoris muscles of old and late adult mice, to

determine the distribution and the density of key cellular proteins involved in RNA pathway (transcription, maturation, and transport). Immunocytochemistry was followed by Uranyl-free and lead citrate staining to reveal ribonuclear proteins and the sub-nuclear areas in which the localization of molecules is detected. During this work, we set up a new staining method using a non-radioactive lanthanide mix solution (Uranyl-free) as contrasting dye for both nucleoplasmic and nucleolar ribonucleoprotein-containing components for high-resolution studies. This procedure allows to avoid the use of radioactive uranyl salts whose application and purchase are nowadays severely restricted in experimental procedure. Moreover, in the same samples, a double immunolabelling reaction was performed to verify a co-transcriptional event. In this case, the use of terbium citrate staining allowed the observation at high resolution of RNA in perichromatin fibrils.

➢ Ultrastructural morphological and morphometrical evaluations were performed on gastrocnemius muscles of old and adult mice in combination with immunofluorescence and proteomic evaluation, in order to understand age-related muscular ECM changes and provide characterization of its composition and structural organization.

➢ Finally, morphological and morphometrical assessment combined with fluorescent immunohistochemistry and proteomic approaches were used to evaluate the effects of treadmill running on some cellular (e.g., mitochondria) and nuclear components (e.g., nucleoli); fibre size, fibre type; muscular ECM composition and architecture of aged skeletal muscle by comparing trained versus sedentary old mice.

Regarding the animal models for these studies, our mice are re-derivates from the INRCA breed (Ancona, Italy). The INRCA breed is a 40-year established Balb-c mice strain which has been widely used for studies of physiological ageing: indeed, these mice have a long life (mean life span 25 months; maximal life span 34 months) with a relatively low incidence of pathologies in comparison with the usual Balb-c strain.

## 2.3. Nanocarriers and co-culture system

Currently, a unique pharmacological treatment is not available to cure sarcopenia. However, nutritional deficiencies such as vitamin D depletion, may influence muscle mass and functionalities. In the second part of the present thesis, we investigated the potential role of phospholipid-based nanosystem, named ethosomes (ET) and transethosomes, as delivery systems for vitamin D3. Particularly, nanocarriers were administered to keratinocytes, fibroblasts and myoblasts, and their *in vitro* cytotoxicity evaluated. Through combined microscopy techniques (bright-field, fluorescence microscopy and transmission electron microscopy), both the uptake and subcellular fate of nanomolecules were investigated. This preliminary investigation may pave the way to novel strategies aimed at evaluating the effects of vitamin D supplementation *in vivo* through transdermal administration in case of muscular deficiencies related to aging, such as sarcopenia.

Finally, a pilot *in vitro* study has been performed in order to evaluate the active interplay between macrophages and muscle satellite cells (SCs). Indeed, we have tried to set-up and characterize an in vitro model using C2C12 murine myoblast cell line co-cultured with bone marrow derived macrophages (BMDMs). To this end, C2C12 cells were treated with etoposide (a drug able to induce a DNA-double strand breaks (DDS) and then co-cultured with BMDMs. The co-culture system was used for two different types of analysis: in one case, muscle cells were sorted through fluorescence-activated single cell sorting (FACS) technique and processed for real-time PCR evaluation, in order to understand if in presence of DNA damage and with or without macrophages, myoblasts respectively gain or lose their intrinsic function; in the second case, the co-culture system has been used for immunocytochemistry reaction, to investigate on the role of macrophages as potential activators of the DNA damage machinery response in muscle cells. This preliminary investigation aimed at recapitulating through an *in vitro* model two altered conditions (e.g., DNA double strand breaks (DDS) accumulation in muscle resident cells and macrophages deficiencies) observed in aged skeletal muscle, avoiding animal testing.

# 3. Aim of the work

The main aim of my doctoral program was the study of ultrastructural features of skeletal muscle and muscle extracellular matrix in sarcopenia. Indeed, sarcopenia is recognised as a multifactorial condition linked to a network of cellular and nuclear age-related alterations. Several proposed processes are: mitochondria dysfunction, heterogeneity in muscle fibres size and number, along with impaired RNA transcription/maturation processes that may hamper the protein turnover. Moreover, age-related remodelling of muscle ECM in both architecture and composition may possibly hinder muscle functionality and repair.

Furthermore, a target of my work was to investigate some interventional approaches aimed at attenuating the course of pathology by analysing the effects of adapted physical exercise on both skeletal muscle and muscle ECM (as non-pharmacological approach) and evaluating the potential of cholecalciferol delivered by NPs to improve muscle performance (as pharmacological strategy).

To achieve these goals, different microscopy techniques (fluorescence and bright-field microscopy and transmission electron microscopy) were used and combined with proteomic analysis performed in collaborative projects.

Finally, during the study period abroad, I collaborated in setting up a co-culture system in order to describe the effects of crosstalk between muscle cells and macrophages under DNA damage conditions.

# RESULTS

# CHAPTER 1

## Skeletal muscle and ECM

**Ultrastructural immunocytochemistry shows impairment of RNA pathways in skeletal muscle nuclei of old mice: a link to sarcopenia?**

*M.A. Lacavalla, B. Cisterna, C. Zancanaro, M. Malatesta*

European Journal of Histochemistry (2021)

**ABSTRACT**

Aging implies a progressive decrease in skeletal muscle strength and size, known as sarcopenia.

The mechanisms underlying sarcopenia are diverse and may include functional alterations in the nucleus such as the pathway of gene expression associated with either genome mutations or impairment in pre-mRNA transcription/splicing. Previous studies have demonstrated in different types of old cells that perichromatin fibrils (PFs) accumulate in the interchromatin space and different mRNA processing factors undergo quantitative modifications and/or partial relocation in interchromatin granules (IGs), suggesting alterations in the mRNA transcription/maturation machinery. Moreover, an unusual distribution of nucleolar factors has been observed in aged myonuclei, suggestive of a defective pre-ribosome biogenesis in elderly.

In the present work, immunocytochemical analyses at the electron microscopy level are performed in order to study the distribution and amount in different sub-nuclear region of various nuclear factors involved in mRNA processing and export in myonuclei of old and adult mice. We selected the quadriceps femoris muscle since it is mainly composed of fast fibres, which are especially affected by sarcopenia. We aimed at understanding the mechanisms responsible for the age-related nuclear alterations described above. In particular, we aimed at verifying the hypothesis that the nuclear degradation and transport pathways may be hindered during aging.

**pagepress**

# Ultrastructural immunocytochemistry shows impairment of RNA pathways in skeletal muscle nuclei of old mice: A link to sarcopenia?

Maria Assunta Lacavalla,* Barbara Cisterna,* Carlo Zancanaro, Manuela Malatesta

*Department of Neurosciences, Biomedicine and Movement Sciences, University of Verona, Italy*

*\*These authors contributed equally*

**ABSTRACT**

During aging, skeletal muscle is affected by sarcopenia, a progressive decline in muscle mass, strength and endurance that leads to loss of function and disability. Cell nucleus dysfunction is a possible factor contributing to sarcopenia because aging-associated alterations in mRNA and rRNA transcription/maturation machinery have been shown in several cell types including muscle cells. In this study, the distribution and density of key molecular factors involved in RNA pathways namely, nuclear actin (a motor protein and regulator of RNA transcription), 5-methyl cytosine (an epigenetic regulator of gene transcription), and ribonuclease A (an RNA degrading enzyme) were compared in different nuclear compartments of late adult and old mice myonuclei by means of ultrastructural immunocytochemistry. In all nuclear compartments, an age-related decrease of nuclear actin suggested altered chromatin structuring and impaired nucleus-to-cytoplasm transport of both mRNA and ribosomal subunits, while a decrease of 5-methyl cytosine and ribonuclease A in the nucleoli of old mice indicated an age-dependent loss of rRNA genes. These findings provide novel experimental evidence that, in the aging skeletal muscle, nuclear RNA pathways undergo impairment, likely hindering protein synthesis and contributing to the onset and progression of sarcopenia.

**Key words:** Transmission electron microscopy; nuclear actin; 5-methylcytosine; ribonuclease A.

OPEN ACCESS

## Introduction

Aging severely affects skeletal muscle with a progressive decline in muscle mass and a parallel decrease in strength and endurance. This condition, known as sarcopenia, leads to frailty, functional loss and disability with significant socioeconomic consequences.[1] A single pathogenic cause for sarcopenia has not yet been settled in. Several contributing factors to sarcopenia have been proposed *e.g.*, impairment of proteolytic and autophagic pathways,[2] loss of satellite cells,[3] mitochondrial dysfunction,[4] chromatin dysregulation,[5] rDNA genome instability,[6] and depletion of myonuclei.[7]

Skeletal muscle is a highly plastic tissue and understanding the regulatory mechanisms that underlie the sarcopenic drive is indeed essential to develop interventional strategies. In particular, protein homeostasis is progressively lost in skeletal muscle during aging,[8] likely contributing to muscle loss and dysfunction.[9] A balanced protein metabolism in the skeletal muscle tissue can be operated by the regulation of both gene expression and protein degradation, as well as the control of mRNA stability and translation rate.[10] Functional alterations of the mRNA-processing machinery are responsible for several age-related diseases (reviewed in[11]) thereby supporting the concept that aging-associated alterations of the gene expression pathways are not necessarily and exclusively related to genomic mutations but may be also associated with impairments in the transcription and/or splicing of pre-mRNAs.

The processing and maturation of mRNA to be exported to the cytoplasm imply several modification steps, where many processing factors operate in a chronologically and spatially defined order and, for the most, co-transcriptionally (reviewed in[12]). The perichromatin fibrils (PFs) are the *in situ* form of nascent transcripts (reviewed in[13]) as well as the splicing,[14] and end-processing products therefrom:[15] PFs are ribonucleoprotein structures morphologically recognized at transmission electron microscopy (TEM) as fine fibrils that mainly locate along the border of condensed chromatin.[16] The factors involved in mRNA transcription and maturation are stored, assembled and modified in the interchromatin granules (IGs[17]), which occur as clusters in the interchromatin space. The already spliced mRNA is stored in the perichromatin granules (PGs): these roundish structures locate at the border of condensed chromatin and act as vectors for the intranuclear and the nucleus-to-cytoplasm transport of mRNA.[13]

Previous studies on different cell types demonstrated that, during aging, the structure, regulation and function of mRNA are affected:[18] the alterations in the mRNA transcription and maturation machinery are associated with a decrease in RNA polymerase II and a partial relocation and/or quantitative modification of factors involved in mRNA processing along with accumulation of PFs and PGs.[19-23] The pre-ribosome biogenesis and ribosome export to the cytoplasm are affected by aging as well, as demonstrated by the reorganization of the nucleolar components,[21,24] the variation in size of nucleoli,[25] and the accumulation of alterations of the nucleolar structure.[26]

Evidence has already been provided of morphological and functional modifications of myonuclei during aging.[21,27] In the nuclei of skeletal myofibers as well as in cultured primary myoblasts[28] from aged animals, a smaller size and a significant increase in condensed chromatin are accompanied by a decrease in RNA transcription and maturation, as demonstrated by the lower immunolabelling density of hybrid DNA/RNA, RNA polymerase II and splicing factors.[21,29] These findings support the concept that reduced/impaired RNA transcription and processing should be included among the multiple causes of sarcopenia.[5-7] In myonuclei of old rodents, the end-processing and nucleus-to-cytoplasm export of RNAs proved to be also affected, as shown by the accumulation of PFs, polyadenylated tails (*i.e.*, markers of mature RNA) and PGs in the interchromatin space,[21,29] as well as increase and/or redistribution of cleavage factors.[21,27,29]

To get a deeper insight into the nuclear pathways involved in the synthesis, transport and degradation of RNAs in skeletal muscle nuclei during aging, we compared the distribution and relative amount of nuclear actin, 5-mC and ribonuclease (RNase) A in myonuclei of rectus femoris muscles from old and late adult mice. As a motor protein, nuclear actin is a marker of intranuclear motility while also being a regulator of RNA transcription;[30] the methylated form of the DNA base cytosine, 5-methyl cytosine (5-mC) is an epigenetic regulator of gene transcription[31] involved in chromatin organization; and RNase A is responsible for the intranuclear degradation of RNA.[32]

We used quantitative ultrastructural immunocytochemistry as a suitable experimental approach to detect and locate in well-defined nuclear domains these molecular factors that play crucial roles in nuclear physiology. The differences we observed in the myonuclei of old (28-months-old) mice *vs.* their late adult counterpart reinforce the notion that during aging myonuclei undergo an impairment of RNA pathways, thereby further supporting a myonuclear involvement in the sarcopenia of aging.

## Materials and Methods

### Animals and tissue processing

Male BALB/c mice aged 19 months (late adult, n=3) and 28 months (old, n=3) were used in this study. Late adult mice were selected as an appropriate control to detect the nuclear modifications that are strictly related to the old age, avoiding the results be influenced by factors other than age.

The animals were bred under controlled environmental conditions with a 12 h light/dark cycle and fed *ad libitum* on a standard commercial chow. The experiment was carried out in accordance with the National and international legislation, and the experimental protocol was approved by the Italian Ministry of Health (ref.: 538/2015-PR).

Mice were deeply anaesthetized with pentobarbital (50 mg/Kg i.p.) and then perfused *via* the ascending aorta with a brief prewash with 0.09% NaCl solution followed by 300 mL of a ready-to-use fixative solution containing 4% buffered formalin in 0.1 M phosphate buffer, pH 7.4. The right and left rectus femoris muscles were quickly removed and further fixed by immersion with 4% paraformaldehyde and 0.5% glutaraldehyde in 0.1 M phosphate buffer saline (PBS) pH 7.4 for 2 h at 4°C, incubated in 0.5 M $NH_4Cl$ in PBS for 30 min at room temperature to block the free aldehyde groups, dehydrated with graded ethanol, and embedded in LRWhite resin.

### Ultrastructural immunocytochemistry

Ultrathin sections (70-90 nm thick) were cut, collected on Formvar-carbon-coated nickel grids and used for the immunocytochemical analyses on the nuclei of the rectus femoris myofibers.

In order to evaluate the nuclear distribution of RNA processing factors, longitudinally-cut sections of rectus femoris muscles were incubated with the following probes: a mouse monoclonal antibody directed against the active phosphorylated form of RNA polymerase II (diluted 1:10, Abcam, Cambridge, UK); rabbit polyclonal antibodies directed against nuclear actin, diluted 1:50 (Sigma-Aldrich, Milan, Italy), 5-mC, diluted 1:100 (GeneTex, Irvine, CA, USA) and RNase A (the probe recognizes both active and inactive form of the enzyme), diluted 1:100 (Abcam). According to Cmarko *et al.*,[14] the ultrathin sections were floated

for 3 min on normal goat serum (NGS) diluted 1:100 in PBS and then incubated at 4°C for 17 h with the primary antibodies diluted in PBS containing 0.05% Tween 20 and 0.1% bovine serum albumin. After rinsing, the sections were floated on NGS, and incubated for 30 min at room temperature with the secondary gold-conjugated probes (Jackson Immuno Research Laboratories, West Grove, PA, USA) diluted 1:20 in PBS. A goat anti-mouse antibody conjugated with 6 nm gold grains and a goat anti-rabbit antibody conjugated with 12 nm gold grains were used. As control, some grids were incubated without the primary antibody and then processed as described above.

Following to immunolabeling, sections were stained for 35 min at room temperature with Uranyl Less EM stain (Electron Microscopy Sciences, Hatfield, PA, USA), followed by Reynolds' lead citrate for 1 min to reduce the chromatin contrast and preferentially reveal the ribonucleoprotein nuclear constituents.

In order to verify that RNA degradation is a co-transcriptional process, a double immunolabeling was performed with antibodies directed against RNA polymerase II and RNase A, followed by the specific secondary antibodies conjugated with either 6 or 12 nm gold, respectively. For the fine specific visualization of RNA in the PFs, the sections were then floated onto 0.2 M terbium citrate for 30 min at room temperature, rapidly rinsed with water and dried.[33] The samples were observed in a Philips Morgagni TEM operating at 80kV and equipped with Megaview III camera for digital image acquisition.

For nuclear actin, 5-mC and RNAse A, a semiquantitative assessment of the immunolabeling was carried out by estimating the gold grain density on selected nuclear compartments in sections of muscles from different mice treated in the same run. The area of different nuclear compartments was measured using the ImageJ software (NIH) on 40 randomly selected nuclear micrographs (x14,000) for each age group. The gold grains were counted, and the labelling density was expressed as number of gold grains/$\mu m^2$. The following nuclear compartments were considered: condensed chromatin, nucleolus and interchromatin space (obtained by subtracting the areas of both condensed chromatin and nucleolus from the total area of the myonucleus). In eight myonuclei from each age group, the percentage of the interchro-

matin space immunolabelled for RNAse A occurring on IGs was evaluated.

The background level for all antibodies was evaluated on section areas devoid of tissue and proved to be negligible (see Figure 2 legend).

### Statistical analysis

Data for each variable were pooled according to the age group and presented as mean ± standard error of the mean (SEM). Statistical group-group comparison was performed with the Mann-Whitney test setting statistical significance at alpha ≤0.05.

## Results and Discussion

The myonuclei of old and late adult mice showed a similar ultrastructural organization; instead, interesting differences were observed in the distribution and density of the investigated nuclear molecular factors.

Nuclear actin (Figure 1A) was found to locate on condensed chromatin, in the interchromatin space (namely, on PFs and IGs) and in the nucleolus at both ages, but the immunolabeling density was significantly lower in myonuclei of old mice compared to late adult animals for all the considered nuclear compartments (condensed chromatin, $p<0.001$; nucleolus, $p\leq0.001$; interchromatin space, $p\leq0.001$) (Figure 2A). Nuclear actin is a motor protein involved in several processes inclusive of movement and organization of chromatin (reviewed in[30]). The decrease of nuclear actin on condensed chromatin would thus support the hypothesis that aging leads to alterations in chromatin structuring. Nuclear actin is also involved in the regulation of mRNA and rRNA transcription and is crucial in the active nuclear-to-cytoplasm transport of both mRNA (reviewed in[34]) and pre-ribosomal subunits.[35,36] Therefore, the significantly lower amount of nuclear actin observed in the interchromatin space and nucleoli of old animals (Figure 2A) is consistent with the previously shown reduction in transcriptional rate and impairment of RNA export in the aged skeletal muscle.[22,29] As for the nucleolus, a previous study[21] on myonuclei of old rats showed
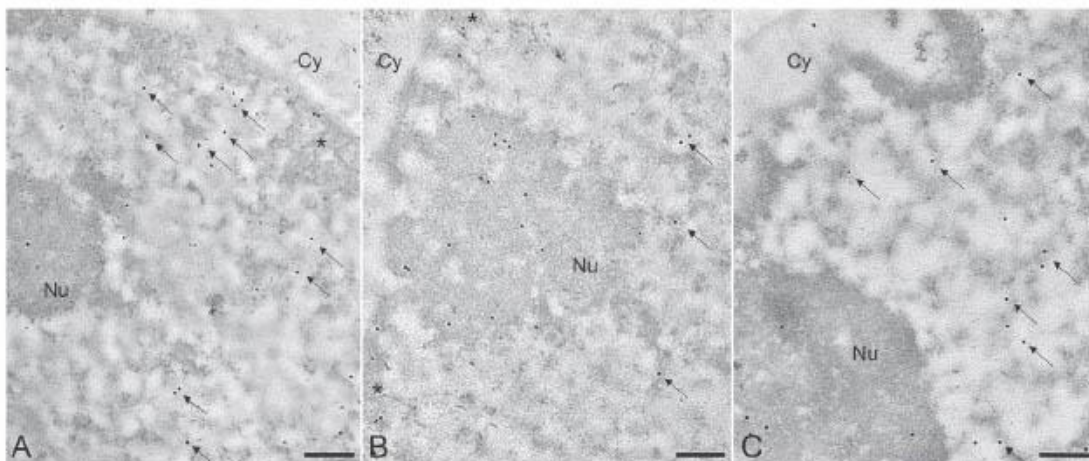


**Figure 1.** Immunoelectron microscopy of myonuclei from late adult mice immunolabelled for nuclear actin (A), 5-mC (B) and RNase A (C). All antibodies label perichromatin fibrils (arrows) in the interchromatin space and nucleolus (Nu). Note the labelling on the condensed chromatin clumps (asterisks) for nuclear actin and 5-mC (A, B). Cy, cytoplasm. Scale bars: 200 nm.

a reduction in rRNA transcription and processing as indicated by decrease of the dense fibrillar component[21] where these processes are known to take place.[37] In the same myonuclei, an increase in the nucleolar granular component (where pre-ribosomes are stored before being exported to the cytoplasm[38]), suggests that ribosomal subunits accumulate in the nucleolus. The lower amount of actin in the myonuclei of old mice may thus be also indicative of an impaired export of the ribosomal subunits in aging. Consistently, using a biochemical fractionation strategy, Cutler *et al.*[23] observed higher amount of ribosomal proteins in myonuclei isolated from aged mice, despite the decrease in ribosome biogenesis found in skeletal muscle of old mice by microarray analysis.[39]

The labelling for 5m-C occurred on condensed chromatin, the interchromatin space (in particular on PFs) and the nucleolus (Figure 1B). Quantitative evaluation of the immunolabeling revealed similar densities of 5m-C on condensed chromatin (p=0.43) and interchromatin space (p=0.14) of myonuclei from late adult and old mice. On the contrary, 5m-C density was significantly lower in nucleoli of old *vs.* late adult mice (p<0.001) (Figure 2B). According to current knowledge, 5-mC is mainly involved in the regulation of gene transcription,[3] being generally associated with transcriptional repression;[40] 5-mC may also occur as an epigenetic modification in RNA,[41,42] acting as signal for the mRNA export adaptor ALYREF in the nucleus-to-cytoplasm transports of mature mRNA.[43] Therefore, the 5-mC labelled PFs in the interchromatin space likely contain mature mRNA ready to leave the nucleus. The presence of 5-mC in silent rRNA genes seems to protect from illicit recombination events that would promote loss of rDNA.[44] The statistically significant decrease of 5m-C in nucleoli, thus, would make the rRNA genes in old mice more prone to an age-dependent loss, as much as it occurs in murine spleen, brain and liver[45] and in the human adipose tissue.[46] This event would be also consistent with the decrease in ribosome biogenesis found in the aged skeletal muscle.[39]

RNase A immunolabeling was found on condensed chromatin, the interchromatin space (namely on PFs and IGs) and the nucleolus (Figure 1C) in both groups of age. Quantitative evaluation revealed that RNase A labelling density on condensed chromatin was similar in late adult and old animals and increased at the limit of statistical significance in the interchromatin space of old myonuclei (p=0.069), whereas it was significantly lower in the nucleolus of old *vs.* late adult mice (p≤0.001) (Figure 2C). RNase A, which is active in skeletal muscle,[47] is a general RNase that catalyzes the cleavage of RNA on the 3' side of pyrimidine nucleotides.[32] The presence of RNase A on condensed chromatin suggests an action of this enzyme in this nuclear compartment where RNA plays a direct role in the chromatin structural organization (reviewed in[48]). In the interchromatin space, the immunolabeling for RNase A on IGs (where factors involved in mRNA transcription and maturation are stored, assembled and modified[17]) were not statistically significant different in late adult and old mice (10.77%±0.05 *vs.* 11.75%±0.04, respectively). The tendency of RNase A to increase in the interchromatin space of old mice could be due to the accumulation of enzyme-containing PFs in the nuclei of old animals.[22] Interestingly, the co-presence of active RNA polymerase II and RNase A on the same PFs (Figure 3) in both late adult and old mice suggests that mRNA degradation occurs cotranscriptionally, as observed for the splicing and ending processing of the mRNA.[49] RNase A is involved in the activation of rDNA transcription in several cell types;[50] thus, the statistically significant lower amount of RNase A in the nucleoli of myonuclei from old mice (Figure 2C) might (directly or indirectly) be related to an age-dependent loss of rRNA genes as suggested by the decreased immunolabeling for 5-mC. Alternatively, as already demonstrated for other factors,[51] it may be hypothesized that the nucleolus acts
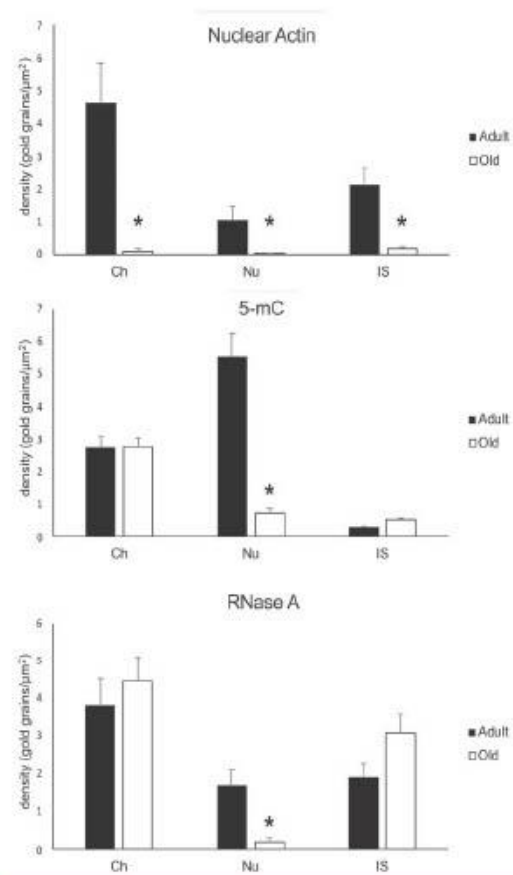


Figure 2. Immunolabeling density of nuclear actin (A), 5-mC (B), RNase A (C) on condensed chromatin (Ch), nucleolus (Nu), interchromatin space (IS) in myonuclei of late adult and old mice. The histograms show the mean value ± SEM of density expressed as gold grains/μm². Statistically significant differences (p≤0.001) are indicated by asterisk. Background density was negligible for all probes (nuclear actin, 0.18 0.05; 5-mC, 0.45 ± 0.03; RNase A, 0.39±0.08).
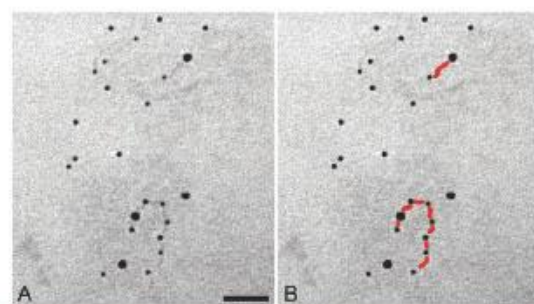


Figure 3. A,B) Transmission electron micrographs of myonuclei from old mice double-immunolabelled for RNA polymerase II (6nm gold grain) and RNase A (12nm gold grain), followed by staining with terbium citrate. B) The RNA of the PFs was digitally colored in red for ease of visualization. Scale bar: 50 nm.

as a transit and storage site for RNase A during aging.[52] In fact, mass-spectrometry-based analyses revealed that numerous proteins involved in functions other than ribosome biogenesis are present in the nucleolus, strongly suggesting a multiple role for this organelle,[53] with important implications in aging.[6]

In conclusion, the fine immunocytochemical analysis carried out in this study provides novel information on the aging-associated changes in the amount of molecular factors involved in chromatin stability as well as transcription, processing and transport of RNAs in myonuclei of old mice, shedding light on the mechanisms underlying alterations of the cell nucleus during aging. In particular, the statistically significant decrease of nuclear actin strongly supports impairment of mRNA transcription and nucleus-to-cytoplasm transport of mRNA and ribosomal subunits, while the decrease of 5-mC and RNase A in nucleoli suggests an age-dependent loss of rRNA genes. These nuclear dysfunctions may hinder protein synthesis and impair the physiological balance between protein anabolism and catabolism typical of the healthy skeletal muscle tissue,[54] thus contributing to the onset and progression of sarcopenia.

## Acknowledgments

## References

1. Cruz-Jentoft AJ, Baeyens JP, Bauer JM, Boirie Y, Cederholm T, Landi F, et al. Sarcopenia: European consensus on definition and diagnosis: report of the European Working Group on sarcopenia in older people. Age Ageing 2010; 39:412–23.

2. Combaret L, Dardevet D, Béchet D, Taillandier D, Mosoni L, Attaix D. Skeletal muscle proteolysis in aging. Curr Opin Clin Nutr Metab Care 2009;12:37-41.

3. Verdijk LB, Koopman R, Schaart G, Meijer K, Savelberg HH, van Loon LJ. Satellite cell content is specifically reduced in type II skeletal muscle fibers in the elderly. Am J Physiol Endocrinol Metab 2007;292:E151-7.

4. Short KR, Bigelow ML, Kahl J, Singh R, Coenen-Schimke J, Raghavakaimal S, et al. Decline in skeletal muscle mitochondrial function with aging in humans. Proc Natl Acad Sci USA 2005;102:5618–23.

5. Pegoraro G, Misteli T. The central role of chromatin maintenance in aging. Aging (Albany NY) 2009;1:1017–22.

6. Tiku V, Antebi A. Nucleolar function in lifespan regulation. Trends Cell Biol 2018;28:662-72.

7. Dirks AJ, Leeuwenburgh C. The role of apoptosis in age-related skeletal muscle atrophy. Sports Med 2005;35:473-83.

8. Brook MS, Wilkinson DJ, Phillips BE, Perez-Schindler J, Philp A, Smith K, et al. Skeletal muscle homeostasis and plasticity in youth and ageing: impact of nutrition and exercise. Acta Physiol (Oxford) 2016;216:15–41.

9. Aversa Z, Zhang X, Fielding RA, Lanza I, LeBrasseur NK. The clinical impact and biological mechanisms of skeletal muscle aging. Bone 2019;127:26-36.

10. Falcone C, Mazzoni C. RNA stability and metabolism in regulated cell death, aging and diseases. FEMS Yeast Res 2018;18:foy050.

11. Meshorer E, Soreq H. Pre-mRNA splicing modulations in senescence. Aging Cell 2002;1:10-6.

12. Wahle E, Ruegsegger U. 3'-end processing of pre-mRNA in eukaryotes. FEMS Microbiol Rev 1999;23:277–95.

13. Fakan S. Ultrastructural cytochemical analyses of nuclear functional architecture. Eur J Histochem 2004;48:5-14.

14. Cmarko D, Verschure PJ, Martin TE, Dahmus ME, Krause S, Fu XD, et al. Ultrastructural analysis of transcription and splicing in the cell nucleus after bromo-UTP microinjection. Mol Biol Cell 1999;10:211–23.

15. Cardinale S, Cisterna B, Sonetti P, Aringhieri C, Biggiogera M, Barabino SML. Subnuclear localization and dynamics of the pre-mRNA 3' end processing factor CFIm68. Mol Biol Cell 2007;18:1282–92.

16. Biggiogera M, Cisterna B, Spedito A, Vecchio L, Malatesta M. Perichromatin fibrils as early markers of transcriptional alterations. Differentiation 2008;76:57-65.

17. Puvion E, Puvion-Dutilleul F. Ultrastructure of the nucleus in relation to transcription and splicing: roles of perichromatin fibrils and interchromatin granules. Exp Cell Res 1996;229:217-25.

18. Cookson MR. Aging - RNA in Development and Disease. Wiley Interdiscip Rev RNA 2012;3:133–43.

19. Malatesta M, Baldelli B, Battistelli S, Fattoretti P, Bertoni-Freddari C. Aging affects the distribution of the circadian CLOCK protein in rat hepatocytes. Microsc Res Tech 2005;68:45-50.

20. Malatesta M, Fattoretti P, Baldelli B, Battistelli S, Balietti M, Bertoni-Freddari C. Effects of ageing on the fine distribution of the circadian CLOCK protein in reticular formation neurons. Histochem Cell Biol 2007;127:641-7.

21. Malatesta M, Perdoni F, Muller S, Zancanaro C, Pellicciari C. Nuclei of aged myofibres undergo structural and functional changes suggesting impairment in RNA processing. Eur J Histochem 2009;53:e12.

22. Malatesta M, Biggiogera M, Cisterna B, Balietti M, Bertoni-Freddari C, Fattoretti P. Perichromatin fibrils accumulation in hepatocyte nuclei reveals alterations of pre-mRNA processing during aging. DNA Cell Biol 2010;29:49-57.

23. Cutler AA, Dammer EB, Doung DM, Seyfried NT, Corbett AH, Pavlath GK. Biochemical isolation of myonuclei employed to define changes to the myonuclear proteome that occur with aging. Aging Cell 2017;16:738-49.

24. Malatesta M, Bertoni-Freddari C, Fattoretti P, Caporaloni C, Fakan S, Gazzanelli G. Altered RNA structural constituents in aging and vitamin E deficiency. Mech Ageing Dev 2003;124:175-81.

25. Buchwalter A, Hetzer MW. Nucleolar expansion and elevated protein translation in premature aging. Nat Commun 2017;8:328.

26. Duncan FE, Jasti S, Paulson A, Kelsh JM, Fegley B, Gerton JL. Age-associated dysregulation of protein metabolism in the mammalian oocyte. Aging Cell 2017;16:1381-93.

27. Malatesta M, Giagnacovo M, Costanzo M, Cisterna B, Cardani R, Meola G. Muscleblind-like1 undergoes ectopic relocation in the nuclei of skeletal muscles in myotonic dystrophy and sarcopenia. Eur J Histochem 2013;57:e15.

28. Cisterna B, Giagnacovo M, Costanzo M, Fattoretti P, Zancanaro C, Pellicciari C et al. Adapted physical exercise enhances activation and differentiation potential of satellite cells in the skeletal muscle of old mice. J Anat 2016;228:771-83.

29. Malatesta M, Fattoretti P, Giagnacovo M, Pellicciari C, Zancanaro C. Physical training modulates structural and functional features of cell nuclei in type II myofibers of old mice. Rejuvenation Res 2011;14:543-52.

30. Kelpsch DJ, Tootle TL. Nuclear actin: From discovery to func-

**Article**

tion. Anat Rec (Hoboken) 2018;301:1999-2013.

31. Kumar S, Chinnusamy V, Mohapatra T. Epigenetics of modified DNA bases: 5-methylcytosine and beyond. Front Genet 2018;9:640.

32. Hahn U, Desai-Hahn R, Rüterjans H. 1H and 15N NMR investigation of the interaction of pyrimidine nucleotides with ribonuclease A. Eur J Biochem 1985;146:705-12.

33. Biggiogera M, Masiello I. Visualizing RNA at electron microscopy by terbium citrate. Methods Mol Biol 2017;1560:277-83.

34. Kristó I, Bajusz I, Bajusz C, Borkúti P, Vilmos P. Actin, actin-binding proteins, and actin-related proteins in the nucleus. Histochem Cell Biol 2016;145:373-88.

35. Cisterna B, Necchi D, Prosperi E, Biggiogera M. Small ribosomal subunits associate with nuclear myosin and actin in transit to the nuclear pores. FASEB J 2006;20:1901-3.

36. Cisterna B, Malatesta M, Dieker J, Muller S, Prosperi E, Biggiogera M. An active mechanism flanks and modulates the export of the small ribosomal subunits. Histochem Cell Biol 2009;131:743-53.

37. Biggiogera M, Malatesta M, Abolhassani-Dadras S, Amalric F, Rothblum LI, Fakan S. Revealing the unseen: the organizer region of the nucleolus. J Cell Sci 2001;114:3199-205.

38. Schwarzacher HG, Wachtler F. The nucleolus. Anat Embryol (Berl) 1993;188:515-36.

39. Kirby TJ, Lee JD, England JH, Chaillou T, Esser KA, McCarthy JJ. Blunted hypertrophic response in aged skeletal muscle is associated with decreased ribosome biogenesis. J Appl Physiol (1985) 2015;119:321-7.

40. Alison I, Bernstein, Peng J. High-throughput sequencing-based mapping of cytosine modifications. In: Y. G. Zheng, Editor. Epigenetic Technological Applications. Academic Press; 2015. p. 39-53.

41. Masiello I, Biggiogera M. Ultrastructural localization of 5-methylcytosine on DNA and RNA. Cell Mol Life Sci 2017;74:3057-64.

42. Trixl L, Lusser A. The dynamic RNA modification 5-methyl-cytosine and its emerging role as an epitranscriptomic mark. Wiley Interdiscip Rev RNA 2019;10:e1510.

43. Yang X, Yang Y, Sun BF, Chen YS, Xu JW, Lai WY, et al. 5-methylcytosine promotes mRNA export—NSUN2 as the methyltransferase and ALYREF as an m5C reader. Cell Res 2017;27:606-25.

44. Guetg C, Lienemann P, Sirri V, Grummt I, Hernandez-Verdun D, Hottiger MO, et al. The NoRC complex mediates the heterochromatin formation and stability of silent rRNA genes and centromeric repeats. EMBO J 2010;29:2135-46.

45. Gaubatz JW, Cutler RG. Age-related differences in the number of ribosomal RNA genes of mouse tissues. Gerontology 1978;24:179-207.

46. Zafiropoulos A, Tsentelierou E, Linardakis M, Kafatos A, Spandidos DA. Preferential loss of 5S and 28S rDNA genes in human adipose tissue during ageing. Int J Biochem Cell Biol 2005;37:409-15.

47. Reilly ME, Erylaz EI, Amir A, Peters TJ, Preedy VR. Skeletal muscle ribonuclease activities in chronically ethanol–treated rats. Alcohol Clin Exp Res 1998;22:876-83.

48. Thakur J, Henikoff S. Architectural RNA in chromatin organization. Biochem Soc Trans 2020;48:1967-78.

49. Masiello I, Siciliani S, Biggiogera M. Perichromatin region: a moveable feast. Histochem Cell Biol 2018;150:227-33.

50. Li S, Hu GF. Angiogenin-mediated rRNA transcription in cancer and neurodegeneration. Int J Biochem Mol Biol 2010;1:26-35.

51. Boisvert FM, van Koningsbruggen S, Navascués J, Lamond AI. The multifunctional nucleolus. Nat Rev Mol Cell Biol 2007;8:574-85.

52. Costanzo M, Cisterna B, Zharskaya OO, Zatsepina OV, Biggiogera M. Discrete foci containing RNase A are found in nucleoli of HeLa cells after aging in culture. Eur J Histochem 2011;55:e15.

53. Ahmad Y, Boisvert FM, Gregor P, Cobley A, Lamond AI. NOPdb: nucleolar proteome database–2008 update. Nucleic Acids Res 2009;37:D181-4.

54. Schiaffino S, Dyar KA, Ciciliot S, Blaauw B, Sandri M. Mechanisms regulating skeletal muscle growth and atrophy. FEBS J 2013;280:4294-314.

OPEN ACCESS

51

**Uranyl-free staining as a suitable contrasting technique for nuclear structures at transmission electron microscopy**

*M.A. Lacavalla, B. Cisterna*

Because of the copyright rules, only the summary of the manuscript can be reported in this thesis.

# Uranyl-Free Staining as a Suitable Contrasting Technique for Nuclear Structures at Transmission Electron Microscopy

Maria Assunta Lacavalla and Barbara Cisterna

## Abstract

Uranyl acetate solution has widely been used as staining reagent for samples processed for ultrastructural morphology, cytochemistry, and immunocytochemistry. Although uranyl acetate guarantees high performance as a staining reagent, the radioactive uranyl salts make its use and purchase severely restricted. In this view, we used a non-radioactive lanthanide mix solution as contrasting dye for both nucleoplasmic and nucleolar ribonucleoprotein-containing components. This method guarantees a good contrast without masking the probe–antigen immunoreaction, thus proving to be a suitable tool for high-resolution studies of both cyto- and immunocytochemistry on acrylic resin-embedded samples.

**Key words** Cytochemistry, Immunocytochemistry, Ribonucleoprotein-containing component, Ultrastructure, Lanthanide stain, Lead citrate

# Age related changes in the matrisome of the mouse skeletal muscle

*F.D. Lofaro, B. Cisterna, M.A. Lacavalla, F. Boschi, M. Malatesta, D.Quagliano, C. Zancanaro, F. Boraldi*

## ABSTRACT

The muscular extracellular matrix (ECM) is composed of different groups of macromolecules (i.e., collagens, non-collagens glycoproteins, glycosaminoglycans and proteoglycans), which regulate several cell functions and represent structural support for muscle fibres, playing a role in muscle development, growth, and repair. Aging is characterized by a progressive decline of skeletal muscle (SM) mass and strength causing mobility loss and frailty in older persons (i.e., sarcopenia). The mechanisms underlying sarcopenia are diverse and may involve the ECM. In fact, ECM is affected by aging in terms of turnover and ratio of specific components, balance between synthesis and degradation, modifications in cellular behaviour through altered cell-matrix interactions, and changes in mechano-sensing pathways. In the present work, we investigated the ECM of gastrocnemius muscle in old and adult mice. Morphological and morphometrical analysis at fluorescence and electron microscopy were carried out to study the structural organization and interactions of ECM components. In parallel, a research group of the University of Modena and Reggio Emilia performed a proteomic analysis to recognize and quantify the ECM molecular components. This collaborative study aimed at getting light on age-related changes in the muscular ECM, to provide the first characterization of the matrisome in the aging gastrocnemius muscle.

*Article*

# Age-Related Changes in the Matrisome of the Mouse Skeletal Muscle

**Francesco Demetrio Lofaro** [1,†], **Barbara Cisterna** [2,†], **Maria Assunta Lacavalla** [2], **Federico Boschi** [3], **Manuela Malatesta** [2], **Daniela Quaglino** [1], **Carlo Zancanaro** [2,*] and **Federica Boraldi** [1,*]

1   Department of Life Sciences, University of Modena and Reggio Emilia, I-44100 Modena, Italy; francescodemetrio.lofaro@unimore.it (F.D.L.); daniela.quaglino@unimore.it (D.Q.)
2   Department of Neurological and Movement Sciences, University of Verona, I-37100 Verona, Italy; barbara.cisterna@univr.it (B.C.); mariaassunta.lacavalla@univr.it (M.A.L.); manuela.malatesta@univr.it (M.M.)
3   Department of Computer Science, University of Verona, I-37100 Verona, Italy; federico.boschi@univr.it
*   Correspondence: carlo.zancanaro@univr.it (C.Z.); federica.boraldi@unimore.it (F.B.)
†   Equal contribution.

**Abstract:** Aging is characterized by a progressive decline of skeletal muscle (SM) mass and strength which may lead to sarcopenia in older persons. To date, a limited number of studies have been performed in the old SM looking at the whole, complex network of the extracellular matrix (i.e., matrisome) and its aging-associated changes. In this study, skeletal muscle proteins were isolated from whole gastrocnemius muscles of adult (12 mo.) and old (24 mo.) mice using three sequential extractions, each one analyzed by liquid chromatography with tandem mass spectrometry. Muscle sections were investigated using fluorescence- and transmission electron microscopy. This study provided the first characterization of the matrisome in the old SM demonstrating several statistically significantly increased matrisome proteins in the old vs. adult SM. Several proteomic findings were confirmed and expanded by morphological data. The current findings shed new light on the mutually cooperative interplay between cells and the extracellular environment in the aging SM. These data open the door for a better understanding of the mechanisms modulating myocellular behavior in aging (e.g., by altering mechano-sensing stimuli as well as signaling pathways) and their contribution to age-dependent muscle dysfunction.

**Keywords:** aging; extracellular matrix; proteomics; ultrastructure; immunohistochemistry; sarcopenia

**check for updates**

## 1. Introduction

Skeletal muscle (SM) is necessary for locomotion, but it also plays important roles in several physiological processes such as bone homeostasis, thermogenesis, and metabolism of amino acids, glucose, and lipids [1,2]. The progressive loss of muscle strength and mass, alterations in tissue composition, and increasing denervation can lead to the development of sarcopenia, a pathological condition which generally occurs in aging but can also occur at a young age [3,4]. Sarcopenia contributes to a lower quality of life since, for example, the risk of falls with consequent fractures and loss of independence increases and may contribute to the development of type II diabetes and of metabolic syndrome [5].

Over the past decades, many studies have shown that sarcopenia is a multifactorial process [6] involving, among other factors: (i) reduction in the size and the number of myofibers [7]; (ii) satellite cell (SC) exhaustion and altered immune and muscle cell crosstalk (necessary for muscle proliferative and regenerative capacity) [8]; (iii) mitochondria dysfunction causing inefficient energy production [9]; (iv) alterations in insulin-like growth factor 1, Notch, and Wnt/beta-catenin signaling pathways [3]; (v) increase of oxidative stress [10]; and (vi) dysregulation of protein synthesis and degradation [11].

The extracellular matrix (ECM) is composed of different groups of macromolecules such as collagens, non-collagenous glycoproteins (e.g., laminin, tenascin, and fibronectin),

glycosaminoglycans (e.g., heparan sulfate), and proteoglycans (e.g., biglycan and lumican) [12]. These macromolecules bind to each other and to cells through integrins, sarcoglycan complex, and dystroglycan to form an intricate network sending biochemical signals to myofibres. ECM regulates several cell functions (e.g., growth, differentiation, and migration) [13] and represents the structural and functional support for muscle fibers, vessels, and nerves, playing a role in the transmission of contractile forces [14], as well as muscle development [15], growth, and repair [16]. ECM is affected by the aging process in terms of turnover and ratio of specific components, the balance between synthesis and degradation of components, modifications in cellular behavior through altered cell-matrix interactions, and changes in mechano-sensing pathways. In age-dependent sarcopenia, changes in ECM architecture and composition and fibrosis [17] are believed to reduce the regenerative capacity of SM and to negatively influence the proliferation and differentiation capability of SC [12,18–20]. The ECM remodeling in sarcopenia has also been linked to mitochondrial deterioration [9,19]. However, until now, a limited number of investigations have been performed in the aging SM looking at the matrisome as the whole complex network of ECM molecules.

In recent years, thanks to the development of mass spectrometry (MS)-based high-throughput proteomic techniques, large-scale protein characterization is less challenging. Proteomic approaches have been successfully applied to SM in different experimental models [21–24]. However, to date, there is little information available on ECM proteins of SM [25] and their aging-associated changes.

The identification and quantification of ECM components and their interactions are essential steps to understand the role of the matrisome in sarcopenia. In this context, we decided to investigate the SM ECM in old compared to adult mice. We are aware that it would be of interest to analyze life-long changes, and thus also include muscles from young animals. However, it has to be underlined that most changes in muscle protein expression are known to take place after middle age [24].

The morphology of old SM has been already characterized in previous work from our laboratory highlighting several typical features of the sarcopenic condition. A significantly smaller myofiber cross-sectional area was observed in the SM of old mice [26,27]. Although the general cytological organization of the old myofiber was not grossly altered, morphometrical studies highlighted several age-related modifications (e.g., accumulation of larger inter-myofibrillar and sub-sarcolemmal mitochondria, larger myonuclei with increased condensed chromatin, impairment of RNA maturation/export pathways, decreased amount of active satellite cells) [28–30]. In this work, the gastrocnemius muscle was selected for analysis since it is prevalently composed of fast-twitch fibers [27], which are especially affected by atrophy during aging.

Therefore, to shed light on age-related changes in the matrisome of the gastrocnemius muscle, we combined a proteomic approach (i.e., liquid chromatography (LC)-MS/MS and bioinformatic analyses) with morphological and morphometrical evaluations of sections observed by fluorescence and transmission electron microscopy.

Results provided novel characterization of the aging matrisome. Higher amounts of several ECM proteins in old vs. adult muscle were demonstrated, thereby shedding new light on the mutually cooperative interplay between cells and the extracellular environment. This study opens the door to a better understanding of the mechanisms modulating myocellular behavior (e.g., alteration of mechano-sensing stimuli and/or signaling pathways).

## 2. Results

### 2.1. Identification of Proteins in the Gastrocnemius Muscle

In this study, samples of gastrocnemius muscle were subjected to three sequential extractions, each one being analyzed by LC-MS/MS. In particular, phosphate buffer saline (PBS) was used to solubilize hydrophilic proteins (PBS extract), and then the insoluble part was treated with a combination of urea (U) and thiourea (T) to extract hydrophobic molecules such as membrane proteins, myofibrillar, and part of ECM proteins (U/T

extract) [31]. Finally, the remaining insoluble fraction was treated with guanidine-HCl (GuHCl extract), one of the most efficient chaotropic agents which is known to extract poorly soluble, heavily cross-linked proteins, and proteoglycans. This approach has been reported to improve protein extraction from ECM-rich tissues (e.g., cartilage, tendon) [32,33] (Figure 1a).
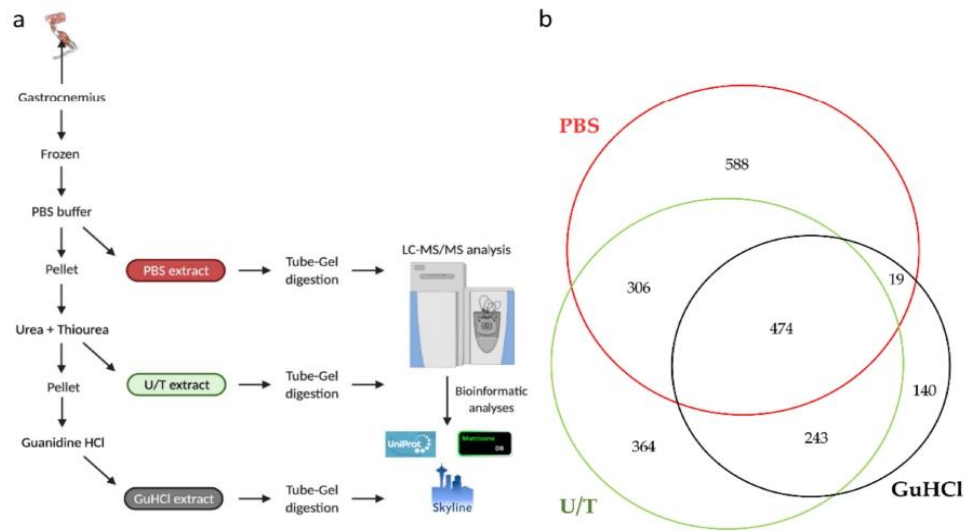


**Figure 1.** (**a**) Sequential protein extraction from gastrocnemius muscle. (**b**) The Venn diagram shows the number of proteins identified in each extract.

This strategy allowed us to identify, with at least 1 unique peptide, 2134 different proteins (Table S1) of which 474 were identified in all 3 extracts, while 588, 364, and 140 proteins were detected in the PBS, U/T, and GuHCl extracts, respectively (Figure 1b).

To reveal the ECM composition of the gastrocnemius muscle, the 2134 identified proteins were further analyzed by interrogating the MatrisomeDB, a database that includes all structural ECM components and proteins that may directly or indirectly interact with the ECM [34]. The matrisome is constituted by a "core matrisome", comprising collagens, proteoglycans, and glycoproteins, and by "matrisome-associated proteins", which include secreted factors, ECM-affiliated proteins, and ECM regulators [35]. As shown in Table 1, 124 proteins were found to be part of ECM; in particular, 14, 38, and 10 proteins belong to the collagen, glycoprotein, and proteoglycan category, respectively. Sixty-two proteins constituted the "matrisome-associated proteins" (i.e., 15, 37, and 10 proteins representing ECM-affiliated proteins, ECM regulators, and secreted factors, respectively). 43% (54/124) of proteins were found only after U/T and GuHCl extract of which 28 polypeptides were identified in both extracts (i.e., U/T and GuHCl) and 13 only with U/T or with GuHCl buffer.

**Table 1.** ECM and ECM-associated components from the gastrocnemius muscle categorized according to MatrisomeDB.

| Protein Symbol | Protein Name | Protein Symbol | Protein Name |
|---|---|---|---|
| **MATRISOME DIVISION:** CORE MATRISOME | | | |
| **Category:** collagen | | | |
| CO1A1 | Collagen alpha-1(I) chain | CO6A1 | Collagen alpha-1(VI) chain |
| CO1A2 | Collagen alpha-2(I) chain | CO6A2 | Collagen alpha-2(VI) chain |
| CO3A1 | Collagen alpha-1(III) chain | CO6A6 | Collagen alpha-6(VI) chain |
| CO4A1 | Collagen alpha-1(IV) chain | COBA1 | Collagen alpha-1(XI) chain |
| CO4A2 | Collagen alpha-2(IV) chain | COEA1 | Collagen alpha-1(XIV) chain |
| CO5A1 | Collagen alpha-1(V) chain | COFA1 | Collagen alpha-1(XV) chain |
| CO5A2 | Collagen alpha-2(V) chain | COIA1 | Collagen alpha-1(XVIII) chain |
| **Category:** ECM-glycoproteins | | | |
| ADIPO | Adiponectin | LAMB1 | Laminin subunit beta-1 |
| AGRIN | Agrin | LAMB2 | Laminin subunit beta-2 |
| BGH3 | Transforming growth factor-beta-induced protein ig-h3 | LAMC1 | Laminin subunit gamma-1 |
| CILP1 | Cartilage intermediate layer protein 1 | MFAP2 | Microfibrillar-associated protein 2 |
| CILP2 | Cartilage intermediate layer protein 2 | MFAP4 | Microfibril-associated glycoprotein 4 |
| COMP | Cartilage oligomeric matrix protein | MFAP5 | Microfibrillar-associated protein 5 |
| CREL1 | Cysteine-rich with EGF-like domain protein 1 | MFGM | Lactadherin |
| DERM | Dermatopontin | NID1 | Nidogen-1 |
| FBN1 | Fibrillin-1 | NID2 | Nidogen-2 |
| FBN2 | Fibrillin-2 | POSTN | Periostin |
| FIBA | Fibrinogen alpha chain | SLIT2 | Slit homolog 2 protein |
| FIBB | Fibrinogen beta chain | SRPX | Sushi-repeat-containing protein SRPX |
| FIBG | Fibrinogen gamma chain | SSPO | SCO-spondin |
| FINC | Fibronectin | TENA | Tenascin |
| IGS10 | Immunoglobulin superfamily member 10 | TINAL | Tubulointerstitial nephritis antigen-like |
| LAMA2 | Laminin subunit alpha-2 | TSP1 | Thrombospondin-1 |
| LAMA3 | Laminin subunit alpha-3 | TSP4 | Thrombospondin-4 |
| LAMA4 | Laminin subunit alpha-4 | VMA5A | von Willebrand factor A domain-containing protein 5A |
| LAMA5 | Laminin subunit alpha-5 | VWA1 | von Willebrand factor A domain-containing protein 1 |
| **Category:** Proteoglycans | | | |
| ASPN | Asporin | PGBM | Basement membrane-specific heparan sulfate proteoglycan core protein |
| CHADL | Chondroadherin-like protein | PGS1 | Biglycan |
| FMOD | Fibromodulin | PGS2 | Decorin |
| LUM | Lumican | PRELP | Prolargin |
| MIME | Mimecan | PRG2 | Bone marrow proteoglycan |
| **MATRISOME DIVISION:** MATRISOME-ASSOCIATED PROTEINS | | | |
| **Category:** ECM affiliated proteins | | | |
| ANXA1 | Annexin A1 | GPC1 | Glypican-1 |
| ANXA2 | Annexin A2 | HEMO | Hemopexin |
| ANXA3 | Annexin A3 | LEG1 | Galectin-1 |
| ANXA4 | Annexin A4 | LEGL | Galectin-related protein |
| ANXA5 | Annexin A5 | LMAN1 | Protein ERGIC-53 |
| ANXA6 | Annexin A6 | PLXA4 | Plexin-A4 |
| ANXA7 | Annexin A7 | PLXB3 | Plexin-B3 |
| ANX11 | Annexin A11 | | |

**Table 1.** *Cont.*

| Protein Symbol | Protein Name | Protein Symbol | Protein Name |
|---|---|---|---|
| **Category:** ECM regulators | | | |
| A1AT1 | Alpha-1-antitrypsin 1-1 | ITIH1 | Inter-alpha-trypsin inhibitor heavy chain H1 |
| A1AT2 | Alpha-1-antitrypsin 1-2 | ITIH2 | Inter-alpha-trypsin inhibitor heavy chain H2 |
| A1AT3 | Alpha-1-antitrypsin 1-3 | ITIH3 | Inter-alpha-trypsin inhibitor heavy chain H3 |
| A1AT4 | Alpha-1-antitrypsin 1-4 | ITIH4 | Inter alpha-trypsin inhibitor, heavy chain 4 |
| A2AP | Alpha-2-antiplasmin | ITIH5 | Inter-alpha-trypsin inhibitor heavy chain H5 |
| AMBP | Protein AMBP | KNG1 | Kininogen-1 |
| ANGT | Angiotensinogen | MMP17 | Matrix metalloproteinase-17 |
| ANT3 | Antithrombin-III | PEDF | Pigment epithelium-derived factor |
| CATB | Cathepsin B | PLMN | Plasminogen |
| CATD | Cathepsin D | PZP | Pregnancy zone protein |
| CBG | Corticosteroid-binding globulin | SERPH | Serpin H1 |
| CPN2 | Carboxypeptidase N subunit 2 | SPA3K | Serine protease inhibitor A3K |
| CYTB | Cystatin-B | SPA3M | Serine protease inhibitor A3M |
| FA12 | Coagulation factor XII | SPA3N | Serine protease inhibitor A3N |
| HEP2 | Heparin cofactor 2 | SPI2 | Serpin I2 |
| HRG | Histidine-rich glycoprotein | SULF2 | Extracellular sulfatase Sulf-2 |
| HYAL2 | Hyaluronidase-2 | TGM2 | Protein-glutamine gamma-glutamyltransferase 2 |
| IC1 | Plasma protease C1 inhibitor | THRB | Prothrombin |
| ILEUA | Leukocyte elastase inhibitor A | | |
| **Category:** secreted factors | | | |
| ANGL7 | Angiopoietin-related protein 7 | S10A1 | Protein S100-A1 |
| FILA2 | Filaggrin-2 | S10A4 | Protein S100-A4 |
| HGFA | Hepatocyte growth factor activator | S10A6 | Protein S100-A6 |
| INHBA | Inhibin beta A chain | S10AA | Protein S100-A10 |
| MEG11 | Multiple epidermal growth factor-like domains protein 11 | WN10A | Protein Wnt-10a |

*2.2. Matrisome Quantification: Old SM vs. Adult SM*

To compare the relative abundance of matrisome proteins between adult and old muscle, we performed a label-free quantification, which was based on the measure of precursor ion intensities. Even though protein quantification can be performed on proteins identified with a single peptide [36], we preferred to quantify matrisome proteins which were identified with at least two peptides (i.e., 91/124 proteins) (for more details see material and methods) (Table S2), as only one peptide can be incorrectly quantified across LC-MS runs [37].

Table 2 lists only proteins that changed significantly between old and adult muscles (i.e., 18, 21, and 3 in PBS, U/T, and GuHCl extracts, respectively). Except for Annexin A6, whose amount was significantly lower in aging SM, all other listed proteins were statistically significantly more abundant in old vs. adult SM. No statistically significant changes were found for proteins belonging to the category of secreted factors.

**Table 2.** List of matrisome proteins whose amount statistically significantly changed in old vs. adult gastrocnemius muscles. Quantification was performed by label-free mass spectrometry.

| | | | PBS Extract | |
|---|---|---|---|---|
| Category | Protein Symbol | Protein Name | Ratio (Old/Adult) Log$_2$ Fold Change | *p*-Value |
| ECM regulators | A1AT2 | Alpha-1-antitrypsin 1-2 | 0.69 | 0.006 |
| | A2AP | Alpha-2-antiplasmin | 1.04 | 0.038 |
| | CATD | Cathepsin D | 0.58 | 0.001 |
| | CBG | Corticosteroid-binding globulin | 1.82 | 0.049 |
| | ILEUA | Leukocyte elastase inhibitor A | 1.11 | 0.008 |
| | ITIH2 | Inter-alpha-trypsin inhibitor heavy chain H2 | 2.00 | 0.038 |
| | ITIH4 | Inter alpha-trypsin inhibitor, heavy chain 4 | 1.42 | 0.018 |
| | KNG1 | Kininogen-1 | 0.97 | 0.043 |
| | PEDF | Pigment epithelium-derived factor | 1.11 | 0.040 |
| | PZP | Pregnancy zone protein | 0.86 | 0.012 |
| | SPA3N | Serine protease inhibitor A3N | 1.77 | 0.028 |
| ECM glycoproteins | FIBA | Fibrinogen alpha chain | 1.19 | 0.001 |
| | FIBB | Fibrinogen beta chain | 1.19 | 0.001 |
| | FIBG | Fibrinogen gamma chain | 1.14 | 0.001 |
| | TSP4 | Thrombospondin-4 | 1.44 | 0.000 |
| | VMA5A | von Willebrand factor A domain-containing protein 5A | 0.81 | 0.000 |
| Proteoglycans | ASPN | Asporin | 0.53 | 0.004 |
| | LUM | Lumican | 0.48 | 0.030 |
| | PRELP | Prolargin | 0.37 | 0.001 |
| ECM affiliated proteins | ANXA4 | Annexin A4 | 0.63 | 0.002 |
| | ANXA5 | Annexin A5 | 0.51 | 0.009 |
| | ANXA6 | Annexin A6 | −0.39 | 0.008 |
| | ANX11 | Annexin A11 | 0.28 | 0.021 |
| | HEMO | Hemopexin | 0.74 | 0.018 |
| | | | U/T Extract | |
| Collagen | CO4A1 | Collagen alpha-1(IV) chain | 1.30 | 0.016 |
| | CO6A1 | Collagen alpha-1(VI) chain | 0.61 | 0.000 |
| | CO6A2 | Collagen alpha-2(VI) chain | 0.59 | 0.001 |
| ECM regulators | A1AT2 | Alpha-1-antitrypsin 1-2 | 0.87 | 0.022 |
| | CATD | Cathepsin D | 1.04 | 0.000 |
| | TGM2 | Protein-glutamine gamma-glutamyltransferase 2 | 0.80 | 0.013 |
| ECM glycoproteins | BGH3 | Transforming growth factor-beta-induced protein ig-h3 | 0.78 | 0.016 |
| | CILP1 | Cartilage intermediate layer protein 1 | 1.47 | 0.000 |
| | DERM | Dermatopontin | 0.51 | 0.004 |
| | FINC | Fibronectin | 1.35 | 0.036 |
| | LAMA2 | Laminin subunit alpha-2 | 0.45 | 0.000 |
| | LAMA5 | Laminin subunit alpha-5 | 0.79 | 0.002 |
| | LAMB1 | Laminin subunit beta-1 | 0.47 | 0.010 |
| | LAMB2 | Laminin subunit beta-2 | 0.53 | 0.000 |
| | LAMC1 | Laminin subunit gamma-1 | 0.56 | 0.000 |
| | NID1 | Nidogen-1 | 0.54 | 0.000 |
| | NID2 | Nidogen-2 | 1.09 | 0.000 |
| | POSTN | Periostin | 1.28 | 0.003 |
| | TENA | Tenascin | 2.55 | 0.022 |
| | TSP4 | Thrombospondin-4 | 1.34 | 0.048 |

**Table 2.** *Cont.*

| | | | | |
|---|---|---|---|---|
| **U/T Extract** | | | | |
| Proteoglycans | ASPN | Asporin | 0.79 | 0.008 |
| | FMOD | Fibromodulin | 0.73 | 0.005 |
| | LUM | Lumican | 0.81 | 0.001 |
| | MIME | Mimecan | 0.54 | 0.008 |
| | PGS1 | Biglycan | 1.05 | 0.002 |
| | PRELP | Prolargin | 0.87 | 0.007 |
| ECM affiliated proteins | ANXA2 | Annexin A2 | 0.42 | 0.005 |
| | ANXA5 | Annexin A5 | 2.28 | 0.002 |
| | HEMO | Hemopexin | 1.59 | 0.007 |
| | ANX11 | Annexin A11 | 0.90 | 0.000 |
| | LEG1 | Galectin-1 | 1.19 | 0.021 |
| **GuHCl Extract** | | | | |
| Collagens | COFA1 | Collagen alpha-1(XV) chain | 0.67 | 0.019 |
| ECM glycoproteins | LAMA5 | Laminin subunit alpha-5 | 0.81 | 0.006 |
| ECM affiliated proteins | ANXA2 | Annexin A2 | 0.67 | 0.046 |

*2.3. Ultrastructural Morphology and Morphometrical Evaluation*

To correlate matrisome changes with structural features, gastrocnemius muscles from adult and old mice were collected and processed for morphological and morphometrical analyses using transmission electron microscopy.

The general organization of myofibers in adult and old mice is shown in Figure 2a,c, confirming previous works from our laboratory [28,29]. In both age groups, the endomysium was comprised of a network of collagen fibrils connected to the basement membrane, which was covering the surface of skeletal muscle cells an electrodense sheath (Figure 2b,d).

Morphometrical evaluation of the endomysium thickness performed measuring the distance between the sarcolemma of two adjacent longitudinally sectioned myofibers, revealed no statistically significant difference in adult vs. old mice ($0.685 \pm 0.041$ and $0.611 \pm 0.048$; $p = 0.25$, Figure 2e). Instead, the thickness of the basement membrane was significantly higher in old vs. adult mice ($29.72 \pm 0.61$ nm vs. $41.88 \pm 1.07$ nm; $p < 0.001$; Figure 2f), in agreement with the increased amount of basement membrane's components identified by proteomic and immunofluorescence analyses (vide infra).

The extracellular matrix of the perimysium was organized in collagen bundles of different sizes and orientations (Figure 3a,c). In comparison with adult animals, old mice perimysium presented statistically significantly larger collagen bundles ($759.16 \pm 52.05$ nm vs. $1461.66 \pm 75.2$ nm; $p < 0.001$; Figure 3e), which were also more linear (linearity index: $1.05 \pm 0.01$ vs. $1.03 \pm 0.03$; $p = 0.03$; Figure 3f). Morphometrical evaluation of the collagen fibrils of the perimysium (Figure 3b,d) revealed no statistically significant difference in size in adult vs. old mice ($21.0 \pm 0.65$ nm and $21.4 \pm 0.50$ nm; $p = 0.62$, Figure 3g). The distance between collagen fibrils was statistically significantly higher in old vs. adult mice ($9.26 \pm 0.92$ nm and $5.84.45 \pm 0.56$ nm; $p = 0.006$; Figure 3h).
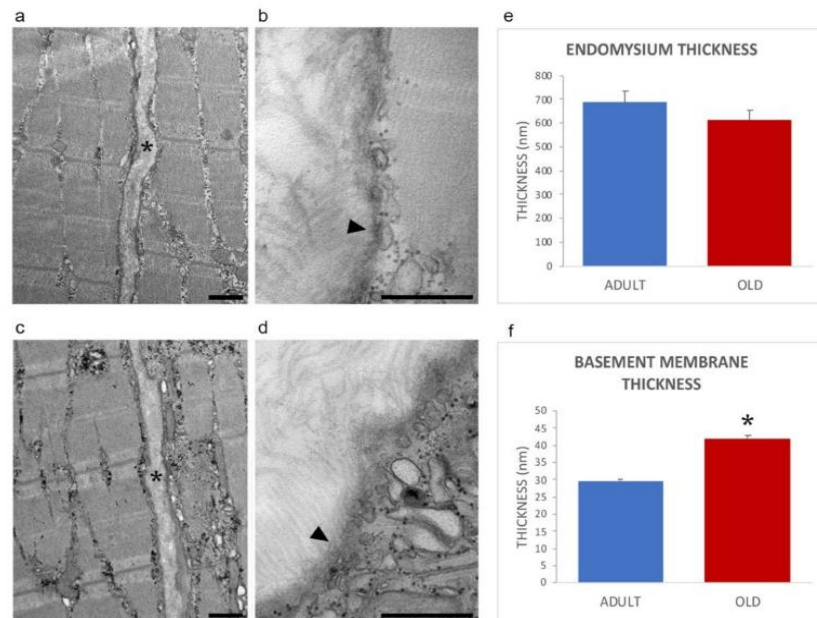
**Figure 2.** Ultrastructural images of the endomysium in adult (**a**,**b**) and old (**c**,**d**) gastrocnemius muscle. *, endomysium; arrowhead, basement membrane. Bars: 500 nm. The endomysium and basement membrane thickness are reported in panels (**e**) and (**f**), respectively. * $p < 0.001$.
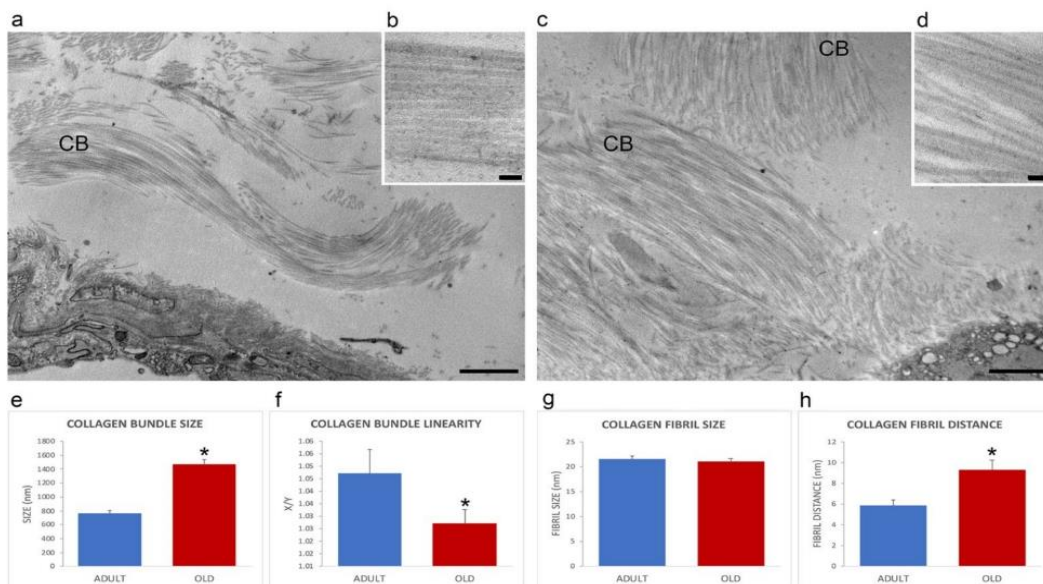


**Figure 3.** Ultrastructural images (**a**–**d**) of the perimysium of adult (**a**,**b**) and old (**c**,**d**) gastrocnemius muscle. CB, collagen bundle. (**a**,**c**), bars: 1 μm; (**b**,**d**), bars: 100 nm. Morphometric analysis of collagen bundles and collagen fibrils features are reported in the histograms (**e**–**h**). X/Y, ratio between the real length of the collagen bundle profile and the corresponding linear length. * $p < 0.05$.

63

*2.4. Evaluation of ECM Components by Immunofluorescence*

Immunofluorescence was performed on gastrocnemius cryosections from adult and old mice using specific antibodies directed against the ECM components collagen type VI (as representative interconnection factor between basement membrane and fibrillar collagen) and laminin (as constituent of the basement membrane) (Figure 4). Differences in the immunolabelling distribution were present in the two age groups. In particular, the immunostaining for both collagen type VI (Figure 4a,d) and laminin (Figure 4b,e) appeared more abundant in old vs. adult mice. Qualitative observations were confirmed by quantifying the area covered by fluorescence-positive pixels through a MATLAB routine. Both type VI collagen ($0.1368 \pm 0.0090$ vs. $0.0621 \pm 0.0097$, $p < 0.001$, Figure 4g) and laminin ($0.1728 \pm 0.0084$ vs. $0.0707 \pm 0.0071$; $p < 0.001$, Figure 4h) were statistically significantly increased in old SM.
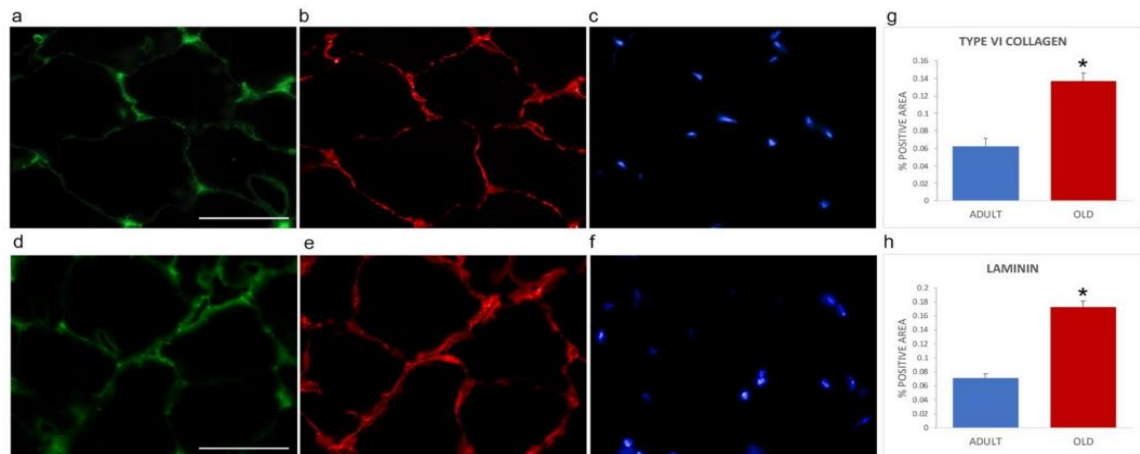


**Figure 4.** Type VI collagen (**a**,**d**) and laminin (**b**,**e**) immunolabelling of gastrocnemius cryosections in adult (**a**–**c**) and old (**d**–**f**) mice. DNA was counterstained with Hoechst (**c**,**f**). Bar: 50 μm. Panels (**g**) and (**h**), respectively, show quantification of the immunolabelling for type VI collagen and laminin expressed as % of total area). * $p < 0.001$.

Immunolabelling for type I collagen (as representative of fibrillar collagens) (Figure 5) revealed qualitatively different staining in the two groups of mice. Quantification of the area covered by fluorescence-positive pixels for type I collagen showed no statistically significant difference in the two age groups (adult, $0.0359 \pm 0.0086$; old, $0.0514 \pm 0.0113$; $p = 0.275$).
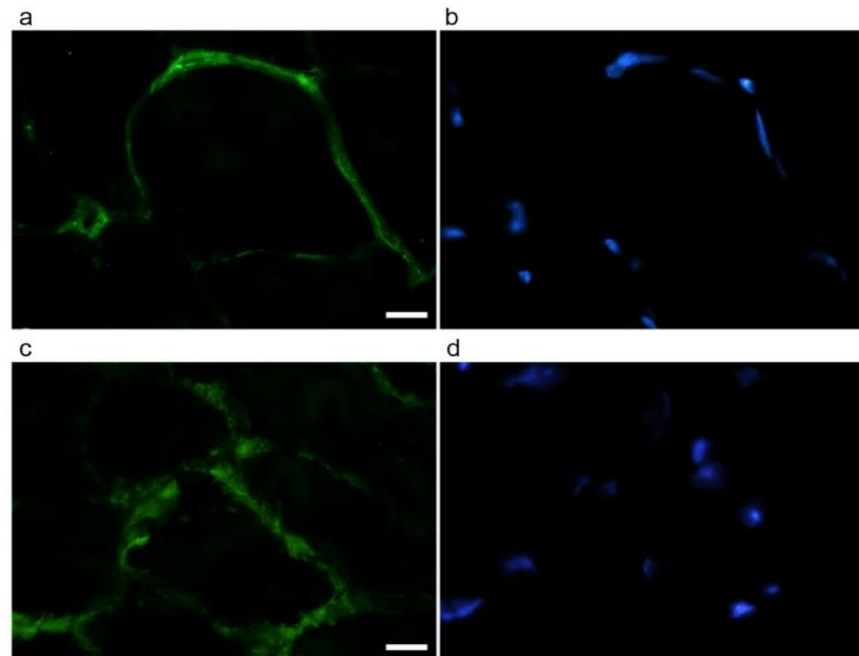
**Figure 5.** Type I collagen (**a**,**c**) immunolabelling of gastrocnemius cryosections of adult (**a**,**b**) and old (**c**,**d**) mice. DNA was counterstained with Hoechst (**b**,**d**). Bar: 10 μm.

### 3. Discussion

In aging, SM can suffer from low muscle strength and low muscle quality and quantity which may lead to sarcopenia [4].

To characterize and to understand the processes of sarcopenia, many studies using diverse techniques (e.g., computerized tomography, magnetic resonance imaging, electron microscopy, transcriptomic analyses) have mainly focused on changes of the SM mechanical properties and/or alterations of myofibers and SC [38,39]. Moreover, thanks to the development of MS-based proteomics, the intracellular proteins of the aged SM were investigated [40,41]. However, little emphasis has been given to the matrisome, despite growing evidence indicating the ECM as an essential player in SM function. In fact, the matrisome not only constitutes the architectural scaffold for myofibers [42,43], but it is also a reservoir for signaling molecules (e.g., cytokines, chemokines, and growth factors) responding to different stimuli and to stress to maintain cellular homeostasis. Actually, the matrisome is a dynamic compartment mediating outside-in signaling and vice-versa between cells and the surrounding environment [44]. Therefore, in this study, we focused on the matrisome of the whole gastrocnemius muscle by applying a sequential extraction procedure in combination with LC-MS/MS analysis to reveal changes occurring with aging. It is worth remembering that, to date, there is no protocol and/or proteomic technique capable of detecting the entire complexity of the proteome, so our strategy was a compromise between sensitivity and quantitative accuracy. We were able to identify many ECM components, some of them (e.g., collagens, proteoglycans, glycoproteins) being only extracted after strong solubilization conditions such as urea/thiourea and/or guanidinium-HCl.

Our proteomic data demonstrated that changes in matrisome proteins mostly consisted of increased protein abundance in old vs. adult skeletal muscles.

65

### 3.1. Alteration of Core Matrisome in Aged vs. Adult Mice

Among the "core matrisome" **collagen** category, we revealed a significant age-dependent increase of collagen type IV and VI, which was confirmed by quantitative immunofluorescence.

Collagen type VI is present in the epimysial, perimysial, and endomysial interstitium playing a key role in maintaining the SM functional integrity as it represents, together with fibronectin and proteoglycans, the major constituent of the "niche", where the balance between differentiation, self-renewal, and maintenance of muscle regeneration capacity takes place [20,45]. Collagen type VI is typically organized as a heterotrimer of $\alpha 1$, $\alpha 2$, and $\alpha 3$ chains, but, recently, three new $\alpha$ chains have been described [46]. Since the $\alpha$ chains have a different length and we have demonstrated an increased abundance of only $\alpha 1$ and $\alpha 2$ chain, it could be suggested that an altered ratio among the various collagen type VI chains affects the stability and the supramolecular assembly of the beaded filaments, altering the role of type VI collagen as an anchoring component of basement membranes through the interactions with collagen type IV, biglycan, fibronectin, sarcolemma integrins, and cell surface proteoglycans [46]. Interestingly, thickening of the immunofluorescence staining area for type VI collagen occurred in the gastrocnemius of old mice, further supporting an age-associated alteration of the organization of the anchoring system.

Collagen type IV is a structural molecule of the basement membrane, and its concentration appeared to increase in old muscle, in agreement with previous observations, [47] although with differences depending on muscle type. Collagen type IV accumulation has been shown to drive out SC from their niche, thus potentially contributing to the satellite cell reduction observed in aging [29,48,49].

It is to be noted that, despite the increased amount of type IV and VI collagen contributing to the increased thickness of basement membranes, the endomysium thickness was not changed in adult and old mice. Accordingly, no overall age-associated hypertrophy of the ECM component was previously demonstrated in mouse skeletal muscle [50]. Moreover, in the present study, the amount of fibrillar collagens (i.e., collagen type I, III, and V) in the mouse gastrocnemius muscle did not change with aging. Data reported in the literature are very heterogeneous [51–54], but the loss of muscle performance has been generally related to fibrosis, although, by transcriptomic analysis, collagen genes (i.e., collagen type I and III) appeared significantly downregulated in aging [55]. The discrepancy among different studies may be related to the type or specific portion of muscles analyzed, to sample preparation, and/or to methods applied to quantify collagen (e.g., hydroxyproline measured by HPLC, collagen staining, transcriptomic analysis, proteomic analysis). Moreover, collagen accumulation may be due to excessive production, the altered balance between degradative enzymes and their inhibitors, a combination of the altered ratio between synthesis and degradation, or may be the result of post-translational modification and glycation crosslinking, thus increasing insolubility and lowering the ability of proteolytic enzymes to provide an efficient turnover [56].

Even if we did not observe statistically significant differences in the amount of collagen type I by LC-MS/MS and immunofluorescence, the fibrillar collagen in the perimysium (predominantly collagen type I) [57] of old animals showed a more linear and loosely organized distribution with an increased distance between collagen fibrils that may likely allow the interposition of other ECM constituents. Interestingly, a statistically significant decrease in collagen fiber "tortuosity" [19] and the accumulation of extensively cross-linked collagen together with the reduced size of most myofibers [26,27] have been advocated as a cause of increased muscle stiffness [49,50]. Muscle stiffness has been recently reported to increase, together with ECM amount, in human skeletal muscle of aged vs. young subjects [58]. Accordingly, muscle stiffness is considered a typical hallmark of muscle aging, [50–52,59] as well as the decreased compliance of myofibers in response to tensile loading [19].

Other components of the matrisome are **glycoproteins** such as laminin, fibronectin, and nidogen, which were detected in higher amounts in old compared to adult SM. Since these glycoproteins act as a bridge between collagen type IV and the sarcolemma of muscle

fibers [60], their increased amount is consistent with the higher thickness of the basement membrane observed in old animals. Moreover, the increase of laminin during aging can modify the ability of the basement membrane to store and release growth factors and other bioactive molecules required to form the SC niche [61] and to activate SC, thus supporting the previous finding of SC reduced activation potential in old mice [29]. In aged muscle, the shift from functional myofiber repair towards increased extracellular matrix deposition is also associated with changes in the micro-environment and the interactions between ECM glycoproteins as fibronectin, periostin, and tenascin. Interestingly, all of these molecules appeared to increase in the old gastrocnemius muscle.

Fibronectin, for instance, is one of the most widespread glycoproteins of the ECM, playing a role in various processes such as cellular adhesion, spreading and migration, as well as cellular development and differentiation. The increased abundance of fibronectin in old gastrocnemius is in agreement with very recent data demonstrating an association between high fibronectin levels in the aged gastrocnemius muscle, the reduced muscular strength, and myogenic regeneration and differentiation [62].

Periostin is a member of the TGF-beta family of proteins with a putative role associated with pathologic fibrotic events [63]. It is present in the endomysial space and functions upstream and downstream of TGF-beta [64]. Its expression is low in adult tissues, but it is strongly induced and secreted after injury or in dystrophic skeletal muscle [65].

Tenascin is present in all musculoskeletal regions in which high mechanical forces are transmitted, is upregulated in the damage/repair cycle [66] being produced in response to degeneration and the release of growth factors as TGF-beta, and was found to accumulate in the endomysium predominantly in the vicinity of necrotic and regenerating myofibers [67]. As it was also observed in association with atrophy and with age-induced atrophy, it may represent a possible cofactor in the etiology of sarcopenia [68,69].

Interestingly, thrombospondin (TSP1) is also an ECM molecule that was observed to be markedly increased in the aging SM. It modulates cell function by binding to matrix proteins and growth factors altering the properties of ECM and engaging signaling receptors on the cell surface with the activation of latent TGF-beta1. TSP1 promotes aging and it is in turn upregulated by age-related factors as ROS, glucose, and hypoxia and negatively affects mitochondria biogenesis and efficiency as well as endothelial cell proliferation [70,71].

TGF-beta signaling and expression may lead to increased collagens' deposition and to the development of an age-dependent fibrotic environment correlated to fibrin/fibrinogen accumulation, thus suggesting a possible involvement of macrophages within a generalized inflammatory response [72]. These data support the concept that inflammatory and coagulation pathways are increasingly active with aging and can contribute to sarcopenia and frailty [73].

The matrisome structure and organization are also sustained by the interaction between **proteoglycans** (PGs) and collagens [74]. For instance, biglycan and lumican bind to collagen regulating collagen fibrillogenesis, collagen fibril thickness, and notably interfibrillar spacing, which are important for tissue integrity. Interestingly, in old vs. adult mice, collagen bundles were characterized by the increased distance between fibrils in the presence of similar fibril size. This necessitates further, more detailed analysis of PGs/collagens interactions in aging skeletal muscle. PGs also bind to different growth factors, influencing their bioavailability, cell proliferation, and matrix deposition [75]. In this study, we have observed higher levels of some PGs (e.g., lumican, biglycan, and asporin) in old compared to adult SM. These results are not consistent with those of a recent study, which highlighted a downregulated gene expression of laminin, fibronectin, nidogen, and biglycan in aged SM [55]. This discrepancy is not surprising as many studies have already demonstrated that transcriptomic data had a low correlation with their corresponding proteins [76–78]. For instance, the decoupling of the proteome and transcriptome can be due to (i) post-transcriptional mechanisms regulating protein abundance; (ii) greater stability of proteins compared to transcripts; (iii) decreased proteolytic activity; and (iv) changes in protein synthesis rates.

*3.2. Alteration of Matrisome-Associated Proteins in Aged vs. Adult Mice*

Among **ECM affiliated proteins**, annexins (ANX) can play a critical role in cell membrane repair. The sarcolemma is subjected to severe mechanical stress and continuous stretching and the repair machinery is required to preserve and maintain membrane integrity. ANXA6 is a key factor in the repair machinery, and accumulates at the site of sarcolemma injury. This event precedes the activation of ANXA1 and ANXA2. ANXA6 is the only protein that we have observed to be significantly reduced in aging muscle. Reduction of ANXA6 inhibits the aggregation of ANXA1, ANXA2, and ANXA5, thus negatively affecting the repair process [79]. Moreover, an excess of ANXA2 that leaks from injured myofibers can activate muscle-resident fibro-adipogenic precursors that differentiate into adipocytes which gradually lead to muscle degeneration [80].

Muscle repair processes are also modulated by myoblasts-matrix interactions through interaction between laminin and galectin 1 [81]. Since galectin 1 is upregulated in old SM, these data confirm the higher expression that was detected in the signature of the age-dependent sarcopenia that is involved in mediating cellular responses to inflammation and apoptosis [82], in the terminal differentiation of myoblasts and the disruption of adhesion of myoblasts to laminin [83].

The homeostasis of the matrisome is finely controlled by different **ECM regulators**.

Both in PBS and U/T extract we revealed an increase of cathepsin D in old compared to adult SM. Cathepsin D exhibits its activity in the lysosome, but when the cells break it is released in the extracellular space. This molecule has been recently proposed as a sarcopenia biomarker, as its levels were significantly higher in sarcopenic patients than in control subjects [84].

Similarly, matrix metalloproteases (MMPs), ECM-associated enzymes, play a crucial role in regulating the degradation of matrisome molecules [85]. Except for MMP17, which did not change in aging, other MMPs or their inhibitors have been not identified in this study. This could be due to either their low concentration in our experimental conditions or stringent parameters applied in this study or different resolutions of LC-MS/MS, which is crucial for identifying scarce proteins.

By contrast, the inter alpha trypsin inhibitor heavy chain (ITIH4) is increased in aged SM. However, despite the name, it does not possess intrinsic trypsin inhibitory activity, is upregulated by IL-6, and is involved in the stabilization of the extracellular matrix [86], further supporting the occurrence of molecules involved and favoring the progressive accumulation of ECM in the environment surrounding myofibers.

Moreover, among ECM regulators, we have observed an increase of PEDF, a molecule that, inducing endothelial cell apoptosis, exerts antiangiogenic properties. Reduction of blood vessels may negatively affect nutrient and oxygen availability and therefore muscle metabolism. PEDF is upregulated in the aging muscle and is highly expressed in mesenchymal stem cells from old donors [87].

**4. Materials and Methods**

*4.1. Reagents*

All reagents were purchased from Sigma-Aldrich (Merk KGaA, Taufkirchen, Germany) unless otherwise stated.

*4.2. Mice*

Male BALB/c mice aged 12 months (adult, n = 9) and 24 months (old, n = 9) were used in this study. The mice, housed in groups of three to four, were maintained under standard conditions (24 ± 1 °C ambient temperature, 60 ± 15% relative humidity, and 12 h light/dark cycle) and fed *ad libitum* with standard commercial chow. The animals had only spontaneous free-moving activity in the cage.

### 4.3. Proteomic Analysis

#### 4.3.1. Preparation of Protein Samples for Proteomic Analysis

The whole gastrocnemius muscles were quickly removed from three mice for each age group and froze for proteomic analysis. Each muscle underwent a three-step sequential extraction (Figure 1a). Frozen muscle was homogenized on ice in phosphate buffer (PBS; 1:10 $w/v$) using a glass homogenizer to solubilize cellular and hydrophilic proteins. Samples were centrifuged at 8000× $g$ for 30 min at 4 °C. After recovering the supernatants (PBS extract), the resulting pellets were resuspended in urea-thiourea buffer (1:10 $w/v$) and incubated at 4 °C for 24 h under continuous shaking. After centrifugation at 15,000× $g$ for 20 min at 4 °C, the supernatant (U/T extract) was recovered, and the pellet was furthermore homogenized in guanidinium-HCl buffer (pH = 8.5, 1:5 $w/v$), heated at 100 °C for 10 min and collected (GuHCl extract).

These last steps were provided to maximize the extracellular matrix protein recovery. The protein concentration of each fraction was quantified using the Bradford method. 200 µg of proteins/fraction/muscle were subjected to proteomic analysis.

For each fraction, a gel-tube digestion was performed as already described [88]. The proteins embedded in the gel-tube were reduced by incubation with 10 mM dithioerythritol/100 mM ammonium bicarbonate for 45 min at 56 °C and then alkylated with 55 mM iodoacetamide/100 mM ammonium bicarbonate for 30 min at RT in the dark. Proteins were digested overnight at 37 °C in 100 mM ammonium bicarbonate pH 8.0 using sequencing grade trypsin at a 1:100 enzyme-to-protein ratio (Promega, Madison, MI, USA). Peptides were extracted from gel-tubes with 100% acetonitrile and dried with a SpeedVac (Eppendorf AG, Hamburg, Germany).

#### 4.3.2. Liquid Chromatography with Tandem Mass Spectrometry (LC-MS/MS)

Peptides obtained from each fraction were resuspended in water/formic acid solution (95:3:2). A UHPLC ultimate 3000 system coupled online to a Q Exactive Hybrid Quadrupole-Orbitrap Mass Spectrometer (Thermo Fisher Scientific, Waltham, MA, USA) was used, as already described [89] with some modifications. Chromatographic separation of peptides took place in a reverse-phase C18 column (100 mm × 2.1 µm ID, 1.9 µm, HyperG Thermo Fischer Scientific) and elution was performed using a binary system of solvents. Solvent A was 0,1% formic acid and solvent B was pure acetonitrile. A linear binary gradient was applied to eluate the peptides: 0–20% solvent B in solvent A for 240 min and further 60 min of 20–40% solvent B in solvent A. The precursor ion detection was done in an m/z-range from 400 to 1800 and the acquisition range for fragment ions was m/z from 200 to 2000. The sample injection flow was 0.5 mL/min, and the column was kept at a constant temperature of 30 °C. Data acquisition was controlled by Xcalibur 2.0.7 Software (Thermo Fisher Scientific, USA). Six independent experiments (three for adult and three for old muscles) were performed and each fraction obtained from each muscle was analyzed in duplicate.

#### 4.3.3. Data Processing for Protein Identification and Quantification

Raw MS/MS data (.raw) were inspected using BatMass (v. 0.3.0). Replicates were aligned using FreeStyle (v.1.5) to check the quality of runs. Raw files were further converted by msConvert ProteoWizard (v.3.0.19239) in MGF file using default settings and uploaded to MASCOT server (v.2.7.0) for MS/MS Ion Search. The search was performed using Uniprot (2018_05) restricted to *Mus musculus* (Taxonomy ID: 10090) and cRAP database to detect most commonly adventitious proteins (https://www.thegpm.org/GPM/index.html (accessed on 6 April 2021:)). Parameters for identification included: (i) trypsin as an enzyme with 1 as maximum missed cleavage; (ii) mass error tolerances for precursor and fragment ions set to 10 ppm and 0.02 Da, respectively; (iii) peptide charge (2+, 3+, 4+); (iv) protein mass no restriction; and (v) carbamidomethyl cysteine (C) was set as fixed modification while deamidation of asparagine and glutamine (NQ), oxidation of methionine (M) and cysteine propionamide (C) were considered as variable modifications. Only confident

peptide identified with a false discovery rate $\leq 1$ and protein with at least one unique peptide were exported.

Mascot results (.dat) obtained for each extraction were imported in Skyline-daily (v.21.0.9.139) to generate the spectral libraries using the following parameters: 0.95 as spectra cut-off score; peptide length of 8-25 amino acids; precursor ion charge 2+, 3+, 4+; MS1 filters were set to "use high selectivity extraction" with a resolving power of 60,000 at 300 m/z; repeated and duplicate peptides were removed. Accordingly, to Skyline "DDA peptide search" workflow, raw files (.raw) were imported and matched to spectral libraries to recover precursor ion intensity. Precursor ion intensity is the sum of areas under the curve of extracted ion chromatograms (XICs) containing precursor ion isotope peaks (M, M+1, M+2) [90]. Fasta files containing proteins with 1% FDR were imported to Skyline to maintain and fix FDR. Finally, quantitative analysis was performed on proteins with at least two peptides. Indeed, protein inference is mainly based on the unique peptides that are not shared by multiple proteins. However, one peptide can be incorrectly quantified across LC-MS runs, producing improper quantification. In this perspective, first of all, a proteome discovery study was performed releasing a list of proteins identified with at least one unique peptide, and secondly, a label-free quantification study was performed only on proteins identified with at least two peptides to reduce incorrect quantification [37].

### 4.4. Bioinformatic Analysis

We interrogated the MatrisomeDB (http://www.pepchem.org/matrisomedb (accessed on 28 May 2021)) to further characterize and categorize proteins identified in our samples. To date, MatrisomeDB is the most complete database of ECM proteomic data and matrisomal proteins are divided into the "core matrisome" (i.e., glycoproteins, collagens, and proteoglycans) and the "matrisome-associated proteins" (i.e., ECM-affiliated proteins, ECM regulators, and secreted factors) [35].

### 4.5. ECM Component Evaluation by Immunofluorescence

Three adult and three old mice were deeply anesthetized with Tribromoethanol and sacrificed by cervical dislocation. Gastrocnemius muscles were quickly removed and frozen in liquid nitrogen-precooled isopentane. Transversally sectioned 7-µm thick cryosections were incubated with 1% bovine serum albumin, 2% normal goat serum, 0.3% Triton® X-100 in phosphate buffer solution (PBS) for 1 h and immunolabelled with the following probes: a rabbit polyclonal antibody direct against type I collagen, diluted 1:50 (GeneTex, Irvine, CA, USA); a human monoclonal antibody direct against type VI collagen, diluted 1:1000 (ICN Biomedicals, Costa Mesa, CA, USA); rabbit polyclonal antibody direct against laminin, diluted 1:800 (Abcam, Cambridge, UK), in double labeling with anti-collagen type VI.

After washing with PBS, cryosections were stained with the proper secondary antibody: Alexafluor 488-anti-mouse antibodies diluted 1:200 for type VI collagen (Molecular Probes, Invitrogen, CA, USA). Alexafluor 594-anti-rabbit diluted 1:200, for laminin and collagen type I. The cryosections were finally counterstained for DNA with 0.1 µg/mL Hoechst 33258 and mounted in PBS:glycerol (1:1).

An Olympus BX51 microscope equipped with a 100W mercury lamp (Olympus Italia, Milan, Italy) was used under the following conditions: 450–480 nm excitation filter (excf), 500 nm dichroic mirror (dm) for Alexa 488; 540 nm excf, 580 nm dm, and 620 nm barrier filter (bf) for Alexa 594; 330–385 nm excf, 400 nm dm, and 420 nm bf, for Hoechst 33342. Images were recorded with an Olympus Magnifire digital camera system (Olympus Italia).

A routine was written in MATLAB (2018b version, Mathworks) to quantify the area covered by fluorescence-positive pixels for the total area in four random images acquired at X20 for each animal.

### 4.6. Ultrastructural Morphological and Morphometrical Evaluation

Three adult and three old mice were deeply anesthetized with Tribromoethanol drug and then perfused via the ascending aorta with 0.1 M PBS followed by 4% paraformalde-

hyde in PBS. The gastrocnemius muscle was quickly removed, and samples (about 1 mm$^3$) were further placed for 2 h at 4 °C in 2.5% glutaraldehyde (Electron Microscopy Sciences, Hatfield, PA, USA) plus 2% paraformaldehyde in 0.1 M PBS. The samples were then rinsed with PBS, postfixed with 1% OsO$_4$ (Electron Microscopy Sciences) and 1.5% potassium ferrocyanide for 2 h at 4 °C, dehydrated with acetone, and embedded in Epon 812 resin (Electron Microscopy Sciences).

Ultrathin sections (70–90 nm thick) were stained with lead citrate for 1 min and observed in a Philips Morgagni transmission electron microscope operating at 80 kV and equipped with a Megaview III camera for digital image acquisition.

The morphometric evaluation of the endomysium thickness was performed on 20 randomly selected electron micrographs (×5600) of longitudinally sectioned muscle, measuring the distance between the sarcolemma of two adjacent muscle cells every 1 μm of sarcolemma length, for a total of 50 measurements per animal.

For morphometric evaluation of the thickness of the basement membrane, a total of 30 measurements per animal were performed. The thickness of the electrodense sheath covering the myofiber was considered on randomly selected electron micrographs (×36,000) of longitudinally sectioned muscles.

The morphometric evaluation of the perimysium collagen bundle size was performed on a total of 10 longitudinally sectioned collagen bundles per animal. The index of collagen bundle linearity (X/Y, expressed as the ratio between the real length of the bundle profile and the corresponding linear length) was assessed on a total of 30 longitudinally sectioned collagen bundles per age group.

For morphometric evaluation of collagen fibrils, measurement of fibril size, as well as the distance between single collagen fibrils, was performed on a total of 100 longitudinally sectioned collagen fibrils per age group.

All measurements were made by using the Radius software for image acquisition and elaboration implemented in the Philips Morgagni transmission electron microscope.

*4.7. Statistical Analysis*

Statistical analysis of proteomic data was performed using Skyline group comparison tool, set as follows: normalization of runs was performed using "Equilize Medians" with 0.95 as the confidence level; Tukey's Median Polish was set as the summary method. The comparison was set comparing the value obtained in old skeletal muscle against those of adult samples. Proteins with a fold change > 1.5 or < 0.66 and a $p$ value < 0.05 were significantly up-and down-regulated, respectively.

Data on the percentage of fluorescent (positive) areas for laminin, collagen type VI, and type I and data of morphometrical evaluation of transmission electron microscopy images for endomysium size, basement membrane thickness, collagen bundle size and linearity, collagen fibril size, and distance were pooled according to the age group and presented as mean ± SEM. The Shapiro–Wilk test showed that data were not normally distributed ($p < 0.001$). Consequently, the subsequent statistical analysis was performed using the non-parametric Mann–Whitney test, setting statistical significance at $p$ value $\leq 0.05$. The IBM-SPSS (v.25, Armonk, NY, USA) statistical package was used for all analyses.

**5. Conclusions**

This study provided the first characterization of the matrisome in the aging gastrocnemius muscle and highlights the higher age-dependent abundance of several identified ECM components (Figure 6).
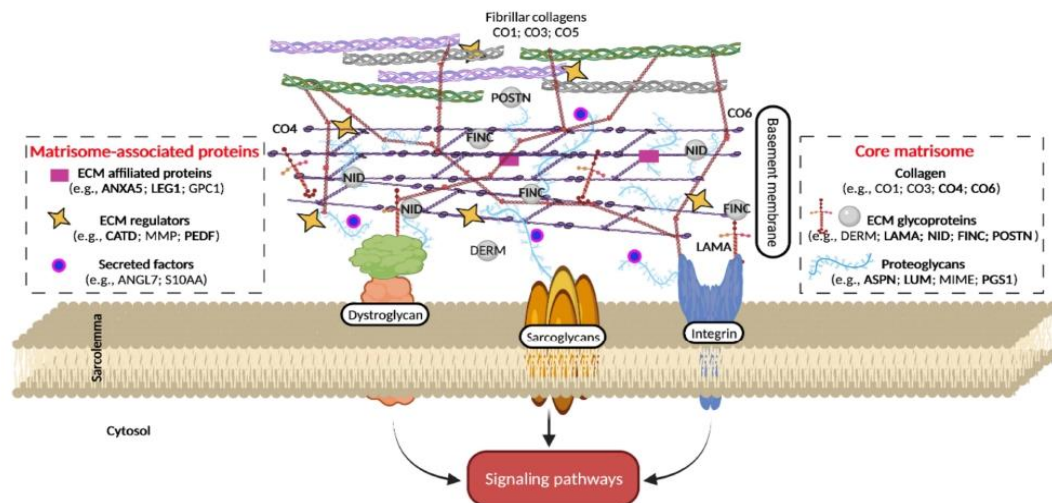
**Figure 6.** Schematic representation of matrix-sarcolemma axis of skeletal muscle fibre. Proteins differentially expressed between old and adult SM are reported in bold. ANGL7, angiopoietin-related protein 7; ANX, annexin; ASPN, asporin; CO, collagen; CATD, cathepsin D; DERM, dermatopontin; FINC, fibronectin; GPC1, Glypican 1; LAMA, laminin; LEG1, galectin 1; LUM, lumican; MMP, matrix metalloproteinase; MIME, mimecan; NID, nidogen; PEDF, pigment epithelium-derived factor; PGS1, biglycan; POSTN, periostin; S10AA, protein S100-A10.

Since interactions between ECM molecules and between ECM and sarcolemma provide not only structural support but also a mechano-sensing transduction system and a source of cytokines and growth factors, the deepen insight on the matrisome in the aged SM can pave the way for a better understanding of the synergic interplay of the whole extracellular environment and of the mechanisms that can contribute to the age-dependent muscle dysfunction by hindering, for instance, fiber contractility [91], lateral force transmission [92,93], tissue stiffness [49,50], and satellite cell function [12] through ECM-driven signaling pathways.

**Author Contributions:** Conceptualization, F.B. (Federica Boraldi) and M.M.; formal analysis, F.D.L., B.C., F.B. (Federica Boraldi), and F.B. (Federico Boschi); investigation, F.D.L., B.C. and M.A.L.; data curation, M.M. and F.B. (Federica Boraldi); writing—original draft preparation, F.D.L. and B.C.; writing—review and editing, F.B. (Federica Boraldi), C.Z. and D.Q.; supervision, D.Q.; funding acquisition, F.B. (Federica Boraldi) and C.Z. All authors have read and agreed to the published version of the manuscript.

**Institutional Review Board Statement:** Animals were handled according to the regulations of the Italian Ministry of Health (DL 4 March 2014, n. 26) and to the European Communities Council (Directive 63/2010/EU of the European Parliament and the Council) directives. The experimental protocol was approved by the Italian Ministry of Health (Ref.: 538/2015-PR).

**Informed Consent Statement:** Not applicable.

**Data Availability Statement:** The mass spectrometry proteomics data have been deposited to the ProteomeXchange Consortium via the PRIDE partner repository with the dataset identifier PXD027895.

## References

1.  Rowland, L.A.; Bal, N.C.; Periasamy, M. The Role of Skeletal-Muscle-Based Thermogenic Mechanisms in Vertebrate Endothermy. *Biol. Rev. Camb. Philos. Soc.* **2015**, *90*, 1279–1297. [CrossRef] [PubMed]
2.  Baskin, K.K.; Winders, B.R.; Olson, E.N. Muscle as a "Mediator" of Systemic Metabolism. *Cell Metab.* **2015**, *21*, 237–248. [CrossRef] [PubMed]
3.  Cruz-Jentoft, A.J.; Sayer, A.A. Sarcopenia. *Lancet* **2019**, *393*, 2636–2646. [CrossRef]
4.  Cruz-Jentoft, A.J.; Bahat, G.; Bauer, J.; Boirie, Y.; Bruyère, O.; Cederholm, T.; Cooper, C.; Landi, F.; Rolland, Y.; Sayer, A.A.; et al. Sarcopenia: Revised European Consensus on Definition and Diagnosis. *Age Ageing* **2019**, *48*, 16–31. [CrossRef]
5.  Marty, E.; Liu, Y.; Samuel, A.; Or, O.; Lane, J. A Review of Sarcopenia: Enhancing Awareness of an Increasingly Prevalent Disease. *Bone* **2017**, *105*, 276–286. [CrossRef] [PubMed]
6.  Walston, J.D. Sarcopenia in Older Adults. *Curr. Opin. Rheumatol.* **2012**, *24*, 623–627. [CrossRef] [PubMed]
7.  Etienne, J.; Liu, C.; Skinner, C.M.; Conboy, M.J.; Conboy, I.M. Skeletal Muscle as an Experimental Model of Choice to Study Tissue Aging and Rejuvenation. *Skelet. Muscle* **2020**, *10*, 4. [CrossRef] [PubMed]
8.  Domingues-Faria, C.; Vasson, M.-P.; Goncalves-Mendes, N.; Boirie, Y.; Walrand, S. Skeletal Muscle Regeneration and Impact of Aging and Nutrition. *Ageing Res. Rev.* **2016**, *26*, 22–36. [CrossRef]
9.  Melouane, A.; Yoshioka, M.; St-Amand, J. Extracellular Matrix/Mitochondria Pathway: A Novel Potential Target for Sarcopenia. *Mitochondrion* **2020**, *50*, 63–70. [CrossRef]
10. Cade, W.T.; Yarasheski, K.E. Metabolic and Molecular Aspects of Sarcopenia. In *Principles of Molecular Medicine*; Runge, M.S., Patterson, C., Eds.; Humana Press: Totowa, NJ, USA, 2006; pp. 529–534. ISBN 978-1-59259-963-9.
11. McCormick, R.; Vasilaki, A. Age-Related Changes in Skeletal Muscle: Changes to Life-Style as a Therapy. *Biogerontology* **2018**, *19*, 519–536. [CrossRef]
12. Thomas, K.; Engler, A.J.; Meyer, G.A. Extracellular Matrix Regulation in the Muscle Satellite Cell Niche. *Connect. Tissue Res.* **2015**, *56*, 1–8. [CrossRef] [PubMed]
13. Zhang, W.; Liu, Y.; Zhang, H. Extracellular Matrix: An Important Regulator of Cell Functions and Skeletal Muscle Development. *Cell Biosci.* **2021**, *11*, 65. [CrossRef] [PubMed]
14. Street, S.F. Lateral Transmission of Tension in Frog Myofibers: A Myofibrillar Network and Transverse Cytoskeletal Connections Are Possible Transmitters. *J. Cell Physiol.* **1983**, *114*, 346–364. [CrossRef] [PubMed]
15. Thorsteinsdóttir, S.; Deries, M.; Cachaço, A.S.; Bajanca, F. The Extracellular Matrix Dimension of Skeletal Muscle Development. *Dev. Biol.* **2011**, *354*, 191–207. [CrossRef] [PubMed]
16. Calve, S.; Odelberg, S.J.; Simon, H.-G. A Transitional Extracellular Matrix Instructs Cell Behavior during Muscle Regeneration. *Dev. Biol.* **2010**, *344*, 259–271. [CrossRef]
17. Kragstrup, T.W.; Kjaer, M.; Mackey, A.L. Structural, Biochemical, Cellular, and Functional Changes in Skeletal Muscle Extracellular Matrix with Aging. *Scand. J. Med. Sci. Sports* **2011**, *21*, 749–757. [CrossRef]
18. Trensz, F.; Lucien, F.; Couture, V.; Söllrald, T.; Drouin, G.; Rouleau, A.-J.; Grandbois, M.; Lacraz, G.; Grenier, G. Increased Microenvironment Stiffness in Damaged Myofibers Promotes Myogenic Progenitor Cell Proliferation. *Skelet. Muscle* **2015**, *5*, 5. [CrossRef]
19. Stearns-Reider, K.M.; D'Amore, A.; Beezhold, K.; Rothrauff, B.; Cavalli, L.; Wagner, W.R.; Vorp, D.A.; Tsamis, A.; Shinde, S.; Zhang, C.; et al. Aging of the Skeletal Muscle Extracellular Matrix Drives a Stem Cell Fibrogenic Conversion. *Aging Cell* **2017**, *16*, 518–528. [CrossRef]
20. Urciuolo, A.; Quarta, M.; Morbidoni, V.; Gattazzo, F.; Molon, S.; Grumati, P.; Montemurro, F.; Tedesco, F.S.; Blaauw, B.; Cossu, G.; et al. Collagen VI Regulates Satellite Cell Self-Renewal and Muscle Regeneration. *Nat. Commun.* **2013**, *4*, 1964. [CrossRef]
21. Højlund, K.; Yi, Z.; Hwang, H.; Bowen, B.; Lefort, N.; Flynn, C.R.; Langlais, P.; Weintraub, S.T.; Mandarino, L.J. Characterization of the Human Skeletal Muscle Proteome by One-Dimensional Gel Electrophoresis and HPLC-ESI-MS/MS. *Mol. Cell Proteom.* **2008**, *7*, 257–267. [CrossRef]
22. Lang, F.; Aravamudhan, S.; Nolte, H.; Türk, C.; Hölper, S.; Müller, S.; Günther, S.; Blaauw, B.; Braun, T.; Krüger, M. Dynamic Changes in the Mouse Skeletal Muscle Proteome during Denervation-Induced Atrophy. *Dis. Model. Mech.* **2017**, *10*, 881–896. [CrossRef]
23. Deshmukh, A.S.; Murgia, M.; Nagaraj, N.; Treebak, J.T.; Cox, J.; Mann, M. Deep Proteomics of Mouse Skeletal Muscle Enables Quantitation of Protein Isoforms, Metabolic Pathways, and Transcription Factors. *Mol. Cell Proteom.* **2015**, *14*, 841–853. [CrossRef] [PubMed]
24. Ubaida-Mohien, C.; Lyashkov, A.; Gonzalez-Freire, M.; Tharakan, R.; Shardell, M.; Moaddel, R.; Semba, R.D.; Chia, C.W.; Gorospe, M.; Sen, R.; et al. Discovery Proteomics in Aging Human Skeletal Muscle Finds Change in Spliceosome, Immunity, Proteostasis and Mitochondria. *eLife* **2019**, *8*, e49874. [CrossRef] [PubMed]
25. Jacobson, K.R.; Lipp, S.; Acuna, A.; Leng, Y.; Bu, Y.; Calve, S. Comparative Analysis of the Extracellular Matrix Proteome across the Myotendinous Junction. *J. Proteome Res.* **2020**, *19*, 3955–3967. [CrossRef] [PubMed]

26.  Malatesta, M.; Fattoretti, P.; Giagnacovo, M.; Pellicciari, C.; Zancanaro, C. Physical Training Modulates Structural and Functional Features of Cell Nuclei in Type II Myofibers of Old Mice. *Rejuvenation Res.* **2011**, *14*, 543–552. [CrossRef]

27.  Zancanaro, C.; Mariotti, R.; Perdoni, F.; Nicolato, E.; Malatesta, M. Physical Training Is Associated with Changes in Nuclear Magnetic Resonance and Morphometrical Parameters of the Skeletal Muscle in Senescent Mice. *Eur. J. Histochem.* **2007**, *51*, 305–310. [CrossRef]

28.  Costanzo, M.; Cisterna, B.; Malatesta, M. Effect of Physical Exercise on the Ultrastructural Features of Skeletal Muscle Mitochondria in Old Mice. *Microscopie* **2013**, *20*, 37–43. [CrossRef]

29.  Cisterna, B.; Giagnacovo, M.; Costanzo, M.; Fattoretti, P.; Zancanaro, C.; Pellicciari, C.; Malatesta, M. Adapted Physical Exercise Enhances Activation and Differentiation Potential of Satellite Cells in the Skeletal Muscle of Old Mice. *J. Anat.* **2016**, *228*, 771–783. [CrossRef]

30.  Malatesta, M.; Giagnacovo, M.; Cardani, R.; Meola, G.; Pellicciari, C. RNA Processing Is Altered in Skeletal Muscle Nuclei of Patients Affected by Myotonic Dystrophy. *Histochem. Cell Biol.* **2011**, *135*, 419–425. [CrossRef]

31.  Malva, A.D.; Albenzio, M.; Santillo, A.; Russo, D.; Figliola, L.; Caroprese, M.; Marino, R. Methods for Extraction of Muscle Proteins from Meat and Fish Using Denaturing and Nondenaturing Solutions. *J. Food Qual.* **2018**, *2018*, e8478471. [CrossRef]

32.  Wilson, R.; Diseberg, A.F.; Gordon, L.; Zivkovic, S.; Tatarczuch, L.; Mackie, E.J.; Gorman, J.J.; Bateman, J.F. Comprehensive Profiling of Cartilage Extracellular Matrix Formation and Maturation Using Sequential Extraction and Label-Free Quantitative Proteomics. *Mol. Cell Proteom.* **2010**, *9*, 1296–1313. [CrossRef] [PubMed]

33.  Sato, N.; Taniguchi, T.; Goda, Y.; Kosaka, H.; Higashino, K.; Sakai, T.; Katoh, S.; Yasui, N.; Sairyo, K.; Taniguchi, H. Proteomic Analysis of Human Tendon and Ligament: Solubilization and Analysis of Insoluble Extracellular Matrix in Connective Tissues. *J. Proteome Res.* **2016**, *15*, 4709–4721. [CrossRef] [PubMed]

34.  Naba, A.; Clauser, K.R.; Ding, H.; Whittaker, C.A.; Carr, S.A.; Hynes, R.O. The Extracellular Matrix: Tools and Insights for the "Omics" Era. *Matrix Biol.* **2016**, *49*, 10–24. [CrossRef] [PubMed]

35.  Shao, X.; Taha, I.N.; Clauser, K.R.; Gao, Y.T.; Naba, A. MatrisomeDB: The ECM-Protein Knowledge Database. *Nucleic Acids Res.* **2020**, *48*, D1136–D1144. [CrossRef] [PubMed]

36.  Théron, L.; Gueugneau, M.; Coudy, C.; Viala, D.; Bijlsma, A.; Butler-Browne, G.; Maier, A.; Béchet, D.; Chambon, C. Label-Free Quantitative Protein Profiling of Vastus Lateralis Muscle during Human Aging. *Mol. Cell Proteom.* **2014**, *13*, 283–294. [CrossRef] [PubMed]

37.  Tsai, T.-H.; Choi, M.; Banfai, B.; Liu, Y.; MacLean, B.X.; Dunkley, T.; Vitek, O. Selection of Features with Consistent Profiles Improves Relative Protein Quantification in Mass Spectrometry Experiments. *Mol. Cell Proteom.* **2020**, *19*, 944–959. [CrossRef]

38.  Malatesta, M.; Perdoni, F.; Muller, S.; Zancanaro, C.; Pellicciari, C. Nuclei of Aged Myofibres Undergo Structural and Functional Changes Suggesting Impairment in RNA Processing. *Eur. J. Histochem.* **2009**, *53*, 97–106. [CrossRef]

39.  Zahn, J.M.; Sonu, R.; Vogel, H.; Crane, E.; Mazan-Mamczarz, K.; Rabkin, R.; Davis, R.W.; Becker, K.G.; Owen, A.B.; Kim, S.K. Transcriptional Profiling of Aging in Human Muscle Reveals a Common Aging Signature. *PLoS Genet.* **2006**, *2*, e115. [CrossRef]

40.  Ohlendieck, K. Proteomics of Skeletal Muscle Differentiation, Neuromuscular Disorders and Fiber Aging. *Expert Rev. Proteom.* **2010**, *7*, 283–296. [CrossRef]

41.  Doran, P.; Donoghue, P.; O'Connell, K.; Gannon, J.; Ohlendieck, K. Proteomics of Skeletal Muscle Aging. *Proteomics* **2009**, *9*, 989–1003. [CrossRef]

42.  Ahmad, K.; Shaikh, S.; Ahmad, S.S.; Lee, E.J.; Choi, I. Cross-Talk Between Extracellular Matrix and Skeletal Muscle: Implications for Myopathies. *Front. Pharmacol.* **2020**, *11*, 142. [CrossRef]

43.  Ahmad, K.; Lee, E.J.; Moon, J.S.; Park, S.-Y.; Choi, I. Multifaceted Interweaving Between Extracellular Matrix, Insulin Resistance, and Skeletal Muscle. *Cells* **2018**, *7*, 148. [CrossRef]

44.  Hynes, R.O. The Extracellular Matrix: Not Just Pretty Fibrils. *Science* **2009**, *326*, 1216–1219. [CrossRef]

45.  Muñoz-Cánoves, P.; Neves, J.; Sousa-Victor, P. Understanding Muscle Regenerative Decline with Aging: New Approaches to Bring Back Youthfulness to Aged Stem Cells. *FEBS J.* **2020**, *287*, 406–416. [CrossRef]

46.  Fitzgerald, J.; Holden, P.; Hansen, U. The Expanded Collagen VI Family: New Chains and New Questions. *Connect. Tissue Res.* **2013**, *54*, 345–350. [CrossRef]

47.  Kovanen, V.; Suominen, H.; Risteli, J.; Risteli, L. Type IV Collagen and Laminin in Slow and Fast Skeletal Muscle in Rats–Effects of Age and Life-Time Endurance Training. *Coll. Relat. Res.* **1988**, *8*, 145–153. [CrossRef]

48.  Snow, M.H. The Effects of Aging on Satellite Cells in Skeletal Muscles of Mice and Rats. *Cell Tissue Res.* **1977**, *185*, 399–408. [CrossRef] [PubMed]

49.  Csapo, R.; Gumpenberger, M.; Wessner, B. Skeletal Muscle Extracellular Matrix—What Do We Know About Its Composition, Regulation, and Physiological Roles? A Narrative Review. *Front. Physiol.* **2020**, *11*, 253. [CrossRef] [PubMed]

50.  Wood, L.K.; Kayupov, E.; Gumucio, J.P.; Mendias, C.L.; Claflin, D.R.; Brooks, S.V. Intrinsic Stiffness of Extracellular Matrix Increases with Age in Skeletal Muscles of Mice. *J. Appl. Physiol.* **2014**, *117*, 363–369. [CrossRef]

51.  Alnaqeeb, M.A.; Al Zaid, N.S.; Goldspink, G. Connective Tissue Changes and Physical Properties of Developing and Ageing Skeletal Muscle. *J. Anat.* **1984**, *139 Pt 4*, 677–689. [PubMed]

52.  Lacraz, G.; Rouleau, A.-J.; Couture, V.; Söllrald, T.; Drouin, G.; Veillette, N.; Grandbois, M.; Grenier, G. Increased Stiffness in Aged Skeletal Muscle Impairs Muscle Progenitor Cell Proliferative Activity. *PLoS ONE* **2015**, *10*, e0136217. [CrossRef] [PubMed]

53. Kovanen, V.; Suominen, H. Age- and Training-Related Changes in the Collagen Metabolism of Rat Skeletal Muscle. *Eur. J. Appl. Physiol. Occup. Physiol.* **1989**, 58, 765–771. [CrossRef] [PubMed]
54. Haus, J.M.; Carrithers, J.A.; Trappe, S.W.; Trappe, T.A. Collagen, Cross-Linking, and Advanced Glycation End Products in Aging Human Skeletal Muscle. *J. Appl. Physiol.* **2007**, 103, 2068–2076. [CrossRef] [PubMed]
55. Chen, W.-J.; Lin, I.-H.; Lee, C.-W.; Chen, Y.-F. Aged Skeletal Muscle Retains the Ability to Remodel Extracellular Matrix for Degradation of Collagen Deposition after Muscle Injury. *Int. J. Mol. Sci.* **2021**, 22, 2123. [CrossRef]
56. Gillies, A.R.; Lieber, R.L. Structure and Function of the Skeletal Muscle Extracellular Matrix. *Muscle Nerve* **2011**, 44, 318–331. [CrossRef] [PubMed]
57. Gelse, K.; Pöschl, E.; Aigner, T. Collagens—Structure, Function, and Biosynthesis. *Adv. Drug Deliv. Rev.* **2003**, 55, 1531–1546. [CrossRef]
58. Pavan, P.; Monti, E.; Bondí, M.; Fan, C.; Stecco, C.; Narici, M.; Reggiani, C.; Marcucci, L. Alterations of Extracellular Matrix Mechanical Properties Contribute to Age-Related Functional Impairment of Human Skeletal Muscles. *Int. J. Mol. Sci.* **2020**, 21, 3992. [CrossRef]
59. Gosselin, L.E.; Martinez, D.A.; Vailas, A.C.; Sieck, G.C. Passive Length-Force Properties of Senescent Diaphragm: Relationship with Collagen Characteristics. *J. Appl. Physiol.* **1994**, 76, 2680–2685. [CrossRef]
60. Hohenester, E.; Yurchenco, P.D. Laminins in Basement Membrane Assembly. *Cell Adhes. Migr.* **2013**, 7, 56–63. [CrossRef]
61. Grzelkowska-Kowalczyk, K. *The Importance of Extracellular Matrix in Skeletal Muscle Development and Function*; IntechOpen: London, UK, 2016; ISBN 978-953-51-2416-0.
62. Sosa, P.; Alcalde-Estévez, E.; Asenjo-Bueno, A.; Plaza, P.; Carrillo-López, N.; Olmos, G.; López-Ongil, S.; Ruiz-Torres, M.P. Aging-Related Hyperphosphatemia Impairs Myogenic Differentiation and Enhances Fibrosis in Skeletal Muscle. *J. Cachexia Sarcopenia Muscle* **2021**. [CrossRef] [PubMed]
63. Conway, S.J.; Izuhara, K.; Kudo, Y.; Litvin, J.; Markwald, R.; Ouyang, G.; Arron, J.R.; Holweg, C.T.J.; Kudo, A. The Role of Periostin in Tissue Remodeling across Health and Disease. *Cell Mol. Life Sci.* **2014**, 71, 1279–1288. [CrossRef] [PubMed]
64. Horiuchi, K.; Amizuka, N.; Takeshita, S.; Takamatsu, H.; Katsuura, M.; Ozawa, H.; Toyama, Y.; Bonewald, L.F.; Kudo, A. Identification and Characterization of a Novel Protein, Periostin, with Restricted Expression to Periosteum and Periodontal Ligament and Increased Expression by Transforming Growth Factor Beta. *J. Bone Miner. Res.* **1999**, 14, 1239–1249. [CrossRef] [PubMed]
65. Lorts, A.; Schwanekamp, J.A.; Baudino, T.A.; McNally, E.M.; Molkentin, J.D. Deletion of Periostin Reduces Muscular Dystrophy and Fibrosis in Mice by Modulating the Transforming Growth Factor-β Pathway. *Proc. Natl. Acad. Sci. USA* **2012**, 109, 10978–10983. [CrossRef]
66. Järvinen, T.A.; Kannus, P.; Järvinen, T.L.; Jozsa, L.; Kalimo, H.; Järvinen, M. Tenascin-C in the Pathobiology and Healing Process of Musculoskeletal Tissue Injury. *Scand. J. Med. Sci. Sports* **2000**, 10, 376–382. [CrossRef]
67. Settles, D.L.; Cihak, R.A.; Erickson, H.P. Tenascin-C Expression in Dystrophin-Related Muscular Dystrophy. *Muscle Nerve* **1996**, 19, 147–154. [CrossRef]
68. Schoser, B.G.; Faissner, A.; Goebel, H.H. Immunolocalization of Tenascin-C in Human Type II Fiber Atrophy. *J. Mol. Neurosci.* **1999**, 13, 167–175. [CrossRef]
69. Flück, M.; Mund, S.I.; Schittny, J.C.; Klossner, S.; Durieux, A.-C.; Giraud, M.-N. Mechano-Regulated Tenascin-C Orchestrates Muscle Repair. *PNAS* **2008**, 105, 13662–13667. [CrossRef] [PubMed]
70. Isenberg, J.S.; Roberts, D.D. Thrombospondin-1 in Maladaptive Aging Responses: A Concept Whose Time Has Come. *Am. J. Physiol. Cell Physiol.* **2020**, 319, C45–C63. [CrossRef]
71. Frazier, E.P.; Isenberg, J.S.; Shiva, S.; Zhao, L.; Schlesinger, P.; Dimitry, J.; Abu-Asab, M.S.; Tsokos, M.; Roberts, D.D.; Frazier, W.A. Age-Dependent Regulation of Skeletal Muscle Mitochondria by the Thrombospondin-1 Receptor CD47. *Matrix Biol.* **2011**, 30, 154–161. [CrossRef] [PubMed]
72. Vidal, B.; Serrano, A.L.; Tjwa, M.; Suelves, M.; Ardite, E.; De Mori, R.; Baeza-Raja, B.; Martínez de Lagrán, M.; Lafuste, P.; Ruiz-Bonilla, V.; et al. Fibrinogen Drives Dystrophic Muscle Fibrosis via a TGFbeta/Alternative Macrophage Activation Pathway. *Genes Dev.* **2008**, 22, 1747–1752. [CrossRef]
73. Kanapuru, B.; Ershler, W.B. Inflammation, Coagulation, and the Pathway to Frailty. *Am. J. Med.* **2009**, 122, 605–613. [CrossRef] [PubMed]
74. Ameye, L.; Young, M.F. Mice Deficient in Small Leucine-Rich Proteoglycans: Novel in Vivo Models for Osteoporosis, Osteoarthritis, Ehlers-Danlos Syndrome, Muscular Dystrophy, and Corneal Diseases. *Glycobiology* **2002**, 12, 107R–116R. [CrossRef] [PubMed]
75. Ludwig, M.S. Proteoglycans and Pathophysiology. *J. Appl. Physiol.* **2007**, 103, 735–736. [CrossRef] [PubMed]
76. Yang, H.; Xu, X.; Ma, H.; Jiang, J. Integrative Analysis of Transcriptomics and Proteomics of Skeletal Muscles of the Chinese Indigenous Shaziling Pig Compared with the Yorkshire Breed. *BMC Genet.* **2016**, 17, 80. [CrossRef]
77. Davey, J.R.; Watt, K.I.; Parker, B.L.; Chaudhuri, R.; Ryall, J.G.; Cunningham, L.; Qian, H.; Sartorelli, V.; Sandri, M.; Chamberlain, J.; et al. Integrated Expression Analysis of Muscle Hypertrophy Identifies *Asb2* as a Negative Regulator of Muscle Mass. *JCI Insight* **2016**, 1. [CrossRef]
78. Kühl, I.; Miranda, M.; Atanassov, I.; Kuznetsova, I.; Hinze, Y.; Mourier, A.; Filipovska, A.; Larsson, N.-G. Transcriptomic and Proteomic Landscape of Mitochondrial Dysfunction Reveals Secondary Coenzyme Q Deficiency in Mammals. *eLife* **2017**, 6, e30952. [CrossRef]

79. Croissant, C.; Gounou, C.; Bouvet, F.; Tan, S.; Bouter, A. Annexin-A6 in Membrane Repair of Human Skeletal Muscle Cell: A Role in the Cap Subdomain. *Cells* **2020**, *9*, 1742. [CrossRef]

80. Croissant, C.; Carmeille, R.; Brévart, C.; Bouter, A. Annexins and Membrane Repair Dysfunctions in Muscular Dystrophies. *Int. J. Mol. Sci.* **2021**, *22*, 5276. [CrossRef]

81. Cooper, D.N.; Barondes, S.H. Evidence for Export of a Muscle Lectin from Cytosol to Extracellular Matrix and for a Novel Secretory Mechanism. *J. Cell Biol.* **1990**, *110*, 1681–1691. [CrossRef]

82. Giresi, P.G.; Stevenson, E.J.; Theilhaber, J.; Koncarevic, A.; Parkington, J.; Fielding, R.A.; Kandarian, S.C. Identification of a Molecular Signature of Sarcopenia. *Physiol. Genom.* **2005**, *21*, 253–263. [CrossRef]

83. Watt, D.J.; Jones, G.E.; Goldring, K. The Involvement of Galectin-1 in Skeletal Muscle Determination, Differentiation and Regeneration. *Glycoconj. J.* **2002**, *19*, 615–619. [CrossRef]

84. L'hôte, C.; Cordier, B.; Labasse, A.; Boileau, C.; Costes, B.; Henrotin, Y. Identification of New Biomarkers for Sarcopenia and Characterization of Cathepsin D Biomarker. *JCSM Rapid Commun.* **2021**, *4*, 122–132. [CrossRef]

85. Alameddine, H.S. Matrix Metalloproteinases in Skeletal Muscles: Friends or Foes? *Neurobiol. Dis.* **2012**, *48*, 508–518. [CrossRef] [PubMed]

86. Chandler, K.B.; Brnakova, Z.; Sanda, M.; Wang, S.; Stalnaker, S.H.; Bridger, R.; Zhao, P.; Wells, L.; Edwards, N.J.; Goldman, R. Site-Specific Glycan Microheterogeneity of Inter-Alpha-Trypsin Inhibitor Heavy Chain H4. *J. Proteome Res.* **2014**, *13*, 3314–3329. [CrossRef] [PubMed]

87. Liang, H.; Hou, H.; Yi, W.; Yang, G.; Gu, C.; Lau, W.B.; Gao, E.; Ma, X.; Lu, Z.; Wei, X.; et al. Increased Expression of Pigment Epithelium-Derived Factor in Aged Mesenchymal Stem Cells Impairs Their Therapeutic Efficacy for Attenuating Myocardial Infarction Injury. *Eur. Heart J.* **2013**, *34*, 1681–1690. [CrossRef] [PubMed]

88. Boraldi, F.; Lofaro, F.D.; Accorsi, A.; Ross, E.; Malagoli, D. Toward the Molecular Deciphering of Pomacea Canaliculata Immunity: First Proteomic Analysis of Circulating Hemocytes. *Proteomics* **2019**, *19*, e1800314. [CrossRef] [PubMed]

89. Boraldi, F.; Moscarelli, P.; Lofaro, F.D.; Sabia, C.; Quaglino, D. The Mineralization Process of Insoluble Elastin Fibrillar Structures: Ionic Environment vs Degradation. *Int. J. Biol. Macromol.* **2020**, *149*, 693–706. [CrossRef]

90. Singhto, N.; Thongboonkerd, V. Exosomes Derived from Calcium Oxalate-Exposed Macrophages Enhance IL-8 Production from Renal Cells, Neutrophil Migration and Crystal Invasion through Extracellular Matrix. *J. Proteom.* **2018**, *185*, 64–76. [CrossRef]

91. Azizi, E.; Deslauriers, A.R.; Holt, N.C.; Eaton, C.E. Resistance to Radial Expansion Limits Muscle Strain and Work. *Biomech. Model. Mechanobiol.* **2017**, *16*, 1633–1643. [CrossRef]

92. Sharafi, B.; Blemker, S.S. A Mathematical Model of Force Transmission from Intrafascicularly Terminating Muscle Fibers. *J. Biomech.* **2011**, *44*, 2031–2039. [CrossRef]

93. Gillies, A.R.; Chapman, M.A.; Bushong, E.A.; Deerinck, T.J.; Ellisman, M.H.; Lieber, R.L. High Resolution Three-Dimensional Reconstruction of Fibrotic Skeletal Muscle Extracellular Matrix. *J. Physiol.* **2017**, *595*, 1159–1171. [CrossRef]

# CHAPTER 2

## *PHYSICAL EXERCISE*

**Morphometrical and immunohistochemical investigation of the gastrocnemius muscle in old sedentary and old trained mice: preliminary data**

**TITLE: MORPHOMETRICAL AND IMMUNOHISTOCHEMICAL INVESTIGATION OF THE GASTROCNEMIUS MUSCLE IN OLD SEDENTARY AND TRAINED MICE: PRELIMINARY DATA**

**INTRODUCTION**

Sarcopenia is characterized by significant loss of muscle mass and strength, a condition linked to increased risk of disability and death [1]. Although the aging process itself is one of the causes responsible for this syndrome, some lifestyle behaviours such as physical inactivity may contribute to muscle weakness [2]. Therefore, several studies performed on both humans and other mammals investigated the effects of physical exercise as a non-pharmacological therapy able to delay the age-associated decline of skeletal muscle and to manage sarcopenia [2]. Among the biological mechanisms positively affected by exercise there are: the recruitment and the activation of satellite cells [3]; the increase of muscle capillarity [4]; enhanced protein synthesis and improvement of insulin sensitivity [5]; the reduction of age-associated inflammation state [6]. However, most of these findings were aimed at understanding changes of single biochemical pathways in response to specific types of physical exercise during aging (e.g., endurance and/or resistance training) [2, 7], while a global structural evaluation of myofibers and their extracellular environment associated with physical exercise have been scarcely investigated.

Moreover, physical training is recommended at all ages as healthy activity able to improve skeletal muscle mass and endurance and is considered a suitable therapy for age-associated sarcopenia [8], but little is known about the effects of mild physical exercise at old age.

In previous works performed by our research group, we demonstrate that several age-related alterations of myofibers are mitigated in old mice (28 months) by aerobic physical exercise on treadmill [3, 9, 10]. Moreover, in a recent study we have characterized the extracellular matrix (ECM) in aged muscle combining a proteomic approach with morphological and morphometrical evaluations by comparing the gastrocnemius muscle of old (24 months) *vs.* adult mice (12 months) [11].

The present work aims to extend the previous findings deepening the analysis of structural modifications of myofibers and muscle ECM network in response to mild physical activity started in old age. The approach we used is based on fluorescence and electron microscopy techniques (morphology, morphometry, and immunocytochemistry) to obtain qualitative and quantitative evaluations of myofibers and extracellular environment of gastrocnemius muscle of old sedentary *vs* trained mice (24 months). We focus our evaluations on gastrocnemius muscle which is mainly composed by fast II fibers that are more affected by sarcopenia [12].

The results obtained from our analysis provide preliminary insights of the mitigating effects of physical exercise in elderly. The next step of our investigation aims at confirming these morphological observations through a proteomic approach performed by a research group of the University of Modena and Reggio Emilia.

**MATERIALS AND METHODS**

**1.1 Mice**

A total of 11 male BALB/c mice aged 24 months were used in this study. The mice, housed in groups of 3-4, were maintained under standard conditions (24 ±1° C ambient temperature, 60 ± 15% relative humidity, and 12 h light/dark cycle) and fed ad libitum with standard commercial chow. The mice were allocated to the sedentary (n = 6) and trained (n=5) group with the "=Rand()" function in Microsoft Excel. The sedentary animal group had only spontaneous free-moving activity in the cage. The trained animal group underwent training on a Harvard Instruments treadmill for 30 min at 9 m/min belt speed (0% incline), 3 days a week for 3 months. In this work, physical training was adapted to optimize old mice compliance to training [13]. In order to avoid possible interference of acute with chronic effects of physical exercise, the mice were sacrificed three days after completion of the experimental training protocol. Evaluation of the results and data analysis were carried out blind to the mouse group.

Animals were handled according to the regulations of the Italian Ministry of Health (DL 4 March 2014, n. 26) and to the European Communities Council (Directive 63/2010/EU of the European Parliament and the Council) directives. The experimental protocol was approved by the Italian Ministry of Health (Ref.: 538/2015-PR).

**1.2 ECM component and myofiber diameter evaluation by immunofluorescence**

Three sedentary and three trained mice were deeply anesthetized with Tribromoethanol drug and sacrificed by cervical dislocation. Gastrocnemius muscles were quickly removed and frozen in liquid nitrogen-precooled isopentane. Transversally sectioned 5-μm thick cryosections were incubated with 1% bovine serum albumin, 2% normal goat serum, 0.3% Triton® X-100 in phosphate buffer solution (PBS) for 1 h and immunolabelled with the following probes: a rabbit polyclonal antibody direct against type I collagen, diluted 1:50 (GeneTex, Irvine, CA, USA) to evaluate collagen content; a rabbit polyclonal antibody direct against laminin, diluted 1:800 (Abcam, Cambridge, UK) for myofiber diameter evaluation. After washing with PBS, cryosections were stained with the proper secondary antibody: Alexafluor 488-anti-rabbit diluted 1:200 for collagen type I and Alexafluor 594-anti-rabbit diluted 1:200 for laminin. The cryosections were finally counterstained for DNA with 0.1

μg/mL Hoechst 33258 and mounted in PBS:glycerol (1:1). An Olympus BX51 microscope equipped with a 100W mercury lamp (Olympus Italia, Milan, Italy) was used under the following conditions: 450–480 nm excitation filter (excf), 500 nm dichroic mirror (dm) for Alexa 488; 540 nm excf, 580 nm dm, and 620 nm barrier filter (bf) for Alexa 594; 330–385 nm excf, 400 nm dm, and 420 nm bf, for Hoechst 33342. Images were recorded with an Olympus Magnifire digital camera system (Olympus Italia). A routine was written in MATLAB (2018b version, Mathworks) to quantify the area covered by collagen I fluorescence-positive pixels for the total area in ten random images acquired at X10 for each animal. The minimum Feret's diameter (the minimum distance of parallel tangents at opposing borders of the muscle fibers [14] was measured on a minimum of 100 myofibers per animal immunolabeled with laminin. The minimum Feret's diameter is very insensitive against deviations from the "optimal" cross-sectioning profile, therefore, reliably detecting differences between muscles [14].

**1.3 Morphological and morphometrical evaluation of myofiber and ECM**

Three sedentary and two trained mice were deeply anesthetized with Tribromoethanol drug and then perfused via the ascending aorta with 0.1 M PBS followed by 4% paraformaldehyde in PBS. The gastrocnemius muscle was quickly removed, and samples (about 1 mm³) were further placed for 2 h at 4°C in 2.5% glutaraldehyde (Electron Microscopy Sciences, Hatfield, PA, USA) plus 2% paraformaldehyde (samples intended for ultrastructure) or 4% paraformaldehyde and 0.2% glutaraldehyde in 0.1 M PBS (samples intended for immunohistochemical evaluation at fluorescence microscopy). After fixation, samples for ultrastructural morphology were rinsed with PBS, postfixed with 1% OsO4 (Electron Microscopy Sciences) and 1.5% potassium ferrocyanide for 2 h at 4°C, dehydrated with acetone, and embedded in Epon 812 resin (Electron Microscopy Sciences). For immunohistochemistry, samples were washed in PBS, treated with 0.5 M NH4Cl solution in PBS for 45 min at 4°C to block free aldehyde groups, dehydrated in graded concentrations of ethanol at room temperature and embedded in LRWhite resin.

For fiber typing, 2 μm-thick cross sections of LRWhite embedded grastrocnemius muscle were submitted to immunohistochemical procedures to distinguish fast and slow fibers [9]. Briefly, sections were incubated for 2 h at room temperature with a mouse monoclonal antibody recognizing the heavy chain of skeletal fast fiber myosin (clone MY-32, Sigma-Aldrich, Buchs, Switzerland) diluted 1:200 in PBS; the antigen–antibody complex was revealed with an Alexa 488 conjugated antibody against mouse IgG (Molecular Probes, Invitrogen, Milan, Italy). The sections were finally counterstained for DNA with 0.1 μg/mL Hoechst 33258. Micrographs were taken with an Olympus BX51 microscope equipped with a 100 W mercury lamp under the following conditions: 330- to 385-

nm excitation filter (excf), 400-nm dichroic mirror (dm), and 420-nm barrier filter (bf), for Hoechst 33258; 450- to 480-nm excf, 500-nm dm, and 515-nm bf for Alexa 488. Images were recorded with an Olympus Camedia C-5050 digital camera. In immunolabeled samples, the percentage of fast and slow muscle fibers was calculated on a minimum of 100 myofibers per animal, with 300 myofibers measured per group (sedentary and trained). Micrographs were taken at magnification of 20× and processed with the ImageJ software (NIH).

For morphometrical evaluation of ultrastructural variables, ultrathin sections (70–90 nm thick) were stained with lead citrate for 1 min and observed in a Philips Morgagni transmission electron microscope operating at 80 kV and equipped with a Megaview III camera for digital image acquisition.

The morphometric evaluation of the endomysium thickness was performed on 20 randomly selected electron micrographs (x5600) of longitudinally sectioned muscle, measuring the distance between the sarcolemma of two adjacent muscle cells every 1 μm of sarcolemma length. A minimum of 50 measurements per animal were performed for a total of 150 measurements per animal group (sedentary and trained).

The thickness of the basement membrane covering the myofiber was measured on randomly selected electron micrographs (x36,000) of longitudinally sectioned muscles. A minimum of 30 measurements per animal were performed for a total of 100 measurements in each animal group (sedentary and trained).

The morphometric evaluation of the perimysium collagen bundle size was performed on a minimum of 25 longitudinally sectioned collagen bundles per animal, for a total of 75 measurement in each animal group. The index of collagen bundle linearity (X/Y, expressed as the ratio between the real length of the bundle profile and the corresponding linear length) was assessed on a total of 30 longitudinally sectioned collagen bundles per group (sedentary and trained). For morphometric evaluation of collagen fibrils, measurement of fibril size, as well as the distance between single collagen fibrils, was performed on a minimum of 30 longitudinally sectioned collagen fibrils per animal with a total of 100 measurements per animal group.

The density of the intermyofibrillar mitochondria was assessed in 40 randomly selected micrographs (x11000) of longitudinally sectioned muscle per animal group avoiding the myofiber periphery. The number of mitochondria was counted and the density was expressed as number of mitochondria/myofiber area (23 $\mu m^2$).

The sectional area of the intermyofibrillar mitochondria as well as the length of outer and inner mitochondrial membrane was measured in 60 mitochondria (x36,000) per animal group (sedentary

and trained). The inner/outer membrane ratio was calculated as an assessment of cristae extension independent of mitochondrial size.

Morphometrical analysis of the nucleolus and the nucleolar components, i.e., fibrillar centres (FCs, circular in shape, contain ribosomal genes and enzymes necessary for transcription [15] [16]), dense fibrillar component (DFC, usually edges the FCs, is the site of transcription and processing of rRNA [17]) and granular component (GC, site of maturation and storage of ribosomal subunit [17]), was performed on 30 randomly selected nucleoli of longitudinally sectioned muscles (×18,000) per animal group. Area of nucleolus as well as of each nucleolar component was measured and the percentage of the nucleolar area occupied by FCs, DFC and GC was calculated.

All measurements were made by using the Radius software for image acquisition and elaboration implemented in the Philips Morgagni transmission electron microscope.

**1.4 Statistical analysis**

Data on the percentage of fluorescent (positive) areas for collagen type I, and data of morphometrical evaluations for ECM (endomysium size, basement membrane thickness, collagen bundle size and linearity, collagen fibril size, and distance), intermyofibrillar mitochondria (mitochondrial density, size, inner/outer membrane), nucleolus (nucleolar area, percentage of area occupied by FC, DFC, GC) and minimum Feret's diameter were pooled according to the animal group (sedentary and trained) and presented as mean ± standard error of the mean (SEM). The Shapiro–Wilk test showed that data were not normally distributed ($p < 0.001$). Consequently, the subsequent statistical analysis was performed using the non-parametric Mann–Whitney test, setting statistical significance at p value< 0.05. The IBM-SPSS (v.25, Armonk, NY, USA) statistical package was used for all analyses.

## RESULTS

### 1.5 Immunohistochemistry and Morphometry

Immunolabeling for the heavy chain of skeletal fast myofibers in both sedentary and trained mice; the percentage of slow fibers was negligible in both groups.

Minimum Feret's diameter of gastrocnemius myofibers was significantly higher in trained vs sedentary mice (26.74 ± 0.47 μm vs. 24.23 ± 0.41 μm; p<0,001) (**Fig.1**).
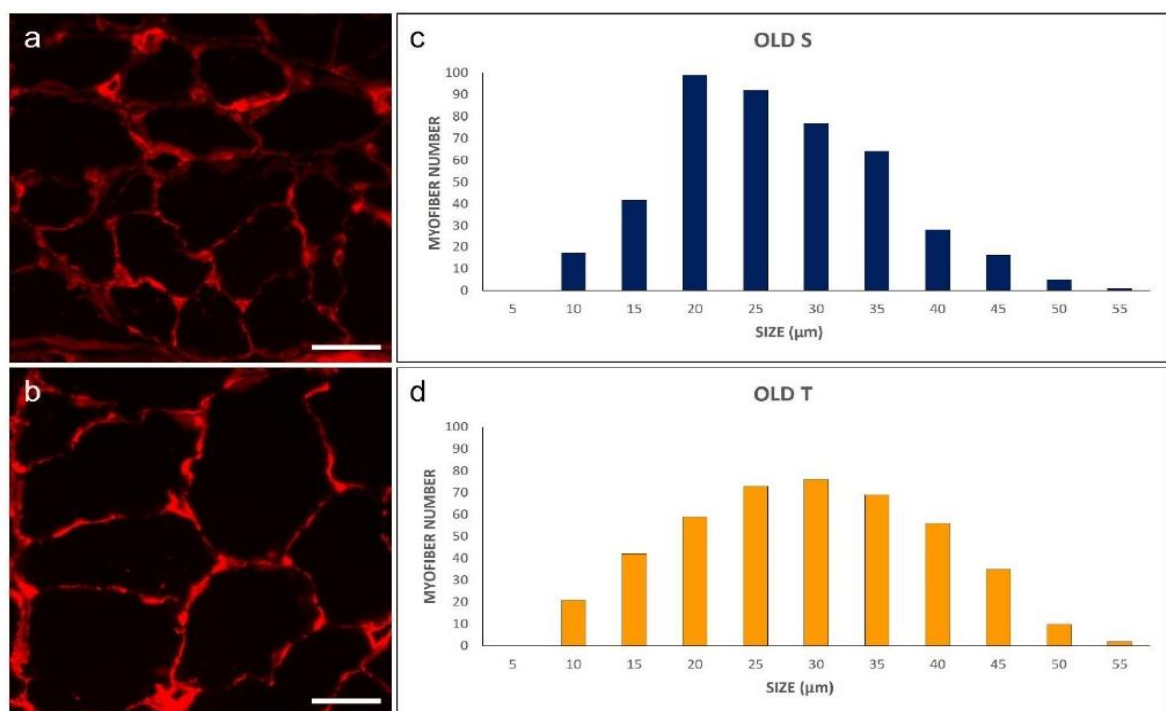


**Fig.1** Laminin immunolabelling of gastrocnemius cryosections in old sedentary (**a**) and old trained mice (**b**), used to measure myofiber's diameter. Bar 50 μm. Panels (**c**) and (**d**), respectively, show the minimum Feret's diameter distribution of myofibers in gastrocnemius muscle of old sedentary (**Old S**) and old trained (**Old T**) mice. The myofibers are grouped in size classes of 10μm and the number of fibers in each class is plotted. *p < 0,001.

Immunolabelling for type I collagen (as representative of fibrillar collagens) revealed qualitatively different staining in the two groups of mice (Figure not showed). Quantification of the area covered by fluorescence-positive pixels for type I collagen was significantly higher in old trained vs old sedentary mice groups (**Graph 2**).
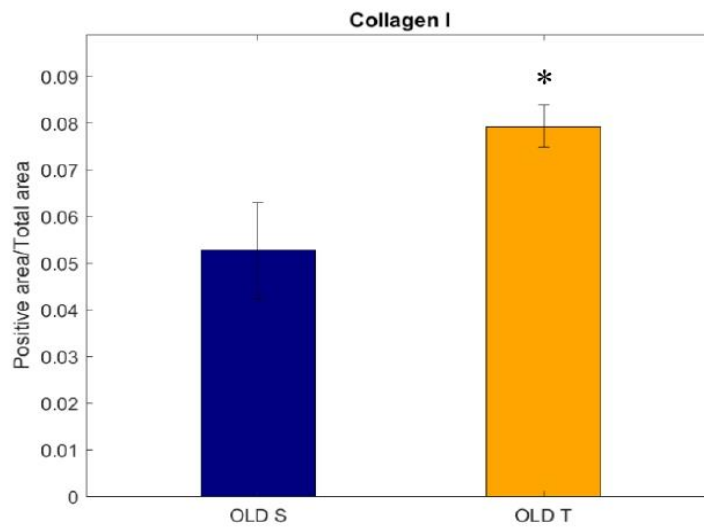


**Graph 2.** Histograms show quantification of the immunolabelling for type I collagen expressed as % of total area. * p < 0.001

### 1.6 Ultrastructural Morphology and Morphometrical Evaluation

The typical organization of the myofibers was maintained in both sedentary and trained old mice confirming previous works from our laboratory [3]. Many myonuclei were located in a subsarcolemmal position and the longitudinally aligned myofibrils occupied almost the entire cytoplasm. The ovoid mitochondria were lined between the myofibrils and in the subsarcolemmal region. In both sedentary and trained animal groups, the endomysium was a network of collagen fibrils connected to the basement membrane. Morphometrical analysis of the endomysium thickness was performed measuring the distance between two adjacent longitudinally myofibers. No significant difference in sedentary vs. trained mice was found (611.49 ± 41.25 nm and 478.08 ± 32.31 nm p=0,170).

The basement lamina, which covered the surface of each myofiber as an electrodense sheath, was significantly thicker in sedentary vs. trained mice (41.88 ± 1.07 nm vs. 30.32 ± 0.58 nm; p < 0.001) (**Fig.2**).
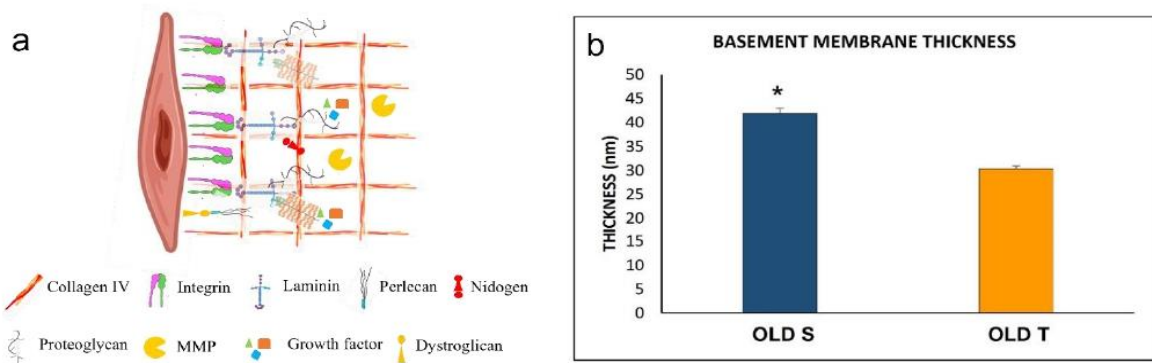
**Fig.2** Representative organization of muscle basement membrane (**a**). Morphometric analysis of basement membrane is reported in the histograms (**b**). *p<0,001

The extracellular matrix of the perimysium was comprised of a network of collagen bundles of different size and orientations. The perimysium of trained mice was characterized by statistically significantly thinner collagen bundles in comparison with the sedentary mice (692.02 ± 51.87 nm vs. 1461.66 ± 75.04 nm; p < 0.001). The collagen bundles were also more tortuous in trained mice (1.04 ± 0.01 vs. 1.12 ± 0.04; p < 0.05) (**Fig.3**).



**Fig.3** Ultrastructural images (**a**–**b**) of the perymisial collagen bundles of old sedentary (**a**) and old trained (**b**) gastrocnemius muscle; bars: 500 nm. Morphometric analysis of collagen bundle features is reported in the histograms (**c**–**d**).

In comparison with the trained animal group, the sedentary counterpart showed statistically significantly larger collagen fibrils (21 ± 0.65 nm vs. 19.02 ± 0.93 nm; p < 0.05), and higher distance between collagen fibrils (16.4 ± 0.92 nm vs. 13.71 ± 0.73 nm; p < 0.05) (**Fig. 4**).
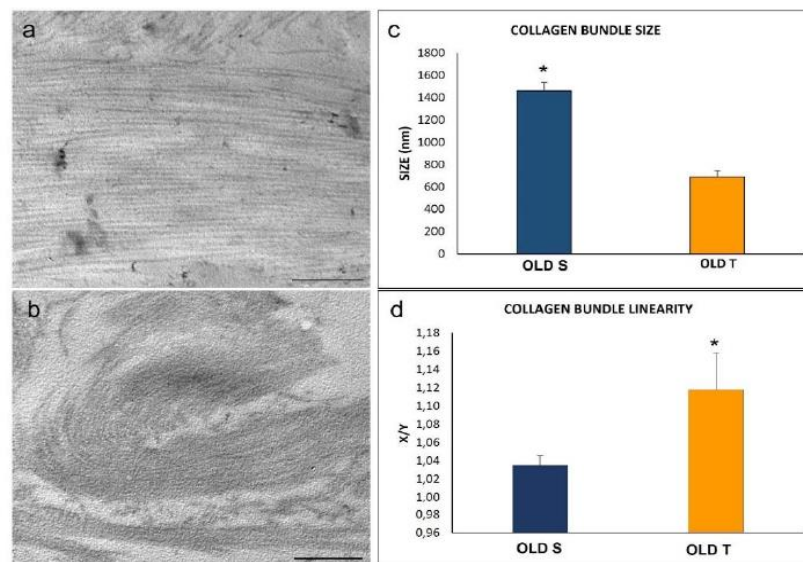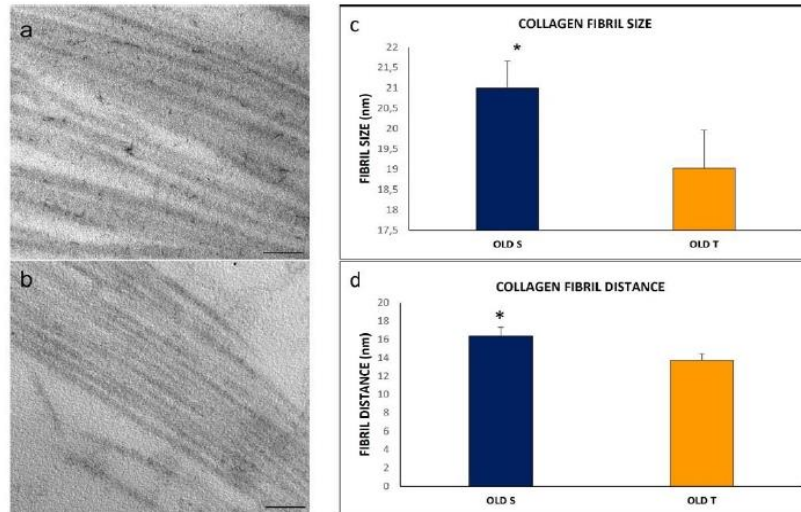
**Fig.4** Ultrastructural images (**a–b**) of the collagen fibrils of old sedentary (**a**) and old trained (**b**) gastrocnemius muscle; bars: 100 nm. Morphometric analysis of collagen fibrils features is reported in the histograms (**c–d**). *p < 0,05.

The mithocondrial density, measured as number of intermiofibrillar mitochondria on myofiber area, was significantly higher in trained vs. sedentary mice (1.48 ± 0.06 vs. 0.96 ± 0.06; p<0.001) (**Fig. 5**).
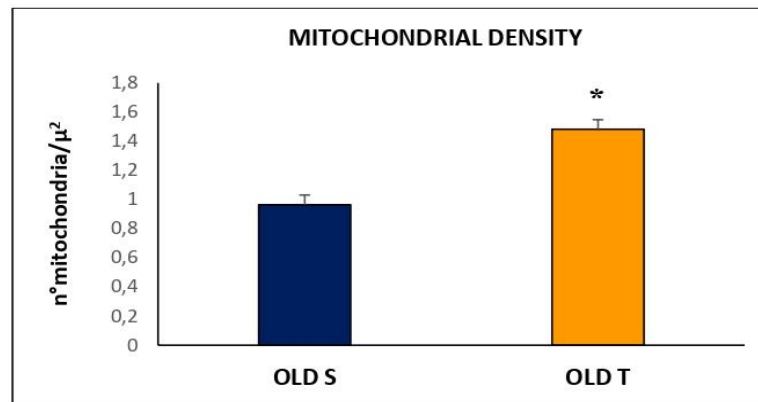


**Fig.5** Morphometrical evaluation of mitochondrial density is reported in the histogram (**c**). *p<0,001.

Morphometrical evaluation demonstrated no difference in intermyofibrillar mitochondrial area of sedentary and trained mice ($0.084 \pm 0.009 \ \mu m^2$ vs. $0.076 \pm 0.007 \ \mu m^2$; p=0.68) as well as in cristae extension (1.206 ± 0.055 vs. 1.233 ± 0.082; p=0.44). (**Graph 4**).
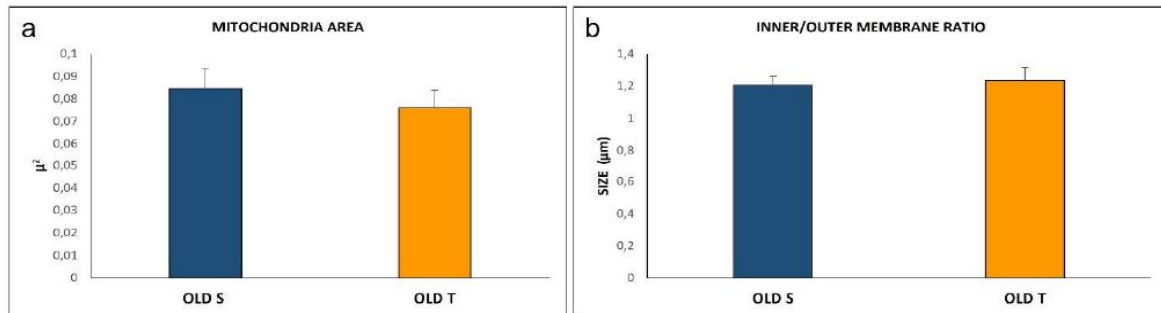
**Graph 4.** Histograms **a** and **b**, respectively, showed that the morphometrical evaluation of mitochondrial area and cristae extension do not show a statistically significant difference between old sedentary vs old trained mice.

In order to assess whether an adapted physical exercise has effect on protein synthesis by influencing the production and export of ribosomal subunits, the morphometrical evaluation of nucleolar area, FC, DFC and GC was carried out measuring the percentage of nucleolar area occupied by each nucleolar component. Morphometrical evaluation showed that there is no difference for nucleolar area measurement in the two animal groups (data not showed). Instead, the percentage of the nucleolar area occupied by FC and DFC was significantly higher in sedentary vs. trained mice ($4.105 \pm 0.657$ vs. $3.751 \pm 1.242$; $3.53 \pm 0.418$ vs. $2.273 \pm 0.513$; $p < 0,05$). Instead, the nucleolus of trained mice was characterized by a significantly higher percentage of area occupied by GC component in comparison to the sedentary mice ($93.97 \pm 1.460$ vs. $92.363 \pm 0.879$; $p < 0,05$) (**Fig.6**).
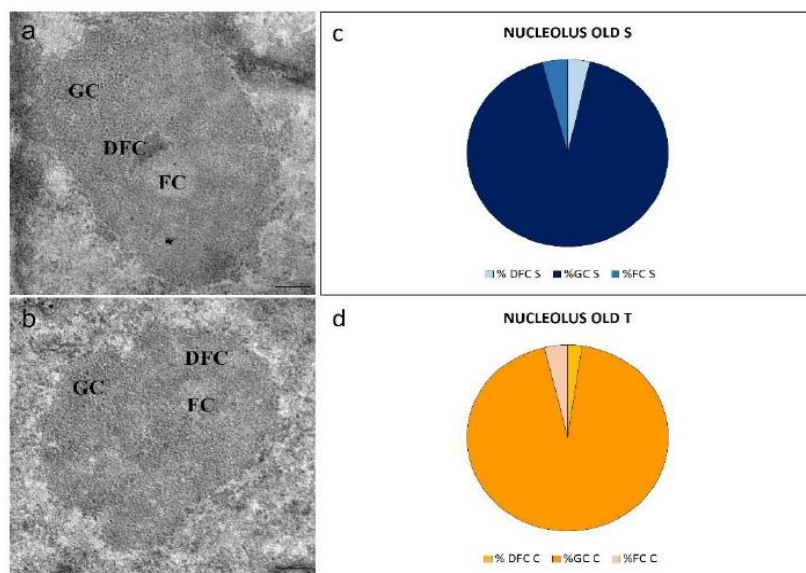


**Fig.6** Ultrastructure images (**a-b**) of nuclelus of old sedentary and old trained gastrocnemius muscle; GC (granular component), DFC (dense fibrillar component), FC (fibrillar centre); bar: 200nm. Morphometrical evaluation of percentage of nucelolar area occupied by DFC, FC, GC components are reported in pie charts (**c-d**). *$p < 0,05$.

**DISCUSSION**

Skeletal muscle is an essential system of the body able to sustain body posture and produce movement [18]. However, aging process leads to gradual loss of muscle mass and endurance, a condition termed sarcopenia [1]. Sedentary lifestyle is known to be one of the major risks of age-related muscle decline. Consequently, physical exercise is considered the by far more suitable tool to counteract sarcopenia progression [2]. In this study, we expanded on previous knowledge by exploring some structural features of the gastrocnemius muscle with combined morphological and morphometric approaches. Several changes were found in both myofiber and muscle ECM in response to mild physical exercise started only at advanced age.

**Physical exercise during aging and myofiber modifications**

Muscle fibers are distinguished in slow-twitch and fast-twitch fibers basing on the expression of MyHC (Myosin Heavy Chain) isoforms that influence their contractile and metabolic features [19]. Recent findings show that muscles can modify fiber type composition under pathological or physiological stress, in order to respond to different functional requirements [20, 21]. Skeletal muscle aging is characterized by fast to slow fiber shift with gradual decrease mainly in number and size of fiber type II [22] [23, 24].

A similar proportion of fast and slow fibers was found in the muscle of old sedentary and trained mice; our observation extend previous findings indicating that significant age-associated fiber type transition does not appear at least up to 20 months [9]. However, old trained mice exhibit a significant increase of myofibers size in comparison with sedentary mice. Previous work on severely sarcopenic mice (28-month-old mice) demonstrated that adapted physical exercise induces a slight increase in type II myofibers [10]. Moreover, it has been reported that myofiber cross sectional area (CSA) of gastrocnemius muscle of old mice submitted to running wheel exercise was comparable to the sedentary middle-aged mice [25]. Thus, our results suggest that a mild physical exercise started at old age may counteract the age-associated decrease of myofibers size seen in old sedentary mice.

Moreover, although it is generally accepted that different type of physical exercise (endurance vs resistance exercise) induce hypertrophy to a different extent depending on fiber type [2, 24], it might be taken in consideration that training frequency, intensity, type and intervention period act at distinct levels, thus influencing the conflicting results reported in literature.

**Physical exercise in aging and mitochondrial morphological changes**

The increase of physical exercise leads to adaptive modifications in skeletal muscle such as mitochondrial biogenesis [26]. Conversely, mitochondria dysfunction relating to inactivity is often

associated with muscle atrophy [27] and aging [28]. In the present study, we focus on the morphology of intermyofibrillar (IMF) mitochondria which dwell between myofibrils [28] and are the site where biochemical pathways related to muscle contraction occur [29]. Morphometrical evaluations on IMF mitochondria of gastrocnemius muscle from old sedentary and trained mice showed that physical exercise induces a significant increase of mitochondria density in old trained mice. Age-related decrease of mitochondrial functionality, number as well as density in muscle could be related to physical inactivity that occurs during aging [30]. Conversely, several studies performed in different experimental conditions showed that physical exercise induces mitochondrial biogenesis, thus increasing skeletal muscle oxidative capacity [31, 32]. These findings support our results suggesting that aged muscles are able to adapt to exercise stimuli increasing mitochondria content. Moreover, it is well known that mitochondria dynamically change their morphology, influencing mitochondrial respiratory capacity in response to different stimuli, such as physical exercise [32, 33]. These structural changes are regulated by specific protein responsible of mitochondria fission (splitting) and fusion (joining) [34]. It has been reported that age-associated unbalance between fission and fusion process is linked to onset of abnormal mitochondria [31]. However, although it is well known that physical exercise influences the expression of proteins involved in fission and fusion process, *Picard et al.* [35], demonstrated that mitochondria morphology is not affected by exercise. Accordingly, in our result no significant change was found for mitochondria size and extension of inner membrane, confirming that physical exercise does not affect mitochondrial structure. Nevertheless, we cannot exclude that duration and intensity of physical training may influence mitochondrial structural changes [36].

**Physical exercise in aging and modification of protein synthesis**

Morphometrical observations do not reveal statistically significant difference of nucleolar area between old sedentary and old trained mice. One of the primary function of nucleolus is ribosome biogenesis which in turn is correlated with protein synthesis [37]. The size of the nucleolus is strictly linked with rRNA synthesis depending on cell growth and metabolism [38]. However, the physical exercise does not induce any alteration of the total nucleolar size.

Nucleolus is composed of three major regions which are strictly related to different functional activities. Factors linked to rRNA transcription reside in the FC; the DFC is the site of proteins and ribonucleoprotein (RNP) complexes that contribute to the processing and maturation of pre-rRNA, whereas GC region is the place of storage and assembly of pre-ribosomal subunits. It has been showed that transcription of rRNA occurs at the boundary between FC and DFC [39]. The percentage of nucleolar area occupied by fibrillar centre (FC) and dense fibrillar component (DFC) was

significantly higher in old sedentary *vs* old trained mice. Instead, the percentage of nucleolar area occupied by granular component (GC) was lower in old sedentary mice in comparison with the trained group. Several evidence show that reduction of protein synthesis rate represents a mechanism leading to extend lifespan [40, 41] and reduce the accumulation of altered proteins observed in aging [42, 43]. Moreover, several studies have reported that high rates of rDNA transcription make it susceptible to genome instability and to accumulation of rDNA damage, two of features of cellular aging [44]. The significant reduction of DFC and FC regions in trained mice may suggest a reduction of ribosomal subunits production, likely leading to a decrease in protein synthesis.

The reduction of protein synthesis rate in response to physical exercise may be also justified by the accumulation of ribosomal subunits in GC, whose enlargement may be due to altered transport mechanism. However, further studies are necessary to better understand these data.

**Physical exercise in aging and muscle ECM ultrastructural changes**

Muscle extracellular matrix (ECM) is composed of three distinct layers: endomysium that surrounds each myofiber; perimysium which separate the fascicles within the muscle and the epimysium that wraps the entire muscle [45]. This network of interconnected layers is made up of different proteins (i.e., collagen, elastic fibers, proteoglycans) and cell types playing an essential role in maintenance muscle structure as well as in the transmission of force during contraction [46]. Moreover, the dynamic balance among deposition, remodeling and degradation process make this structure able to respond to different mechanical stimuli [47].

Skeletal muscle aging is characterized by an accumulation of extracellular matrix components [48] that leads to muscle fibrosis, one of the hallmarks of muscular aging [49]. One of the mechanisms related to alteration of ECM network in aging is thought to be linked to its defective degradation process [50]. In the present study, immunofluorescence quantification performed on cryosections of gastrocnemius muscle revealed a significant increase of fibrillar collage type I in old trained mice compared to old sedentary group. Accordingly, recent findings showed a concomitant up-regulation of collagen type I and proteins involved in ECM degradation process in skeletal muscle of old trained rats [51]. Thus, our data may suggest that physical exercise plays a crucial role in activating collagen metabolism. Furthermore, higher levels of collagen synthesis may be related to the regenerative process triggered by tissue damage after physical training [52].

Morphometrical evaluation show that the perimysial collagen bundles are thinner and more tortuous and characterized by decreased thickness of collagen fibrils and reduced interfibrillar space in old trained mice vs old sedentary mice. The age-related decrease of collagen fibers "tortuosity" [53] and an extensive accumulation of cross-linked collagen proteins [54] together with reduced myofiber size

[9, 10], result in increased muscle stiffness observed in aging [55]. Moreover, the slower collagen turnover rate in aging, causes the connective tissue area to appear more enlarged [56]. Physical exercise demonstrates to promote a remodelling of collagenous ECM. Since physical training induces increased expression of matrix metalloproteinase (MMP) that have the ability to break down ECM in skeletal muscle [57], we supposed that this mechanisms is involved in the reduction of collagen bundle size.

In trained mice myofibers show increased size. It is known that physical exercise can increase muscle fiber cross sectional area and reduce age-related cross linked collagen molecules that cause muscle stiffness [56].

Our results suggest that exercise started at old age acts at different levels in modifying muscle ECM: i) the activation of degradation pathway may reduce the accumulation of perimysial constitutive components, resulting in more thinner and more close collagen fibrils; as consequence, the more compact disposition of each collagen fibrils may reduce the size of perimysial collagen bundle; ii) on the other hand, the ECM remodelling may at least partly justify the increase of myofiber size observed in our old trained mice.

No change in endomysium thickness was found between the old trained vs old sedentary mice. These data are consistent with previous results in which no overall age-related hypertrophy of muscle ECM components was founded in mouse skeletal muscle [48]. Moreover, it has been reported that different types of physical exercise showed no effects on intramuscular connective tissue content in gastrocnemius muscle of rats [58]).

The basement membrane, mainly composed of collagen type IV and laminin, interfaces with sarcolemma of myofibers acting as a storage of growth factors required to constitute SCs niche [59] as well as a scaffold necessary for lateral transfer of force from the myofiber to the surrounding connective tissue during muscle contraction [60].

Ultrastructural evaluation performed at electron microscopy showed a significant decrease of basement membrane thickness in gastrocnemius muscle of old trained *vs* old sedentary mice. Data reported in literature about the effects of physical exercise on basement membrane are very heterogeneous. However, it has been reported that endurance exercise improves the expression levels of collagen type IV and type VI together with MMP14 and HSP47, two enzymes that act respectively in degradation and folding process of collagen type IV, in skeletal muscle of aged rats [61]. Again, it might be hypostasized that a more efficient basement membrane components turnover is promoted after physical exercise. Moreover, since basement membrane protects each myofibers from mechanical stimuli [62], its positive remodelling may occur as adaptative response of skeletal muscle to physical exercise.

CONCLUSION

The morphological and morphometrical evaluations performed in the present study aimed at investigating the beneficial effects of a mild physical exercise starting during aging on myofiber as well as on muscle ECM. Our preliminary results will be extended through an immunocytochemical analysis and proteomic approach performed by the research group of Modena and Reggio Emilia.

**References**

1.  Cruz-Jentoft, A.J. and A.A. Sayer, *Sarcopenia.* Lancet, 2019. **393**(10191): p. 2636-2646.
2.  Landi, F., et al., *Exercise as a remedy for sarcopenia.* Curr Opin Clin Nutr Metab Care, 2014. **17**(1): p. 25-31.
3.  Cisterna, B., et al., *Adapted physical exercise enhances activation and differentiation potential of satellite cells in the skeletal muscle of old mice.* J Anat, 2016. **228**(5): p. 771-83.
4.  Marzetti, E., et al., *Modulation of age-induced apoptotic signaling and cellular remodeling by exercise and calorie restriction in skeletal muscle.* Free Radic Biol Med, 2008. **44**(2): p. 160-8.
5.  Cartee, G.D., et al., *Exercise Promotes Healthy Aging of Skeletal Muscle.* Cell Metab, 2016. **23**(6): p. 1034-1047.
6.  Beyer, I., T. Mets, and I. Bautmans, *Chronic low-grade inflammation and age-related sarcopenia.* Curr Opin Clin Nutr Metab Care, 2012. **15**(1): p. 12-22.
7.  Marzetti, E., et al., *Physical activity and exercise as countermeasures to physical frailty and sarcopenia.* Aging Clin Exp Res, 2017. **29**(1): p. 35-42.
8.  Yoo, S.Z., et al., *Role of exercise in age-related sarcopenia.* J Exerc Rehabil, 2018. **14**(4): p. 551-558.
9.  Zancanaro, C., et al., *Physical training is associated with changes in nuclear magnetic resonance and morphometrical parameters of the skeletal muscle in senescent mice.* Eur J Histochem, 2007. **51**(4): p. 305-10.
10. Malatesta, M., et al., *Physical training modulates structural and functional features of cell nuclei in type II myofibers of old mice.* Rejuvenation Res, 2011. **14**(5): p. 543-52.
11. Lofaro, F.D., et al., *Age-Related Changes in the Matrisome of the Mouse Skeletal Muscle.* Int J Mol Sci, 2021. **22**(19).
12. Larsson, L., B. Sjödin, and J. Karlsson, *Histochemical and biochemical changes in human skeletal muscle with age in sedentary males, age 22--65 years.* Acta Physiol Scand, 1978. **103**(1): p. 31-9.
13. Fabene, P.F., et al., *Forced mild physical training-induced effects on cognitive and locomotory behavior in old mice.* J Nutr Health Aging, 2008. **12**(6): p. 388-90.
14. Briguet, A., et al., *Histological parameters for the quantitative assessment of muscular dystrophy in the mdx-mouse.* Neuromuscul Disord, 2004. **14**(10): p. 675-82.
15. Recher, L., J. Whitescarver, and L. Briggs, *The fine structure of a nucleolar constituent.* J Ultrastruct Res, 1969. **29**(1): p. 1-14.
16. Goessens, G., *Nucleolar structure.* Int Rev Cytol, 1984. **87**: p. 107-58.
17. Schwarzacher, H.G. and F. Wachtler, *The functional significance of nucleolar structures.* Ann Genet, 1991. **34**(3-4): p. 151-60.
18. Heeransh, D. D., Micah, S., Varacallo, M Anatomy, Skeletal Muscle. 2022
19. Schiaffino, S., C. Reggiani, and M. Murgia, *Fiber type diversity in skeletal muscle explored by mass spectrometry-based single fiber proteomics.* Histol Histopathol, 2020. **35**(3): p. 239-246.
20. Ørtenblad, N., et al., *The Muscle Fiber Profiles, Mitochondrial Content, and Enzyme Activities of the Exceptionally Well-Trained Arm and Leg Muscles of Elite Cross-Country Skiers.* Front Physiol, 2018. **9**: p. 1031.
21. Talbot, J. and L. Maves, *Skeletal muscle fiber type: using insights from muscle developmental biology to dissect targets for susceptibility and resistance to muscle disease.* Wiley Interdiscip Rev Dev Biol, 2016. **5**(4): p. 518-34.
22. Nilwik, R., et al., *The decline in skeletal muscle mass with aging is mainly attributed to a reduction in type II muscle fiber size.* Exp Gerontol, 2013. **48**(5): p. 492-8.

23.   Lee, S.M., et al., *Muscle fiber type-dependence effect of exercise on genomic networks in aged mice models.* Aging (Albany NY), 2022. **14**(8): p. 3337-3364.

24.   Deschenes, M.R., *Effects of aging on muscle fibre type and size.* Sports Med, 2004. **34**(12): p. 809-24.

25.   Olesen, A.T., et al., *Age-related myofiber atrophy in old mice is reversed by ten weeks voluntary high-resistance wheel running.* Exp Gerontol, 2021. **143**: p. 111150.

26.   Yan, Z., et al., *Regulation of exercise-induced fiber type transformation, mitochondrial biogenesis, and angiogenesis in skeletal muscle.* J Appl Physiol (1985), 2011. **110**(1): p. 264-74.

27.   Romanello, V., et al., *Mitochondrial fission and remodelling contributes to muscle atrophy.* Embo j, 2010. **29**(10): p. 1774-85.

28.   Figueiredo, P.A., et al., *The role of mitochondria in aging of skeletal muscle.* Biogerontology, 2008. **9**(2): p. 67-84.

29.   Müller, W., *Subsarcolemmal mitochondria and capillarization of soleus muscle fibers in young rats subjected to an endurance training. A morphometric study of semithin sections.* Cell Tissue Res, 1976. **174**(3): p. 367-89.

30.   Distefano, Giovanna; Goodpaster, Bret H. (2017). Effects of Exercise and Aging on Skeletal Muscle. Cold Spring Harbor Perspectives in Medicine, (), a029785–. doi:10.1101/cshperspect.a029785

31.   Peterson, C.M., D.L. Johannsen, and E. Ravussin, *Skeletal muscle mitochondria and aging: a review.* J Aging Res, 2012. **2012**: p. 194821.

32.   Philp, A.M., et al., *The influence of aerobic exercise on mitochondrial quality control in skeletal muscle.* J Physiol, 2021. **599**(14): p. 3463-3476.

33.   Cogliati, S., et al., *Mitochondrial cristae shape determines respiratory chain supercomplexes assembly and respiratory efficiency.* Cell, 2013. **155**(1): p. 160-71.

34.   Youle, R.J. and A.M. van der Bliek, *Mitochondrial fission, fusion, and stress.* Science, 2012. **337**(6098): p. 1062-5.

35.   Picard, M., et al., *Acute exercise remodels mitochondrial membrane interactions in mouse skeletal muscle.* J Appl Physiol (1985), 2013. **115**(10): p. 1562-71.

36.   Huertas, J.R., et al., *Human muscular mitochondrial fusion in athletes during exercise.* Faseb j, 2019. **33**(11): p. 12087-12098.

37.   Tiku, V. and A. Antebi, *Nucleolar Function in Lifespan Regulation.* Trends Cell Biol, 2018. **28**(8): p. 662-672.

38.   Boulon, S., et al., *The nucleolus under stress.* Mol Cell, 2010. **40**(2): p. 216-27.

39.   Boisvert, F.M., et al., *The multifunctional nucleolus.* Nat Rev Mol Cell Biol, 2007. **8**(7): p. 574-85.

40.   Syntichaki, P., K. Troulinaki, and N. Tavernarakis, *Protein synthesis is a novel determinant of aging in Caenorhabditis elegans.* Ann N Y Acad Sci, 2007. **1119**: p. 289-95.

41.   Pan, K.Z., et al., *Inhibition of mRNA translation extends lifespan in Caenorhabditis elegans.* Aging Cell, 2007. **6**(1): p. 111-9.

42.   Hipkiss, A.R., *On why decreasing protein synthesis can increase lifespan.* Mech Ageing Dev, 2007. **128**(5-6): p. 412-4.

43.   Basaiawmoit, R.V. and S.I. Rattan, *Cellular stress and protein misfolding during aging.* Methods Mol Biol, 2010. **648**: p. 107-17.

44.   Tsekrekou, M., K. Stratigi, and G. Chatzinikolaou, *The Nucleolus: In Genome Maintenance and Repair.* Int J Mol Sci, 2017. **18**(7).

45.   Borg, T.K. and J.B. Caulfield, *Morphology of connective tissue in skeletal muscle.* Tissue Cell, 1980. **12**(1): p. 197-207.

46.   Kragstrup, T.W., M. Kjaer, and A.L. Mackey, *Structural, biochemical, cellular, and functional changes in skeletal muscle extracellular matrix with aging.* Scand J Med Sci Sports, 2011. **21**(6): p. 749-57.

47.    Kjaer, M., *Role of extracellular matrix in adaptation of tendon and skeletal muscle to mechanical loading.* Physiol Rev, 2004. **84**(2): p. 649-98.

48.    Wood, L.K., et al., *Intrinsic stiffness of extracellular matrix increases with age in skeletal muscles of mice.* J Appl Physiol (1985), 2014. **117**(4): p. 363-9.

49.    Mahdy, M.A.A., *Skeletal muscle fibrosis: an overview.* Cell Tissue Res, 2019. **375**(3): p. 575-588.

50.    Chen, W.J., et al., *Aged Skeletal Muscle Retains the Ability to Remodel Extracellular Matrix for Degradation of Collagen Deposition after Muscle Injury.* Int J Mol Sci, 2021. **22**(4).

51.    Guzzoni, V., et al., *Effect of Resistance Training on Extracellular Matrix Adaptations in Skeletal Muscle of Older Rats.* Front Physiol, 2018. **9**: p. 374.

52.    Close, G.L., et al., *Skeletal muscle damage with exercise and aging.* Sports Med, 2005. **35**(5): p. 413-27.

53.    Stearns-Reider, K.M., et al., *Aging of the skeletal muscle extracellular matrix drives a stem cell fibrogenic conversion.* Aging Cell, 2017. **16**(3): p. 518-528.

54.    Olson, L.C., et al., *Advanced Glycation End-Products in Skeletal Muscle Aging.* Bioengineering (Basel), 2021. **8**(11).

55.    Csapo, R., M. Gumpenberger, and B. Wessner, *Skeletal Muscle Extracellular Matrix - What Do We Know About Its Composition, Regulation, and Physiological Roles? A Narrative Review.* Front Physiol, 2020. **11**: p. 253.

56.    Mavropalias, G., et al., *Exercise builds the scaffold of life: muscle extracellular matrix biomarker responses to physical activity, inactivity, and aging.* Biol Rev Camb Philos Soc, 2022.

57.    Rullman, E., et al., *Endurance exercise activates matrix metalloproteinases in human skeletal muscle.* J Appl Physiol (1985), 2009. **106**(3): p. 804-12.

58.    Olesen, A.T., et al., *Intramuscular connective tissue content and mechanical properties: Influence of aging and physical activity in mice.* Exp Gerontol, 2022. **166**: p. 111893.

59.    Katarzyna, G.-K., *The Importance of Extracellular Matrix in Skeletal Muscle Development and Function*, in *Composition and Function of the Extracellular Matrix in the Human Body*, T. Francesco, Editor. 2016, IntechOpen: Rijeka. p. Ch. 1.

60.    Garg, K. and M.D. Boppart, *Influence of exercise and aging on extracellular matrix composition in the skeletal muscle stem cell niche.* J Appl Physiol (1985), 2016. **121**(5): p. 1053-1058.

61.    Kanazawa, Y., et al., *Effects of Endurance Exercise on Basement Membrane in the Soleus Muscle of Aged Rats.* Acta Histochem Cytochem, 2021. **54**(5): p. 167-175.

62.    Sanes, J.R., *The basement membrane/basal lamina of skeletal muscle.* J Biol Chem, 2003. **278**(15): p. 12601-4.

# CHAPTER 3

*NANOTECHNOLOGY*

# Formulative study and intracellular fate evaluation of ethosomes and transethosomes for vitamin D3 delivery

*M. Costanzo, E. Esposito, M. Sguizzato, M.A. Lacavalla, M. Drechsler, G. Valacchi, C. Zancanaro, M. Malatesta*

International Journal of Molecular Science (2021)

**ABSTRACT**

In this pilot study, ethosomes and transethosomes were investigated as potential delivery systems for cholecalciferol (vitamin D3), whose decrease has been correlated to many disorders such as dermatological diseases and sarcopenia. A formulative study on the influence of pharmaceutically acceptable ionic and non-ionic surfactants allowed the preparation of different transethosomes. In vitro cytotoxicity was evaluated in different cell types (keratinocytes, fibroblasts and muscle cells). Then, the selected nanocarriers were further investigated at light and transmission electron microscopy to evaluate their internalization and intracellular fate. Both ethosomes and transethosomes proven to have physicochemical properties optimal for transdermal penetration and efficient vitamin D3 loading; moreover, nanocarriers were easily internalized by all cell types, although they followed distinct intracellular fates: ethosomes persisted for long times inside the cytoplasm, without inducing subcellular alteration, while transethosomes went through rapid degradation giving rise to an intracellular accumulation of lipids. These basic results provide a solid scientific background to in vivo investigations aimed at exploring the efficacy of vitamin D3 transdermal administration in different experimental and pathological conditions.

*Article*

# Formulative Study and Intracellular Fate Evaluation of Ethosomes and Transethosomes for Vitamin D3 Delivery

**Manuela Costanzo** [1,†], **Elisabetta Esposito** [2,†], **Maddalena Sguizzato** [2], **Maria Assunta Lacavalla** [1], **Markus Drechsler** [3], **Giuseppe Valacchi** [4,5], **Carlo Zancanaro** [1] and **Manuela Malatesta** [1,*]

[1] Department of Neurosciences, Biomedicine and Movement Sciences, University of Verona, I-37134 Verona, Italy; manuela.costanzo@univr.it (M.C.); mariaassunta.lacavalla@univr.it (M.A.L.); carlo.zancanaro@univr.it (C.Z.)
[2] Department of Chemical, Pharmaceutical and Agricultural Sciences, University of Ferrara, I-44121 Ferrara, Italy; elisabetta.esposito@unife.it (E.E.); sgzmdl@unife.it (M.S.)
[3] Bavarian Polymer Institute (BPI) Keylab Electron and Optical Microscopy, University of Bayreuth, D-95440 Bayreuth, Germany; markus.drechsler@uni-bayreuth.de
[4] Department of Neurosciences and Rehabilitation, University of Ferrara, I-44121 Ferrara, Italy; vlcgpp@unife.it
[5] Animal Science Department, Plants for Human Health Institute, NC Research Campus, NC State University, Kannapolis, NC 28081, USA
[*] Correspondence: manuela.malatesta@univr.it
[†] These authors contributed equally to this work.

**Abstract:** In this pilot study, ethosomes and transethosomes were investigated as potential delivery systems for cholecalciferol (vitamin D3), whose deficiency has been correlated to many disorders such as dermatological diseases, systemic infections, cancer and sarcopenia. A formulative study on the influence of pharmaceutically acceptable ionic and non-ionic surfactants allowed the preparation of different transethosomes. In vitro cytotoxicity was evaluated in different cell types representative of epithelial, connective and muscle tissue. Then, the selected nanocarriers were further investigated at light and transmission electron microscopy to evaluate their uptake and intracellular fate. Both ethosomes and transethosomes proven to have physicochemical properties optimal for transdermal penetration and efficient vitamin D3 loading; moreover, nanocarriers were easily internalized by all cell types, although they followed distinct intracellular fates: ethosomes persisted for long times inside the cytoplasm, without inducing subcellular alteration, while transethosomes underwent rapid degradation giving rise to an intracellular accumulation of lipids. These basic results provide a solid scientific background to in vivo investigations aimed at exploring the efficacy of vitamin D3 transdermal administration in different experimental and pathological conditions.

**Keywords:** cell culture; cholecalciferol; cryogenic transmission electron microscopy; in vitro test; light microscopy; lipid nanocarriers; transmission electron microscopy

## 1. Introduction

The role of vitamin D (VD) on health is well established; indeed, it directly affects lymphocytes functions and cytokines secretion, exerting in this way anti-inflammatory properties [1]. The exposure of skin to ultraviolet radiation induces the synthesis of the steroid hormone cholecalciferol from 7-dehydrocholesterol. Many dermatological disorders, systemic infections, and cancers can be related to low VD levels [2]. Since cholecalciferol (or vitamin D3, VD3) and other VD analogues (e.g., ergocalciferol, or vitamin D2) are characterized by anti-proliferative and pro-differentiating effects, they have been demonstrated to be highly efficient in the treatment of several skin conditions, including psoriasis vulgaris [3]. In addition, the synthesis of VD in the skin plays an important role for the prevention of many diseases, such as ultraviolet B-induced melanoma [3]. Furthermore, recent findings demonstrated that VD deficiency influences muscle mass and responses [4]. Indeed, VD supplementation can limit sarcopenia and improve muscle

performance in elder people [5,6]. Notwithstanding some dietary supplements of VD can be effective in reducing its deficiency, further VD topical application could represent a strategy to counteract skin disease and/or improve muscular function, especially in the case of people suffering from VD deficiency associated with nutrition problems, aging, and hepatic or renal disorders.

In this context, the possibility of delivering VD through the skin either to improve cutaneous conditions or to reach internal organs represents an important target. The difficulty in skin administration of highly lipophilic active ingredients such as VD is represented by the impossibility of crossing the barrier of the *stratum corneum*. Indeed, when administered in cream formulations, VD tends to deposit on the skin surface due to its affinity with the vehicle [7,8]. In order to overcome this drawback and to promote VD permeation through the skin, despite its physicochemical characteristics, specialized transdermal delivery systems with penetration enhancement properties are required. In this regard, recently, a liposomal formulation of VD was proposed for cutaneous application in the treatment of photoaging [9], while many commercial oral nutritional supplements declare the presence of liposome containing VD in their composition. Liposomes are vesicular systems mainly constituted of phospholipids, such as phosphatidylcholine (PC), and water, representing the first generation of nanosystems for drug encapsulation and transdermal delivery. Their peculiar composition results in the formation of multilamellar vesicular systems, characterized by a supramolecular structure resembling the three-dimensional organization of the epidermis *stratum corneum*. Notwithstanding their well-known potential as a drug delivery system, liposomes present instability problems that can lead to sedimentation, rupture of vesicles and leakage of the encapsulated drug [10].

To solve these drawbacks, new generations of lipid-based nanosystems have been proposed, such as transferosomes and ethosomes (ET) [11–13]. ET are vesicular systems made of PC, ethanol (20–45%) and water, characterized by a higher thermodynamic stability and loading capacity with respect to liposomes. Indeed, the presence of ethanol stabilizes vesicles, improves the solubility of lipophilic drugs and confers to ET a particular softness [9–11]. At the same time, ethanol associated to PC helps to open ways through the *stratum corneum* barrier, thus promoting ET passage through the skin [14,15]. Indeed, some studies have demonstrated the capability of ET to cross different biological membranes [16–18]. Moreover, recent studies have been performed to improve the transdermal potential of lipid nanosystems by modifying the vesicle compositions [19,20]. Particularly in the case of transferosomes and transethosomes, the addition as edge activators of surfactants to the phospholipid matrix has been proposed, thus modifying the vesicle deformability and improving transdermal penetration once applied on the skin [20].

The present work is a pilot study aimed at investigating the suitability of ET and transethosomes as nanocarriers to deliver VD3. Particularly, a formulative study has been conducted investigating the influence of pharmaceutically acceptable ionic and non-ionic surfactants in the preparation of different transethosomes. Vesicle size distribution, morphology, VD3 entrapment efficiency and relative vesicle deformability were determined. The cytotoxicity of ET and transethosomes in vitro was assessed on cells of different histological lineages that may be found in the skin; namely, keratinocytes (as the epithelial cells composing the epidermis), fibroblasts (as the typical cells in the connective tissues) and myoblasts (as cells of the skeletal muscle tissue). The selected nanocarriers were further investigated for their biological suitability by monitoring their uptake and intracellular fate in the three cell types at light and transmission electron microscopy.

## 2. Results

### 2.1. Preparation of Ethosomes and Transethosomes

In order to find vehicles suitable for non-invasive administration of VD3 to the skin and muscle tissue, biocompatible transdermal nanosystems were investigated. Particularly, ET were considered, being phospholipid-based vesicular systems containing high amounts of ethanol, characterized by penetration enhancer properties. In addition, the influence

of non-ionic and ionic surfactants as edge activators added to the ethosomal composition was considered. Particularly, ET made of PC ethanol solution and water (30:70 $v/v$) were produced, while the addition of polysorbate 80 (T80), sodium cholate (SC) or dimethyl-didodecylammonium bromide (DD) to the PC ethanol solution resulted in transethosomes, respectively, named TET, SCET or DET, as reported in Table 1. A cold method enabled one to spontaneously and rapidly obtain milky dispersions in the case of ET and translucent dispersions in the case of TET, SCET or DET.

**Table 1.** Composition of nanocarriers ($w/w\%$).

| Components | ET | TET | SCET | DET | ET-VD3 [1] | TET-VD3 [2] |
|---|---|---|---|---|---|---|
| PC | 0.90 | 0.89 | 0.89 | 0.89 | 0.89 | 0.90 |
| T80 | - | 0.3 | - | - | 0.3 | - |
| SC | - | - | 0.1 | - | - | - |
| DD | - | - | - | 0.2 | - | - |
| VD3 | - | - | - | - | 0.1 | 0.1 |
| Ethanol | 29.10 | 28.81 | 29.01 | 28.91 | 28.80 | 29.00 |
| Water | 70 | 70 | 70 | 70 | 70 | 70 |

[1] ET loaded with VD3; [2] TET loaded with VD3.

### 2.2. Size Distribution

In order to shed light on the size distribution of ET, TET, SCET and DET, and to select the formulations suitable to transdermally deliver VD3, a dynamic light scattering analysis was performed by photon correlation spectroscopy (PCS). Vesicle mean diameters expressed as Z Average and dispersity indexes are reported in Table 2. Z Average values ranged between 111 and 277 nm, while dispersity index values were below 0.2, indicating a homogeneous size population [21]. The mean diameter of ET vesicle was around 200 nm. With regard to transethosomes, the smallest mean diameter was achieved in the case of DET, while the largest mean diameter was found in SCET. The use of the non-ionic surfactant T80 resulted in TET vesicles whose mean diameter was 186 nm. In order to choose vesicles with sizes compatible with transcutaneous administration, ET, TET and DET were selected.

**Table 2.** Size distribution parameters of ET and transethosomes, entrapment capacity and deformability of the indicated formulations.

| Parameters | ET | TET | SCET | DET | ET-VD3 | TET-VD3 |
|---|---|---|---|---|---|---|
| Z Average (nm) [1] | 206.3 | 186.2 | 276.7 | 111.2 | 209.5 | 246.6 |
| ±s.d. | ±33 | ±20 | ±10 | ±9 | ±13 | ±5 |
| Dispersity index [1] | 0.146 | 0.131 | 0.125 | 0.085 | 0.136 | 0.163 |
| ±s.d. | ±0.00 | ±0.00 | ±0.01 | ±0.02 | ±0.00 | ±0.02 |
| EC (%) [2] | - | - | - | - | 100 | 100 |
| ±s.d. | | | | | ±1.5 | ±1.0 |
| Def [3] | 6.23 | 12.55 | - | - | 16.65 | 8.74 |
| ±s.d. | ±0.7 | ±0.5 | | | ±0.3 | ±0.8 |

[1] as determined by PCS; [2] entrapment capacity; [3] vesicle deformability; s.d.: standard deviation; data are the mean of three independent determinations on different batches.

### 2.3. Cytotoxicity of Ethosomes and Transethosomes

Treatment with DET induced a massive cell death and consequent detachment from the substrate at all the concentrations tested already after 2 h incubation; therefore, no MTT was performed. Due to this high cytotoxicity, DET were excluded from the further experiments.

On the contrary, ET and TET proved to be safe for all the cell types at all time points considered up to the PC concentration of 86.6 μg (Figure 1). The concentration of 173.1 μg increased cell death in myoblasts and fibroblasts and was thus excluded from the subsequent experimentation.
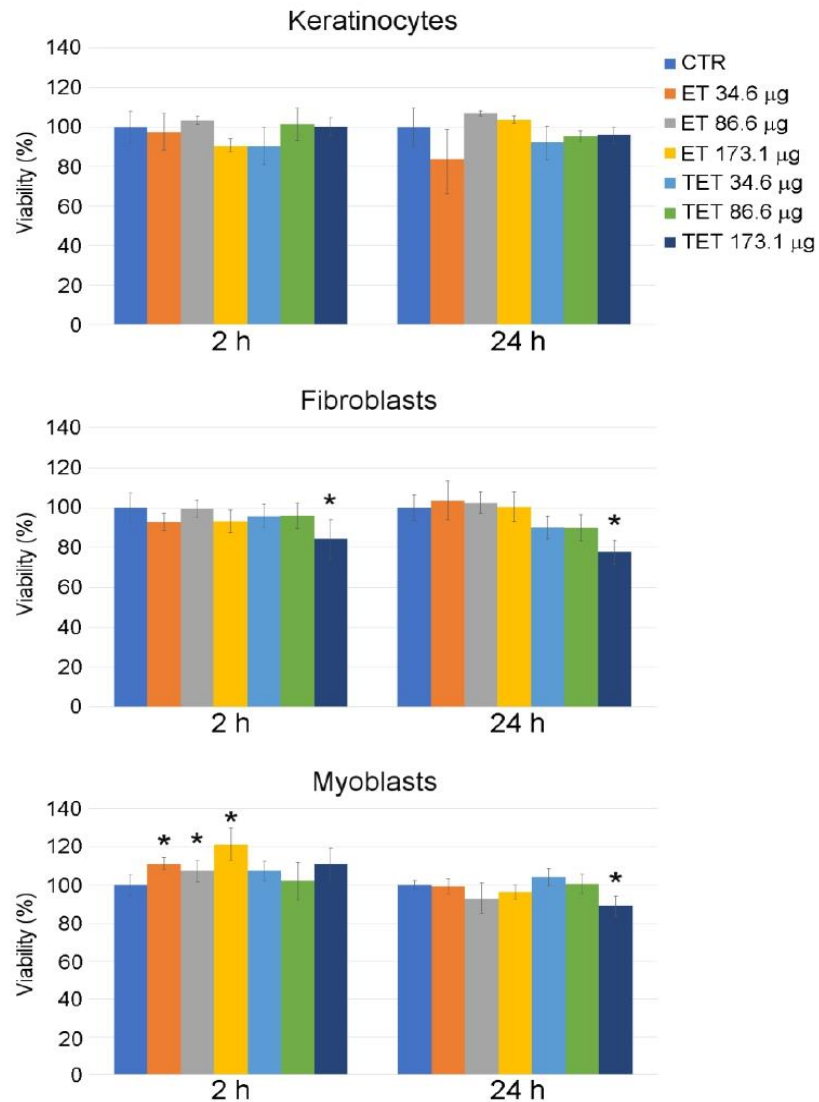
**Figure 1.** Effect of ET and TET on cell viability of cultured keratinocytes, fibroblasts and myoblasts, as measured by MTT assay. Histograms show the mean percentage value ± s.d. of cell viability after 2 h and 24 h of incubation with ET and TET at different concentrations. CTR: control (untreated) cells. * $p < 0.05$.

ET incubation for 2 h resulted in an increase in MTT signal in myoblasts, according to previous findings that PC-based nanoparticles may increase cell viability by the activation of the MEK-ERK1/2 pathway or cell metabolism [22].

*2.4. Preparation and Characterization of Vitamin D3 Containing Ethosomes and Transethosomes*

The viability test enabled one to select ET and TET as non-toxic formulations to be loaded with VD3. To this aim, the drug was added to the PC ethanol solution, before

water addition, resulting in ET-VD3 and TET-VD3 formulations, whose compositions are reported in Table 1.

The PCS analysis of size distribution revealed that adding the drug slightly increased the vesicles' mean diameter; namely, 40 nm in the case of ET-VD3 and 20 nm in the case of TET-VD3 (Table 2), without affecting the dispersity index. Vesicle morphology was visualized by cryogenic transmission electron microscopy (cryo-TEM): ET-VD3 appeared as spherical or ovoid vesicles with a multilamellar structure, typical of the PC double-layer organization (Figure 2a), while TET-VD3 appeared as unilamellar vesicles (Figure 2b). These different morphological features suggest that, in the presence of VD3, T80 disorganizes the multilamellar structure of PC, possibly because of an interaction between T80 and PC, arranging their polar heads towards the aqueous phase and the hydrophobic tails inside the double layer of the vesicles. T80 is supposed to sterically hamper the multilayer organization of PC in the presence of VD3, while retaining the vesicle double layer (inset in Figure 2b).
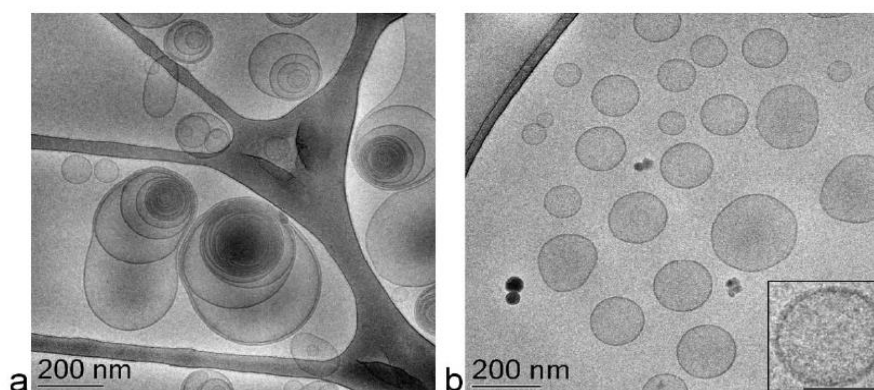


**Figure 2.** Cryo-TEM images of ET-VD3 (**a**) and TET-VD3 (**b**). The bar corresponds to 200 nm in panels (**a**) and (**b**), 100 nm in the inset of panel (**b**).

Both ET-VD3 and TET-VD3 were able to completely entrap the drug within the vesicles, as determined by ultracentrifugation, disaggregation and HPLC analyses. Indeed, VD3 was entirely associated to the PC phase, resulting in 100% EC values (Table 2) due to VD3 high solubility in ethanol. Notably, the cold method of preparation avoids thermal stresses that might possibly result in drug degradation.

### 2.5. Cytotoxicity of Vitamin D3 Containing Ethosomes and Transethosomes

After entrapping VD3 into ET and TET formulations previously found to be safe (i.e., PC concentrations of 34.6 μg and 86.6 μg), both nanocarriers confirmed their safety at all time points, except TET-VD3 25 μM, which increased cell death in myoblasts after 24 h incubation (Figure 3). A 25 μM VD3 solution increased cell death after both 2 h and 24 h incubation.

Again, incubation for 2 h with ET resulted in an increase in MTT signal in myoblasts, although only at the PC concentration of 34.6 μg/mL. In this case, the highly metabolizing and proliferative action of PC [22] was probably counterbalanced by the anti-proliferative effect of VD3 [23].
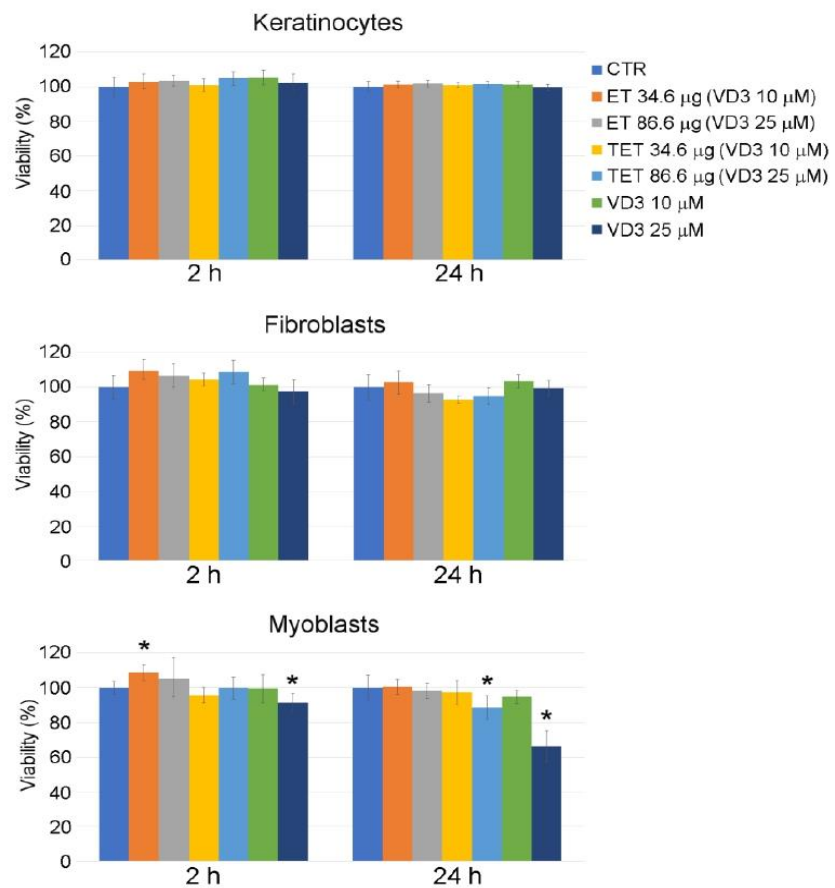
**Figure 3.** Effect of ET-VD3, TET-VD3 and VD3 on cell viability of cultured keratinocytes, fibroblasts and myoblasts, as measured by MTT assay. Histograms show the mean percentage value $\pm$ s.d. of cell viability after 2 h and 24 h of incubation with nanocarriers or VD3 as in at different concentrations. * $p < 0.05$.

### 2.6. Deformability Study

The process of ET and TET penetration through the skin is related to the ethanol capability to fluidize the lipid domain of the *stratum corneum*, and to the vesicle peculiar capability to deform [19]. To compare vesicle deformability, ET, TET, ET-VD3 and TET-VD3 were subjected to extrusion tests, measuring the variation of mean diameter before and after the extrusion process. The relative deformability values are reported in Table 2. The deformability values of TET and TET-VD3 were almost double with respect to ET and ET-VD3, suggesting that the presence of T80 increases vesicle softness, both in the presence and in the absence of VD3.

### 2.7. Stability Evaluation

Vesicle mean diameters and dispersity indexes were evaluated by PCS after 3 months, storing samples in the light at 22 °C in order to check their size stability. As reported in Figure 4a, vesicle size underwent a slight increase in the case of ET and TET ($\approx$20 nm) after 90 days from the production, while a higher increase was detected in the case of VD3-containing vesicles, especially for TET-VD3, displaying a 100 nm increase. Dispersity

indexes did not increase, being always below 0.2, suggesting a homogeneous size distribution. In order to compare the effectiveness of ET-VD3 and TET-VD3 in controlling drug degradation, VD3 entrapment was evaluated within 3 months from ET-VD3 and TET-VD3 preparation. Notably, ET and TET firmly entrapped VD3 up to 1 month; afterwards VD3 content decreased, especially in the case of TET-VD3, being 52% after 90 days of storage, suggesting a firmer retention of VD3 within the multilamellar structure of ET with respect to the TET unilamellar structure (Figure 4b). Conversely, liposomes loaded with VD3, described by other authors, appeared markedly unstable with respect to ET-VD3 and TET-VD3, displaying a 20 nm increase in vesicle mean diameter and decrease in drug content just at day 9 from production [9].
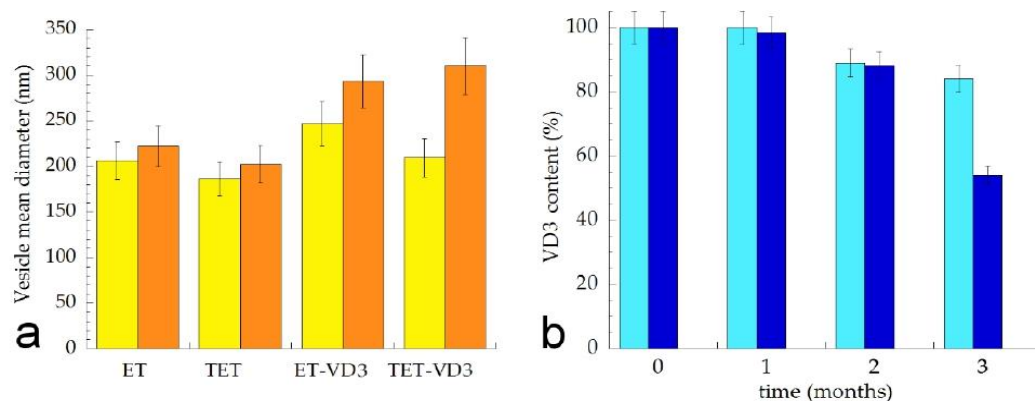


**Figure 4.** (**a**) Mean diameter variation for the indicated ET and TET. Mean diameters were measured by PCS after 0 (yellow) and 3 months (orange) from production and expressed as Z average. Data are the mean of three determinations on different samples; (**b**) Variation of VD3 content in ET-VD3 (light blue) and TET-VD3 (blue) determined up to 3 months from production. Bars indicate s.d.

### 2.8. Light Microscopy

Microscopy observations on the uptake and intracellular fate of ET and TET were similar in the three cell types.

At fluorescence microscopy, both ET and TET appeared as green fluorescing spots, while the cytoplasm was counterstained in red and the nucleus in blue (Figure 5). Both ET and TET entered the cells after 2 h incubation, mainly appearing as isolated spots. After 24 h, internalized ET markedly increased in number, while TET did not show evident accumulation. No ET or TET formed large clusters.

Observation of Oil Red O-stained samples at bright-field microscopy (Figure 6) revealed the presence of scarce lipid droplets of small size in all untreated (control) cell types. After 24 h incubation, in cells treated with ET, the amount of lipid droplets remained unchanged, whereas in cells treated with TET, the amount of lipid droplets drastically increased.

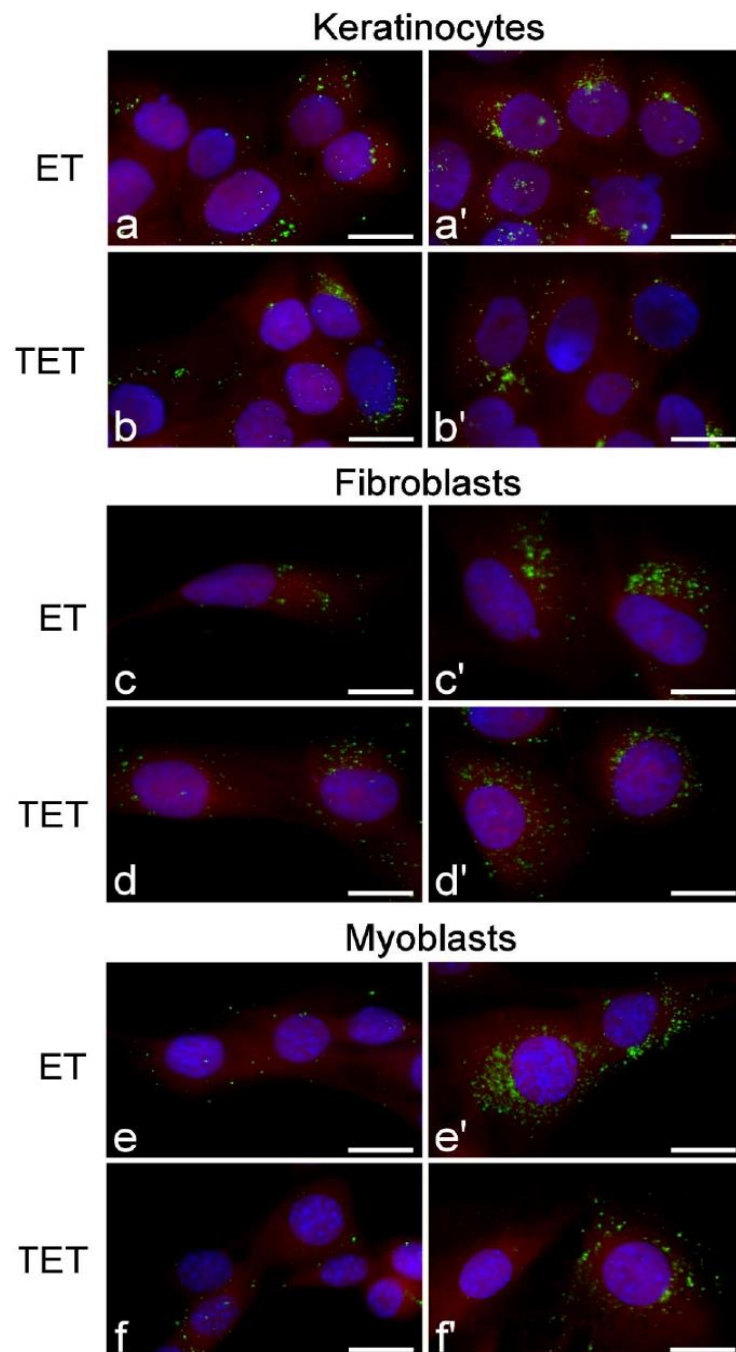**Figure 5.** Fluorescence micrographs of keratinocytes, fibroblasts and myoblasts after 2 h (**a–f**) and 24 h (**a′–f′**) incubation with ET or TET. Nanocarriers in green (PKH67), cytoplasm in red (trypan blue) and nucleus in blue (Hoechst 33342). Bars 20 μm.
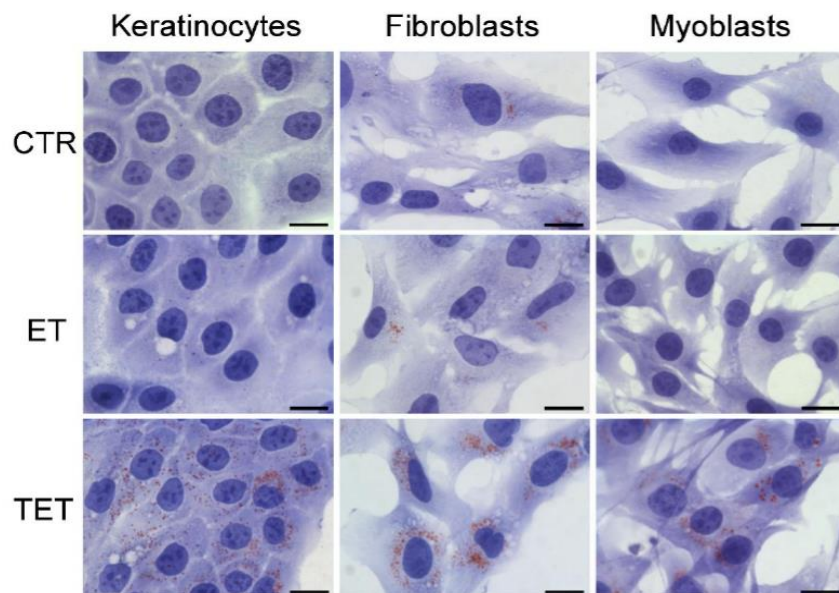
**Figure 6.** Bright-field micrographs of keratinocytes, fibroblasts and myoblasts after 24 h incubation with ET or TET; CTR are control (untreated) cells. Oil Red O-staining for neutral lipids, hematoxylin counterstaining. Note the marked increase in lipid droplets in TET-treated cells. Bars 20 μm.

### 2.9. Transmission Electron Microscopy

At TEM, ET and TET showed similar behavior in keratinocytes, fibroblasts and myoblasts; therefore, the following description refers to all the cell types.

Both ET and TET appeared as isolated, roundish electron-dense vesicles; when sectioned near their equatorial plane, they showed a dark rim, corresponding to the PC double layer, and a grey core (Figures 7 and 8). No morphological difference was evident between ET and TET after 2 h incubation, but ET showed a larger size than TET (mean diameter ± s.d.: 237.38 ± 6.06 nm vs. 182.17 ± 10.17 nm, respectively; $p < 0.001$, one-way ANOVA test). No statistical comparison was made at 24 h between ET and TET, due to the very limited number of morphologically recognizable TET. ET showed unchanged sizes at 2 h vs. 24 h incubation (237.38 ± 6.06 nm vs. 241.73 ± 11.16 nm, respectively; $p = 0.842$), thus confirming their stability also in the intracellular milieu.

Both ET and TET were found free in the cytosol (Figures 7 and 8a–c); they were ubiquitously distributed in the cytoplasm, from the peripheral to the perinuclear region, but were never found inside the cell nucleus (although some of them occurred very close to the nuclear envelope) (Figures 7g and 8c). Both ET and TET were mostly surrounded by abundant smooth endoplasmic reticulum; some endoplasmic vesicles and cisternae were frequently found to contact the nanocarrier surface and even penetrate into nanocarrier invaginations (Figure 7c–e,i,j and Figure 8c). Some ET and TET took a crescent shape and showed areas of decreased electron density (Figure 7d,e,i,j and Figure 8c,i); in addition, many of them occurred in close proximity of mitochondria (Figures 7b and 8c). ET or TET were never found enclosed in vacuoles, even when occurring very close to the plasma membrane (Figures 7a and 8b).
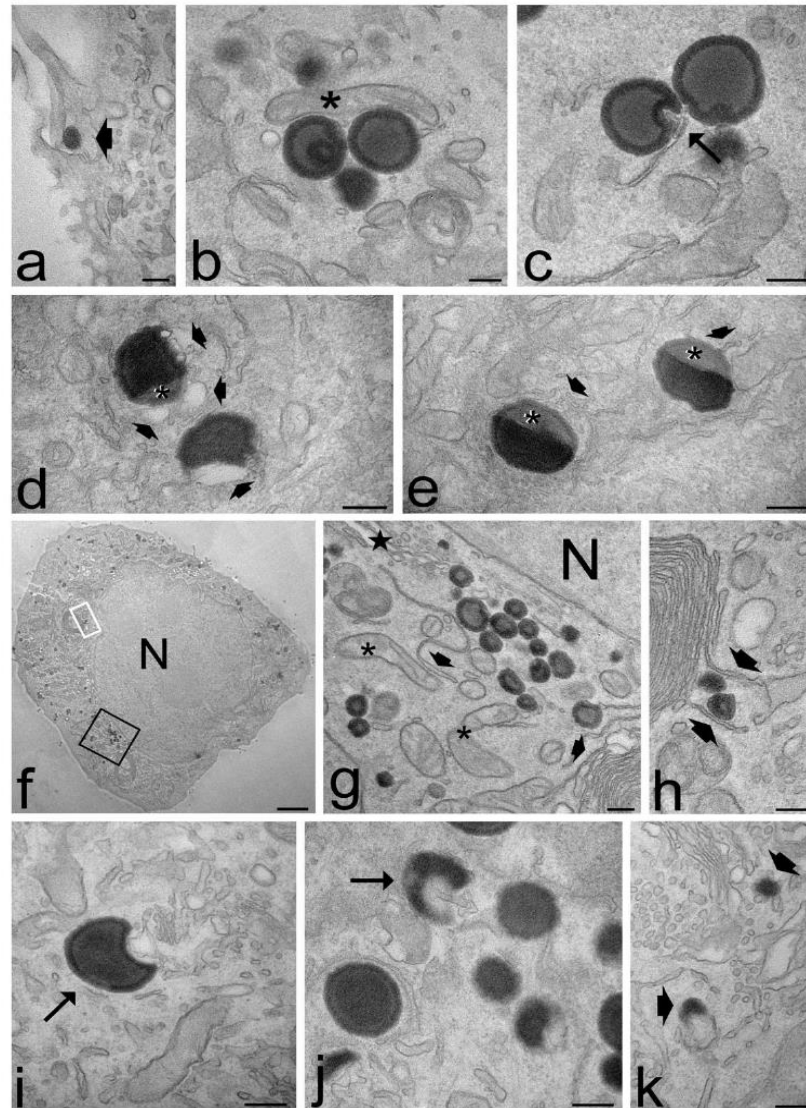
**Figure 7.** Transmission electron micrographs of keratinocytes (**a**,**d**,**j**,**k**), myoblasts (**b**,**f**,**g**,**h**) and fibroblasts (**c**,**e**,**i**) after 2 h (**a**–**e**) and 24 h incubation (**f**–**k**) with ET. (**a**) An ET (arrowhead) is entering the cell. (**b**) A mitochondrion (asterisk) occurs very close to ET distributed in the cytosol. (**c**) Smooth endoplasmic reticulum into an ET indentation (arrow). (**d**,**e**) ET at various degree of degradation: note the smooth vesicles at their periphery (thin arrows) and the decreased electron density (asterisks). (**f**,**g**) After 24 h incubation, many ET are distributed in the cytoplasm, sometimes very close to the nucleus (N); note the well-preserved morphology of mitochondria (asterisks), endoplasmic reticulum (arrowheads) and Golgi apparatus (star). (**h**) Smooth endoplasmic reticulum cisternae surround two ET (arrowheads). (**g**,**h**) High magnification details corresponding to the black and white framed areas in (**f**), respectively. (**i**,**j**) Crescent-like ET with smooth endoplasmic reticulum inside their concavity. (**k**) ET remnants (arrows) surrounded by many smooth vesicles and tubules. Bars 200 nm (**a**–**e**,**g**–**k**), 2 μm (**f**).
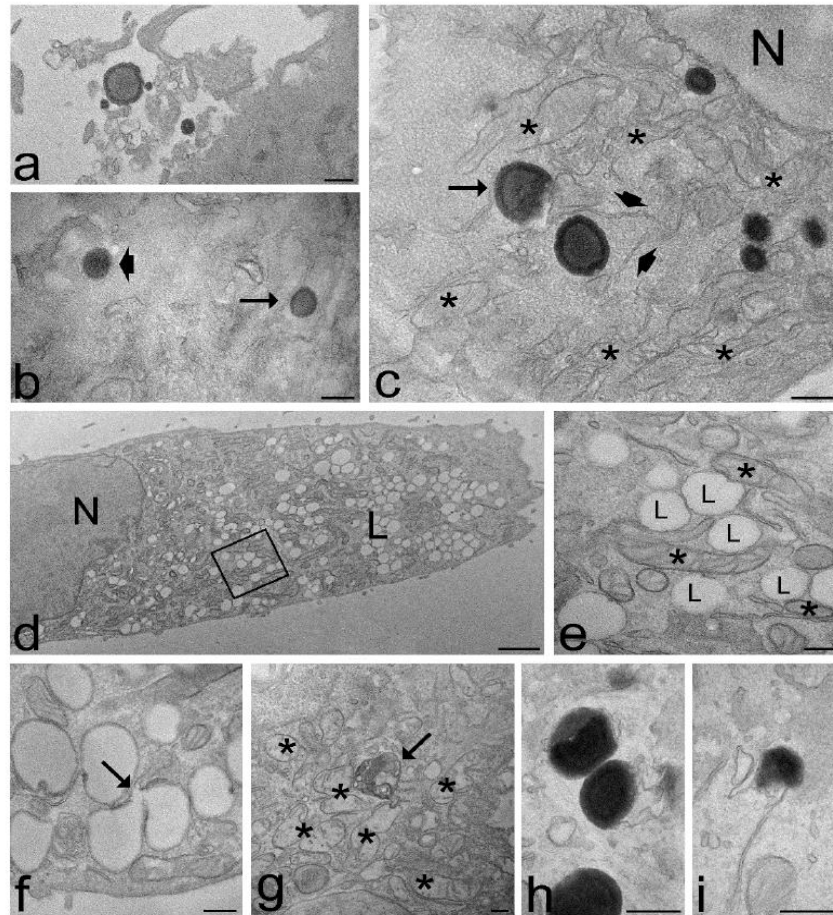
**Figure 8.** Transmission electron micrographs of keratinocytes (**a**,**f**,**g**,**h**), fibroblasts (**d**,**e**) and myoblasts (**b**,**c**,**i**) and after 2 h (**a**–**c**) and 24 h incubation (**d**–**i**) with TET. (**a**) Some TET occur among microvilli on the cell surface. (**b**) A TET (arrowhead) is entering the cell, while another TET (arrow) occurs free in the cytosol. (**c**) Some TET are distributed in the cytoplasm, sometimes very close to the nucleus (N); note the crescent-like TET (arrow) and the good morphology of mitochondria (asterisks) and endoplasmic reticulum (arrowheads). (**d**,**e**) After 24 h incubation, the cells contain large amounts of lipid droplets (L) of small size; they occur very close each other and are often surrounded by mitochondria (asterisks); (**e**) high magnification detail corresponding to the framed area in (**d**). (**f**) Two coalescing lipid droplets (arrow). (**g**) After 24 h incubation with TET, some mitochondria swell and lose their cristae (asterisks), and residual bodies (arrows) occur. (**h**,**i**) The scarce morphologically recognizable TET show different degradation steps. Bars 200 nm (**a**–**c**,**e**–**i**), 1 μm (**d**).

After 2 h incubation, the intracellular distribution of nanocarriers, their morphology or the cell structural features were similar in cells treated with ET or TET. On the contrary, after 24 h incubation, the intracellular fate of ET and TET appeared strikingly different. ET accumulated in large amounts in the whole cytoplasm maintaining the same morphological features and spatial relationships with cell organelles as observed after 2 h incubation (Figure 7f–h), although some ET remnants were found surrounded by numerous smooth vesicles (Figure 7k). On the other hand, in the cells incubated with TET, only a few morphologically recognizable nanocarriers were observed (Figure 8h,i), while huge amounts

of small lipid droplets (mean area $\pm$ s.d.: $0.06 \pm 0.02$ μm$^2$) accumulated in the cytoplasm (Figure 8d,e); they were frequently very close to each other, but were only occasionally observed to fuse (Figure 8f). Moreover, many mitochondria were found to border lipid droplets (Figure 8e).

The ultrastructural analysis demonstrated that no morphological alteration or damage of cell organelles occurred after 2 h incubation with for both ET and TET, and after 24 h incubation with ET. Conversely, after 24 h incubation with TET, swollen mitochondria with damaged cristae, and residual bodies were sometimes observed (Figure 8g).

## 3. Discussion

The results of this study demonstrated that ET and TET are potential candidates for the transdermal delivery of VD3, being characterized by suitable size, morphology, deformability and entrapment efficiency [14,15]. These nanocarriers are particularly interesting for two reasons: (i) they are mainly made of PC, the most abundant phospholipid in eukaryotic cells [24], which is a promising pre-requisite for their biocompatibility, (ii) the presence of ethanol confers softness and malleability to ET and TET, and acts as penetration enhancer, promoting their passage through the biological membranes [17,18].

Accordingly, the in vitro cytotoxicity assay revealed that two formulations were safe for all the cell types tested: ET and TET administration did not increase death rate after both short (2 h) and long (24 h) incubation times, up to 86.8 μg PC. Similarly, ET-VD3 and TET-VD3 proved to be mostly safe at the same PC concentrations (the only exception will be discussed below). Checking cell viability and identifying the safe concentrations is essential to evaluate the possible negative impacts of nanocarrier administration since the occurrence of cell death is a main trigger for inflammatory responses [25].

Knowing the internalization mechanisms and intracellular pathways of nanocarriers is also crucial to design efficient delivery strategies [26]. Our combined fluorescence microscopy and TEM analyses provided original information about the uptake and intracellular fate of ET and TET, demonstrating that both efficiently enter keratinocytes, fibroblasts and myoblasts without apparent difference due to cell type. ET and TET occur in the cytoplasm as single units and are unable to enter the cell nucleus: therefore avoiding possible interactions with the nucleic acids and/or nuclear factors that, in a cascade effect, could unpredictably affect nuclear and cellular functions. This observation further confirms the biocompatibility of ET and TET.

Both ET and TET were never observed inside endosomes, even when they occurred close to the plasma membrane; moreover, no plasma membrane invagination typical of early endocytosis was ever found when the nanocarriers were in contact with the cell surface. This suggests that ET/TET cellular uptake does not takes place by classic endocytic processes. ET and TET share chemical and structural similarities with the plasma membrane, thus likely facilitates their interactions: the nanocarriers are made of PC, which is a main phospholipid component of plasma membrane [24], and both nanocarriers and plasmalemma are composed of lipids whose hydrophilic heads are oriented towards water domain, while hydrophobic tails are oriented towards each other, forming bilayers. The easy penetration of ET inside cultured cells has been ascribed to an increase in membrane permeability due to the penetration enhancer effect of ethanol that would, in turn, promote the ET fusion with the plasma membrane and the delivery of ET and loaded molecules inside the cell [27,28]. Our TEM analysis provides unequivocal evidence that both ET and TET maintain their structural integrity after passing through the plasma membrane, as previously observed for liposomes, which, however, rapidly disaggregated once into the cytoplasm [29–31]. It may be hypothesized that the presence of ethanol in ET/TET may induce disordering effects in the plasmalemma region making contact with the nanocarrier, loosening lipid packaging [32], thus allowing the passage of these malleable nanocarriers without the typical endosome formation. The uptake mechanism of ET and TET remains unclear, highlighting the need of further research on their interactions with the biological membranes.

Anyway, bypassing the classic endocytic route, ET and TET avoid the rapid degradation due to lysosomal enzymes. However, our ultrastructural observations provided evidence that ET and TET may undergo the action of smooth endoplasmic reticulum-resident enzymes but following distinct intracellular fates. In fact, at short times, both ET and TET occur free in the cytosol, establishing spatial relationships with smooth endoplasmic reticulum and mitochondria. Conversely, at long times, ET mostly preserve their original morphology (which indicates that cell enzymes are unable to massively attack these nanoconstructs), whereas TET are hardly detectable, suggesting that TET are almost completely degraded, while a large amount of lipid droplets accumulate in the cytoplasm, as visualized by both light microscopy cytochemistry and ultrastructural morphology. TEM observations are consistent with the fluorescence images showing an evident accumulation of ET but not of TET after 24 h incubation.

Both ET and TET are made of PC, whose excess in cells is known to be degraded by various enzymes to maintain membrane homeostasis [33–36]; the main degrading enzyme is phospholipase D that mostly locates in the cell membranes of the smooth endoplasmic reticulum, Golgi complex, endosomes and lysosomes [37]. This explains the close spatial proximity of ET or TET with smooth vesicles and tubules, which were even found penetrating into nanocarrier invaginations. The crescent shape and the concomitant decrease in electron density frequently observed in many ET and TET would indicate a partial nanocarrier degradation. Therefore, the ultrastructural evidence demonstrates that the degradation of both ET and TET occurs through physiological pathways already after 2 h from the uptake (consistent with their safety proved by the cytotoxicity test), but the degradation rate proceeds slowly for ET (which are still present in large amounts after 24 h) while being very fast for TET (which are hardly detectable at TEM after 24 h). The faster degradability of TET is likely due to the presence of T80 that may affect the molecular packing of PC in the bilayer, thus making the TET vesicles more prone to degradation by the phospholipases of the smooth endoplasmic reticulum.

The hydrolysis products of PC include diacylglycerol, phosphocholine, glycerophosphocholine and free fatty acids [33,38]. As high concentrations of free fatty acids are toxic [39], they are incorporated into neutral lipids such as triacylglycerol (a main storage lipid [40]), giving rise to lipid droplets [41–43]. Accordingly, numerous lipid droplets were found in cells where massive PC breakdown occurred [43]. Similarly, the massive degradation of TET would release in the cytosol large amounts of PC-derived products, which would accumulate in lipid droplets, whereas the products of the slow degradation of ET would more slowly be released, thus being gradually suitable for multiple metabolic pathways. Moreover, the degradation of T80, occurring only in TET, leads to the formation of free fatty acids and several degradation products including short-chain organic acids [44] that could increase the number of molecules migrating to lipid droplets.

The PC overloading and the consequent lipid droplets accumulation caused by the rapid degradation of TET is likely responsible for some cell stress, as suggested by the presence of altered organelles after 24 h from the treatment. In addition, it is known that T80 degradation gives rise also to peroxides, aldehydes, alkanes, epoxides, ketones [44], which could further increase TET cytotoxicity. Anyway, this stress is evidently unable to affect cell viability even at long term, as demonstrated by the cytotoxicity assay.

Lipid droplets are dynamic organelles able to rapidly change in size and number [45]; they consist of a neutral lipid core of triacylglycerol and cholesteryl ester surrounded by a monolayer mainly composed of PC [46,47] that acts as a surfactant increasing the stability of lipid droplets and preventing their coalescence [48,49]. Accordingly, no large lipid droplets were found in cells treated with TET despite their huge amount: the droplets remained separated even when very close each other and only rare lipid fusions were observed.

PC is also a main component of mitochondrial membranes; however, these organelles lack enzymes for its synthesis, so PC molecules are translocated to mitochondria to be assembled into their membranes [50]. This would explain the frequent finding of mitochondria adhering to the surface of partially degraded ET or TET as well as of lipid droplets.

112

When ET and TET were loaded with VD3, they did not alter cell viability apart from TET loaded with 25 μm VD3, which increased cell death in myoblasts only after 24 h incubation. All cell types used in this study express enzymes having 25-hydroxylase activity [23,51,52]; accordingly, the administered VD3 did not have toxic effects. However, it has been demonstrated that the administration of high amounts of VD3 can increase cell death in C2C12 cells [52]. TET-VD3 toxicity for myoblasts would be therefore related to the additional stress caused by the massive release of the loaded VD3 in cells already stressed by PC overloading following nanocarrier degradation. Interestingly, after 24 h incubation, VD3 solution induced the highest myoblasts death (about 35%), followed by VD3 administered by TET (about 15%), while VD3 administered by ET was completely safe, demonstrating the capability of nanocarriers to sustain the safe release of high amounts of VD3. This observation further supports the notion that the thorough knowledge of the nanocarrier intracellular degradation pathways is crucial to select the most appropriate formulation strategies for drug-delivery nanoconstructs.

## 4. Materials and Methods

### 4.1. Materials for Ethosome and Transethosome Preparation

Cholecalciferol (VD3), polyoxyethylenesorbitan monooleate, T80, sodium cholate (SC) or dimethyldidodecylammonium bromide (DD) and sodium cholate (SC) were purchased from Sigma-Aldrich (St Louis, MO, USA). Soybean lecithin (PC) (90% PC) was Epikuron 200 from Lucas Meyer (Hamburg, Germany). Solvents were of HPLC grade and all other chemicals were of analytical grade.

### 4.2. Ethosome and Transethosome Preparation

ET and TET were produced by the "cold method"; briefly, PC was firstly solubilized in ethanol (30% $w/v$). Afterwards, bidistilled water was slowly added to the ethanol phase up to a final 70:30 ($v/v$) ratio, maintaining magnetic stirring at 750 rpm (IKA RCT basic, IKA®-Werke GmbH & Co. KG, Staufen, Germany) for 30 min at 22–25 °C [53]. For TET preparation, the surfactant (i.e., T80 or SC) was solubilized in the PC ethanol solution before water addition. In the case of VD3-containing ET and TET, VD3 (1 mg/mL) was added to PC ethanol solution and rapidly mixed (IKA Vortex 1, IKA®-Werke GmbH & Co. KG, Staufen, Germany) before the addition of water. Table 1 reports ET and TET compositions.

### 4.3. Photon Correlation Spectroscopy

Vesicle size analysis of ET and TET was conducted using a Zetasizer Nano-S90 (Malvern Instr., Malvern, England) with a 5 mW helium neon laser and a wavelength output of 633 nm. Measurements were performed at 25 °C at a 90° angle and a run time of at least 180 s. Samples have been diluted with bidistilled water in a 1:20 $v/v$ ratio. Data were analyzed using the "CONTIN" method [54]. Measurements were performed thrice for 3 months from ET and TET production.

### 4.4. Cryo-Transmission Electron Microscopy

Samples for cryo-TEM were vitrified putting sample droplets (2 μL) for some seconds on a lacey-carbon-filmed copper grid (Science Services, München) [53]. Afterwards, most of the liquid has been removed by blotting paper, obtaining a thin film stretched over the lace holes. The rapid immersion of specimen into liquid ethane cooled to approximately 90 K by liquid nitrogen in a temperature-controlled freezing unit (Leica EMGP, Leica, Germany) instantly allowed their vitrification. All sample preparation steps were conducted at controlled constant temperature in the Leica EMGP chamber. The vitrified specimen was transferred to a Zeiss/Leo EM922 Omega EFTEM (Zeiss Microscopy GmbH, Jena, Germany) transmission electron microscope using a cryoholder (CT3500, Gatan, Munich, Germany). During the microscopy observations, the sample temperature was kept below 100 K. Specimens were examined with reduced doses ≈ 1000–2000 e/nm$^2$ at 200 kV. Zero-loss

113

filtered images ($\Delta$E = 0 eV) were recorded by a CCD digital camera (Ultrascan 1000, Gatan, Munich, Germany) and analyzed using a GMS 1.9 software (Gatan, Munich, Germany).

### 4.5. Deformability Measurement

The deformability of ET and TET vesicles was determined by extrusion through polycarbonate filter membrane (pore diameter 50 nm). Namely, a stainless steel, 25 mm diameter filter holder (extruder, Lipex Biomembranes, Vancouver, Canada) was employed applying a 2.5 bar pressure at 25 °C and measuring the volume of formulation extruded in 1 min. The mean diameter of vesicles was measured by PCS before and after the extrusion. The deformability of vesicles membrane was calculated according to the following equation:

$$Def = J \times (rv/rp)^2 \tag{1}$$

where Def is the vesicle deformability, J is the ratio between the volume of extruded formulation (mL) and the time of extrusion (min); rv is the vesicle size (after extrusion); and rp is the pore size of the filter membrane [15,53].

### 4.6. Vitamin D3 Content of Ethosomes and Transethosomes

The entrapment capacity (EC) of VD3 in ET and TET was determined 1 and 90 days after production. Five hundred microliters of ET and TET were loaded in a centrifugal filter (Microcon centrifugal filter unit YM-10 membrane, nmWCO 10 kDa, Sigma-Aldrich, St. Louis, MO, USA) and ultra-centrifuged (Spectrafuge™ 24D Digital Microcentrifuge, Woodbridge, NJ, USA) at 4000 rpm for 15 min. Afterwards, a 100 μL aliquot of supernatant was diluted with ethanol (1:10, *v/v*) and maintained under magnetic stirring for 30 min [18,53]. After filtration of the solution by nylon syringe filters (0.22 μm pores), the amount of VD3 was analyzed by HPLC, as reported below. The EC was determined as follows:

$$EC = VD3/T_{VD3} \times 100 \tag{2}$$

where VD3 is the amount of drug measured by HPLC and $T_{VD3}$ is the total amount of VD3 employed for ET and TET production.

### 4.7. HPLC Procedure

For HPLC analyses, a two-plungers alternative pump (Agilent Technologies 1200 series, Santa Clara, CA, USA), a UV-detector operating at 325 nm, and a 7125 Rheodyne injection valve with a 50 μL loop were employed. Analyses were conducted eluting a stainless-steel C-18 reverse-phase column (15 × 0.46 cm) packed with 5 μm particles (Platinum C18, Apex Scientific, Alltech, Nicholasville, KY, USA) with a mobile phase containing methanol/water 95:5 *v/v*, at a flow rate of 0.6 mL/min. In these conditions, the VD3 retention time was 7.8 min.

### 4.8. Cell Culture and Treatment

HaCaT keratinocytes (an immortalized human cell line purchased from ATCC® PCS-200-011™), fibroblasts (an immortalized human cell line purchased from ATCC® PCS-201-013™) and C2C12 myoblasts (an immortalized murine cell line purchased from ECACC 91031101) were cultured in 75 cm$^2$ plastic flasks using Dulbecco's modified Eagle medium, supplemented with 10% (*v/v*) FBS, 1% (*w/v*) glutamine, 0.5% (*v/v*) amphotericin B, 100 units/mL of penicillin–streptomycin (Gibco, Thermo Fisher Scientific, Waltham, MA, USA) and incubated at 37 °C with 5% CO$_2$. Cells were trypsinized in 0.05% EDTA in phosphate buffered saline (PBS) and seeded in flat-bottom 96-well plates (keratinocytes 12 × 10$^3$ cells/well; fibroblasts 4 × 10$^3$ cells/well; myoblasts 3 × 10$^3$ cells/well) for MTT assay or onto glass coverslips (12 mm in diameter) in 24-multiwell (keratinocytes 4 × 10$^4$ cells/well; fibroblasts 15 × 10$^3$ cells/well; myoblasts 8 × 10$^3$ cells/well) for microscopy analyses. Twenty-four hours after seeding, the cells were treated with the nanocar-

riers for increasing times and then processed according to the specific analysis protocol (see below).

### 4.9. Cytotoxicity Assay

The MTT assay was used to assess the cytotoxicity of ET, TET and DET, as well as of VD3 30% *v/v* ethanol solution, ET-VD3 and TET-VD3 on keratinocytes, fibroblasts and myoblasts. The MTT assay is an indicator of cell metabolism and the reduction in absorbance value is related to a loss of oxidoreductase enzyme activity due to the toxicity of the treatment [55]. Cells were treated with blank nanocarrier at different concentrations (from 34.6 to 173.1 µg/mL of PC) selected on the basis of their VD3 entrapment capacity and on VD3 concentrations previously administered in vitro [56]; then, the ET and TET concentrations found to be safe were loaded with VD3 and the MTT assay was applied to ET-VD3 and TET-VD3 in order to verify if drug entrapment changes their safety profile. Cytotoxicity was evaluated after 2 h, in order to detect acute toxic effects, and after 24 h, a longer time than the cell cycle of all cell lines used. Cytotoxicity was not assessed for times longer than 24 h because cell death at such long times may be due to the combined effect of the internalized nanocarriers and the accumulation of toxic products released by the non-internalized nanocarriers undergoing degradation in the medium. Untreated cell samples were used as the control. Some cells were treated with VD3 solution to compare the cytotoxic effect vs. ET-VD3 and TET-VD3 loaded with the same VD3 amounts.

The cytotoxicity assay was performed as follows. At each incubation time, the medium was replaced by 100 µL of MTT solution (Thiazolyl Blue Tetrazolium Bromide, Sigma-Aldrich) (0.5 mg/mL in medium) and incubated for 4 h at 37 °C in a cell incubator. Then, MTT solution was removed, and formazan crystals were dissolved in 100 µL of dimethyl sulfoxide. The absorbance was measured at 570 nm using a ChroMate 4300 ELISA microplate reader (Awareness Technology Inc., Palm City, FL, USA). Experiments were performed in triplicate. Statistical comparisons between the control and experimental conditions were made by the Mann–Whitney pairwise test and significant difference was set at $p \leq 0.05$.

### 4.10. Light Microscopy

For nanocarriers' visualization at fluorescence microscopy, ET and TET (i.e., blank nanocarriers) were stained with PKH67 Green Fluorescent Cell Linker Kit for General Cell Membrane Labeling (Sigma-Aldrich) [57]. PKH67 dye was diluted in 500 µL of Diluent C to a concentration of 4 µm (dye solution). Then, 20 µL of ET or TET were diluted in 80 µL of Diluent C and incubated with 100 µL of dye solution (final dye concentration 2 µm) for 5 min while being mixed with gentle pipetting. The reaction was stopped by adding 1 mL of complete medium containing 10% (*v/v*) FBS and cells were treated with stained nanocarriers. This technique allowed for the staining of nanocarriers immediately before their use, thus avoiding fluorophore release in the stock ethanol solution. After 2 h and 24 h incubation with either ET or TET, cells were fixed with 4% (*v/v*) paraformaldehyde in PBS, pH 7.4 for 30 min at room temperature. Cells were then permeabilized with 0.05% PBS Tween, washed in PBS, incubated with 0.04% Trypan blue (Gibco) in PBS for 30 s, stained for DNA with Hoechst 33342 (0.5 µg/mL in PBS), rinsed in PBS, and finally mounted in 1:1 mixture of glycerol:PBS.

For lipid droplet visualization at bright-field microscopy, the Oil Red O staining for neutral lipids was applied. After 24 h incubation with ET or TET, cells were fixed with 4% (*v/v*) paraformaldehyde in PBS, pH 7.4 for 13 min at room temperature. Cells were then rinsed in PBS, incubated with filtered Oil Red O (Bio-Optica, Milan, Italy) for 20 min at room temperature, washed in PBS, stained with Mayer's Hematoxylin ready-to-use solution (Bio-Optica) for 1 min at room temperature, washed again in PBS, and finally mounted in 1:1 mixture of glycerol:PBS.

The samples were observed with an Olympus BX51 (Olympus Italia Srl, Milan, Italy) microscope using a 40× objective either under bright field mode or in fluorescence (100 W

mercury lamp) mode under the following conditions: 450–480 nm excitation filter (excf), 500 nm dichroic mirror (dm), and 515 nm barrier filter (bf), for PKH67; 540 nm excf, 580 nm dm, and 620 nm bf, for trypan blue; 330–385 nm excf, 400 nm dm, and 420 nm bf, for Hoechst 33342. Images were recorded with an QICAM Fast 1394 digital camera (QImaging, Surrey, BC, Canada) and processed using Image-Pro Plus 7.0 software (Media Cybernetics Inc., Rockville, MD, USA). All images were processed using Paint Shop Pro software (JASC Software Inc., Eden Prairie, MN, USA).

*4.11. Transmission Electron Microscopy*

For TEM, control cells and cells treated with ET or TET (i.e., blank nanocarriers) were fixed with 2.5% ($v/v$) glutaraldehyde and 2% ($v/v$) paraformaldehyde in 0.1 M phosphate buffered saline, pH 7.4, for 2 h at 4 °C, post-fixed with 1.5% potassium ferrocyanide and 1% osmium tetroxide for 1 h, dehydrated with acetone and embedded in Epon resin. In order to preserve the spatial relationships between cells and NPs, both myoblasts and myotubes were processed for TEM as monolayers [58]. Ultrathin sections were observed in a Philips Morgagni transmission electron microscope (FEI Company Italia Srl, Milan, Italy) operating at 80 kV and equipped with a Megaview II camera for digital image acquisition. All images were processed using Paint Shop Pro software (JASC Software Inc., Eden Praire, MN, USA).

Quantitative size evaluation of nanocarriers and lipid droplets was performed by using ImageJ software (NIH). The diameter of 200 nanocarriers per sample was measured in cells treated with ET for 2 h and 24 h, and with TET for 2 h, while the number of TET in cells treated for 24 h was too small for a reliable quantitative evaluation. The sectional area of 200 lipid droplets was measured in cells treated with TET for 24 h.

The mean values ± s.d. of nanocarrier diameter and lipid droplet area were calculated for each time point (2 h and 24 h). Statistical comparisons were performed using one-way ANOVA followed by Dunn's post hoc test. Significant difference was set at $p \leq 0.05$.

## 5. Conclusions

Our pilot study demonstrated that both ET and TET are characterized by physico-chemical properties optimal for transdermal penetration and efficient VD3 loading, and are safely and easily internalized by cells from epithelial, connective or muscle tissues. Moreover, our detailed ultrastructural study provided original information on the intracellular pathways of ET and TET in cells from these different histological origins. Both nanocarriers are able to intact enter the cells, but they follow distinct intracellular fates: ET persist for long times inside the cytoplasm, without inducing subcellular alteration, while TET undergo rapid degradation, giving rise to an intracellular accumulation of lipids. Therefore, the capability of ET to maintain their structural integrity for long times in the intracellular milieu makes them especially suitable for sustained VD3 release. On the other hand, the rapid intracellular degradation of TET makes them more appropriate for the faster release of VD3.

Based on our results, both ET and TET thus proved to be biocompatible and efficient nanocarriers and may be envisaged as very promising tools for the transdermal delivery of VD3; this paves the way to in vivo study aimed to understand their biodistribution following cutaneous application and to test their therapeutic efficiency in different experimental and pathologic conditions.

**Author Contributions:** Conceptualization, E.E.; C.Z. and M.M.; methodology, M.C. and E.E.; investigation, M.C.; E.E.; M.S.; M.A.L.; M.D. and M.M.; data curation, M.C.; writing—original draft preparation, M.C.; E.E. and M.M.; writing—review and editing, E.E., G.V.; C.Z. and M.M.; supervision, M.M.; funding acquisition, E.E.; M.D. and M.M. All authors have read and agreed to the published version of the manuscript.

**Institutional Review Board Statement:** Not applicable.

**Informed Consent Statement:** Not applicable.

**Data Availability Statement:** Data are contained within the article. Additional data are available from the corresponding author, upon reasonable request.

**Conflicts of Interest:** The authors declare no conflict of interest.

## References

1. Kechichian, E.; Ezzedine, K. Vitamin D and the Skin: An Update for Dermatologists. *Am. J. Clin. Dermatol.* **2018**, *19*, 223–235. [CrossRef]
2. Lehmann, B.; Querings, K.; Reichrath, J. Vitamin D and skin: New aspects for dermatology. *Exp. Dermatol.* **2004**, *13*, 11–55. [CrossRef] [PubMed]
3. Lehmann, B. Role of the vitamin D3 pathway in healthy and diseased skin-facts, contradictions and hypotheses. *Exp. Dermatol.* **2009**, *18*, 97–108. [CrossRef] [PubMed]
4. Dawson-Hughes, B. Vitamin D and muscle function. *J. Steroid Biochem. Mol. Biol.* **2017**, *173*, 313–316. [CrossRef] [PubMed]
5. Abiri, B.; Vafa, M. Vitamin D and Muscle Sarcopenia in Aging. *Methods Mol. Biol.* **2020**, *2138*, 29–47. [CrossRef]
6. Uchitomi, R.; Oyabu, M.; Kamei, Y. Vitamin D and Sarcopenia: Potential of Vitamin D Supplementation in Sarcopenia Prevention and Treatment. *Nutrients* **2020**, *12*, 3189. [CrossRef]
7. Alsaqr, A.; Rasoully, M.; Musteata, F.M. Investigating Transdermal Delivery of Vitamin D3. *AAPS PharmSciTech* **2015**, *16*, 963–972. [CrossRef] [PubMed]
8. D'Angelo Costa, G.M.; Sales de Oliveira Pinto, C.A.; Rodrigues Leite-Silva, V.; Rolim Baby, A.; Robles Velasco, M.V. Is Vitamin D3 Transdermal Formulation Feasible? An Ex Vivo Skin Retention and Permeation. *AAPS PharmSciTech* **2018**, *19*, 2418–2425. [CrossRef]
9. Bi, Y.; Xia, H.; Li, L.; Lee, R.J.; Xie, J.; Lium, Z.; Qiu, Z.; Teng, L. Liposomal Vitamin D(3) as an Anti-aging Agent for the Skin. *Pharmaceutics* **2019**, *11*, 311. [CrossRef]
10. Akbarzadeh, A.; Rezaei-Sadabady, R.; Davaran, S.; Joo, S.W.; Zarghami, N.; Hanifehpour, Y.; Samiei, M.; Kouhi, M.; Nejati-Koshki, K. Liposome: Classification, preparation, and applications. *Nanoscale Res. Lett.* **2013**, *8*, 102. [CrossRef]
11. Touitou, E.; Dayan, N.; Bergelson, L.; Godin, B.; Eliaz, M. Ethosomes-novel vesicular carriers for enhanced delivery: Characterization and skin penetration properties. *J. Control. Release* **2000**, *65*, 403–418. [CrossRef]
12. Natsheh, H.; Vettorato, E.; Touitou, E. Ethosomes for dermal administration of natural active molecules. *Curr. Pharm. Des.* **2019**, *25*, 2338. [CrossRef] [PubMed]
13. Godin, B.; Touitou, E. Ethosomes: New prospects in transdermal delivery. *Crit. Rev. Ther. Drug Carrier Syst.* **2003**, *20*, 63–102. [CrossRef] [PubMed]
14. Shen, L.N.; Zhang, Y.T.; Wang, Q.; Xu, L.; Feng, N.P. Enhanced in vitro and in vivo skin deposition of apigenin delivered using ethosomes. *Int. J. Pharm.* **2014**, *460*, 280–288. [CrossRef] [PubMed]
15. Jain, S.; Tiwary, A.K.; Sapra, B.; Jain, N.K. Formulation and evaluation of ethosomes for transdermal delivery of lamivudine. *AAPS PharmSciTech* **2007**, *8*, E111. [CrossRef] [PubMed]
16. Bendas, E.R.; Tadros, M.I. Enhanced transdermal delivery of salbutamol sulfate via ethosomes. *AAPS PharmSciTech* **2007**, *8*, E107. [CrossRef] [PubMed]
17. Elsayed, M.M.M.; Abdallah, O.Y.; Naggar, V.F.; Khalafallah, N.M. Deformable liposomes and ethosomes: Mechanism of enhanced skin delivery. *Int. J. Pharm.* **2006**, *322*, 60–66. [CrossRef]
18. Sguizzato, M.; Mariani, P.; Spinozzi, F.; Benedusi, M.; Cervellati, F.; Cortesi, R.; Drechsler, M.; Prieux, R.; Valacchi, G.; Esposito, E. Ethosomes for coenzyme Q10 cutaneous administration: From design to 3D skin tissue evaluation. *Antioxidants* **2020**, *9*, 485–504. [CrossRef] [PubMed]
19. El Zaafarany, G.M.; Awad, G.A.S.; Holayel, S.M.; Mortada, N.D. Role of edge activators and surface charge in developing ultradeformable vesicles with enhanced skin delivery. *Int. J. Pharm.* **2010**, *397*, 164–172. [CrossRef]
20. Abdulbaqi, I.M.; Darwis, Y.; Khan, N.A.; Assi, R.A.; Khan, A.A. Ethosomal nanocarriers: The impact of constituents and formulation techniques on ethosomal properties, in vivo studies, and clinical trials. *Int. J. Nanomed.* **2016**, *11*, 2279–2304. [CrossRef]
21. Danaei, M.; Dehghankhold, M.; Ataei, S.; Hasanzadeh Davarani, F.; Javanmard, R.; Dokhani, A.; Khorasani, S.; Mozafari, M.R. Impact of Particle Size and Polydispersity Index on the Clinical Applications of Lipidic Nanocarrier Systems. *Pharmaceutics* **2018**, *10*, 57. [CrossRef]
22. Gándola, Y.B.; Pérez, S.E.; Irene, P.E.; Sotelo, A.I.; Miquet, J.G.; Corradi, G.R.; Carlucci, A.M.; Gonzalez, L. Mitogenic effects of phosphatidylcholine nanoparticles on MCF-7 breast cancer cells. *Biomed. Res. Int.* **2014**, *2014*, 687037. [CrossRef] [PubMed]

23. Bikle, D.; Christakos, S. New aspects of vitamin D metabolism and action - addressing the skin as source and target. *Nat. Rev. Endocrinol.* **2020**, *16*, 234–252. [CrossRef] [PubMed]
24. van Meer, G.; Voelker, D.R.; Feigenson, G.W. Membrane lipids: Where they are and how they behave. *Nat. Rev. Mol. Cell. Biol.* **2008**, *9*, 112–124. [CrossRef] [PubMed]
25. Kono, H.; Kimura, Y.; Latz, E. Inflammasome activation in response to dead cells and their metabolites. *Curr. Opin. Immunol.* **2014**, *30*, 91–98. [CrossRef] [PubMed]
26. Malatesta, M. Transmission electron microscopy for nanomedicine: Novel applications for long-established techniques. *Eur. J. Histochem.* **2016**, *60*, 2751. [CrossRef] [PubMed]
27. Touitou, E.; Godin, B.; Dayan, N.; Weiss, C.; Piliponsky, A.; Levi-Schaffer, F. Intracellular delivery mediated by an ethosomal carrier. *Biomaterials.* **2001**, *22*, 3053–3059. [CrossRef]
28. Godin, B.; Touitou, E. Mechanism of bacitracin permeation enhancement through the skin and cellular membranes from an ethosomal carrier. *J. Control. Release* **2004**, *94*, 365–379. [CrossRef]
29. Costanzo, M.; Carton, F.; Marengo, A.; Berlier, G.; Stella, B.; Arpicco, S.; Malatesta, M. Fluorescence and electron microscopy to visualize the intracellular fate of nanoparticles for drug delivery. *Eur. J. Histochem.* **2016**, *60*, 2640. [CrossRef]
30. Costanzo, M.; Vurro, F.; Cisterna, B.; Boschi, F.; Marengo, A.; Montanari, E.; Meo, C.D.; Matricardi, P.; Berlier, G.; Stella, B.; et al. Uptake and intracellular fate of biocompatible nanocarriers in cycling and noncycling cells. *Nanomedicine* **2019**, *14*, 301–316. [CrossRef]
31. Guglielmi, V.; Carton, F.; Vattemi, G.; Arpicco, S.; Stella, B.; Berlier, G.; Marengo, A.; Boschi, F.; Malatesta, M. Uptake and intracellular distribution of different types of nanoparticles in primary human myoblasts and myotubes. *Int. J. Pharm.* **2019**, *560*, 347–356. [CrossRef] [PubMed]
32. Feller, S.E.; Brown, C.A.; Nizza, D.T.; Gawrisch, K. Nuclear Overhauser enhancement spectroscopy cross-relaxation rates and ethanol distribution across membranes. *Biophys. J.* **2002**, *82*, 1396–1404. [CrossRef]
33. Baburina, I.; Jackowski, S. Cellular responses to excess phospholipids. *J. Biol. Chem.* **1999**, *274*, 9400–9408. [CrossRef] [PubMed]
34. Barbour, S.E.; Kapur, A.; Deal, C.L. Regulation of phosphatidylcholine homeostasis by calcium-independent phospholipase A2. *Biochim. Biophys. Acta* **1999**, *1439*, 77–88. [CrossRef]
35. Lagace, T.A.; Storey, M.K.; Ridgway, N.D. Regulation of phosphatidylcholine metabolism in Chinese hamster ovary cells by the sterol regulatory element-binding protein (SREBP)/SREBP cleavage-activating protein pathway. *J. Biol. Chem.* **2000**, *275*, 14367–14374. [CrossRef]
36. Zaccheo, O.; Dinsdale, D.; Meacock, P.A.; Glynn, P. Neuropathy target esterase and its yeast homologue degrade phosphatidyl-choline to glycerophosphocholine in living cells. *J. Biol. Chem.* **2004**, *279*, 24024–24033. [CrossRef]
37. Peng, X.; Frohman, M.A. Mammalian phospholipase D physiological and pathological roles. *Acta Physiol.* **2012**, *204*, 219–226. [CrossRef]
38. Fagone, P.; Jackowski, S. Phosphatidylcholine and the CDP-choline cycle. *Biochim. Biophys. Acta* **2013**, *1831*, 523–532. [CrossRef] [PubMed]
39. Martins de Lima, T.; Cury-Boaventura, M.F.; Giannocco, G.; Nunes, M.T.; Curi, R. Comparative toxicity of fatty acids on a macrofage cell line (J774). *Clin. Sci.* **2006**, *111*, 307–317. [CrossRef]
40. Coleman, R.A.; Lee, D.P. Enzymes of triacylglycerol synthesis and their regulation. *Prog. Lipid Res.* **2004**, *43*, 134–176. [CrossRef]
41. Jackowski, S.; Wang, J.; Baburina, I. Activity of the phosphatidylcholine biosynthetic pathway modulates the distribution of fatty acids into glycerolipids in proliferating cells. *Biochim. Biophys. Acta* **2000**, *1483*, 301–315. [CrossRef]
42. Waite, K.A.; Vance, D.E. Why expression of phosphatidylethanolamine N-methyltransferase does not rescue Chinese hamster ovary Cells that have an impaired CDP-choline pathway. *J. Biol. Chem.* **2000**, *275*, 21197–21202. [CrossRef] [PubMed]
43. Testerink, N.; van der Sanden, M.H.; Houweling, M.; Helms, J.B.; Vaandrager, A.B. Depletion of phosphatidylcholine affects endoplasmic reticulum morphology and protein traffic at the Golgi complex. *J. Lipid Res.* **2009**, *50*, 2182–2192. [CrossRef]
44. Kishore, R.S.; Kiese, S.; Fischer, S.; Pappenberger, A.; Grauschopf, U.; Mahler, H.C. The degradation of polysorbates 20 and 80 and its potential impact on the stability of biotherapeutics. *Pharm. Res.* **2011**, *28*, 1194–1210. [CrossRef]
45. Walther, T.C.; Farese, R.V., Jr. The life of lipid droplets. *Biochim. Biophys. Acta* **2009**, *1791*, 459–466. [CrossRef] [PubMed]
46. Tauchi-Sato, K.; Ozeki, S.; Houjou, T.; Taguchi, R.; Fujimoto, T. The surface of lipid droplets is a phospholipid monolayer with a unique fatty acid composition. *J. Biol. Chem.* **2002**, *277*, 44507–44512. [CrossRef] [PubMed]
47. Liu, P.; Ying, Y.; Zhao, Y.; Mundy, D.I.; Zhu, M.; Anderson, R.G. Chinese hamster ovary K2 cell lipid droplets appear to be metabolic organelles involved in membrane traffic. *J. Biol. Chem.* **2004**, *279*, 3787–3792. [CrossRef]
48. Krahmer, N.; Guo, Y.; Wilfling, F.; Hilger, M.; Lingrell, S.; Heger, K.; Newman, H.W.; Schmidt-Supprian, M.; Vance, D.E.; Mann, M.; et al. Phosphatidylcholine synthesis for lipid droplet expansion is mediated by localized activation of CTP:phosphocholine cytidylyltransferase. *Cell Metab.* **2011**, *14*, 504–515. [CrossRef]
49. Thiam, A.R.; Farese, R.V., Jr.; Walther, T.C. The biophysics and cell biology of lipid droplets. *Nat. Rev. Mol. Cell. Biol.* **2013**, *14*, 775–786. [CrossRef]
50. Flis, V.V.; Daum, G. Lipid transport between the endoplasmic reticulum and mitochondria. *Cold Spring Harb. Perspect. Biol.* **2013**, *5*, a013235. [CrossRef]
51. Ellfolk, M.; Norlin, M.; Gyllensten, K.; Wikvall, K. Regulation of human vitamin D(3) 25-hydroxylases in dermal fibroblasts and prostate cancer LNCaP cells. *Mol. Pharmacol.* **2009**, *75*, 1392–1399. [CrossRef] [PubMed]

52. van der Meijden, K.; Bravenboer, N.; Dirks, N.F.; Heijboer, A.C.; den Heijer, M.; de Wit, G.M.J.; Offringa, C.; Lips, P.; Jaspers, R.T. Effects of 1,25(OH)2 D3 and 25(OH)D3 on C2C12 Myoblast Proliferation, Differentiation, and Myotube Hypertrophy. *J. Cell Physiol.* **2016**, *231*, 2517–2528. [CrossRef] [PubMed]
53. Hallan, S.S.; Sguizzato, M.; Mariani, P.; Cortesi, R.; Huang, N.; Simelière, F.; Marchetti, N.; Drechsler, M.; Ruzgas, T.; Esposito, E. Design and Characterization of Ethosomes for Transdermal Delivery of Caffeic Acid. *Pharmaceutics* **2020**, *12*, 740. [CrossRef]
54. Pecora, R. Dynamic light scattering measurement of nanometer particles in liquids. *J. Nanopart. Res.* **2000**, *2*, 123–131. [CrossRef]
55. Stockert, J.C.; Horobin, R.W.; Colombo, L.L.; Blázquez-Castro, A. Tetrazolium salts and formazan products in Cell Biology: Viability assessment, fluorescence imaging, and labeling perspectives. *Acta Histochem.* **2018**, *120*, 159–167. [CrossRef]
56. Ramezanli, T.; Kilfoyle, B.E.; Zhang, Z.; Michniak-Kohn, B.B. Polymeric nanospheres for topical delivery of vitamin D3. *Int. J. Pharm.* **2017**, *516*, 196–203. [CrossRef]
57. Pužar Dominkuš, P.; Stenovec, M.; Sitar, S.; Lasič, E.; Zorec, R.; Plemenitaš, A.; Žagar, E.; Kreft, M.; Lenassi, M. PKH26 labeling of extracellular vesicles: Characterization and cellular internalization of contaminating PKH26 nanoparticles. *Biochim. Biophys. Acta Biomembr.* **2018**, *1860*, 1350–1361. [CrossRef] [PubMed]
58. Costanzo, M.; Malatesta, M. Embedding cell monolayers to investigate nanoparticle-plasmalemma interactions at transmission electron microscopy. *Eur. J. Histochem.* **2019**, *63*, 3026. [CrossRef] [PubMed]

# CHAPTER 4

## *IN VITRO STUDY*

**Immune regulation of satellite cells: the setting up of in vitro co-culture system. Preliminary data**

**IMMUNE REGULATION OF SATELLITE CELLS: THE SETTING UP OF IN VITRO CO-CULTURE SYSTEM. PRELIMINARY DATA**

**INTRODUCTION**

Aging is a physiological process characterized by a progressive decline in stem cells' function and number in different tissues, including the skeletal muscle, resulting in impaired tissue homeostasis, repair, and regeneration[1].

Skeletal muscle contains a population of adult stem cells called satellite cells (SCs) that reside in specialized niches located below the basal lamina and adjacent to the sarcolemma of myofibers.

In homeostatic muscle, the satellite cells are normally quiescent. However, when stimulated by degenerative muscle disease or injury these cells are activated, begin to proliferate and subsequently they either exit the cell cycle, differentiate and fuse to form new fibres in order to repair the damaged ones, or they self-renew to replenish the satellite cell pool[2].

It has been shown that the regenerative potential of skeletal muscle can be compromised by satellite cells intrinsic impairment and dysregulations in the environment coordinating the repair process.[3]

*INTRINSIC IMPAIRMENT*

The long-lasting persistence of satellite cells in the organism makes them inclined to the accumulation of intracellular damage, such as DNA damage[4].

The studies carried out on satellite cells isolated from aged mice, revealed increased levels of DNA damage. Furthermore, over 28 months old mice exhibit senescent satellite cells[5]; since senescence is often coupled with DNA damage, this could support the idea of DNA damage occurrence in satellite cells during aging[6]. Additionally, genetic manipulation of genes involved in DNA DAMAGE RESPONSE (DDR) leads to various muscle stem cell defects that mirror aging phenotypes[6].

*ENVIROMENTAL IMPAIRMENT: IMMUNE CELLS*

Some muscle-resident cells such as immune cells regulate satellite cells maintenance and their microenvironment. In case of injury immune cells, and in particular macrophages, rapidly increase their number and stimulate satellite cells function[2]. Indeed, macrophages not only clear the damaged areas by phagocyting tissue debris, but also sustain the regenerative myogenesis producing several factors such as Tumor Necrosis Factor-α (Tnf-α), Interleukin-6 (IL-6), Interleukin-1 beta (IL-1b) which sustain the SCs proliferation and influence the intrinsic capabilities of muscle cells, suggesting an active interplay between macrophages and muscle resident cells involved in the repair process[7].

It has been reported that during aging, under regenerative stress, there can be defective recruitment of myeloid cells and deficiencies in their function that affect the muscle regeneration process[8]. Interestingly, recent studies revealed that a transient macrophages depletion in a dystrophic mouse model was associated with the appearance of a cell population, referred to as α7Sca1 cells, that co-

express both α7integrin, as stem cell antigen, and Sca1 as fibroadipogenic progenitors (FAPs) marker[7]. Surprisingly, preliminary data obtained from Neves-Victor Lab showed the appearance of α7Sca1 cells also in muscles of aged mice: these cells showed a reduced proliferation rate, morphological arrangement modifications and increased amount of DNA damage, compared to SCs.

**AIM OF THE STUDY**

Since in aging satellite cells have more DNA damage, macrophages are reduced in the aged regenerating skeletal muscle and the depletion of the latter is also associated with the appearance of Mix Lin influencing the proliferation/differentiation balance of myogenic progenitors, the present study aimed at getting light if in presence of DNA damage, macrophages could preserve SCs identity playing a role in solving the DNA double strand breaks.

To achieve this goal, we try to set-up and characterize an *in vitro* model using C2C12 murine myoblast cell line co-cultured with primary macrophages.

A) C2C12 cells are collected and processed for RT-qPCR. We evaluate the mRNA expression of different factors involved in the regeneration process of injured muscle. Our investigation aimed at understanding if in presence of DNA damage and with or without macrophages, myoblasts respectively gain or lose their intrinsic function.

B) Immunohistochemistry reaction, to better understand if macrophages play a role in the activation of the DNA damage machinery response in C2C12 cells.

**MATERIALS AND METHODS**

**Gene expression analysis by RT-qPCR**

- C2C12 cells recapitolate SCs in vitro. They are growth in plastic cell culture dishes in DMEM supplemented with 10% FBS and 1% P/S in a humidified incubator kept at 37 °C and 5% $CO_2$. When cells reached 60-70% confluency, myoblasts are stained in plate with 20μL of Dil dye, a fluorescent cell membrane dye diluted in 5mL of DMEM.
- C2C12 are quickly washed, centrifuged, and seeded at 300.000 (in triplicates) onto 6 well plates:
  A) C2C12 (Ctr)
  B) C2C12 co-cultured with macrophages (C2C12 M)
  C) C2C12 treated with Etoposide (C2C12 ETO+)
  D) C2C12 treated with Etoposide and co-cultured with macrophages (C2C12 M ETO+)

- After 24 hours, C2C12 are treated with ETO (1:1000), a drug which provokes a DNA double-strand breaks.
- At the same time the Bone Marrow Derived Macrophages, collected from femur and tibia of wild type mice, are thawed.
- After 6 hours C2C12 are quickly washed with PBS, macrophages are seeded at 300.000 per well and the plates are incubated overnight at 37°C.
- The day after, the cells are trypsinized, centrifuged and resuspended in FACS buffer for FACS (fluorescence-activated single cell sorting) analysis.
- Only the C2C12 "positive" for Dil dye are sorted and collected in DMEM.
- The C2C12 are then processed for RT-qPCR: briefly, total RNA from freshly sorted cells for each condition is extracted and then quantified with NanoDrop. For mRNA analysis, the RNA from each sample is retrotranscribed in cDNA and amplified at qPCR with SYBR Green PCR Master Mix using specific murine primers pairs for each gene.
- For each sample is evaluated the expression of the following genes:
  - **MyoD,** a transcription factor that acts in myotube differentiation.
  - **MGN,** a late marker for muscle cell differentiation.
  - **GADD45b,** a marker of cell stress.
  - **Sca1,** a marker of FAP cells in the skeletal muscle.
  - **TNF-alpha, IL-6 and IL-1beta,** pro-inflammatory cytokines released by macrophages, satellite cells and myofibers that are involved in the regeneration process of injured skeletal muscle.

For instance, TNF-alpha and IL-6 positively affect SCs proliferation after muscle injury[7].

IL-1beta, acts by recruiting immune cells to the site of injury and influencing the intrinsic capabilities of myoblasts. Indeed, following skeletal muscle injury, IL-1beta is highly expressed by muscle cells, neutrophils and macrophages recruited around the injured area, promoting the proliferation of primary muscle cells[9,10].

We obtained three values of each gene for each condition and the analysis of output values are made using standard ΔΔCt method.

A statistical analysis is performed by Kruskall-Wallis non-parametric test. Data for each variable were presented as mean ± standard error (SE) and statistical significance was set at $p \leq 0.05$.

**Results**

Kruskall-Wallis test did not demonstrate a statistical significant difference among samples for each gene expression tested. However, C2C12 co-cultured with macrophages and C2C12 co-cultured with M and treated with etoposide, showed a higher average value of TNF-alpha expression in comparison with other samples (Fig. 1A). At the same time, C2C12 co-cultured with MACs and treated with etoposide showed a higher average value of IL-1beta expression, in comparison with other samples (Fig. 1B).
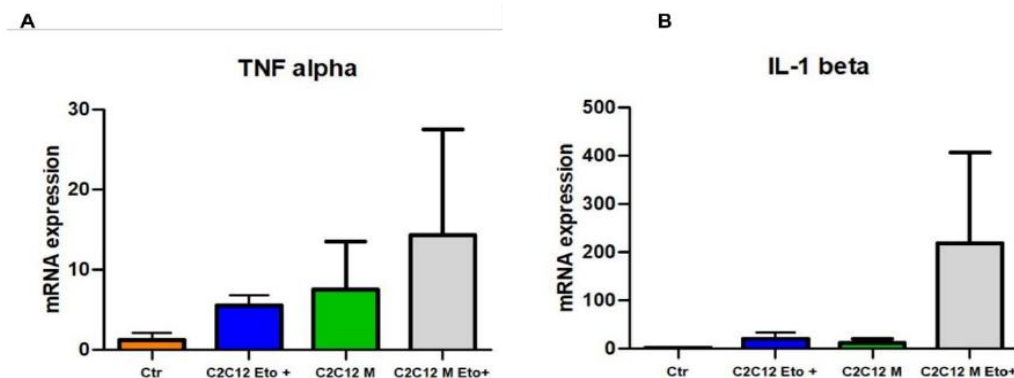


**Fig.1 (A)** TNF-alpha gene expression (mean ± SE) in Ctr; C2C12 Eto+; C2C12 M; C2C12 M Eto+. **(B)** IL-1 beta gene expression (mean ± SE) in Ctr; C2C12 Eto+; C2C12 M; C2C12 M Eto+.

Although TNF-alpha and IL-1beta can be released from myoblasts under regenerative stress, to deeply understand if the increased expression of TNF-alpha and IL-1beta genes in C2C12 M and C2C12 M ETO+ samples are due to macrophage's contamination, we evaluated through RT-qPCR the expression of the following genes, in the samples described above:

-**EMR1,** also known as F4/80, a marker of murine macrophages populations.

-**mac1,** a cell surface receptor expressed by myeloid cells (i.e., macrophages).

The results obtained with RT-qPCR showed an overexpression of EMR1 and Mac1 in C2C12 M and in C2C12 M ETO+ samples, thus supporting the hypothesis of macrophages persistence in sorted myoblasts (Fig. 2 A-B).
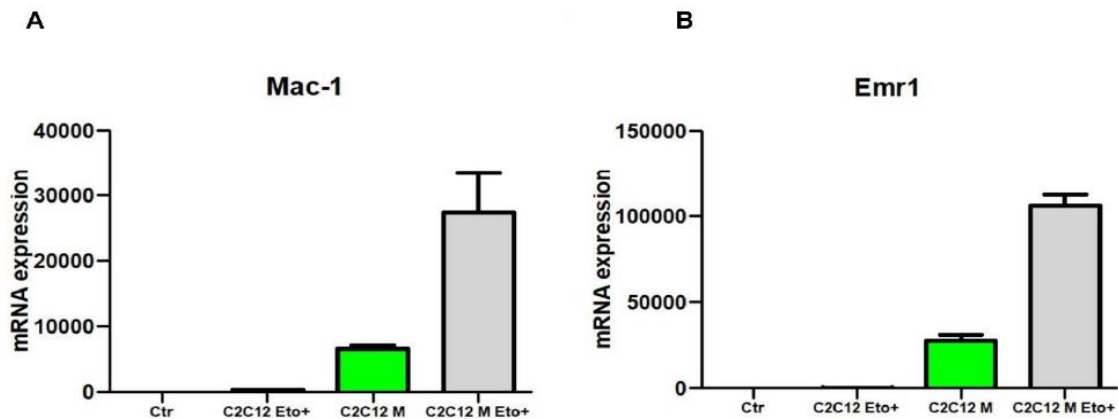
**Fig.2** **(A)** gene expression (mean ± SE) in Ctr; C2C12 Eto+; C2C12 M; C2C12 M Eto+. **(B)** IL-1 beta gene expression (mean ± SE) in Ctr; C2C12 Eto+; C2C12 M; C2C12 M Eto+.

In order to improve the sorting strategy of C2C12, we have set-up a new experiment: briefly, after C2C12 staining with Dil dye as mentioned above, macrophages are stained in suspension with CSFE (a dye able to bind covalently to intracellular proteins) and then co-cultured with myoblasts; through FACS technique, C2C12 and macrophages are separated basing on them cell phenotype and different fluorescent labelling.

The figure **3** showed the gating strategies applied to identify and separate the two different cell populations in C2C12 M samples through FACS technique: there have been selected C2C12 positive for Dil dye and Mac's positive for CSFE dye. The figure **3d** showed an intriguing sub-population: a Mac's sub-population that appears to be Dil dye positive ($\rightarrow$).
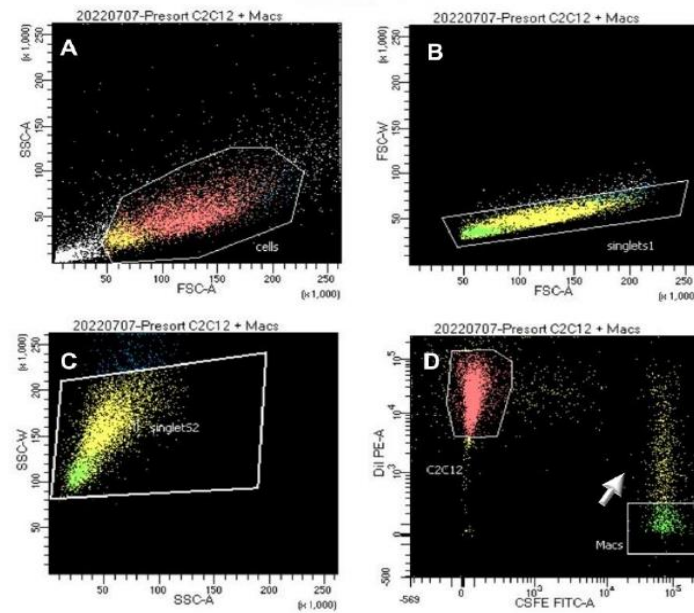
After cell sorting, samples are collected and only C2C12 cells are processed for RT-qPCR. The expression of the following genes is evaluated:

-**MyoD**, as a marker of myoblasts.

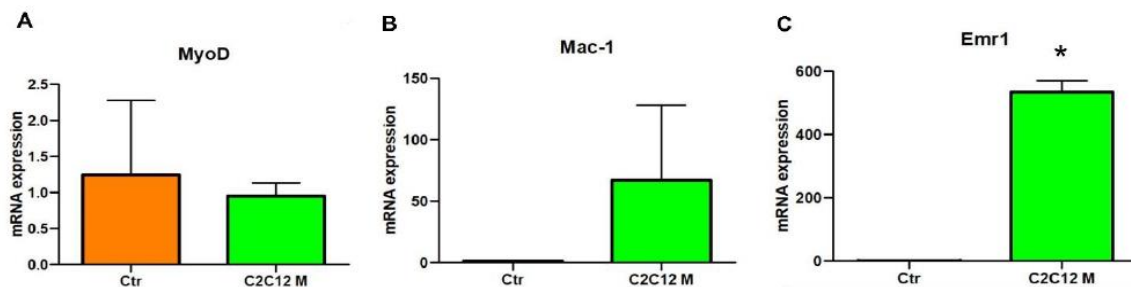-**mac1** and **EMR1**, as markers of macrophages.



**Fig.4** (**A**) MyoD gene expression (mean ± SE) in Ctr; C2C12 M. (**B**) Mac-1 gene expression (mean ± SE) in Ctr; C2C12 M. (**C**) Emr1 gene expression (mean ± SE) in Ctr; C2C12 M.

Although different staining has been adopted for the two cell types, statistical evaluation showed that Emr1 gene expression is significantly higher in C2C12 co-cultured with Ms compared to control (**Fig.4 C**), thus supporting the hypothesis of macrophages persistence in sorted myoblasts.

In order to confirm the data obtained with RT-qPCR, we repeated the last experiment described above but, after FACS, both C2C12 and C2C12 Ms are directly seeded onto 6 well plate, fixed with PFA 4% after 24hours and observed at confocal microscopy.

The observation of samples at confocal microscopy revealed the persistence of macrophages in sorted myoblasts; some of them showed red vesicles inside the cytoplasm, the proof that they ingested some C2C12.

**Conclusion**

Further strategies are needed to better understand the role of Ms when they are co-cultured with C2C12 in presence of DNA damage. In particular, a co-culture system where the two subpopulations are physically separated could be adopted to avoid the contamination, using cell culture inserts. However, it is unclear whether the phagocytic process could happen normally under these conditions.

**MATERIALS AND METHODS**

**Immunohistochemistry reaction**

The same experimental design is adopted for immunohistochemistry reaction.

- C2C12 are stained in plate with 20µL of **Dil dye**.
- The C2C12 are quickly washed, centrifuged, and seeded at **15.000** cells onto glass coverslips previously placed in 24 well plates.
- After 24 hours, C2C12 are treated with a double amount of ETO compared to protocol adopted for RT-qPCR analysis.
- At the same time, the BMDMs are thawed.
- After 6 hours, Ms are stained with 5µL **DiO**, a fluorescent lipophilic dye diluted in 1mL of DMEM. Ms are quickly washed, centrifuged, and seeded at **25.000** cells per well. The plates are incubated overnight at 37°C.
- After 24h, the cells are fixed in PFA 4%.
- The samples are quickly washed in PBS and incubate 15 min at RT in citrate buffer, in order to unmask the nuclear antigen and then, incubated 30 min at RT in PBS containing 10% of horse serum (HS), to prevent the non- specific binding.
- The cells are incubated overnight at 4°C with a rabbit polyclonal antibody recognizing **γH₂AX**, the phosphorylated form of the histone $H_2AX$, as a marker of DSBs, diluted 1:100 in PBS/10%HS.

- After washing in PBS, the samples are incubated for 1h with an Alexa Fluor 647-conjugated donkey anti-rabbit secondary antibody, diluted 1:400 in PBS/10%HS.
- After washing, the cells are stained for 5 min, with DAPI, a nuclear specific dye, mounted in mounting media and observed at confocal microscopy.

**γH₂AX foci counting**

Fluorescent staining of the cell nuclei for γH₂AX allows the quantification of DNA DSB's in C2C12 Eto and C2C12 M Eto+ samples. We define a threshold to consider three categories of DNA damage: n°of foci >5 and <20, as "mild" DNA damage; n°of foci >20, as "strong" DNA damage.

We evaluated in 10 randomly selected fields (10X) per experimental condition the following measurement:

- The percentage of C2C12 with DNA damage;
- The percentage of C2C12 with "mild" and "strong" damage;
- The frequency with which Ms touch C2C12 cells with and without DNA damage, to measure the interactions between the two cell types.

Data are collected and presented in graph with average value. The measurements taken from IHC analysis need to be done in triplicate to perform a significant statistical evaluation.

**Results**

Under confocal fluorescence microscope, γH₂AX positive C2C12 showed red labelled foci in nuclear region; DNA is counterstained in blue (**Fig 5 b-c**). The percentage of C2C12 with DNA damage seemed to increase in C2C12 Ms Eto+ sample in comparison with C2C12 Eto+ (**Fig. 6 a**). However, looking at the extent of damage, C2C12 cells treated with etoposide showed an increased percentage of "mild" and "strong" DNA damage compared with C2C12 M Eto+ sample (**Fig. 6 b**). The rate at which Ms had contact with C2C12 γH₂AX negative seemed to increase when compared to C2C12 γH₂AX positive. In this case the DNA damage may have been already resolved in C2C12 γH₂AX negative and this is why the frequency with which Ms touch C2C12 γH₂AX negative is higher in comparison with C2C12 still damaged (**Fig. 6 c**).
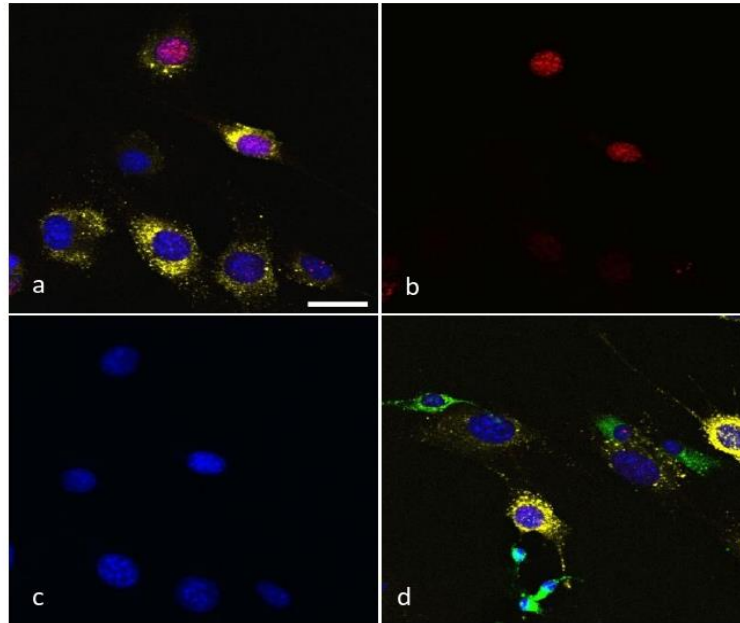
**Fig. 5.** Representative fluorescence microscopy images of C2C12 stained with Dil dye (yellow) (**a**), immunolabelled for γH₂AX (red) (**b**), stained for DNA with DAPI (blue) (**c**), Bar, 100 μm. Representative fluorescence microscopy images of C2C12 touched by macrophages stained with DiO dye (green), (**d**).
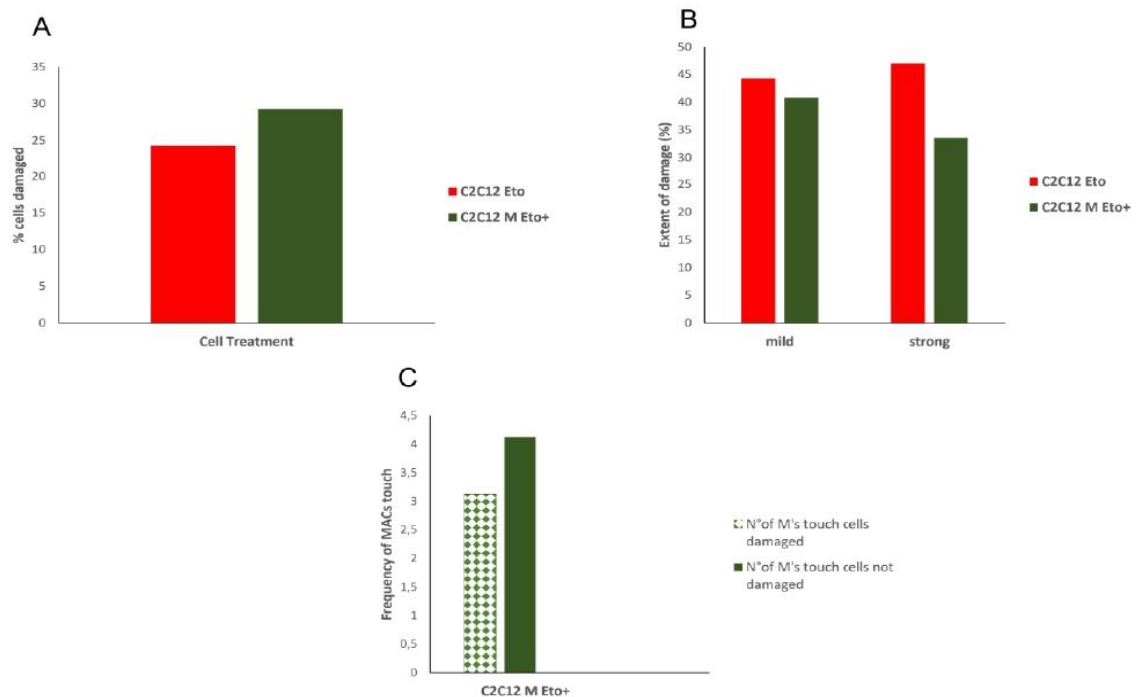


**Fig. 6.** Representative histogram of percentage of C2C12 with DNA damage in C2C12 Eto+ and C2C12 M Eto+ samples (**a**). Representative histogram of the extent of DNA damage expressed as "mild" and "strong" percentage in C2C12 Eto+ and C2C12 M Eto+ samples (**b**). Representative histogram of the frequency with which Ms touch C2C12 cells with and without DNA damage, measured in C2C12 M Eto+ sample (**c**).

**Conclusion**

The measurements taken from IHC analysis need to be done in triplicate to perform a significant statistical evaluation. In this way we will be able to predict the Ms effects on C2C12 with DNA damage.

Moreover, by using different DNA DSB's markers and/or DNA damage response markers, we might measure if they localize in damaged C2C12 nuclei when touched by macrophages, supporting the hypothesis of Ms role in solving the DNA damage on muscle cells.

**References**

1. Suchitra D. Gopinath,Thomas A. Rando. 2008. Stem Cell Review Series: Aging of the skeletal muscle stem cell niche. Volume 7, issue 4; 590-598. https://doi.org/10.1111/j.1474-9726.2008.00399.x

2. Hang Yin, Feodor Price, and Michael A. Rudnicki. 2013. Satellite Cells and the Muscle Stem Cell Niche. Physiol Rev. 93(1): 23–67.doi: 10.1152/physrev.00043.2011

3. Alessandra Sacco, Pier Lorenzo Puri . Regulation and reversibility of muscle satellite cell function in tissue homeostasis and aging. Cell Stem Cell.; 16(6): 585587.doi: 10.1016/j.stem.2015.05.007

4. Juhyun Oh, Yang David Lee, Amy J Wagers. 2014 Stem cell aging: mechanisms, regulators and therapeutic opportunities. Nat Med.; 20(8): 870–880. doi: 10.1038/nm.3651

5. Pedro Sousa-Victor, Susana Gutarra, Laura García-Prat, Javier Rodriguez-Ubreva, Laura Ortet, Vanessa Ruiz-Bonilla, Mercè Jardí, Esteban Ballestar, Susana González, Antonio L. Serrano, Eusebio Perdiguero, Pura Muñoz-Cánoves. 2014. Geriatric muscle stem cells switch reversible quiescence into senescence. *Nature* volume 506, pages316–321.

6. Taylor McNeely, Michael Leone, Hagai Yanai, and Isabel Beerman. 2020. DNA damage in aging, the stem cell perspective. Hum Genet. 139(3): 309–331. doi: 10.1007/s00439-019-02047-z

7. Madaro L, Torcinaro A, De Bardi M, Contino FF, Pelizzola M, Diaferia GR, et al. (2019). Macrophages fine tune satellite cell fate in dystrophic skeletal muscle of mdx mice. PLoS Genet., 15(10): e1008408. https://doi.org/10.1371/ journal.pgen.1008408

8. Neuza S. Sousa, Margarida F. Brás, Inês B. Antunes, Päivi Lindholm, Joana Neves, Pedro Sousa-Victor. Ageing disrupts MANF-mediated immune modulation during skeletal muscle regeneration. doi: https://doi.org/10.1101/2022.07.20.500588

9. Shuen-Ei Chen, Bingwen Jin, Yi-Ping Li Am. 2007 .TNF-α regulates myogenesis and muscle regeneration by activating p38 MAPK J Physiol Cell Physiol., 292(5): C1660–C1671. doi: 10.1152/ajpcell.00486.2006.

10. Angela M. Alvarez, Carlos DeOcesano-Pereira, Catarina Teixeira, Vanessa Moreira. 2020. IL-1β and TNF-α Modulation of Proliferated and Committed Myoblasts: IL-6 and COX-2-Derived Prostaglandins as Key Actors in the Mechanisms Involved. Cells., 9(9): 2005. doi: 10.3390/cells9092005

# *CONCLUDING REMARKS*

# CONCLUDING REMARKS

Skeletal muscle tissue makes up about 45% of the human body contributing to body metabolism and playing a central role in producing movement. This unique plastic tissue is of considerable interest because some of its alterations in molecular and cellular mechanisms are associated with aging and many other muscular diseases. The need to understand the age-associated modifications in muscle structure and function is rising dramatically due to demographic increase of elderly individuals, a condition that implies several consequences in health care services.

Sarcopenia refers to a progressive loss of skeletal muscle mass and strength as individuals age.

Nowadays, the identification of a single risk factor for this condition is still unpredictable due to its "multifactorial" nature.

During the three years of my PhD, I took a multivariate approach to explore the aging of skeletal muscle. Indeed, I combined histochemical techniques at fluorescence microscopy with the high-resolution morphology provided by electron microscopy, to investigate the age-associated alterations of some key components of muscle biology: myonuclei, sarcoplasm and muscle extracellular matrix (ECM). In this thesis, ultrastructural immunocytochemistry of rectus femoris muscle showed that aging induces changes in the distribution and density of nuclear actin, 5-mC, and RNaseA in different sub-nuclear compartments, suggesting impairment of RNA pathways in aged skeletal muscle.

Furthermore, looking at the whole skeletal muscle, I combined our methodological approaches with proteomic analysis to respectively shed light on the structural organization and composition of aged muscle ECM. Observations on gastrocnemius muscle of old (24 months) mice demonstrated that aging is characterized by the accumulation of core molecular components of muscle ECM that mainly interfere in the organization and function of perimysial layer, satellite cells (SCs) microenvironment and basement membrane. These results suggest that age-associated alterations in architecture of muscle ECM may be involved in increased muscle stiffness, reduced activation of SCs and impairment of basement membrane as storage site of bioactive/molecular factors.

Several works stressed the importance of physical exercise to counteract the age-related muscle loss. Thus, physical exercise may represent a promising non-pharmacological approach to slow down sarcopenia in old patients and it could be also combined with pharmacological therapy.

In this regard, I presented in this thesis preliminary results of an ongoing study aimed at exploring the potential effects of mild physical exercise starting at old age on myofibers and muscle ECM network. Morphological and morphometrical evaluations on gastrocnemius muscle of old trained mice (24 months) demonstrated some beneficial responses in myofiber size and subcellular components (e.g., increased mitochondrial density, redistribution of nucleolar subcompartments) in comparison to sedentary control. Moreover, physical exercise was associated to an improved structural organization of muscle ECM network in old trained mice suggesting a more efficient remodelling mechanisms.

The preliminary results presented in this thesis on a nanotechnological approach to treat skeletal muscle aging are encouraging, although further work is necessary to plan translation *in vivo.* Ethosomes (ET) and transethosomes (TET) were investigated as potential carrier to deliver vitamin D3 (VD3) because VD3 deficiency has been related to sarcopenia. Both could be used in principle to this purpose; indeed, neither toxic effects nor subcellular alterations have been shown. Despite both types of nanoparticles proved to be promising VD3 carriers, further studies are necessary to investigate their internalisation and cellular response when loaded with cholecalciferol.

Finally, the research period abroad allowed me to explore the involvement of immune system in aged skeletal muscle, improving my laboratory skills in the field of molecular biology. I collaborated in developing a co-culture system containing muscle cells and primary macrophages to study their interplay when the muscle cells were harmed. The aim of this project was to mimic *in vitro* two altered conditions linked to skeletal muscle aging: the accumulation of DNA damage in muscle cells and the scarcity of macrophages. Although the co-culture system needs further technical improvements, it is a promising strategy aimed also at avoiding experiments involving animals.

# REFERENCES

1. Cruz-Jentoft, A.J. and A.A. Sayer, *Sarcopenia.* Lancet, 2019. **393**(10191): p. 2636-2646.
2. Curcio, F., et al., *Biomarkers in sarcopenia: A multifactorial approach.* Exp Gerontol, 2016. **85**: p. 1-8.
3. Supriya, R., et al., *A Multifactorial Approach for Sarcopenia Assessment: A Literature Review.* Biology (Basel), 2021. **10**(12).
4. Cruz-Jentoft, A.J., et al., *Sarcopenia: revised European consensus on definition and diagnosis.* Age Ageing, 2019. **48**(1): p. 16-31.
5. Giovannini, S., et al., *Sarcopenia: Diagnosis and Management, State of the Art and Contribution of Ultrasound.* J Clin Med, 2021. **10**(23).
6. Rosenberg, I.H., *Sarcopenia: origins and clinical relevance.* Clin Geriatr Med, 2011. **27**(3): p. 337-9.
7. Falcon, L.J. and M.O. Harris-Love, *Sarcopenia and the New ICD-10-CM Code: Screening, Staging, and Diagnosis Considerations.* Fed Pract, 2017. **34**(7): p. 24-32.
8. Dao, T., et al., *Sarcopenia and Muscle Aging: A Brief Overview.* Endocrinol Metab (Seoul), 2020. **35**(4): p. 716-732.
9. Moreira-Pais, A., et al., *A neuromuscular perspective of sarcopenia pathogenesis: deciphering the signaling pathways involved.* Geroscience, 2022. **44**(3): p. 1199-1213.
10. Franceschi, C., et al., *Inflamm-aging. An evolutionary perspective on immunosenescence.* Ann N Y Acad Sci, 2000. **908**: p. 244-54.
11. Priego, T., et al., *Role of hormones in sarcopenia.* Vitam Horm, 2021. **115**: p. 535-570.
12. Nelke, C., et al., *Skeletal muscle as potential central link between sarcopenia and immune senescence.* EBioMedicine, 2019. **49**: p. 381-388.
13. Liguori, I., et al., *Sarcopenia: assessment of disease burden and strategies to improve outcomes.* Clin Interv Aging, 2018. **13**: p. 913-927.
14. Tieland, M., I. Trouwborst, and B.C. Clark, *Skeletal muscle performance and ageing.* J Cachexia Sarcopenia Muscle, 2018. **9**(1): p. 3-19.
15. Ali, S. and J.M. Garcia, *Sarcopenia, cachexia and aging: diagnosis, mechanisms and therapeutic options - a mini-review.* Gerontology, 2014. **60**(4): p. 294-305.
16. Coen, P.M., et al., *Mitochondria as a Target for Mitigating Sarcopenia.* Front Physiol, 2018. **9**: p. 1883.
17. Pegoraro, G. and T. Misteli, *The central role of chromatin maintenance in aging.* Aging (Albany NY), 2009. **1**(12): p. 1017-22.
18. Lacavalla, M.A., et al., *Ultrastructural immunocytochemistry shows impairment of RNA pathways in skeletal muscle nuclei of old mice: A link to sarcopenia?* Eur J Histochem, 2021. **65**(2).
19. Alway, S.E., M.J. Myers, and J.S. Mohamed, *Regulation of satellite cell function in sarcopenia.* Front Aging Neurosci, 2014. **6**: p. 246.
20. Ziaaldini, M.M., et al., *Biochemical Pathways of Sarcopenia and Their Modulation by Physical Exercise: A Narrative Review.* Front Med (Lausanne), 2017. **4**: p. 167.

21. Schiaffino, S. and C. Reggiani, *Fiber types in mammalian skeletal muscles.* Physiol Rev, 2011. **91**(4): p. 1447-531.
22. de Rezende Pinto, W.B., P.V. de Souza, and A.S. Oliveira, *Normal muscle structure, growth, development, and regeneration.* Curr Rev Musculoskelet Med, 2015. **8**(2): p. 176-81.
23. Lang, T., et al., *Sarcopenia: etiology, clinical consequences, intervention, and assessment.* Osteoporos Int, 2010. **21**(4): p. 543-59.
24. Talbot, J. and L. Maves, *Skeletal muscle fiber type: using insights from muscle developmental biology to dissect targets for susceptibility and resistance to muscle disease.* Wiley Interdiscip Rev Dev Biol, 2016. **5**(4): p. 518-34.
25. Nilwik, R., et al., *The decline in skeletal muscle mass with aging is mainly attributed to a reduction in type II muscle fiber size.* Exp Gerontol, 2013. **48**(5): p. 492-8.
26. Lexell, J., *Human aging, muscle mass, and fiber type composition.* J Gerontol A Biol Sci Med Sci, 1995. **50 Spec No**: p. 11-6.
27. Perkisas, S., et al., *Physiological and architectural changes in the ageing muscle and their relation to strength and function in sarcopenia.* European Geriatric Medicine, 2016. **7**.
28. Rowan, S.L., et al., *Denervation causes fiber atrophy and myosin heavy chain co-expression in senescent skeletal muscle.* PLoS One, 2012. **7**(1): p. e29082.
29. Larsson, L., et al., *Sarcopenia: Aging-Related Loss of Muscle Mass and Function.* Physiol Rev, 2019. **99**(1): p. 427-511.
30. Brook, M.S., et al., *Skeletal muscle homeostasis and plasticity in youth and ageing: impact of nutrition and exercise.* Acta Physiol (Oxf), 2016. **216**(1): p. 15-41.
31. Ferri, E., et al., *Role of Age-Related Mitochondrial Dysfunction in Sarcopenia.* Int J Mol Sci, 2020. **21**(15).
32. Spinelli, J.B. and M.C. Haigis, *The multifaceted contributions of mitochondria to cellular metabolism.* Nat Cell Biol, 2018. **20**(7): p. 745-754.
33. López-Otín, C., et al., *The hallmarks of aging.* Cell, 2013. **153**(6): p. 1194-217.
34. Bellanti, F., A. Lo Buglio, and G. Vendemiale, *Mitochondrial Impairment in Sarcopenia.* Biology (Basel), 2021. **10**(1).
35. Hiona, A. and C. Leeuwenburgh, *The role of mitochondrial DNA mutations in aging and sarcopenia: implications for the mitochondrial vicious cycle theory of aging.* Exp Gerontol, 2008. **43**(1): p. 24-33.
36. Scarpulla, R.C., R.B. Vega, and D.P. Kelly, *Transcriptional integration of mitochondrial biogenesis.* Trends Endocrinol Metab, 2012. **23**(9): p. 459-66.
37. Sun, N., R.J. Youle, and T. Finkel, *The Mitochondrial Basis of Aging.* Mol Cell, 2016. **61**(5): p. 654-666.
38. Costanzo, M., Cisterna, B., & Malatesta, M. (2013). Effect of physical exercise on the ultrastructural features of skeletal muscle mitochondria in old mice. Microscopie, 20(2), 37–43. https://doi.org/10.4081/microscopie.2013.4988
39. Van Remmen, H. and A. Richardson, *Oxidative damage to mitochondria and aging.* Exp Gerontol, 2001. **36**(7): p. 957-68.
40. Picard, M., K. White, and D.M. Turnbull, *Mitochondrial morphology, topology, and membrane interactions in skeletal muscle: a quantitative three-dimensional electron microscopy study.* J Appl Physiol (1985), 2013. **114**(2): p. 161-71.

41.     Müller, W., *Subsarcolemmal mitochondria and capillarization of soleus muscle fibers in young rats subjected to an endurance training. A morphometric study of semithin sections.* Cell Tissue Res, 1976. **174**(3): p. 367-89.

42.     Willingham, T.B., P.T. Ajayi, and B. Glancy, *Subcellular Specialization of Mitochondrial Form and Function in Skeletal Muscle Cells.* Front Cell Dev Biol, 2021. **9**: p. 757305.

43.     Joseph, A.M., et al., *The impact of aging on mitochondrial function and biogenesis pathways in skeletal muscle of sedentary high- and low-functioning elderly individuals.* Aging Cell, 2012. **11**(5): p. 801-9.

44.     Sakuma, K. and A. Yamaguchi, *Sarcopenic obesity and endocrinal adaptation with age.* Int J Endocrinol, 2013. **2013**: p. 204164.

45.     Petersen, K.F., et al., *Impaired mitochondrial activity in the insulin-resistant offspring of patients with type 2 diabetes.* N Engl J Med, 2004. **350**(7): p. 664-71.

46.     Halestrap, A.P. and J.L. Dunlop, *Intramitochondrial regulation of fatty acid beta-oxidation occurs between flavoprotein and ubiquinone. A role for changes in the matrix volume.* Biochem J, 1986. **239**(3): p. 559-65.

47.     Malatesta, M., et al., *Fine structural modifications of liver, pancreas and brown adipose tissue mitochondria from hibernating, arousing and euthermic dormice.* Cell Biol Int, 2001. **25**(2): p. 131-8.

48.     Marzetti, E. and C. Leeuwenburgh, *Skeletal muscle apoptosis, sarcopenia and frailty at old age.* Exp Gerontol, 2006. **41**(12): p. 1234-8.

49.     Attaix, D., et al., *Altered responses in skeletal muscle protein turnover during aging in anabolic and catabolic periods.* Int J Biochem Cell Biol, 2005. **37**(10): p. 1962-73.

50.     Murton, A.J., *Muscle protein turnover in the elderly and its potential contribution to the development of sarcopenia.* Proc Nutr Soc, 2015. **74**(4): p. 387-96.

51.     Churchward-Venne, T.A., L. Breen, and S.M. Phillips, *Alterations in human muscle protein metabolism with aging: Protein and exercise as countermeasures to offset sarcopenia.* Biofactors, 2014. **40**(2): p. 199-205.

52.     Gumucio, J.P. and C.L. Mendias, *Atrogin-1, MuRF-1, and sarcopenia.* Endocrine, 2013. **43**(1): p. 12-21.

53.     Altun, M., et al., *Muscle wasting in aged, sarcopenic rats is associated with enhanced activity of the ubiquitin proteasome pathway.* J Biol Chem, 2010. **285**(51): p. 39597-608.

54.     Hornsby, P.J., *Genes, hormones, and aging.* Mol Cell Endocrinol, 1991. **80**(1-3): p. C175-80.

55.     Falcone, C. and C. Mazzoni, *RNA stability and metabolism in regulated cell death, aging and diseases.* FEMS Yeast Res, 2018. **18**(6).

56.     Meshorer, E. and H. Soreq, *Pre-mRNA splicing modulations in senescence.* Aging Cell, 2002. **1**(1): p. 10-6.

57.     Fakan, S., *Ultrastructural cytochemical analyses of nuclear functional architecture.* Eur J Histochem, 2004. **48**(1): p. 5-14.

58.     Cmarko, D., et al., *Ultrastructural analysis of transcription and splicing in the cell nucleus after bromo-UTP microinjection.* Mol Biol Cell, 1999. **10**(1): p. 211-23.

59.     Puvion, E. and F. Puvion-Dutilleul, *Ultrastructure of the nucleus in relation to transcription and splicing: roles of perichromatin fibrils and interchromatin granules.* Exp Cell Res, 1996. **229**(2): p. 217-25.

60. Malatesta, M., et al., *Nuclei of aged myofibres undergo structural and functional changes suggesting impairment in RNA processing.* Eur J Histochem, 2009. **53**(2): p. e12.

61. Malatesta, M., et al., *Physical training modulates structural and functional features of cell nuclei in type II myofibers of old mice.* Rejuvenation Res, 2011. **14**(5): p. 543-52.

62. Malatesta, M., et al., *Muscleblind-like1 undergoes ectopic relocation in the nuclei of skeletal muscles in myotonic dystrophy and sarcopenia.* Eur J Histochem, 2013. **57**(2): p. e15.

63. Fuchs, E. and H.M. Blau, *Tissue Stem Cells: Architects of Their Niches.* Cell Stem Cell, 2020. **27**(4): p. 532-556.

64. Hong, X., et al., *Stem cell aging in the skeletal muscle: The importance of communication.* Ageing Res Rev, 2022. **73**: p. 101528.

65. Price, F.D., et al., *Inhibition of JAK-STAT signaling stimulates adult satellite cell function.* Nat Med, 2014. **20**(10): p. 1174-81.

66. Baghdadi, M.B., et al., *Reciprocal signalling by Notch-Collagen V-CALCR retains muscle stem cells in their niche.* Nature, 2018. **557**(7707): p. 714-718.

67. Muñoz-Cánoves, P., J. Neves, and P. Sousa-Victor, *Understanding muscle regenerative decline with aging: new approaches to bring back youthfulness to aged stem cells.* Febs j, 2020. **287**(3): p. 406-416.

68. Oh, J., Y.D. Lee, and A.J. Wagers, *Stem cell aging: mechanisms, regulators and therapeutic opportunities.* Nat Med, 2014. **20**(8): p. 870-80.

69. Sinha, M., et al., *Restoring systemic GDF11 levels reverses age-related dysfunction in mouse skeletal muscle.* Science, 2014. **344**(6184): p. 649-52.

70. Rogakou, E.P., et al., *DNA double-stranded breaks induce histone H2AX phosphorylation on serine 139.* J Biol Chem, 1998. **273**(10): p. 5858-68.

71. Sousa-Victor, P., et al., *Geriatric muscle stem cells switch reversible quiescence into senescence.* Nature, 2014. **506**(7488): p. 316-21.

72. McNeely, T., et al., *DNA damage in aging, the stem cell perspective.* Hum Genet, 2020. **139**(3): p. 309-331.

73. Conboy, I.M., et al., *Rejuvenation of aged progenitor cells by exposure to a young systemic environment.* Nature, 2005. **433**(7027): p. 760-4.

74. Conboy, I.M. and T.A. Rando, *Aging, stem cells and tissue regeneration: lessons from muscle.* Cell Cycle, 2005. **4**(3): p. 407-10.

75. Neves, J., P. Sousa-Victor, and H. Jasper, *Rejuvenating Strategies for Stem Cell-Based Therapies in Aging.* Cell Stem Cell, 2017. **20**(2): p. 161-175.

76. Yin, H., F. Price, and M.A. Rudnicki, *Satellite cells and the muscle stem cell niche.* Physiol Rev, 2013. **93**(1): p. 23-67.

77. Chen, S.E., B. Jin, and Y.P. Li, *TNF-alpha regulates myogenesis and muscle regeneration by activating p38 MAPK.* Am J Physiol Cell Physiol, 2007. **292**(5): p. C1660-71.

78. Alvarez, A.M., et al., *IL-1ϐ and TNF-α Modulation of Proliferated and Committed Myoblasts: IL-6 and COX-2-Derived Prostaglandins as Key Actors in the Mechanisms Involved.* Cells, 2020. **9**(9).

79. Madaro, L., et al., *Macrophages fine tune satellite cell fate in dystrophic skeletal muscle of mdx mice.* PLoS Genet, 2019. **15**(10): p. e1008408.

80. Street, S.F., *Lateral transmission of tension in frog myofibers: a myofibrillar network and transverse cytoskeletal connections are possible transmitters.* J Cell Physiol, 1983. **114**(3): p. 346-64.

81.     Calve, S., S.J. Odelberg, and H.G. Simon, *A transitional extracellular matrix instructs cell behavior during muscle regeneration.* Dev Biol, 2010. **344**(1): p. 259-71.

82.     Zhang, W., Y. Liu, and H. Zhang, *Extracellular matrix: an important regulator of cell functions and skeletal muscle development.* Cell Biosci, 2021. **11**(1): p. 65.

83.     Mahdy, M.A.A., *Skeletal muscle fibrosis: an overview.* Cell Tissue Res, 2019. **375**(3): p. 575-588.

84.     Zhou, J., et al., *Elevated H3K27ac in aged skeletal muscle leads to increase in extracellular matrix and fibrogenic conversion of muscle satellite cells.* Aging Cell, 2019. **18**(5): p. e12996.

85.     Lofaro, F.D., et al., *Age-Related Changes in the Matrisome of the Mouse Skeletal Muscle.* Int J Mol Sci, 2021. **22**(19).

86.     Chen, W.J., et al., *Aged Skeletal Muscle Retains the Ability to Remodel Extracellular Matrix for Degradation of Collagen Deposition after Muscle Injury.* Int J Mol Sci, 2021. **22**(4).

87.     Csapo, R., M. Gumpenberger, and B. Wessner, *Skeletal Muscle Extracellular Matrix - What Do We Know About Its Composition, Regulation, and Physiological Roles? A Narrative Review.* Front Physiol, 2020. **11**: p. 253.

88.     Wood, L.K., et al., *Intrinsic stiffness of extracellular matrix increases with age in skeletal muscles of mice.* J Appl Physiol (1985), 2014. **117**(4): p. 363-9.

89.     Lacraz, G., et al., *Increased Stiffness in Aged Skeletal Muscle Impairs Muscle Progenitor Cell Proliferative Activity.* PLoS One, 2015. **10**(8): p. e0136217.

90.     Stearns-Reider, K.M., et al., *Aging of the skeletal muscle extracellular matrix drives a stem cell fibrogenic conversion.* Aging Cell, 2017. **16**(3): p. 518-528.

91.     Olson, L.C., et al., *Advanced Glycation End-Products in Skeletal Muscle Aging.* Bioengineering (Basel), 2021. **8**(11).

92.     Woodley, D.T., et al., *Interactions of basement membrane components.* Biochim Biophys Acta, 1983. **761**(3): p. 278-83.

93.     Kovanen, V., et al., *Type IV collagen and laminin in slow and fast skeletal muscle in rats--effects of age and life-time endurance training.* Coll Relat Res, 1988. **8**(2): p. 145-53.

94.     Brack, A.S., et al., *Increased Wnt signaling during aging alters muscle stem cell fate and increases fibrosis.* Science, 2007. **317**(5839): p. 807-10.

95.     Alexakis, C., T. Partridge, and G. Bou-Gharios, *Implication of the satellite cell in dystrophic muscle fibrosis: a self-perpetuating mechanism of collagen overproduction.* Am J Physiol Cell Physiol, 2007. **293**(2): p. C661-9.

96.     Sanes, J.R., *The basement membrane/basal lamina of skeletal muscle.* J Biol Chem, 2003. **278**(15): p. 12601-4.

97.     Sousa, N.S., et al., *Ageing disrupts MANF-mediated immune modulation during skeletal muscle regeneration.* bioRxiv, 2022: p. 2022.07.20.500588.

98.     Gopinath, S.D. and T.A. Rando, *Stem cell review series: aging of the skeletal muscle stem cell niche.* Aging Cell, 2008. **7**(4): p. 590-8.

99.     Sousa-Victor, P., L. García-Prat, and P. Muñoz-Cánoves, *Control of satellite cell function in muscle regeneration and its disruption in ageing.* Nat Rev Mol Cell Biol, 2022. **23**(3): p. 204-226.

100.    Chazaud, B., *Inflammation and Skeletal Muscle Regeneration: Leave It to the Macrophages!* Trends Immunol, 2020. **41**(6): p. 481-492.

101. Perdiguero, E., et al., *p38/MKP-1-regulated AKT coordinates macrophage transitions and resolution of inflammation during tissue repair.* J Cell Biol, 2011. **195**(2): p. 307-22.

102. Tidball, J.G., et al., *Aging of the immune system and impaired muscle regeneration: A failure of immunomodulation of adult myogenesis.* Exp Gerontol, 2021. **145**: p. 111200.

103. Sorensen, J.R., et al., *An altered response in macrophage phenotype following damage in aged human skeletal muscle: implications for skeletal muscle repair.* Faseb j, 2019. **33**(9): p. 10353-10368.

104. Wang, Y., et al., *Aging of the immune system causes reductions in muscle stem cell populations, promotes their shift to a fibrogenic phenotype, and modulates sarcopenia.* Faseb j, 2019. **33**(1): p. 1415-1427.

105. Landi, F., et al., *Exercise as a remedy for sarcopenia.* Curr Opin Clin Nutr Metab Care, 2014. **17**(1): p. 25-31.

106. Goodpaster, B.H., et al., *Effects of physical activity on strength and skeletal muscle fat infiltration in older adults: a randomized controlled trial.* J Appl Physiol (1985), 2008. **105**(5): p. 1498-503.

107. Cisterna, B., et al., *Adapted physical exercise enhances activation and differentiation potential of satellite cells in the skeletal muscle of old mice.* J Anat, 2016. **228**(5): p. 771-83.

108. Gosselin, L.E., et al., *Effect of exercise training on passive stiffness in locomotor skeletal muscle: role of extracellular matrix.* J Appl Physiol (1985), 1998. **85**(3): p. 1011-6.

109. Lavin, K.M., et al., *Effects of aging and lifelong aerobic exercise on basal and exercise-induced inflammation.* J Appl Physiol (1985), 2020. **128**(1): p. 87-99.

110. Landi, F., et al., *Anorexia of Aging: Assessment and Management.* Clin Geriatr Med, 2017. **33**(3): p. 315-323.

111. Briefel, R.R., et al., *Total energy intake of the US population: the third National Health and Nutrition Examination Survey, 1988-1991.* Am J Clin Nutr, 1995. **62**(5 Suppl): p. 1072s-1080s.

112. Landi, F., et al., *Protein Intake and Muscle Health in Old Age: From Biological Plausibility to Clinical Evidence.* Nutrients, 2016. **8**(5).

113. Gaffney-Stomberg, E., et al., *Increasing dietary protein requirements in elderly people for optimal muscle and bone health.* J Am Geriatr Soc, 2009. **57**(6): p. 1073-9.

114. Calvani, R., et al., *Current nutritional recommendations and novel dietary strategies to manage sarcopenia.* J Frailty Aging, 2013. **2**(1): p. 38-53.

115. Dawson-Hughes, B., *Vitamin D and muscle function.* J Steroid Biochem Mol Biol, 2017. **173**: p. 313-316.

116. Uchitomi, R., M. Oyabu, and Y. Kamei, *Vitamin D and Sarcopenia: Potential of Vitamin D Supplementation in Sarcopenia Prevention and Treatment.* Nutrients, 2020. **12**(10).

117. Abiri, B. and M. Vafa, *Vitamin D and Muscle Sarcopenia in Aging.* Methods Mol Biol, 2020. **2138**: p. 29-47.

118. Costanzo, M., et al., *Formulative Study and Intracellular Fate Evaluation of Ethosomes and Transethosomes for Vitamin D3 Delivery.* Int J Mol Sci, 2021. **22**(10).

119.    Yoshimura, Y., et al., *Interventions for Treating Sarcopenia: A Systematic Review and Meta-Analysis of Randomized Controlled Studies.* J Am Med Dir Assoc, 2017. **18**(6): p. 553.e1-553.e16.

120.    Marzetti, E., et al., *The "Sarcopenia and Physical fRailty IN older people: multi-componenT Treatment strategies" (SPRINTT) randomized controlled trial: Case finding, screening and characteristics of eligible participants.* Exp Gerontol, 2018. **113**: p. 48-57.

121.    Rosenthal, N. and S. Brown, *The mouse ascending: perspectives for human-disease models.* Nat Cell Biol, 2007. **9**(9): p. 993-9.

122.    Dutta, S. and P. Sengupta, *Men and mice: Relating their ages.* Life Sci, 2016. **152**: p. 244-8.

123.    Xie, W.Q., et al., *Mouse models of sarcopenia: classification and evaluation.* J Cachexia Sarcopenia Muscle, 2021. **12**(3): p. 538-554.

124.    Pasquali, P., *The importance of animal models in research.* Res Vet Sci, 2018. **118**: p. 144-145.

125.    Liu, E.T., et al., *Of mice and CRISPR: The post-CRISPR future of the mouse as a model system for the human condition.* EMBO Rep, 2017. **18**(2): p. 187-193.

126.    Baek, K.W., et al., *Rodent Model of Muscular Atrophy for Sarcopenia Study.* J Bone Metab, 2020. **27**(2): p. 97-110.

127.    Christian, C.J. and G.M. Benian, *Animal models of sarcopenia.* Aging Cell, 2020. **19**(10): p. e13223.

128.    Tournadre, A., et al., *Sarcopenia.* Joint Bone Spine, 2019. **86**(3): p. 309-314.

129.    Mitchell, S.J., et al., *Animal models of aging research: implications for human aging and age-related diseases.* Annu Rev Anim Biosci, 2015. **3**: p. 283-303.

130.    Azzu, V. and T.G. Valencak, *Energy Metabolism and Ageing in the Mouse: A Mini-Review.* Gerontology, 2017. **63**(4): p. 327-336.

131.    Kim, C. and J.K. Hwang, *The 5,7-Dimethoxyflavone Suppresses Sarcopenia by Regulating Protein Turnover and Mitochondria Biogenesis-Related Pathways.* Nutrients, 2020. **12**(4).

132.    Kadoguchi, T., et al., *Promotion of oxidative stress is associated with mitochondrial dysfunction and muscle atrophy in aging mice.* Geriatr Gerontol Int, 2020. **20**(1): p. 78-84.

133.    Mankhong, S., et al., *Experimental Models of Sarcopenia: Bridging Molecular Mechanism and Therapeutic Strategy.* Cells, 2020. **9**(6).

134.    Baek, K.W., et al., *Two Types of Mouse Models for Sarcopenia Research: Senescence Acceleration and Genetic Modification Models.* J Bone Metab, 2021. **28**(3): p. 179-191.

135.    Cannon, C.M., et al., *A novel combination of methods to assess sarcopenia and muscle performance in mice.* Biomed Sci Instrum, 2005. **41**: p. 116-21.

136.    Cohen, S., J.A. Nathan, and A.L. Goldberg, *Muscle wasting in disease: molecular mechanisms and promising therapies.* Nat Rev Drug Discov, 2015. **14**(1): p. 58-74.

137.    Justice, M.J. and P. Dhillon, *Using the mouse to model human disease: increasing validity and reproducibility.* Dis Model Mech, 2016. **9**(2): p. 101-3.

138.    Vanhooren, V. and C. Libert, *The mouse as a model organism in aging research: usefulness, pitfalls and possibilities.* Ageing Res Rev, 2013. **12**(1): p. 8-21.

139.    Kalache, A. and A. Gatti, *Active ageing: a policy framework.* Adv Gerontol, 2003. **11**: p. 7-18.

140.    Balls, M., *It's Time to Reconsider The Principles of Humane Experimental Technique.* Altern Lab Anim, 2020. **48**(1): p. 40-46.

141.    Sikes, R.S., *2016 Guidelines of the American Society of Mammalogists for the use of wild mammals in research and education.* J Mammal, 2016. **97**(3): p. 663-688.

142.    Favero, G., et al., *A comparison of melatonin and α-lipoic acid in the induction of antioxidant defences in L6 rat skeletal muscle cells.* Age (Dordr), 2015. **37**(4): p. 9824.

143.    Strohman, R.C., et al., *Cell fusion and terminal differentiation of myogenic cells in culture.* J Anim Sci, 1974. **38**(5): p. 1103-10.

144.    Carter, S. and T.P.J. Solomon, *In vitro experimental models for examining the skeletal muscle cell biology of exercise: the possibilities, challenges and future developments.* Pflugers Arch, 2019. **471**(3): p. 413-429.

145.    Moustogiannis, A., et al., *Characterization of Optimal Strain, Frequency and Duration of Mechanical Loading on Skeletal Myotubes' Biological Responses.* In Vivo, 2020. **34**(4): p. 1779-1788.

146.    Morgan, J.E. and T.A. Partridge, *Muscle satellite cells.* Int J Biochem Cell Biol, 2003. **35**(8): p. 1151-6.

147.    Moustogiannis, A., et al., *The Effects of Muscle Cell Aging on Myogenesis.* Int J Mol Sci, 2021. **22**(7).

148.    Taye, N., S. Stanley, and D. Hubmacher, *Stable Knockdown of Genes Encoding Extracellular Matrix Proteins in the C2C12 Myoblast Cell Line Using Small-Hairpin (sh)RNA.* J Vis Exp, 2020(156).

149.    Liang, R., et al., *Modeling Myotonic Dystrophy 1 in C2C12 Myoblast Cells.* J Vis Exp, 2016(113).

150.    Arifuzzaman, M., et al., *Fabricating Muscle-Neuron Constructs with Improved Contractile Force Generation.* Tissue Eng Part A, 2019. **25**(7-8): p. 563-574.

151.    Venter, C. and C. Niesler, *A triple co-culture method to investigate the effect of macrophages and fibroblasts on myoblast proliferation and migration.* Biotechniques, 2018. **64**(2): p. 52-58.

152.    Bareja, A., et al., *Human and mouse skeletal muscle stem cells: convergent and divergent mechanisms of myogenesis.* PLoS One, 2014. **9**(2): p. e90398.

153.    Brzeszczyńska, J., et al., *Alterations in the in vitro and in vivo regulation of muscle regeneration in healthy ageing and the influence of sarcopenia.* J Cachexia Sarcopenia Muscle, 2018. **9**(1): p. 93-105.

154.    Kim, J.A., et al., *Sinensetin regulates age-related sarcopenia in cultured primary thigh and calf muscle cells.* BMC Complement Altern Med, 2019. **19**(1): p. 287.

155.    Urban, R.J., et al., *Translational studies in older men using testosterone to treat sarcopenia.* Trans Am Clin Climatol Assoc, 2014. **125**: p. 27-42; discussion 42-4.

156.    Murgia, M., et al., *Single Muscle Fiber Proteomics Reveals Fiber-Type-Specific Features of Human Muscle Aging.* Cell Rep, 2017. **19**(11): p. 2396-2409.

# APPENDICES

# APPENDICES

During my doctoral program, in addition to my main research topic, I was also involved in collaborative studies of different subjects. My contribution consisted in the application of morphological, cytochemical and immunocytochemical techniques at the light and electron microscopy level.

In the first (Cisterna et al., 2021) and second work (Lacavalla et al., 2022), we expanded previous studies in collaboration with Dr. Gabriele Tabaracci (San Rocco Clinic, Montichiari, BS, Italy) in order to investigate the cellular and molecular effects of exposure to low ozone concentration respectively on fibroblast and HMC3 cell lines. The multimodal approaches used in these studies aimed at exploring a panel of cell structural and functional features, combining light and electron microscopy, Western blot analysis, real-time quantitative polymerase chain reaction, and multiplex assays for cytokines.

In the last work (Andreana et al., 2022), performed in collaboration with the research group led by Prof.ssa Barbara Stella (Department of Drug Science and Technology, University of Torino, Italy), ultrastructural and morphological observation were performed in order to: i) assess the targeting ability of PLGA nanoparticels associated with a derivate of L-carnitine; ii) understand the NP's cellar uptake in C2C12 myoblasts and myotubes.

The articles in this thesis have been reproduced with the permission of the publisher.

*Article*

# Low Ozone Concentrations Differentially Affect the Structural and Functional Features of Non-Activated and Activated Fibroblasts In Vitro

**Barbara Cisterna** [1], **Manuela Costanzo** [1], **Maria Assunta Lacavalla** [1], **Mirco Galiè** [1], **Osvaldo Angelini** [2], **Gabriele Tabaracci** [2] **and Manuela Malatesta** [1,*]

[1] Department of Neurosciences, Biomedicine and Movement Sciences, Anatomy and Histology Section, University of Verona, Strada Le Grazie 8, I-37134 Verona, Italy; barbara.cisterna@univr.it (B.C.); manuela.costanzo@univr.it (M.C.); mariaassunta.lacavalla@univr.it (M.A.L.); mirco.galie@univr.it (M.G.)

[2] San Rocco Clinic, Via Monsignor G.V. Moreni 95, I-25018 Montichari, Italy; osva.ange@virgilio.it (O.A.); tabaracci@sanrocco.net (G.T.)

*   Correspondence: manuela.malatesta@univr.it

**Abstract:** Oxygen–ozone ($O_2$–$O_3$) therapy is increasingly applied as a complementary/adjuvant treatment for several diseases; however, the biological mechanisms accounting for the efficacy of low $O_3$ concentrations need further investigations to understand the possibly multiple effects on the different cell types. In this work, we focused our attention on fibroblasts as ubiquitous connective cells playing roles in the body architecture, in the homeostasis of tissue-resident cells, and in many physiological and pathological processes. Using an established human fibroblast cell line as an in vitro model, we adopted a multimodal approach to explore a panel of cell structural and functional features, combining light and electron microscopy, Western blot analysis, real-time quantitative polymerase chain reaction, and multiplex assays for cytokines. The administration of $O_2$–$O_3$ gas mixtures induced multiple effects on fibroblasts, depending on their activation state: in non-activated fibroblasts, $O_3$ stimulated proliferation, formation of cell surface protrusions, antioxidant response, and IL-6 and TGF-β1 secretion, while in LPS-activated fibroblasts, $O_3$ stimulated only antioxidant response and cytokines secretion. Therefore, the low $O_3$ concentrations used in this study induced activation-like responses in non-activated fibroblasts, whereas in already activated fibroblasts, the cell protective capability was potentiated.

**Keywords:** oxygen–ozone therapy; cell proliferation; cell surface protrusions; nuclear factor erythroid 2-related factor 2 (Nrf2); heme oxygenase 1 (Hmox1) gene; interleukin-6; transforming growth factor (TGF)-β1; fluorescence microscopy; scanning electron microscopy; real-time quantitative polymerase chain reaction (RT-qPCR)

## 1. Introduction

In the last decades, the medical use of gaseous ozone ($O_3$) has been progressively increasing as a complementary/adjuvant treatment for several diseases [1–4]. $O_3$ is a highly unstable gas rapidly decomposing to oxygen, and it is applied for therapeutic purposes as $O_2$–$O_3$ mixtures with low $O_3$ concentrations. In fact, the mild oxidative stress induced by low doses of $O_3$ activates the nuclear factor erythroid 2-related factor 2 (Nrf2)-mediated Keap1-dependent pathway, which, in turn, stimulates gene expression of antioxidant response elements (ARE) [5–7]. In fact, the exposure to low $O_3$ concentrations promotes an antioxidant cytoprotective response [8,9], which is consistent with the principle of hormesis, i.e., "the beneficial effect of a low-level exposure to an agent that is harmful at high levels" [10].

Despite the wide application of $O_2$–$O_3$ administration in clinical practice, the biological mechanisms accounting for the therapeutic efficacy of $O_3$ have been only partially unveiled,

and further investigations are necessary to understand the multiple effects of this gas on the different cell types in tissues and organs. As an example, appropriate $O_2$–$O_3$ gas mixtures proved to exert an adipogenic effect in human adipose-derived adult stem cells [11] and to reduce lipid loss in explanted adipose tissue [6]. In addition, it has recently been demonstrated that, besides activating an antioxidant response through the Nrf2–ARE pathway, $O_2$–$O_3$ gas mixtures are able to modulate cytokine secretion in T lymphocytes [7].

In the present work, we focused our attention on the fibroblast as a primary target of $O_2$–$O_3$ therapy. In fact, it is worth noting that, whatever the administration route (intramuscular, intra- and peri-articular or subcutaneous injection, topical bagging, rectal or vaginal insufflation, autohemotherapy), $O_2$–$O_3$ mixtures inevitably act on fibroblasts; actually, these are ubiquitous cells playing multiple roles in the architecture of organs and the whole body, in the homeostasis of tissue-resident cells, and in many physiological (e.g., wound healing) and pathological processes, such as autoimmunity, fibrosis, and cancer [12]. It is therefore likely to expect that fibroblasts may be involved in the pathways activated by $O_2$–$O_3$ administration and, in turn, in the therapeutic outcome.

An established human fibroblast cell line was used as a suitable in vitro model to study the response to $O_2$–$O_3$ treatment under strictly controlled experimental conditions. We investigated the structural and functional effects of low $O_3$ concentrations on fibroblasts in non-activated and lipopolysaccharide (LPS)-activated state with the aim to analyze the response of these tissue-resident cells in a steady state or after the response to activating stimuli (as it happens following tissue injury and/or inflammation, when they are committed to restore homeostasis [13]). We used gas mixtures with 10, 20, and 30 µg $O_3$/mL $O_2$—concentrations usually applied in clinical practice. In order to explore a panel of structural and functional cell features, a multimodal approach was adopted, by combining light (bright field and fluorescence) microscopy, scanning electron microscopy (SEM), Western blot analysis, real-time quantitative polymerase chain reaction (RT-qPCR), and multiplex assays for cytokines.

## 2. Results

### 2.1. Cytotoxicity

At 24 h after the gas exposure, the percentage of dead cells (estimated by the LDH release) was similar (<6%) in all samples of non-activated fibroblasts, irrespective of the treatment ($p = 0.77$, Figure 1). Similarly, no difference in cell death was found among the LPS-activated samples ($p = 0.11$; Figure 1). LPS-activated control samples showed a significantly lower value (<2%; $p = 0.02$) in comparison with the non-activated controls.
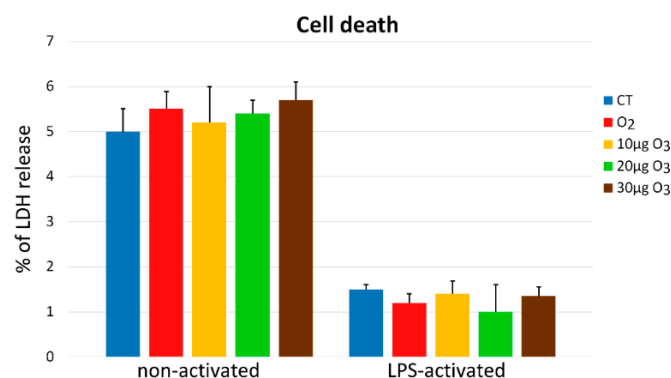


**Figure 1.** Percentages of dead cells (mean values ± SE) 24 h after the treatment (one experiment in triplicate). No significant difference was found among the samples of either group. CT—untreated control.

## 2.2. S-Phase Evaluation

Under a conventional fluorescence microscope, bromodeoxyuridine (BrdU)-positive fibroblasts appeared labelled in green, while DNA was counterstained in blue (Figure 2a–c). At 24 h after the gas treatment, significant difference in the percentage of BrdU-positive cells was found in non-activated fibroblasts ($p = 0.01$); post-hoc analysis revealed that only cells exposed to 10 μg $O_3$ showed a significantly increased proliferation rate in comparison with the controls ($p = 0.04$) (Figure 2d). In LPS-activated fibroblasts, the exposure to $O_2$ or $O_3$ did not alter the percentage of BrdU-positive cells ($p = 0.52$) (Figure 2d). LPS-activated control samples showed a significantly lower cell proliferation in comparison with the non-activated controls ($p < 0.001$).
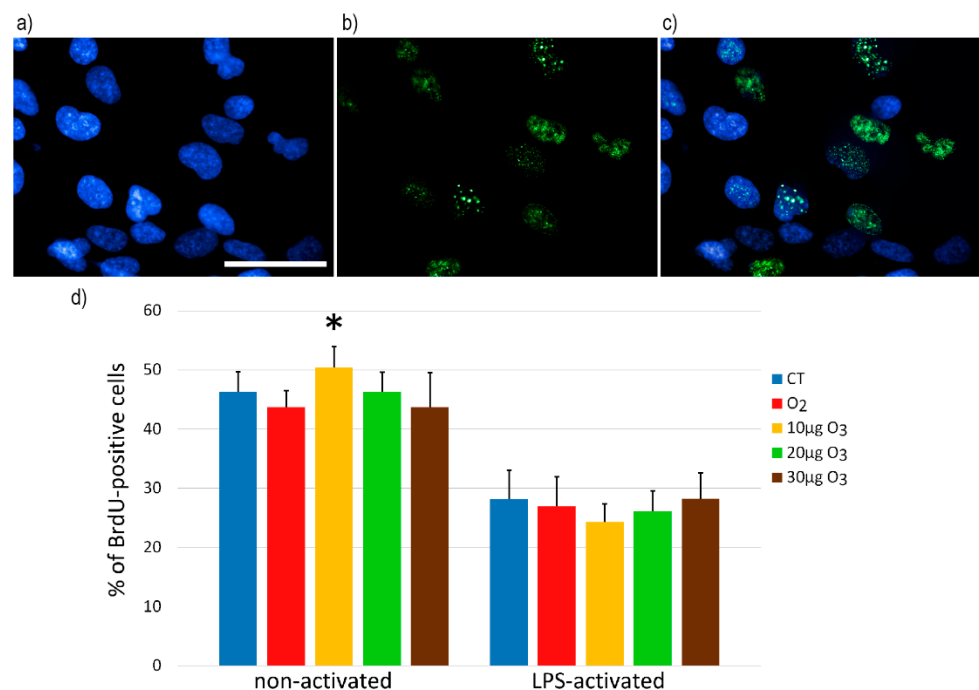


**Figure 2.** (**a**–**c**) Representative fluorescence microscopy images of fibroblasts stained for DNA with Hoechst 33342 (blue) (**a**), immunolabelled for BrdU (green) (**b**), and merged (**c**). Bar, 100 μm. (**d**) Mean values $\pm$ SE of percentages of BrdU-positive cells 24 h after the treatment (one experiment in triplicate). The asterisk (*) indicates significant difference in comparison with the respective control (CT).

## 2.3. Wound Healing Assay

The wound healing assay (representative images in Figure 3a,b) showed similar migration rates in all samples of both non-activated (Figure S1) and LPS-activated (Figure S2) fibroblasts 2 h ($p = 0.21$ and $p = 0.33$, respectively) and 6 h ($p = 0.06$ and $p = 0.76$, respectively) (Figure 3c,d) after gas exposure. After 24 h, the wound was completely healed in all samples (not shown).
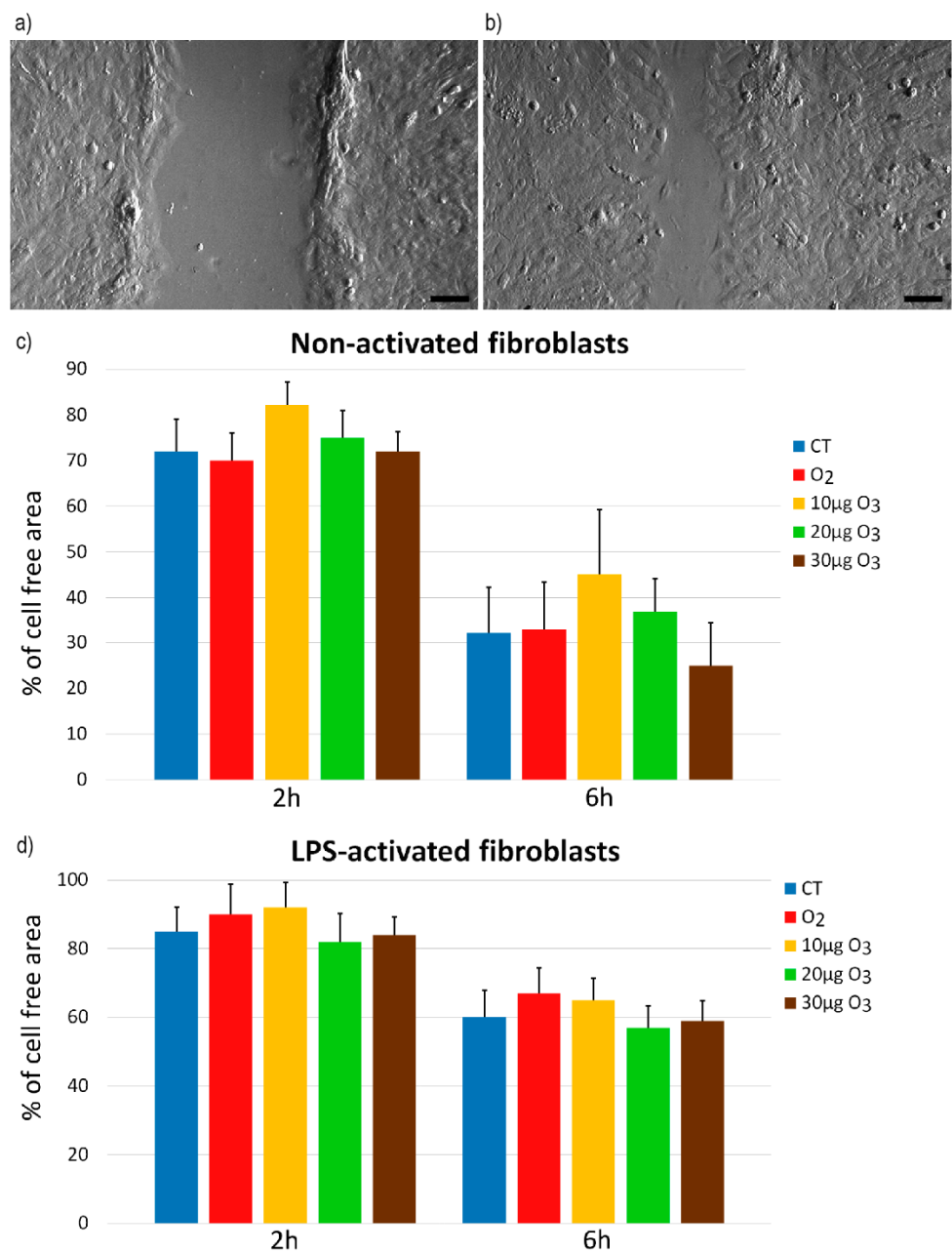
**Figure 3.** (**a**,**b**) Representative inverted microscope images of fibroblasts at 2 h (**a**) and 6 h (**b**) of the wound healing assay. Bars, 200 μm. (**c**,**d**) Means ± SE of percentages of cell-free areas of control (CT), $O_2$- and $O_3$-treated non-activated (**c**) and LPS-activated (**d**) fibroblasts at 2 h and 6 h of the wound healing assay (three experiments). No statistical difference was found for both non-activated and LPS-activated samples.

### 2.4. Scanning Electron Microscopy

In non-activated condition, control and $O_2$-treated fibroblasts appeared flattened and irregularly polygonal in shape, with scarce filamentous protrusions of the cell surface (Figure 4a,b). $O_3$-treated fibroblasts maintained the polygonal shape but showed an increase in the surface projections (Figure 4c–e). In LPS-activated condition, all samples showed evident surface protrusions (Figure 4f–j).
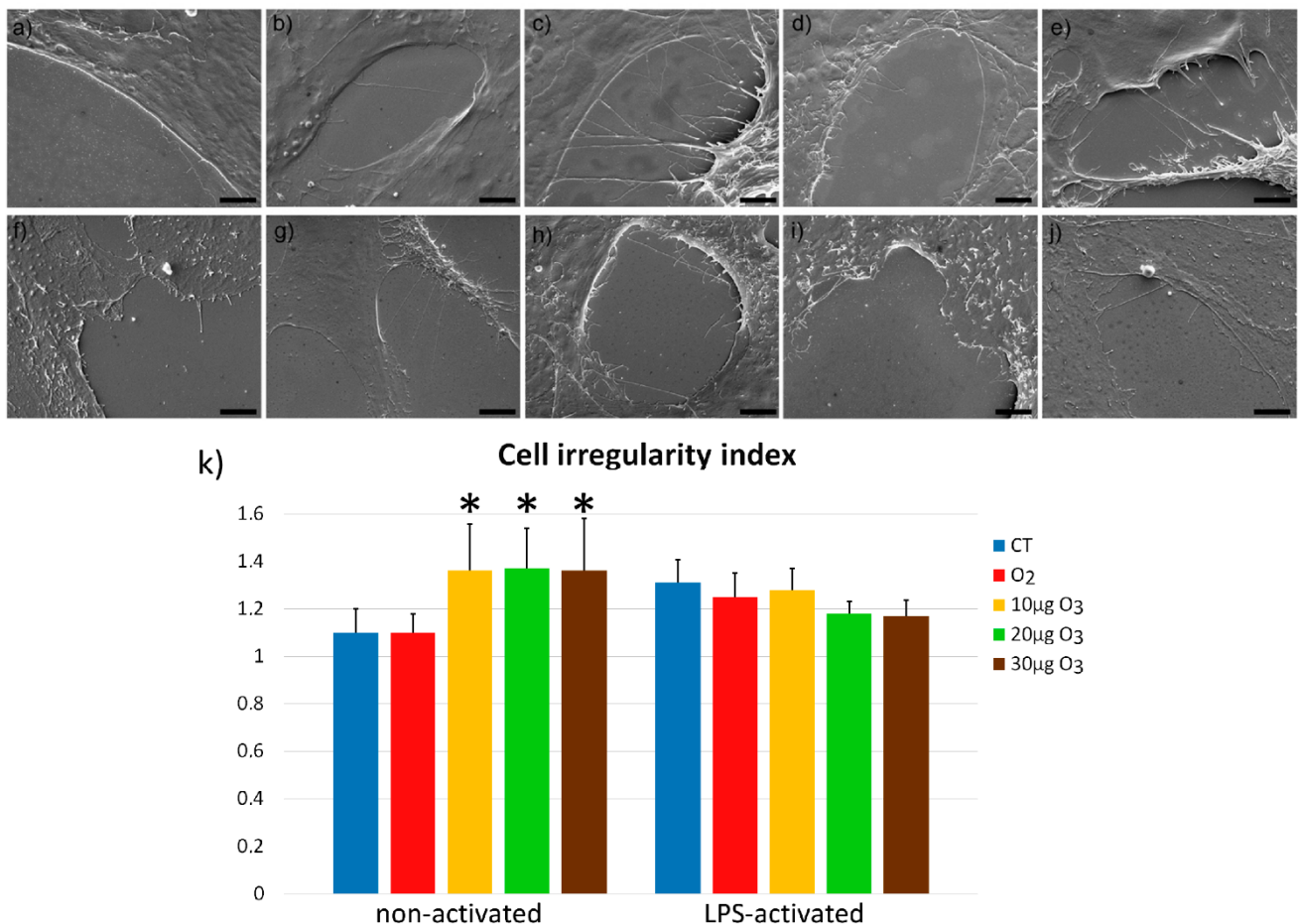
**Figure 4.** Scanning electron micrographs of non-activated (**a–e**) and LPS-activated (**f–j**) fibroblasts in control (**a,f**) and 24 h after exposure to $O_2$ (**b,g**), 10 µg $O_3$ (**c,h**), 20 µg $O_3$ (**d,i**), and 30 µg $O_3$ (**e,j**). Bars, 10 µm. (**k**) Means ± SE of the cell irregularity index at 24 h after the treatment in non-activated or LPS-activated fibroblasts (one experiment). Significant increase in the cell irregularity index was found in non-activated fibroblasts after $O_3$ treatments (*).

Quantitative evaluation of the surface irregularities showed significant differences in non-activated fibroblasts ($p = 0.006$), confirming that the protrusions of $O_3$-treated samples significantly increased ($p < 0.01$) in comparison with control and $O_2$-treated samples (Figure 4k). No significant difference in surface irregularity was found among LPS-activated samples ($p = 0.09$) (Figure 4k).

In LPS-activated condition, control samples had a significant increase in surface protrusions in comparison with the non-activated controls ($p = 0.03$).

### 2.5. Western Blot Analysis

In non-activated fibroblasts, the total amount of Nrf2 protein was similar in all samples (Figure 5a). In LPS-activated fibroblasts, the Nrf2 protein content showed an evident increase in the samples treated with 20 µg $O_3$ and 30 µg $O_3$ in comparison with the control (Figure 5b).
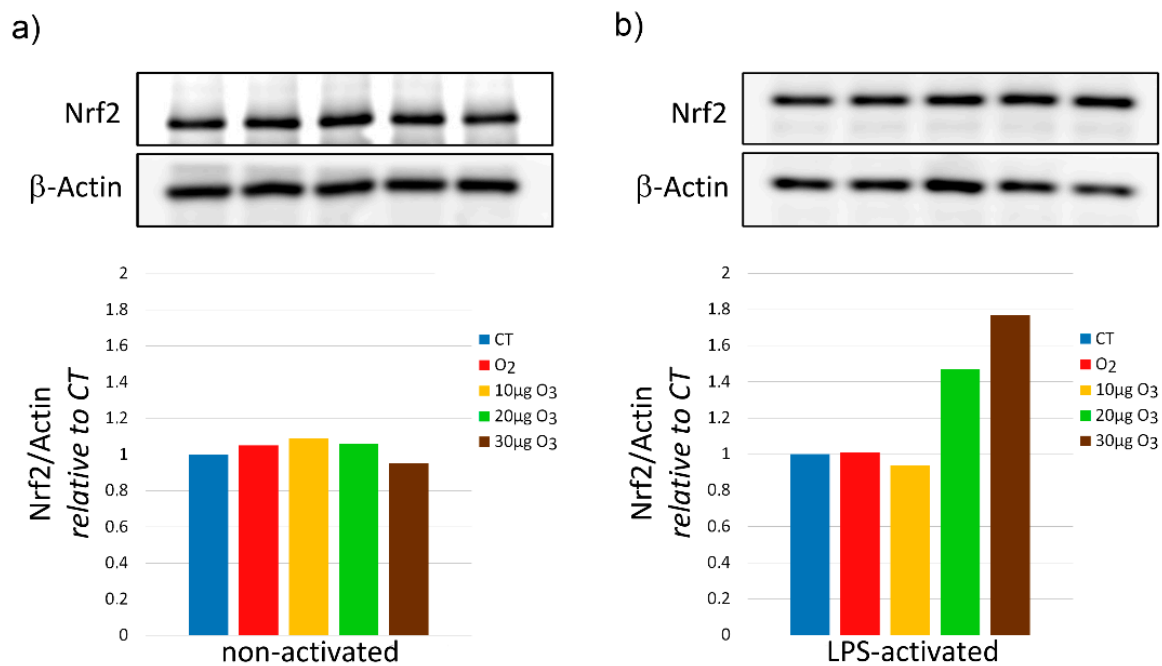
**Figure 5.** Western blot of Nrf2 protein at 20 min after treatment of non- activated (**a**) and activated (**b**) fibroblasts (one experiment in duplicate). Data were normalized to the level of a housekeeping protein (actin) and expressed as in proportion to the levels in control (CT) sample.

### 2.6. Real-Time Quantitative Polymerase Chain Reaction

In non-activated fibroblasts, the one-way ANOVA test demonstrated significantly different Heme oxygenase 1 (Hmox1) gene expression ($p = 0.03$) among samples; in particular, 20 µg $O_3$-treated fibroblasts showed values significantly higher in comparison with control ($p = 0.002$) (Figure 6a). On the other hand, no significant linear trend was found ($p = 0.09$). In LPS-activated fibroblasts, the one-way ANOVA test showed no significant difference ($p = 0.07$) among samples (Figure 6b), but the test for linear trend demonstrated a dose-dependent trend ($p = 0.03$).
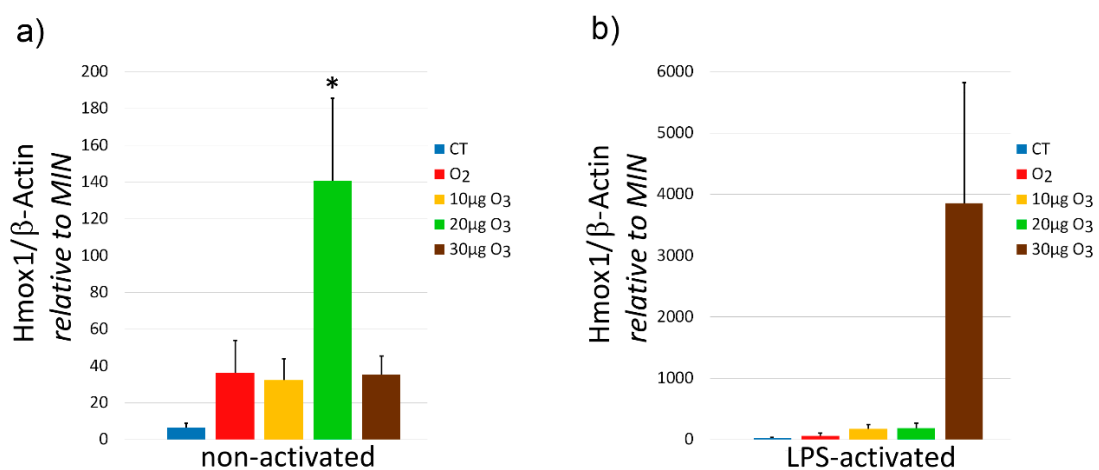


**Figure 6.** Hmox1 gene expression (means $\pm$ SE) in non-activated (**a**) and LPS-activated (**b**) fibroblasts at 24 h after treatment (one experiment in triplicate). Asterisk (*) indicates significant difference with control (CT).

### 2.7. Interleukin-6 and Transforming Growth Factor-β1 Secretion

In the non-activated condition, a significant difference was found in the amount of interleukin (IL)-6 secreted into the medium ($p = 0.03$); in particular, a significantly

higher value was found in 10 μg $O_3$-treated samples in comparison with all other samples ($p < 0.05$) (Figure 7). Significant difference was found also in the LPS-activated state ($p = 0.004$), where $O_3$-treated samples secreted a significantly higher amount of IL-6 in comparison with control and $O_2$-treated samples ($p < 0.05$).
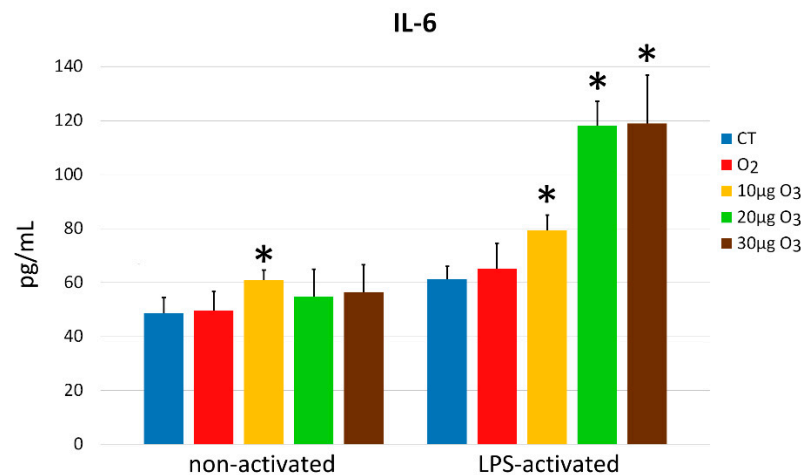


**Figure 7.** IL-6 amounts (mean values ± SE) detected in the medium of non-activated and LPS-activated cell samples 24 h after gas treatment (two experiments in duplicate). Asterisks (*) indicate significant differences from the respective controls (CT).

Moreover, LPS-activated control fibroblasts secreted significantly higher IL-6 amounts in comparison with non-activated control samples ($p = 0.02$) (Figure 7).

In the non-activated condition, a significant difference was found in the amount of transforming growth factor (TGF)-β1 secreted into the medium ($p = 0.01$); in detail, a significantly higher value was found in 10 μg $O_3$-treated samples in comparison with all other samples ($p < 0.05$) (Figure 8). Similarly, significant difference was found in LPS-activated fibroblasts ($p < 0.001$), where the treatment with 10 μg $O_3$ induced a significant increase in secreted TGF-β1 in comparison with the other samples ($p < 0.05$), while the value in 30 μg $O_3$-treated samples was below the detection limit.
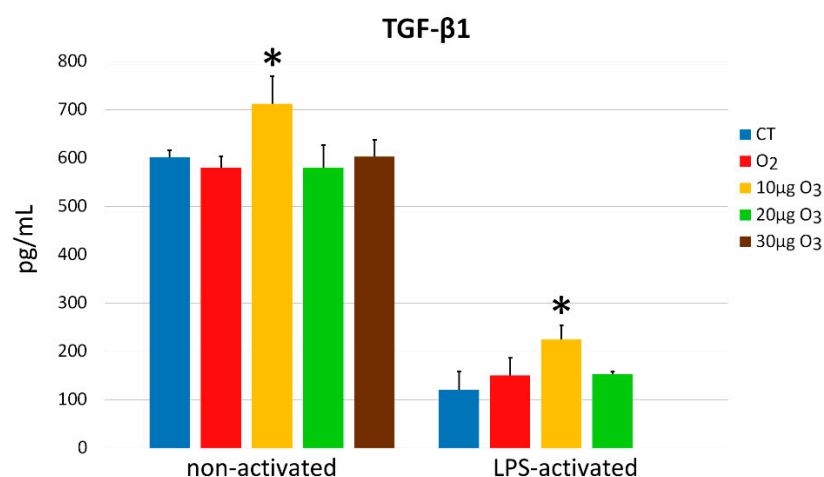


**Figure 8.** TGF-β1 amounts (mean values ± SE) detected in the medium of non-activated and LPS-activated cell samples 24 h after gas treatment (two experiments in duplicate). In LPS-activated condition, the value of 30 μg $O_3$-treated samples was below the detection limit. Asterisks (*) indicate significant differences from the respective controls (CT).

In addition, LPS-activated fibroblasts secreted significantly lower amounts of TGF-β1 than non-activated control samples ($p = 0.03$) (Figure 8).

## 3. Discussion

In the present investigation, we evaluated the effects of the exposure to $O_2$–$O_3$ mixtures at low $O_3$ concentrations on the structural and functional features of fibroblasts as a cell type ubiquitously distributed in body tissues. Being primarily responsible for the deposition and degradation of the extracellular matrix, fibroblasts play a key role in tissue remodeling [14] and wound healing [12] and are also involved in the immune response and, more generally, in the maintenance of tissue homeostasis [13]. The molecular and cellular effects of low $O_3$ concentrations were investigated in both non-activated and LPS-activated fibroblasts, with the aim of getting information on the possibly differential response due to the cell functional state.

LDH assay showed that the exposure to any of the gas mixtures used did not induce significant cytotoxicity compared with the controls, in both non-activated and LPS-activated fibroblasts, consistent with previous data on other cell types [6,7,11,15,16]. The LDH values were lower for the LPS-treated than for the non-activated samples: this is likely due to the activated state itself, as it has been demonstrated that pro-survival mechanisms are stimulated in activated fibroblasts when these cells are committed to tissue repair [17].

Based on the evaluation of BrdU-positive S-phase cells, non-activated fibroblasts proved to be stimulated by the exposure to 10 μg $O_3$, suggesting that the eustress induced by this mild concentration may promote cell growth, which is especially advantageous in the post-injury tissue repair [18,19]. Accordingly, non-activated fibroblasts treated with 10 μg $O_3$ showed a tendency ($p = 0.06$) to be more efficient than the other samples in the wound healing assay, thus accounting for the observed positive effects of oxygen–ozone therapy on wound healing [20,21].

The proliferation rate of LPS-activated fibroblasts was unaffected by the exposure to any gas, but a significantly lower proliferation was found in LPS-activated fibroblasts in comparison with the non-activated ones. This finding may be also related to the activated state of the cells: consistent with the results in the present investigation, a decreased proliferation rate (without an increase in the LDH release) has already been reported in lung fibroblasts submitted to LPS treatment [22,23].

As already recalled, fibroblasts are involved in wound healing and mediate the formation and remodeling of connective and epithelial tissues [24–26]. Migrating fibroblasts are motile cells characterized by superficial cellular protrusions, such as lamellipodia and filopodia [27]; in addition, filamentous projections are formed to remodel the collagen-rich extracellular matrix during wound healing [28]. Under our experimental conditions, surface protrusions were scarce in control and $O_2$-treated non-activated fibroblasts, but they evidently increased after $O_3$ exposure. It is worth noting that small local changes in the amount of reactive oxygen species (ROS), as induced by mild ozonation [15], may stimulate the polymerization of cytoskeletal actin [29–31] that is essential to form cell protrusions and promote adhesion [32,33]. However, the wound healing assay showed that the $O_3$-induced increase in the surface processes was not paralleled by a higher migration rate, consistent with previous evidence that $O_3$ exposure does not affect the cell migration capability [34].

On the other hand, $O_3$ did not affect surface protrusions in LPS-activated fibroblasts, whose control samples showed similar amounts of these membrane processes as the $O_3$-treated non-activated fibroblasts. This is consistent with the finding that cultured fibroblasts treated with LPS increase their ROS production [35–37], which in turn affects the organization of cytoskeletal proteins [29–31]. It can therefore be inferred that the low $O_3$ concentrations tested in the present study are able to induce activation-like changes of the cell membrane in non-activated fibroblasts but do not affect already LPS-activated fibroblasts, thus avoiding their overstimulation and the possible scarring of the extracellular matrix [28].

It is known that the administration of low $O_3$ concentrations is able to restore impaired Nrf2 pathways in many pathological conditions [38–44], thus inducing a cytoprotective response accounting for the therapeutic potential of $O_3$. The mechanism relies on the stabilization of Nrf2 that mediates an antioxidant response by the Keap1/Nrf2 dependent pathway [5]: ozonation prevents Keap1-mediated degradation of Nrf2 and promotes its translocation to the nucleus [5,7]), where it activates the expression of ARE-driven genes [5–7,16]. This enables an efficient and rapid transcription of antioxidant genes without requiring a de novo synthesis of Nrf2. Accordingly, in the present study, the total amount of Nrf2 protein was unchanged in non-activated fibroblasts, while the expression of Hmox1 (i.e., the marker gene for the mild-$O_3$-induced antioxidant response) increased in samples treated with 20 µg $O_3$, similarly as it was observed in nervous cells [16]. Genes involved in oxidative stress responses were found to be upregulated also in primary periodontal ligament fibroblasts treated with $O_3$ ultrafine bubble water [45]. In LPS-activated fibroblasts, the Nrf2 protein increased in 20 µg $O_3$- and 30 µg $O_3$-treated samples, probably due to the combined oxidative stress due to LPS and $O_3$ exposure. Consistently, Hmox1 expression increased in a dose-dependent manner in $O_3$-treated samples.

As stated above, fibroblasts are also involved in the regulation of the immune response (with complex and mutual interactions with the cells of the immune system) and are able to secrete different cytokines [46]. In particular, cultured fibroblasts secrete both IL-6 and TGF-β1 [47], as observed in our experimental model. Our data are also consistent with previous findings demonstrating that IL-6 secretion increases after LPS activation in vitro [48], while cell proliferation is inhibited in an autocrine pathway [22].

IL-6 exerts a pleiotropic effect on a broad spectrum of biological events and participates in the immune response as a potent pro-inflammatory cytokine involved in the acute inflammatory response; on the other hand, it also coordinates anti-inflammatory or repair-oriented activities essential for the resolution of inflammation [49]. In injured tissues, IL-6 is a major systemic alarm signal [50–52] involved in the activation of a variety of local and systemic host-defense mechanisms aimed at limiting tissue injury while stimulating angiogenesis, collagen production and organization, keratinocyte proliferation, and leukocyte infiltration [53–56]. The ability of low $O_3$ concentrations to stimulate IL-6 secretion in fibroblasts is therefore compatible with the efficacy of $O_2$–$O_3$ therapy in wound healing and, more generally, in tissue repair [57–60]. In particular, low $O_3$ concentrations seem to stimulate IL-6 secretion in LPS-activated fibroblasts more efficiently than in non-activated ones: this could be related to the activated state that makes the cells more responsive to stimuli. Interestingly, pre-treatment with low $O_3$ concentrations proved to reduce IL-6 secretion in skin fibroblasts receiving doxorubicin, thus preventing the inflammatory effect of this potent cytotoxic drug [44]. Moreover, repeated and prolonged exposure of synovial fibroblasts isolated from patients affected by rheumatoid arthritis led to a decreased production of IL-6 [61]. The immunomodulation potential of $O_3$ on fibroblasts therefore deserves detailed studies in view of targeted therapeutic approaches.

TGF-β1 also plays important roles as a key cytokine in the wound healing process, where it acts bidirectionally [62], promoting the synthesis of various extracellular matrix proteins [63–67] and potentiating angiogenesis [68–70], while inhibiting extracellular matrix degradation [71] and inflammatory response [72,73]. TGF-β1 has been also reported to enhance fibroblasts proliferation [74,75]. Therefore, its increased secretion in non-activated fibroblasts following 10 µg $O_3$ treatment may be related to the higher proliferation rate found in this sample. On the other hand, LPS activation in vitro inhibits TGF-β1 production [48], consistently with the very low amount of TGF-β1 found in our LPS-activated fibroblasts. However, despite the inhibiting effect of LPS, 10 µg $O_3$ proved to be capable of increasing TGF-β1 secretion also in LPS-activated fibroblasts; on the contrary, 20 µg $O_3$ and 30 µg $O_3$ treatments induce a higher stress and a stronger TGF-β1 inhibition, likely due to the activation of the Nrf2/ARE-mediated antioxidant signaling [76–78]. The stimulating effect of low $O_3$ concentrations on TGF-β1 secretion observed in our in vitro model is con-

sistent with the upregulation of this cytokine reported in cutaneous wounds undergoing accelerated repair following ozonated oil treatment [79,80].

## 4. Materials and Methods

### 4.1. Cell Culture and Treatment

Human lung fibroblasts (WI-26, ATCC) were chosen for the present study as a suitable in vitro model previously used to investigate the effects of drugs on extracellular matrix deposition [81] and remodeling [82] as well as the response to various stimuli [83–85]. The fibroblasts were grown in Dulbecco's modified Eagle's medium supplemented with 10% (*v/v*) fetal bovine serum, 1% (*w/v*) glutamine, 100 U of penicillin and 100 μg/mL streptomycin (all reagents were purchased from Gibco, Walthem, MA, USA) at 37 °C in a 5% $CO_2$ humidified atmosphere.

The cells were treated with $O_2$–$O_3$ gas mixtures produced from medical-grade $O_2$ by an OZO2 FUTURA apparatus (Alnitec, Cremosano, CR, Italy) that allows photometric real-time control of gas flow rate and $O_3$ concentration. The concentrations of 10, 20, and 30 μg $O_3$/mL $O_2$ were chosen as these are usually administered in clinical practice and had been shown to be non-cytotoxic for different cultured cells [7,11,15,16]. The treatment with pure $O_2$ was performed in order to discriminate the effect of $O_3$ from $O_2$ in the context of the $O_2$–$O_3$ gas mixtures. Controls consisted in cells submitted to the same handling but without exposure to gas.

The cells were trypsinized (0.25% trypsin in PBS containing 0.05% EDTA) (Gibco), when sub-confluent. For Western blot analysis and RT-qPCR, samples of $4 \times 10^6$ cells were suspended in 10 mL medium into a 20 mL polypropylene syringe, then 10 mL of gas was added into the syringe using a sterile filter (Alnitec, Cremosano, CR, Italy) and the cell suspension was gently mixed with the gas for 10 min to allow the full reaction of cells with the gas [86]. For S-phase cells evaluation, SEM analysis, and wound healing assay, after trypsinization, the cells were seeded on glass slides placed in multi-well microplates, let to adhere for at least 24 h and then submitted to gas treatment as described in [87]. For LDH and cytokine assays, $2 \times 10^4$ cells per 24-multi-well plate were seeded after gas treatment. At 24 h, the medium was collected and stored at $-80$ °C until analysis.

Some fibroblast samples were pre-incubated with 1 μg/mL LPS for 24 h as previously reported [23,88] in order to induce cell activation, and then processed as above.

### 4.2. Cytotoxicity

LDH, a cytosolic enzyme released by lysed cells, was evaluated as an estimate of the cytotoxic effect of gas exposure by using the CytoTox96 nonradioactive assay (Promega, Milan, MI, Italy). Cytotoxicity rate was estimated 24 h after the gas treatment in both non-activated and LPS-activated fibroblasts. Aliquots of medium were collected for each condition, placed in a 96-multi-well plate, mixed with the CytoTox 96 reagent and incubated for 30 min at room temperature. After addition of the stop solution, the absorbance was measured at 492 nm, and the data were corrected for culture medium background and normalized to the maximum LDH release (i.e., the one of lysed samples).

### 4.3. S-Phase Evaluation

The percentage of S-phase cells was assessed 24 h after treatment in both non-activated and LPS-activated fibroblasts, as a measure of the cell proliferation rate. The cells ($2 \times 10^4$ cells per 24 mm × 24 mm slides) were pulse-labelled with 20 μM BrdU (Sigma-Aldrich, St. Louis, MO, USA) for 30 min at 37 °C, then fixed with 70% ethanol and incubated for 20 min at room temperature in 2 N HCl to partially denature DNA; after neutralization with 0.1 M sodium tetraborate (pH 8.2) (Sigma-Aldrich) for 3 min, samples were washed in PBS, permeabilized for 15 min in PBS containing 0.1% bovine serum albumin and 0.05% Tween-20 (Sigma-Aldrich), and incubated for 1 h with a mouse monoclonal antibody recognizing BrdU (BD Diagnostics, Franklin Lakes, NJ, USA) diluted 1:20 in PBS. After two washes with PBS, samples were incubated for 1 h with an Alexa

Fluor 488-conjugated anti-mouse secondary antibody (Molecular Probes, Invitrogen, Milan, MI, Italy), diluted 1:200. The cell samples were washed with PBS, stained for DNA with 0.1 μg/mL Hoechst 33342 (Abcam, Cambridge, United Kingdom) in PBS for 10 min, and finally mounted in PBS/glycerol (1:1). The percentage of BrdU-positive cells was evaluated in 30 randomly selected fields (40×) per experimental condition. For observation of all samples, an Olympus BX51 microscope (Olympus Italia S.r.l., Segrate, MI, Italy) equipped with a 100 W mercury lamp was used under the following conditions: 450–480 nm excitation filter (excf), 500 nm dichroic mirror (dm), and 515 nm barrier filter (bf) for Alexa Fluor 488; 330–385 nm excf, 400 nm dm, and 420 nm bf, for Hoechst 33342. Images were recorded with a QICAM Fast 1394 Digital Camera (QImaging, Surrey, BC, Canada) and processed with Image-Pro Plus software (Media Cybernetics, Inc., Rockville, MD, USA).

### 4.4. Wound Healing Assay

For the wound healing assay, $20 \times 10^4$ cells per well were seeded on 24 mm × 24 mm slides. After 24 h, when the cells were confluent, the cell monolayers were scratched with a sterile 200 μL pipette tip and immediately exposed to gas treatment. To evaluate cell migration, images at 4× magnification were taken at 0 h, 2 h, 6 h, and 24 h post-treatment using an inverted microscope (Leica DMIL, Leica Microsystems S.r.l., Buccinasco, MI, Italy) equipped with a camera (Optika Microscopes, Ponteranica, BG, Italy): the cell-free area was measured in a total of 12 randomly selected microscope fields per sample (4 fields in 3 independent experiments). The progressive reduction of the cell-free area was expressed as percentage, considering the value at time 0 as 100%.

### 4.5. Scanning Electron Microscopy

For SEM analysis, $2 \times 10^4$ cells (both non-activated and LPS-activated fibroblasts) per well were seeded on round slides of 12 mm in diameter. After 24 h, the cell monolayers were gas exposed. At 24 h after the treatment, the cells were fixed with 2.5% glutaraldehyde in PBS for 2 h at 4 °C, washed in the same buffer, post-fixed with 1% $OsO_4$ at 4 °C for 1 h and dehydrated with graded ethanol. The samples were then treated by a critical point dryer (CPD 030, BAL- TEC AG, Balzers, Liechtenstein), mounted on metallic specimen stubs and sputter-coated with gold (MED 010, BAL- TEC AG). SEM imaging was performed by an XL30 ESEM (FEI Italia S.r.l., Milan, Italy). Using ImageJ software (NIH), the length of cell surface facing the edge of the monolayers was measured both including and excluding cell protrusions in 20 cells per sample; the ratio between the two values was then calculated in order to obtain an index of cell surface irregularity (the higher the value, the rougher the cell).

### 4.6. Western Blot Analysis

Non-activated and LPS-activated fibroblast samples were collected at 20 min post-gas-treatment and immediately frozen in liquid nitrogen to be then placed at −80 °C. Proteins were extracted according to standard procedures in RIPA buffer (150 mM NaCl, 10 mM Tris pH7.5, 1% NP40, 1% deoxycholate, 0.1% SDS) supplemented with phosphatase and protease inhibitors (Sigma-Aldrich).

Samples were resolved on Tris–glycine 4–20% gradient SDS-PAGE (BIO-RAD, Segrate, MI, Italy), blotted on PVDF membrane (BIO-RAD), and developed with ECL Western Blotting Substrate (Thermo Scientific, Rodano, MI, Italy). The following antibodies were used: anti-Nrf2 1:1000 (ab62532 Abcam) and Actin 1:5000 (ab8226 Abcam).

### 4.7. Real-Time Quantitative Polymerase Chain Reaction

RNA was extracted from non-activated and LPS-activated fibroblast samples after 24 h after the gas exposure by using the Qiagen RNeasy Plus mini kit (ref. 74134) (Qiagen S.r.l., Milan, Italy). cDNA was generated by SuperScript™ III Reverse Transcriptase (Invitrogen, cat. no. 18080093) (Thermo Fisher Scientific Inc., Waltham, MA, USA) and amplified at qPCR with Applied Biosystems™ SYBR™ Green PCR Master Mix (Applied

Biosystems™ 4309155) (Thermo Fisher Scientific Inc.) using 2 distinct sets of primers specific for human Hmox1 (primers set 1: Forw: CCTAAACTTCAGAGGGGGCG, Rev: GACAGCTGCCACATTAGGGT; primers set 2: Forw: AGTCTTCGCCCCTGTCTACT, Rev: CTTCACATAGCGCTGCATGG). The Applied Biosystems Step-One Real-Time PCR System was used for amplification (Thermo Fisher Scientific Inc.).

### 4.8. IL-6 and TGF-β1 Secretion

The amount of IL-6 and TGF-β1 secreted was evaluated in the culture medium of both non-activated and LPS-activated fibroblasts 24 h after the gas treatment. For each sample, $4 \times 10^5$ cells/mL were treated with gas; experiments were performed four times per sample and the medium was collected, centrifuged at 1500 g for 15 min, and the supernatants were finally stored at −80 °C. Quantitation of IL-6 and TGF-β1 was conducted on a Luminex Bio-Rad Bio-Plex 100 instrument (Bio-Rad Laboratories, Segrate, MI, Italy) coupled to the Bio-Plex Manager software, v6.0, which allows measuring multiple proteins in a single well. Briefly, 50 μL aliquots of undiluted cell medium were put in a 96-well plate (samples were run in duplicate). Superparamagnetic microspheres (beads) conjugated with fluorophores and antibodies against IL-6 and TGF-β were added to the assay wells. Incubation and washing steps were performed as per manufacturer's recommendations, then the plate was loaded into the Luminex system for reading and signal quantitation.

### 4.9. Statistical Analysis

Data for each variable were presented as mean ± standard error (SE). Statistical comparison was performed by either the Kruskal–Wallis non-parametric test (cytotoxicity; wound healing assay, cytokines) followed by the Mann–Whitney test for pairwise comparison or the one-way analysis of variance (ANOVA) test (S-phase evaluation; index of cell surface irregularity, RT-qPCR) followed by Bonferroni's post-hoc test. To RT-qPCR results, the test for linear trend was also applied. Statistical significance was set at $p \leq 0.05$.

## 5. Conclusions

Taken together, the results of the present study not only extend to fibroblasts the notion that low $O_3$ concentrations are safe for cells, but also provide original evidence that the administration of $O_2$–$O_3$ gas mixtures induces multiple effects on fibroblasts, depending on their activation state. In sum, in non-activated fibroblasts, $O_3$ is able to stimulate proliferation, formation of cell surface protrusions, antioxidant response, and IL-6 and TGF-β1 secretion, while in LPS-activated fibroblasts, $O_3$ stimulates antioxidant response and cytokines secretion without affecting cell proliferation and motility. It is therefore evident that the low $O_3$ concentrations used in this study induce activation-like responses in non-activated fibroblasts, whereas, in fibroblasts already activated by LPS, the gas exposure potentiates the cell protective capability. Interestingly, most of the effects observed in non-activated fibroblasts are due to the exposure to 10 or 20 μg $O_3$, i.e., the concentrations that have been already found as optimal for safely inducing positive response in various cell models [5–7,11,15,16]. This perfectly agrees with the low-dose concept in the medical use of $O_3$ [89,90], which is increasingly applied in clinical practice.

The simple in vitro model used in the present study was a suitable tool to shed light on the specific responses of fibroblasts to low $O_3$ concentrations; however, the observed effects should be investigated in a more complex network of mutual interactions of different cells and humoral factors, as it occurs in a living organism. Based on the present findings, further in vivo studies will elucidate the contribution of fibroblasts in the response to $O_2$–$O_3$ therapy, taking into account their multiple roles in tissue repair and homeostasis; this will provide novel information to properly modulate the $O_3$ administration protocols for specific therapeutic needs.

**Supplementary Materials:** The following are available online at https://www.mdpi.com/article/10.3390/ijms221810133/s1, Figure S1: Wound healing assay of non-activated fibroblasts, Figure S2: Wound healing assay of LPS-activated fibroblasts.

## References

1. Re, L.; Mawsouf, M.N.; Menéndez, S.; León, O.S.; Sánchez, G.M.; Hernández, F. Ozone therapy: Clinical and basic evidence of its therapeutic potential. *Arch. Med. Res.* **2008**, *39*, 17–26. [CrossRef]
2. Elvis, A.M.; Ekta, J.S. Ozone therapy: A clinical review. *J. Nat. Sci. Biol. Med.* **2011**, *2*, 66–70. [CrossRef]
3. Bocci, V. How a calculated oxidative stress can yield multiple therapeutic effects. *Free Radic. Res.* **2012**, *46*, 1068–1075. [CrossRef]
4. Scassellati, C.; Galoforo, A.C.; Bonvicini, C.; Esposito, C.; Ricevuti, G. Ozone: A natural bioactive molecule with antioxidant property as potential new strategy in aging and in neurodegenerative disorders. *Ageing Res. Rev.* **2020**, *63*, 101138. [CrossRef] [PubMed]
5. Galiè, M.; Costanzo, M.; Nodari, A.; Boschi, F.; Calderan, L.; Mannucci, S.; Covi, V.; Tabaracci, G.; Malatesta, M. Mild ozonisation activates antioxidant cell response by the Keap1/Nrf2 dependent pathway. *Free. Radic. Biol. Med.* **2018**, *124*, 114–121. [CrossRef]
6. Cisterna, B.; Costanzo, M.; Nodari, A.; Galiè, M.; Zanzoni, S.; Bernardi, P.; Covi, V.; Tabaracci, G.; Malatesta, M. Ozone activates the Nrf2 pathway and improves preservation of explanted adipose tissue in vitro. *Antioxidants* **2020**, *9*, 989. [CrossRef] [PubMed]
7. Cappellozza, E.; Costanzo, M.; Calderan, L.; Galiè, M.; Angelini, O.; Tabaracci, G.; Malatesta, M. Low ozone concentrations affect the structural and functional features of jurkat T cells. *Processes* **2021**, *9*, 1030. [CrossRef]
8. Sagai, M.; Bocci, V. Mechanisms of action involved in ozone therapy: Is healing induced via a mild oxidative stress? *Med. Gas Res.* **2011**, *1*, 29. [CrossRef] [PubMed]
9. Galiè, M.; Covi, V.; Tabaracci, G.; Malatesta, M. The role of Nrf2 in the antioxidant cellular response to medical ozone exposure. *Int. J. Mol. Sci.* **2019**, *20*, 4009. [CrossRef]
10. Goldman, M. Cancer risk of low-level exposure. *Science* **1996**, *271*, 1821–1822. [CrossRef]
11. Costanzo, M.; Boschi, F.; Carton, F.; Conti, G.; Covi, V.; Tabaracci, G.; Sbarbati, A.; Malatesta, M. Low ozone concentrations promote adipogenesis in human adipose-derived adult stem cells. *Eur. J. Histochem.* **2018**, *62*, 2969. [CrossRef] [PubMed]
12. Koliaraki, V.; Prados, A.; Armaka, M.; Kollias, G. The mesenchymal context in inflammation, immunity and cancer. *Nat. Immunol.* **2020**, *21*, 974–982. [CrossRef] [PubMed]
13. Buechler, M.B.; Pradhan, R.N.; Krishnamurty, A.T.; Cox, C.; Calviello, A.K.; Wang, A.W.; Yang, Y.A.; Tam, L.; Caothien, R.; Roose-Girma, M.; et al. Cross-tissue organization of the fibroblast lineage. *Nat. Cell Biol.* **2021**, *593*, 575–579. [CrossRef]
14. Hinz, B.; Lagares, D. Evasion of apoptosis by myofibroblasts: A hallmark of fibrotic diseases. *Nat. Rev. Rheumatol.* **2020**, *16*, 11–31. [CrossRef]
15. Costanzo, M.; Cisterna, B.; Vella, A.; Cestari, T.; Covi, V.; Tabaracci, G.; Malatesta, M. Low ozone concentrations stimulate cytoskeletal organization, mitochondrial activity and nuclear transcription. *Eur. J. Histochem.* **2015**, *59*, 2515. [CrossRef]
16. Scassellati, C.; Costanzo, M.; Cisterna, B.; Nodari, A.; Galiè, M.; Cattaneo, A.; Covi, V.; Tabaracci, G.; Bonvicini, C.; Malatesta, M. Effects of mild ozonisation on gene expression and nuclear domains organization in vitro. *Toxicol. In Vitro* **2017**, *44*, 100–110. [CrossRef]
17. Zhang, H.-Y.; Phan, S. Inhibition of myofibroblast apoptosis by transforming growth factor β1. *Am. J. Respir. Cell Mol. Biol.* **1999**, *21*, 658–665. [CrossRef] [PubMed]
18. Xie, Z.; Paras, C.B.; Weng, H.; Punnakitikashem, P.; Su, L.-C.; Vu, K.; Tang, L.; Yang, J.; Nguyen, K.T. Dual growth factor releasing multi-functional nanofibers for wound healing. *Acta Biomater.* **2013**, *9*, 9351–9359. [CrossRef]
19. Zhang, X.; Kang, X.; Jin, L.; Bai, J.; Liu, W.; Wang, Z. Stimulation of wound healing using bioinspired hydrogels with basic fibroblast growth factor (bFGF). *Int. J. Nanomed.* **2018**, *13*, 3897–3906. [CrossRef] [PubMed]
20. Cowin, A.J.; Hatzirodos, N.; Teusner, J.T.; Belford, D.A. Differential effect of wounding on actin and its associated proteins, paxillin and gelsolin, in fetal skin explants. *J. Investig. Dermatol.* **2003**, *120*, 1118–1129. [CrossRef]

21. Lees, J.; Ching, Y.W.; Adams, D.; Bach, C.T.; Samuel, M.; Kee, A.J.; Hardeman, E.C.; Gunning, P.; Cowin, A.; O'Neill, G.M. Tropomyosin regulates cell migration during skin wound healing. *J. Investig. Dermatol.* **2013**, *133*, 1330–1339. [CrossRef]

22. Zhang, J.; Wu, L.; Qu, J.-M. Inhibited proliferation of human lung fibroblasts by LPS is through IL-6 and IL-8 release. *Cytokine* **2011**, *54*, 289–295. [CrossRef]

23. Yang, H.; Hu, C.; Li, F.; Liang, L.; Liu, L. Effect of lipopolysaccharide on the biological characteristics of human skin fibroblasts and hypertrophic scar tissue formation. *IUBMB Life* **2013**, *65*, 526–532. [CrossRef] [PubMed]

24. Rodemann, H.P.; Müller, G.A. Characterization of human renal fibroblasts in health and disease: II. In vitro growth, differentiation, and collagen synthesis of fibroblasts from kidneys with interstitial fibrosis. *Am. J. Kidney Dis.* **1991**, *17*, 684–686. [CrossRef]

25. Brown, R.A.; Prajapati, R.; McGrouther, D.A.; Yannas, I.V.; Eastwood, M. Tensional homeostasis in dermal fibroblasts: Me-chanical responses to mechanical loading in three-dimensional substrates. *J. Cell Physiol.* **1998**, *175*, 323–332. [CrossRef]

26. Simian, M.; Hirai, Y.; Navre, M.; Werb, Z.; Lochter, A.; Bissell, M.J. The interplay of matrix metalloproteinases, morphogens and growth factors is necessary for branching of mammary epithelial cells. *Development* **2001**, *128*, 3117–3131. [CrossRef]

27. Fraley, S.; Feng, Y.; Krishnamurthy, R.; Kim, D.-H.; Celedon, A.; Longmore, G.D.; Wirtz, D. A distinctive role for focal adhesion proteins in three-dimensional cell motility. *Nat. Cell Biol.* **2010**, *12*, 598–604. [CrossRef] [PubMed]

28. Padhi, A.; Singh, K.; Franco-Barraza, J.; Marston, D.J.; Cukierman, E.; Hahn, K.M.; Kapania, R.K.; Nain, A.S. Force-exerting perpendicular lateral protrusions in fibroblastic cell contraction. *Commun. Biol.* **2020**, *3*, 1–11. [CrossRef]

29. Sakai, J.; Li, J.; Subramanian, K.K.; Mondal, S.; Bajrami, B.; Hattori, H.; Jia, Y.; Dickinson, B.C.; Zhong, J.; Ye, K.; et al. Reactive oxygen species-induced actin glutathionylation controls actin dynamics in neutrophils. *Immunity* **2012**, *37*, 1037–1049. [CrossRef]

30. Taulet, N.; Delorme-Walker, V.D.; DerMardirossian, C. Reactive oxygen species regulate protrusion efficiency by controlling actin dynamics. *PLoS ONE* **2012**, *7*, e41342. [CrossRef]

31. Muliyil, S.; Narasimha, M. Mitochondrial ROS regulates cytoskeletal and mitochondrial remodeling to tune cell and tissue dynamics in a model for wound healing. *Dev. Cell* **2014**, *28*, 239–252. [CrossRef]

32. Huang, C.-H.; Tang, M.; Shi, C.; Iglesias, P.A.; Devreotes, P.N. An excitable signal integrator couples to an idling cytoskeletal oscillator to drive cell migration. *Nat. Cell Biol.* **2013**, *15*, 1307–1316. [CrossRef]

33. Gardel, M.L.; Schneider, I.; Aratyn-Schaus, Y.; Waterman, C.M. Mechanical integration of actin and adhesion dynamics in cell migration. *Annu. Rev. Cell Dev. Biol.* **2010**, *26*, 315–333. [CrossRef]

34. Costanzo, M.; Romeo, A.; Cisterna, B.; Calderan, L.; Bernardi, P.; Covi, V.; Tabaracci, G.; Malatesta, M. Ozone at low concentrations does not affect motility and proliferation of cancer cells in vitro. *Eur. J. Histochem.* **2020**, *64*, 3119. [CrossRef]

35. Bhattarai, G.; Poudel, S.B.; Kook, S.-H.; Lee, J.-C. Resveratrol prevents alveolar bone loss in an experimental rat model of periodontitis. *Acta Biomater.* **2016**, *29*, 398–408. [CrossRef] [PubMed]

36. Gasparrini, M.; Giampieri, F.; Forbes-Hernandez, T.Y.; Afrin, S.; Cianciosi, D.; Reboredo-Rodriguez, P.; Varela-López, A.; Zhang, J.; Quiles, J.L.; Mezzetti, B.; et al. Strawberry extracts efficiently counteract inflammatory stress induced by the endotoxin lipopolysaccharide in human dermal fibroblast. *Food Chem. Toxicol.* **2018**, *114*, 128–140. [CrossRef] [PubMed]

37. Huang, C.; Zhang, C.; Yang, P.; Chao, R.; Yue, Z.; Li, C.; Guo, J.; Li, M. Eldecalcitol inhibits LPS-induced NLRP3 inflammasome-dependent pyroptosis in human gingival fibroblasts by activating the Nrf2/HO-1 signaling pathway. *Drug Des. Dev. Ther.* **2020**, *14*, 4901–4913. [CrossRef] [PubMed]

38. Re, L.; Martínez-Sánchez, G.; Bordicchia, M.; Malcangi, G.; Pocognoli, A.; Morales-Segura, M.A.; Rothchild, J.; Rojas, A. Is ozone pre-conditioning effect linked to Nrf2/EpRE activation pathway in vivo? A preliminary result. *Eur. J. Pharmacol.* **2014**, *742*, 158–162. [CrossRef] [PubMed]

39. Yu, G.; Liu, X.; Chen, Z.; Chen, H.; Wang, L.; Wang, Z.; Qiu, T.; Weng, X. Ozone therapy could attenuate tubulointerstitial injury in adenine-induced CKD rats by mediating Nrf2 and NF-kappaB. *Iran. J. Basic Med. Sci.* **2016**, *19*, 1136–1143. [PubMed]

40. Delgado-Roche, L.; Riera-Romo, M.; Mesta, F.; Hernández-Matos, Y.; Barrios, J.M.; Martínez-Sánchez, G.; Al-Dalaien, S.M. Medical ozone promotes Nrf2 phosphorylation reducing oxidative stress and pro-inflammatory cytokines in multiple sclerosis patients. *Eur. J. Pharmacol.* **2017**, *811*, 148–154. [CrossRef]

41. Meng, W.; Xu, Y.; Li, D.; Zhu, E.; Deng, L.; Liu, Z.; Zhang, G.; Liu, H. Ozone protects rat heart against ischemia-reperfusion injury: A role for oxidative preconditioning in attenuating mitochondrial injury. *Biomed. Pharmacother.* **2017**, *88*, 1090–1097. [CrossRef]

42. Siniscalco, D.; Trotta, M.C.; Brigida, A.L.; Maisto, R.; Luongo, M.; Ferraraccio, F.; D'Amico, M.; di Filippo, C. Intraperitoneal administration of oxygen/ozone to rats reduces the pancreatic damage induced by streptozotocin. *Biology* **2018**, *7*, 10. [CrossRef]

43. Wang, Z.; Zhang, A.; Meng, W.; Wang, T.; Li, D.; Liu, Z.; Liu, H. Ozone protects the rat lung from ischemia-reperfusion injury by attenuating NLRP3-mediated inflammation, enhancing Nrf2 antioxidant activity and inhibiting apoptosis. *Eur. J. Pharmacol.* **2018**, *835*, 82–93. [CrossRef]

44. Simonetti, V.; Quagliariello, V.; Franzini, M.; Iaffaioli, R.V.; Maurea, N.; Valdenassi, L. Ozone exerts cytoprotective and anti-inflammatory effects in cardiomyocytes and skin fibroblasts after incubation with doxorubicin. *Evid. Based Complement. Altern. Med.* **2019**, *2019*, 1–9. [CrossRef] [PubMed]

45. Leewananthawet, A.; Arakawa, S.; Okano, T.; Kinoshita, R.D.; Ashida, H.; Izumi, Y.; Suzuki, T. Ozone ultrafine bubble water induces the cellular signaling involved in oxidative stress responses in human periodontal ligament fibroblasts. *Sci. Technol. Adv. Mater.* **2019**, *20*, 590–599. [CrossRef] [PubMed]

46. Apte, R.N. Mechanisms of cytokine production by fibroblasts-implications for normal connective tissue homeostasis and pathological conditions. *Folia Microbiol.* **1995**, *40*, 392–404. [CrossRef]

47. Bengtsson, T.; Zhang, B.; Selegård, R.; Wiman, E.; Aili, D.; Khalaf, H. Dual action of bacteriocin PLNC8 αβ through inhibition of *Porphyromonas gingivalis* infection and promotion of cell proliferation. *Pathog. Dis.* **2017**, *75*, 064. [CrossRef] [PubMed]

48. Maita, E.; Sato, M.; Yamaki, K. Effect of tranilast on matrix metalloproteinase-1 secretion from human gingival fibroblasts in vitro. *J. Periodontol.* **2004**, *75*, 1054–1060. [CrossRef]

49. Scheller, J.; Chalaris, A.; Schmidt-Arras, D.; Rose-John, S. The pro- and anti-inflammatory properties of the cytokine interleukin-6. *Biochim. Biophys. Acta* **2011**, *1813*, 878–888. [CrossRef]

50. Van Oers, M.H.; van der Heyden, A.A.; Aarden, L.A. Interleukin 6 (IL-6) in serum and urine of renal transplant recipients. *Clin. Exp. Immunol.* **1988**, *71*, 314–319. [PubMed]

51. Fong, Y.; Moldawer, L.L.; Marano, M.; Wei, H.; Tatter, S.; Clarick, R.H.; Santhanam, U.; Sherris, D.; May, L.T.; Sehgal, P.B. Endotoxemia elicits increased circulating beta 2-IFN/IL-6 in man. *J. Immunol.* **1989**, *142*, 2321–2324.

52. Helfgott, D.C.; Tatter, S.; Santhanam, U.; Clarick, R.H.; Bhardwaj, N.; May, L.T.; Sehgal, P.B. Multiple forms of IFN-beta 2/IL-6 in serum and body fluids during acute bacterial infection. *J. Immunol.* **1989**, *142*, 948–953.

53. Lin, Z.-Q.; Kondo, T.; Ishida, Y.; Takayasu, T.; Mukaida, N. Essential involvement of IL-6 in the skin wound-healing process as evidenced by delayed wound healing in IL-6-deficient mice. *J. Leukoc. Biol.* **2003**, *73*, 713–721. [CrossRef] [PubMed]

54. Baum, C.L.; Arpey, C.J. Normal cutaneous wound healing: Clinical correlation with cellular and molecular events. *Dermatol. Surg.* **2006**, *31*, 674–686. [CrossRef] [PubMed]

55. Basso, F.G.; Soares, D.G.; Pansani, T.N.; Cardoso, L.M.; Scheffel, D.; de Souza Costa, C.A.; Hebling, J. Proliferation, migration, and expression of oral-mucosal-healing-related genes by oral fibroblasts receiving low-level laser therapy after inflammatory cytokines challenge. *Lasers Surg. Med.* **2016**, *48*, 1006–1014. [CrossRef] [PubMed]

56. Saglam, M.; Köseoglu, S.; Pekbagriyanik, T.; Savran, L.; Enhos, S. Effects of high powerpulsed Nd: YAG laser irradiation on the release of transforming growth factor-beta (TGF-β) and vascular endothelial growth factor (VEGF) from human gingival fibroblasts. *J. Cosmet. Laser Ther.* **2017**, *19*, 469–474. [CrossRef]

57. Valacchi, G.; Lim, Y.; Ms, G.B.; Miracco, C.; Zanardi, I.; Bocci, V.; Travagli, V. Ozonated sesame oil enhances cutaneous wound healing in SKH1 mice. *Wound Repair Regen.* **2010**, *19*, 107–115. [CrossRef]

58. Martínez-Sánchez, G.; Al-Dalain, S.M.; Menéndez, S.; Re, L.; Giuliani, A.; Candelario-Jalil, E.; Álvarez, H.; Fernández-Montequín, J.I.; León, O.S. Therapeutic efficacy of ozone in patients with diabetic foot. *Eur. J. Pharmacol.* **2005**, *523*, 151–161. [CrossRef] [PubMed]

59. Taşdemir, Z.; Alkan, B.A.; Albayrak, H. Effects of ozone therapy on the early healing period of deepithelialized gingival grafts: A randomized placebo-controlled clinical trial. *J. Periodontol.* **2016**, *87*, 663–671. [CrossRef]

60. Karakaya, E.; Akdur, A.; Ayvazoğlu Soy, E.; Araz, C.; Ok Atilgan, A.; Özturan Özer, E.; Şençelikel, T.; Haberal, M. Effect of subcutaneous topical ozone therapy on second-degree burn wounds in rats: An experimental study. *J. Burn. Care Res.* **2021**, *16*, 110. [CrossRef] [PubMed]

61. Chang, J.D.S.; Lu, H.-S.; Chang, Y.-F.; Wang, D. Ameliorative effect of ozone on cytokine production in mice injected with human rheumatoid arthritis synovial fibroblast cells. *Rheumatol. Int.* **2004**, *26*, 142–151. [CrossRef] [PubMed]

62. Wahl, S.M.; Hunt, D.A.; Wakefield, L.M.; McCartney-Francis, N.; Roberts, A.B.; Sporn, M.B. Transforming growth factor type beta induces monocyte chemotaxis and growth factor production. *Proc. Natl. Acad. Sci. USA* **1987**, *84*, 5788–5792. [CrossRef] [PubMed]

63. Ignotz, R.A.; Endo, T.; Massagué, J. Regulation of fibronectin and type I collagen mRNA levels by transforming growth factor-beta. *J. Biol. Chem.* **1987**, *262*, 6443–6446. [CrossRef]

64. Varga, J.; Rosenbloom, J.; Jimenez, S. Transforming growth factor β (TGFβ) causes a persistent increase in steady-state amounts of type I and type III collagen and fibronectin mRNAs in normal human dermal fibroblasts. *Biochem. J.* **1987**, *247*, 597–604. [CrossRef]

65. Peltonen, J.; Kähäri, L.; Jaakkola, S.; Kähäri, V.-M.; Varga, J.; Uitto, J.; Jimenez, S.A. Evaluation of transforming growth factor β and type I procollagen gene expression in fibrotic skin disease by in situ hybridization. *J. Investig. Dermatol.* **1990**, *94*, 365–371. [CrossRef]

66. Grässel, S.; Tan, E.M.; Timpl, R.; Chu, M.-L. Collagen type XVI expression is modulated by basic fibroblast growth factor and transforming growth factor-β. *FEBS Lett.* **1998**, *436*, 197–201. [CrossRef]

67. Kissin, E.Y.; Lemaire, R.; Korn, J.H.; Lafyatis, R. Transforming growth factor β induces fibroblast fibrillin-1 matrix formation. *Arthritis Rheum.* **2002**, *46*, 3000–3009. [CrossRef] [PubMed]

68. Wang, X.; Abraham, S.; McKenzie, J.A.G.; Jeffs, N.; Swire, M.; Tripathi, V.B.; Luhmann, U.F.; Lange, C.A.K.; Zhai, Z.; Arthur, H.; et al. LRG1 promotes angiogenesis by modulating endothelial TGF-β signalling. *Nat. Cell Biol.* **2013**, *499*, 306–311. [CrossRef] [PubMed]

69. Zhao, M.; Hu, Y.; Jin, J.; Yu, Y.; Zhang, S.; Cao, J.; Zhai, Y.; Wei, R.; Shou, J.; Cai, W.; et al. Interleukin 37 promotes angiogenesis through TGF-β signaling. *Sci. Rep.* **2017**, *7*, 6113. [CrossRef] [PubMed]

70. Miscianinov, V.; Martello, A.; Rose, L.; Parish, E.; Cathcart, B.; Mitić, T.; Gray, G.A.; Meloni, M.; Zen, A.A.H.; Caporali, A. MicroRNA-148b targets the TGF-β pathway to regulate angiogenesis and endothelial-to-mesenchymal transition during skin wound healing. *Mol. Ther.* **2018**, *26*, 1996–2007. [CrossRef] [PubMed]

71. Baricos, W.H.; Cortez, S.L.; Deboisblanc, M.; Xin, S. Transforming growth factor-β is a potent inhibitor of extracellular matrix degradation by cultured human mesangial cells. *J. Am. Soc. Nephrol.* **1999**, *10*, 790–795. [CrossRef] [PubMed]

72. Silverio-Ruiz, K.G.; Martinez, A.E.T.; Garlet, G.P.; Barbosa, C.F.; Silva, J.S.; Cicarelli, R.M.B.; Valentini, S.R.; Abi-Rached, R.S.G.; Junior, C.R. Opposite effects of bFGF and TGF-β on collagen metabolism by human periodontal ligament fibroblasts. *Cytokine* **2007**, *39*, 130–137. [CrossRef]

73. Safavi, S.M.; Kazemi, B.; Esmaeili, M.; Fallah, A.; Modarresi, A.; Mir, M. Effects of low-level He–Ne laser irradiation on the gene expression of IL-1β, TNF-α, IFN-γ, TGF-β, bFGF, and PDGF in rat's gingiva. *Lasers Med Sci.* **2007**, *23*, 331–335. [CrossRef]

74. Meran, S.; Thomas, D.W.; Stephens, P.; Enoch, S.; Martin, J.; Steadman, R.; Phillips, A.O. Hyaluronan facilitates transforming growth factor-β1-mediated fibroblast proliferation. *J. Biol. Chem.* **2008**, *283*, 6530–6545. [CrossRef]

75. Khalil, N.; Xu, Y.D.; O'Connor, R.; Duronio, V. Proliferation of pulmonary interstitial fibroblasts is mediated by transforming growth factor-β1-induced release of extracellular fibroblast growth factor-2 and phosphorylation of p38 MAPK and JNK. *J. Biol. Chem.* **2005**, *280*, 43000–43009. [CrossRef]

76. Cui, Y.; Xin, H.; Tao, Y.; Mei, L.; Wang, Z. *Arenaria kansuensis* attenuates pulmonary fibrosis in mice via the activation of Nrf2 pathway and the inhibition of NF-kB/TGF -beta1/Smad2/3 pathway. *Phytother. Res.* **2021**, *35*, 974–986. [CrossRef]

77. Oh, C.J.; Kim, J.-Y.; Min, A.-K.; Park, K.-G.; Harris, R.A.; Kim, H.-J.; Lee, I.-K. Sulforaphane attenuates hepatic fibrosis via NF-E2-related factor 2-mediated inhibition of transforming growth factor-β/Smad signaling. *Free. Radic. Biol. Med.* **2012**, *52*, 671–682. [CrossRef] [PubMed]

78. Oh, C.J.; Kim, J.-Y.; Choi, Y.-K.; Kim, H.-J.; Jeong, J.-Y.; Bae, K.-H.; Park, K.-G.; Lee, I.-K. Dimethylfumarate attenuates renal fibrosis via nf-e2-related factor 2-mediated inhibition of transforming growth factor-β/Smad signaling. *PLoS ONE* **2012**, *7*, e45870. [CrossRef]

79. Kim, H.S.; Noh, S.U.; Han, Y.W.; Kim, K.M.; Kang, H.; Kim, H.O.; Park, Y.M. Therapeutic effects of topical application of ozone on acute cutaneous wound healing. *J. Korean Med. Sci.* **2009**, *24*, 368–374. [CrossRef]

80. Xiao, W.; Tang, H.; Wu, M.; Liao, Y.; Li, K.; Li, L.; Xu, X. Ozone oil promotes wound healing by increasing the migration of fibroblasts via PI3K/Akt/mTOR signaling pathway. *Biosci. Rep.* **2017**, *37*, 20170658. [CrossRef] [PubMed]

81. Poulalhon, N.; Farge, D.; Roos, N.; Tacheau, C.; Neuzillet, C.; Michel, L.; Mauviel, A.; Verrecchia, F. Modulation of collagen and mmp-1 gene expression in fibroblasts by the immunosuppressive drug rapamycin. *J. Biol. Chem.* **2006**, *281*, 33045–33052. [CrossRef]

82. Roos, N.; Poulalhon, N.; Farge, D.; Madelaine, I.; Mauviel, A.; Verrecchia, F. In vitro evidence for a direct antifibrotic role of the immunosuppressive drug mycophenolate mofetil. *J. Pharmacol. Exp. Ther.* **2007**, *321*, 583–589. [CrossRef] [PubMed]

83. Hovest, M.G.; Brüggenolte, N.; Hosseini, K.S.; Krieg, T.; Herrmann, G. Senescence of human fibroblasts after psoralen photoactivation is mediated by ATR kinase and persistent DNA damage foci at telomeres. *Mol. Biol. Cell* **2006**, *17*, 1758–1767. [CrossRef]

84. Neutelings, T.; Lambert, C.A.; Nusgens, B.V.; Colige, A.C. Effects of mild cold shock (25 °C) followed by warming up at 37 °C on the cellular stress response. *PLoS ONE* **2013**, *8*, e69687. [CrossRef]

85. Nunes, R.R.; Costa, M.D.S.; Santos, B.D.R.; da Fonseca, A.L.; Ferreira, L.S.; Chagas, R.C.R.; da Silva, A.M.; Varotti, F.D.P.; Taranto, A.G. Successful application of virtual screening and molecular dynamics simulations against antimalarial molecular targets. *Memórias Inst. Oswaldo Cruz* **2016**, *111*, 721–730. [CrossRef] [PubMed]

86. Larini, A.; Bianchi, L.; Bocci, V. The ozone tolerance: I) Enhancement of antioxidant enzymes is ozone dose-dependent in Jurkat cells. *Free Radic. Res.* **2003**, *37*, 1163–1168. [CrossRef]

87. Costanzo, M.; Cisterna, B.; Covi, V.; Tabaracci, G.; Malatesta, M. An easy and inexpensive method to expose adhering cultured cells to ozonization. *Microscopie* **2015**, *23*, 46–52. Available online: https://www.pagepressjournals.org/index.php/microscopie/article/view/5164/4554 (accessed on 28 August 2021).

88. Li, X.-P.; Liu, P.; Li, Y.-F.; Zhang, G.-L.; Zeng, D.-S.; Liu, D.-L. LPS induces activation of the TLR4 pathway in fibroblasts and promotes skin scar formation through collagen I and TGF-β in skin lesions. *Int. J. Clin. Exp. Pathol.* **2019**, *12*, 2121–2129.

89. Viebahn-Hänsler, R.; Fernández, O.S.L.; Fahmy, Z. Ozone in medicine: The low-dose ozone concept—Guidelines and treatment strategies. *Ozone Sci. Eng.* **2012**, *34*, 408–424. [CrossRef]

90. Viebahn-Haensler, R.; Fernández, O.L. Ozone in medicine. The low-dose ozone concept and its basic biochemical mechanisms of action in chronic inflammatory diseases. *Int. J. Mol. Sci.* **2021**, *22*, 7890. [CrossRef]

RESEARCH ARTICLE

MICROSCOPY
RESEARCH & TECHNIQUE WILEY

# Ozone at low concentration modulates microglial activity in vitro: A multimodal microscopy and biomolecular study

Maria Assunta Lacavalla[1] | Chiara Rita Inguscio[1] | Barbara Cisterna[1] |
Paolo Bernardi[1] | Manuela Costanzo[1] | Mirco Galiè[1] | Ilaria Scambi[1] |
Osvaldo Angelini[2] | Gabriele Tabaracci[2] | Manuela Malatesta[1]

[1]Department of Neurosciences, Biomedicine and Movement Sciences, Anatomy and Histology Section, University of Verona, Verona, Italy

[2]San Rocco Clinic, Montichiari, Italy

**Correspondence**
Manuela Malatesta, Department of Neurosciences, Biomedicine and Movement Sciences, Anatomy and Histology Section, University of Verona, Strada Le Grazie 8, Verona I-37134, Italy.
Email: manuela.malatesta@univr.it

**Funding information**
University of Verona

**Review Editor:** Alberto Diaspro

## Abstract

Oxygen-ozone ($O_2$-$O_3$) therapy is an adjuvant/complementary treatment based on the activation of antioxidant and cytoprotective pathways driven by the nuclear factor erythroid 2-related factor 2 (Nrf2). Many drugs, including dimethyl fumarate (DMF), that are used to reduce inflammation in oxidative-stress-related neurodegenerative diseases, act through the Nrf2-pathway. The scope of the present investigation was to get a deeper insight into the mechanisms responsible for the beneficial result of $O_2$-$O_3$ treatment in some neurodegenerative diseases. To do this, we used an integrated approach of multimodal microscopy (bright-field and fluorescence microscopy, transmission and scanning electron microscopy) and biomolecular techniques to investigate the effects of the low $O_3$ concentrations currently used in clinical practice in lipopolysaccharide (LPS)-activated microglial cells human microglial clone 3 (HMC3) and in DMF-treated LPS-activated (LPS + DMF) HMC3 cells. The results at light and electron microscopy showed that LPS-activation induced morphological modifications of HMC3 cells from elongated/branched to larger roundish shape, cytoplasmic accumulation of lipid droplets, decreased electron density of the cytoplasm and mitochondria, decreased amount of Nrf2 and increased migration rate, while biomolecular data demonstrated that Heme oxygenase 1 gene expression and the secretion of the pro-inflammatory cytokines, Interleukin-6, and tumor necrosis factor-$\alpha$ augmented. $O_3$ treatment did not affect cell viability, proliferation, and morphological features of both LPS-activated and LPS + DMF cells, whereas the cell motility and the secretion of pro-inflammatory cytokines were significantly decreased. This evidence suggests that modulation of microglia activity may contribute to the beneficial effects of the $O_2$-$O_3$ therapy in patients with neurodegenerative disorders characterized by chronic inflammation.

**Highlights**

- Low-dose ozone ($O_3$) does not damage activated microglial cells in vitro
- Low-dose $O_3$ decreases cell motility and pro-inflammatory cytokine secretion in activated microglial cells in vitro
- Low-dose $O_3$ potentiates the effect of an anti-inflammatory drug on activated microglial cells

**KEYWORDS**

fluorescence microscopy, nuclear factor erythroid 2-related factor 2, oxygen-ozone therapy, scanning electron microscopy, transmission electron microscopy

## 1 | INTRODUCTION

Oxygen-ozone ($O_2$-$O_3$) therapy is a modestly invasive procedure used in medicine as an adjuvant/complementary treatment for a variety of diseases (Bocci, 2012; Delgado-Roche et al., 2017; Elvis & Ekta, 2011; Re et al., 2008). $O_3$ is a highly unstable gas that quickly dissolves and decomposes in the body fluids (being tenfold more water-soluble than $O_2$). $O_3$ therefore acts as a pro-drug because it does not react directly on the cells but gives rise to molecular messengers that, in turn, diffuse in the whole organism (some of them being even able to pass the blood brain barrier (Masan et al., 2021)) thus activating multiple pathways responsible for the therapeutic response (Sagai & Bocci, 2011). Molecular evidence shed light on some basic biological mechanisms responsible for the dose-dependent effects of $O_3$ exposure (Sagai & Bocci, 2011; Viebahn-Haensler & Fernández, 2021): high $O_3$ concentrations induce an inflammatory response by activating the redox-sensitive nuclear factor kappa-light-chain-enhancer of activated B cells, which promotes the transcription of pro-inflammatory cytokines and, in turn, the expression of several proteins involved in the antioxidant response (Sagai & Bocci, 2011); on the contrary, low $O_3$ concentrations induce a moderate oxidative stress that stimulates the transcription of Antioxidant Response Elements-driven genes through the translocation of the nuclear factor erythroid 2-related factor 2 (Nrf2) from the cytoplasm to the cell nucleus, where it promotes the transcription of several genes involved in the antioxidant response (Galiè et al., 2018). Therefore, the therapeutic efficacy of low-dose $O_3$ would rely on the induction of an oxidative "eustress" (Niki, 2016) that stimulates the antioxidant cell defense pathways via Nrf2 activation (Galiè et al., 2019) without inducing injury or inflammation.

Interestingly, there is increasing evidence on the role of the Nrf2 pathway in reducing oxidative stress and inflammation in neurodegenerative conditions, thus making the Nrf2 a promising therapeutic target for these diseases (Buendia et al., 2016; Dinkova-Kostova et al., 2018; Johnson & Johnson, 2015; Liu et al., 2021; Lu et al., 2016; McBean et al., 2017; Miller et al., 2019; Robledinos-Antón et al., 2019; Shaw & Chattopadhyay, 2020). Consistently, some drugs, such as dimethyl fumarate (DMF) (Scannevin et al., 2012), are able to reduce inflammation in neurodegenerative diseases acting through the Nrf2 pathway.

In the present investigation, we focused our attention on microglial cells in the frame of a basic research aimed at unveiling the biological mechanisms accounting for the therapeutic efficacy of low-dose $O_3$ on different cell types. Microglia are resident phagocytes and innate immune cells in the central nervous system (CNS), where they contribute to the homeostasis and rapidly activate in response to noxious stimuli, thus playing a primary role in inflammatory processes (Prinz et al., 2019; Wolf et al., 2017; Woodburn et al., 2021).

To ensure controlled and standardized experimental conditions, we selected as an in vitro system the human microglial clone 3 (HMC3) cell line, which is widely employed for basic studies (Dello Russo et al., 2018). HMC3 cells were administered the low $O_3$ concentrations currently used in clinical practice after activation with lipopolysaccharide (LPS) (which induces neuroinflammatory responses and upregulates the expression of pro-inflammatory cytokines (Lu et al., 2021)); to mimic the effect of $O_3$ on activated microglia under a pharmacological anti-inflammatory treatment, we also treated HMC3 cells with the same gas concentrations after both LPS activation and DMF administration (Scannevin et al., 2012). To evaluate the effects of $O_3$ on the structural and functional features of HMC3 cells we used an integrated approach of multimodal microscopy (bright-field and fluorescence microscopy, transmission and scanning electron microscopy) and biomolecular techniques.

## 2 | MATERIALS AND METHODS

### 2.1 | Cell culture and treatment

Human microglial clone 3 cell line, HMC3 (ATCC), were chosen for the present study as a suitable in vitro system widely used in investigations on neurodegenerative diseases (Dello Russo et al., 2018). HMC3 cells were grown in Minimum Essential Medium supplemented with 11% (vol/vol) fetal bovine serum, 1% (wt/vol) glutamine, 100 U of penicillin and 100 g/ml streptomycin (all reagents were purchased from Gibco, Walthem, MA, USA) at 37°C in a 5% $CO_2$ humidified atmosphere. At sub-confluence, the cells were trypsinized with 0.25% trypsin in phosphate buffered saline (PBS) containing 0.05% EDTA (Gibco), and seeded for specific analyses.

Cells were exposed to $O_2$–$O_3$ gas mixtures produced from medical-grade $O_2$ by an OZO2 FUTURA apparatus (Alnitec, Cremosano, CR, Italy), which allows photometric real-time control of gas flow rate and $O_3$ concentration. $O_3$ was used at the concentrations of 10 and 20 µg $O_3$/ml $O_2$ because they are currently administered in the clinical practice. In addition, these concentrations proved be non-toxic for various cultured cells and tissues (Cappellozza et al., 2021; Cisterna et al., 2020; Cisterna et al., 2021; Costanzo et al., 2018; Costanzo et al., 2015; Scassellati et al., 2017). Concentrations of 30 and 50 µg $O_3$/ml $O_2$ were used as highly oxidizing conditions.

Pure $O_2$ was used to distinguish the effect of $O_3$ from $O_2$ in the context of the $O_2$–$O_3$ mixtures. Cells undergoing the same handling as gas-treated cells but without exposure to $O_2$ or $O_2$–$O_3$ gas were considered as control (CT).

As for cells grown adhering to glass slides, two coverslips were placed in a 50 ml polypropylene syringe with 16 ml culture medium, then 16 ml of gas was added into the syringe using a sterile filter (Alnitec, Cremosano, CR, Italy), and the medium was gently mixed with the gas for 10 min (Costanzo et al., 2015). As for cells treated in suspension, samples of $4 \times 10^6$ cells were suspended in 10 ml medium into a 20 ml syringe, then 10 ml of gas was added into the syringe and gently mixed with the gas for 10 min (Larini et al., 2003).

For mitotic index and S-phase assessment, wound healing assay, TEM analyses, and SEM analyses, the cells were seeded on glass slides in multi-well microplates, let to adhere for at least 24 h and then submitted to gas treatment. For cytotoxicity evaluation, RT-qPCR and cytokine assays, cells were treated in suspension. Then, for methyl thiazolyl tetrazolium (MTT) assay, cells were seeded in 96-multi-well plate after gas treatment, and analysed. For cytokine evaluation, cells were seeded after gas treatment in 24-multi-well plates and, after 24 h, the medium was collected and stored at −80°C.

Before gas treatment, some HMC3 samples were incubated with 1 µg/ml LPS for 24 h as previously reported (Dello Russo et al., 2018) to induce cell activation. Some other HMC3 samples were incubated with both 4 µM DMF and 1 µg/ml LPS for 24 h in order to counteract cell activation with an antioxidant drug (Scannevin et al., 2012). Sample of HMC3 cells non-activated was used as reference condition to verify the efficacy of LPS activation and DMF treatment.

## 2.2 | Cell viability assay

The effect of gas treatment was evaluated by the MTT assay. Cells were seeded in flat-bottom 96 multiwell plates at the density of $5 \times 10^3$ cells/well. Five wells for each condition were seeded.

MTT assay was performed at 24, 48, and 72 h after gas treatment in LPS-activated and LPS + DMF HMC3 cells. To evaluate the effect of higher $O_3$ concentrations on cell viability, samples of non-activated cells were exposed to 30 and 50 µg $O_3$/ml $O_2$. Briefly, the medium was replaced with 100 µl of 0.5 mg/ml MTT (Sigma, Italy) in culture medium and incubated for 4 h at 37°C in a cell culture incubator. Then, MTT solution was removed, formazan crystals were dissolved in 100 µl of dimethyl sulfoxide (DMSO) and the absorbance was measured at 570 nm. The percentage of cell viability was calculated.

Cell death for the highly oxidizing conditions of 30 and 50 µg $O_3$/ml $O_2$ was estimated at the same times of MTT assay (24, 48, and 72 h after gas treatment) staining the cells with 0.1% Trypan blue for 2 min. The cells were observed using a Leica DM IL inverted microscope equipped with 20× objective lens.

## 2.3 | Mitotic index

The percentage of mitotic cells was assessed 48 h after treatment in LPS-activated and LPS + DMF HMC3 cells, as a measure of the cell proliferation rate. Non-activated cell sample was also considered as basal condition. The cells ($2 \times 10^4$ seeded cells per 24 mm × 24 mm slides) were fixed with 70% ethanol for 30 min, washed with PBS and stained for deoxyribonucleic acid (DNA) with 0.1 µg/ml Hoechst 33342 (Abcam, Cambridge, United Kingdom) in PBS for 10 min. The samples were finally mounted in PBS/glycerol (1:1).

For observation, an Olympus BX51 microscope (Olympus Italia S. r.l., Segrate, MI, Italy) equipped with a 100 W mercury lamp was used under the appropriate light excitation and emission conditions for Hoechst 33342. Images were recorded with a QICAM Fast 1394 Digital Camera (QImaging, Surrey, BC, Canada) and processed with Image-Pro Plus software (Media Cybernetics, Inc., Rockville, MD, USA).

## 2.4 | S-phase evaluation

In order to assess cell proliferation rate, HMC3 S-phase evaluation was performed in LPS-activated and LPS + DMF cells 48 h after treatment. Non-activated cell sample was also considered as basal condition. After $2 \times 10^4$ cells were seeded on 24 mm × 24 mm slides, pulse-labeled with 20 µM Bromodeoxyuridine (BrdU) (Sigma-Aldrich, St. Louis, MO, USA) at 37°C for 30 min and fixed with 70% ethanol. To partially denature DNA, cells were incubated with 2 N HCl for 20 min at room temperature, then neutralized for 3 min with 0.1 M sodium tetraborate (pH 8.2) (Sigma-Aldrich). Samples were washed with PBS and permeabilized with PBS containing 0.1% bovine serum albumin and 0.05% Tween-20 (Sigma-Aldrich) for 15 min, then incubated with a mouse monoclonal antibody recognizing BrdU (BD Diagnostics, Franklin Lakes, NJ, USA) diluted 1:20 in PBS for 1 h. Following two washes with PBS, cells were incubated with Alexa Fluor 488-conjugated anti-mouse secondary antibody (Molecular Probes, Invitrogen, Milan, MI, Italy) diluted 1:200 for 1 h, washed with PBS twice and DNA stained for 10 min with 0.1 µg/ml Hoechst 33342 (Abcam, Cambridge, United Kingdom) in PBS. Samples were finally mounted with PBS/glycerol 1:1 solution.

BrdU-positive cells percentage was assessed in 30 randomly selected fields (40× magnification) for every experimental condition. Observation of samples was performed using an Olympus BX51 microscope (Olympus Italia S.r.l., Segrate, MI, Italy) equipped with a 100 W mercury lamp, under the following conditions: 450–480 nm excitation filter (excf), 500 nm dichroic mirror (dm), and 515 nm barrier filter (bf) for Alexa Fluor 488; 330–385 nm excf, 400 nm dm, and 420 nm bf, for Hoechst 33342. Images were acquired with a QICAM

Fast 1394 Digital Camera (QImaging, Surrey, BC, Canada) and processed with Image-Pro Plus software (Media Cybernetics, Inc., Rockville, MD, USA).

## 2.5 | Wound healing assay

For the wound healing assay, $2 \times 10^5$ cells per well were seeded on 24 mm $\times$ 24 mm slides. After 24 h, the confluent cell monolayers were scratched with a sterile pipette tip and then treated with gas. To evaluate cell migration, images at $4\times$ magnification were taken at 0, 6, 24, and 48 h post-treatment using an inverted microscope (Leica DMIL, Leica Microsystems S.r.l., Buccinasco, MI, Italy) equipped with a camera (Optika Microscopes, Ponteranica, BG, Italy). The scratched area free of cells was measured in four randomly chosen fields in three independent experiments, for a total of 12 fields per sample. The value of the cell-free area was expressed as a percentage of the value at time 0 (considered as 100%).

## 2.6 | Scanning electron microscopy (SEM)

For SEM examination, $2 \times 10^4$ cells were seeded on round slides of 20 mm in diameter. After 24 h, the cell monolayers of LPS-activated and LPS + DMF samples were scratched as described above and treated with gas. Non-activated cell sample was also considered as basal condition. After 24 h post-treatment, the cells were fixed with 2.5% glutaraldehyde in PBS at 4°C for 2 h, post-fixed with 1% $OsO_4$ at 4°C for 1 h, and dehydrated with ethanol. Then, the cell monolayers were dehydrated with a critical point dryer (CPD 030, BAL-TEC AG, Balzers, Liechtenstein), mounted on metallic specimen stubs and sputter-coated with gold (MED 010, BAL-TEC AG). SEM observations were performed by an XL30 ESEM (FEI Italia S.r.l., Milan, Italy). Using ImageJ software (NIH), the surface length of 15 cells per sample facing the scratch was measured. Measure was made by including and excluding cell protrusions and the ratio between the two values gave the index of cell surface irregularity (the higher the value, the rougher the cell).

## 2.7 | Transmission electron microscopy (TEM)

Morphological and immunocytochemical analyses were carried out at TEM in order to analyze the effects of the exposure to low $O_3$ concentrations on the fine cell features and Nrf2 nuclear translocation. Based on our previous investigations (Galiè et al., 2018), the effects were evaluated 24 h after gas treatment, in order to clearly detect morphological changes and Nrf2 translocation on the transcriptional sites. Non-activated cell sample was also considered as basal condition. The cells ($2 \times 10^4$ cells per well) were seeded on round slides of 20 mm in diameter. After 24 h, the cell monolayers were treated with gas. After 24 h post-treatment, the cells were fixed with 2.5% glutaraldehyde and 2% paraformaldehyde in 0.1 M phosphate buffer, pH 7.4, at 4°C for 1 h, washed, post-fixed with 1% $OsO_4$ at 4°C for 30 min, dehydrated with acetone and embedded in Epon as monolayer (Costanzo & Malatesta, 2019).

For ultrastructural morphology, ultrathin sections were collected and stained with Reynolds lead citrate. For immunocytochemistry, ultrathin sections were collected and immunolabeled. Briefly, sections were floated on normal goat serum diluted 1:100 in PBS, incubated overnight at 4°C with the anti-Nrf2 antibody (Abcam #ab62352, Cambridge, United Kingdom) diluted 1:2 with PBS containing 0.1% bovine serum albumin (Fluka, Buchs, Switzerland) and 0.05% Tween 20. Sections were then floated on normal goat serum and incubated for 30 min with a goat anti-rabbit IgG secondary antibody conjugated with 12-nm gold particles (Jackson ImmunoResearch Laboratories Inc., West Grove, PA, USA), diluted 1:20 in PBS. After rinsing with PBS and water, the sections were finally air-dried and weakly stained with Reynolds lead citrate for 1 min. As immunostaining controls, the primary antibody was omitted.

The samples were observed in a Philips Morgagni transmission electron microscope (FEI Company Italia Srl, Milan, Italy) operating at 80 kV; a Megaview III camera (FEI Company Italia Srl) was used for image acquisition.

Quantitation of anti-Nrf2 immunolabeling was performed by estimating the gold particle density on sections treated in the same run: the area of nucleoplasmic regions and resin regions (as an intra-sample negative control) was measured on 15 micrographs ($28,000\times$) per sample. Background evaluation was performed in sections processed for immunocytochemistry without the primary antibody. In each measured area, the gold particles were counted manually and the labeling density (i.e., the number of gold particles/$\mu m^2$ of nucleoplasm) was calculated.

## 2.8 | Real-time quantitative polymerase chain reaction

Ribonucleic acid (RNA) was extracted from LPS-activated and LPS + DMF HMC3 samples 24 h after the gas exposure by using the Qiagen RNeasy Plus mini kit (ref. 74134) (QiagenS.r.l., Milan, Italy). cDNA was generated by SuperScript™ III Reverse Transcriptase (Invitrogen, cat. no. 18080093) (Thermo Fisher Scientific Inc., Waltham, MA, USA) and amplified at qPCR with Applied Biosystems™ SYBR™ Green PCR Master Mix (Applied Biosystems™ 4309155) (Thermo Fisher Scientific Inc.) using two distinct sets of primers specific for human Heme oxygenase 1 (Hmox1) (primers set 1: Forw: CCTAAACTTCAGAGGGGGCG, Rev: GACAGCTGCCACATTAGGGT; primers set 2: Forw: AGTCTTCGCCCCTGTCTACT, Rev: CTTCACA-TAGCGCTGCATGG). The Applied Biosystems Step-One Real-Time PCR System was used for amplification (Thermo Fisher Scientific Inc.).

## 2.9 | IL-6, TNF-$\alpha$, and IL-13 secretion

The amount of IL-6, TNF-$\alpha$, and Interleukin-13 (IL-13) secreted was evaluated in the culture medium of LPS-activated and LPS + DMF HMC3 cells, 24 h after the gas treatment (Dello Russo et al., 2018).

Non-activated cell sample was also considered as basal condition. The pro-inflammatory IL-6 and TNF-$\alpha$ are known to be produced by HMC3 (Dello Russo et al., 2018). Recently it has been demonstrated that HMC3 cells are able to synthesize and secrete also small amounts of the anti-inflammatory IL-13 (Caruso et al., 2021; Pallio et al., 2021).

For each sample, $2 \times 10^4$ cells per 24-multi-well plate were seeded after gas treatment; experiments were performed in duplicate. The medium collected from each cell sample was centrifuged at 1500 g for 15 min, and stored at $-80°$C. Quantitation of IL-6, TNF-$\alpha$, and IL-13 were quantified using a Luminex Bio-Rad Bio-Plex 100 (Bio-Rad Laboratories, Segrate, MI, Italy) and the Bio-Plex Manager software, v6.0. A total of 50 μl aliquots of undiluted medium were placed in a 96-well plate, beads conjugated with fluorophores and antibodies against IL-6, TNF-$\alpha$, and IL-13 were added and, after appropriate incubation and washing, the plate was read by the Luminex system. Samples were run in duplicate.

## 2.10 | Statistical analysis

For each variable mean value ± SD were calculated. For statistical analysis of MTT assay, wound healing assay, and cytokine secretion, the Kruskal–Wallis non-parametric test followed by the Mann–Whitney test for pairwise comparison was applied. For statistical comparison of the mitotic index and the index of cell surface irregularity, the one-way analysis of variance (ANOVA) test followed by Bonferroni's post-hoc test was used. A $p$ value ≤0.05 indicated statistical significance.

## 3 | RESULTS

### 3.1 | Cell viability assay

The effect of gas treatment on cell viability was assessed in LPS-activated (Figure 1) and LPS + DMF HMC3 cells (Figure 2).
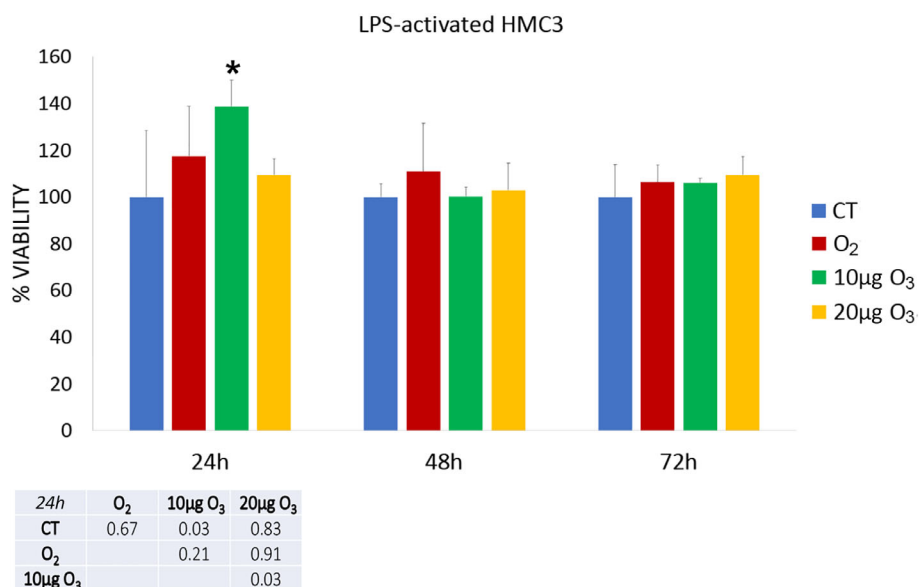
After 24 h of gas exposure, 10 μg $O_3$ LPS-activated HMC3 samples showed a statistically significant increase in cell viability in comparison with CT and 20 μg $O_3$-treated cells. After both 48 and 72 h, no statistically significant difference resulted among the LPS-activated samples ($p = 0.68$ and $p = 0.75$, respectively).

In LPS + DMF cells, gas exposure did not change significantly cell viability in comparison with CT samples (a statistically significant decrease was only observed in 20 μg $O_3$ LPS + DMF cells in comparison with $O_2$-treated cells). After 48 h of post-treatment, no statistically significant difference was found among the LPS + DMF samples ($p = 0.17$). At 72 h, 20 μg $O_3$ LPS + DMF cells showed significantly lower cell viability in comparison to all the other samples.

The exposure to 30 and 50 μg $O_3$/ml $O_2$ induced a drastic decrease of the cell viability already 24 h post-treatment as verified by the trypan blue test (not shown). The concentrations of 30 and 50 μg $O_3$/ml $O_2$ were indeed excluded from the experimentation.

### 3.2 | Cell proliferation

The proliferation activity of HMC3 cells was assessed by evaluating the mitotic index and the percentage of S-phase positive cells by BrdU incorporation. Mitotic index was assessed in non-activated HMC3 cells (3.49 ± 0.64, as basal condition) and compared with CT samples of LPS-activated and LPS + DMF cells, revealing no statistically significant difference ($p = 0.51$). The percentage of mitotic cells observed 48 h after treatment in LPS-activated and LPS + DMF cells showed no statistically significant difference between CT and treated cells ($p = 0.80$, $p = 0.78$, and $p = 0.98$, respectively) (Figure 3).

The percentage of BrdU-positive HMC3 cells (Figure 4a–c) did not significantly change in non-activated (29.99 ± 1.29) and CT samples of LPS-activated and LPS + DMF cells ($p = 0.30$ for both comparisons).

After 48 h of gas treatment, no significant difference in the percentage of BrdU-positive HMC3 cells was found among CT and gas-
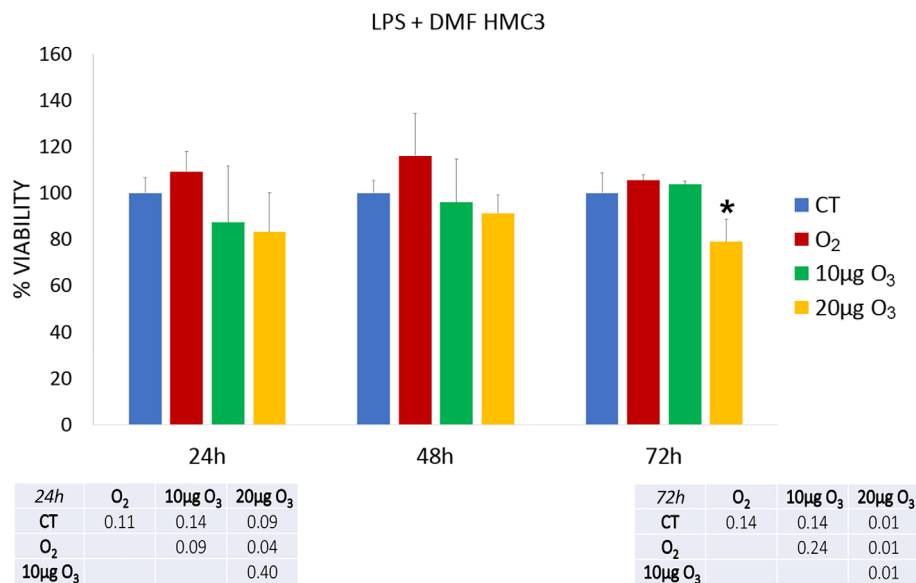


**FIGURE 1** Cell viability 24, 48, and 72 h after $O_2$-$O_3$ treatment in LPS-activated HMC3 cells as assessed by the MTT assay. Histograms show the mean values ± SD of percentage of cell viability; the table reports the $p$ values for all the comparisons made. Asterisk (*) indicates the statistically significant difference from the corresponding CT sample ($p < 0.05$). HMC3, human microglial clone 3; LPS, lipopolysaccharide

| 24h | $O_2$ | 10μg $O_3$ | 20μg $O_3$ |
|---|---|---|---|
| CT | 0.67 | 0.03 | 0.83 |
| $O_2$ | | 0.21 | 0.91 |
| 10μg $O_3$ | | | 0.03 |

**FIGURE 2** Cell viability 24, 48, and 72 h after the treatment in LPS + DMF HMC3 cells as assessed by the MTT assay. Histograms show the mean values ± SD of percentage of cell viability; the table reports the $p$ values for all the comparisons made. Asterisk (*) indicates the statistically significant difference from the respective CT sample ($p < 0.05$). DMF, dimethyl fumarate; HMC3, human microglial clone 3; LPS, lipopolysaccharide
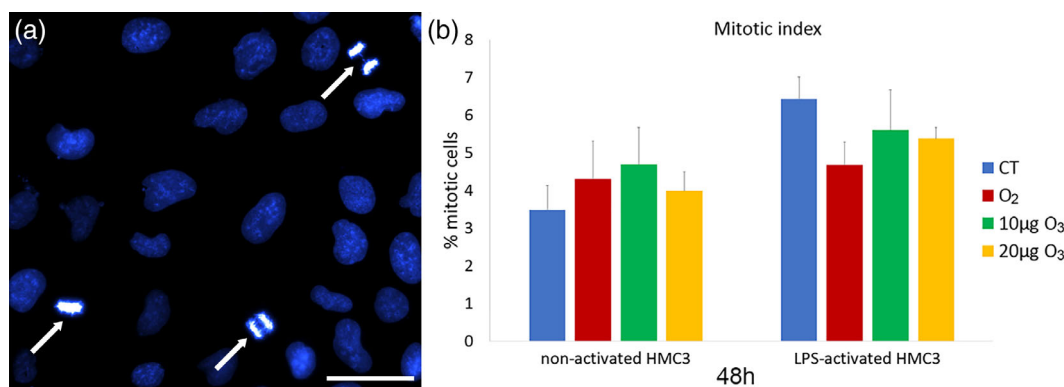
| 24h | $O_2$ | 10μg $O_3$ | 20μg $O_3$ |
|---|---|---|---|
| CT | 0.11 | 0.14 | 0.09 |
| $O_2$ | | 0.09 | 0.04 |
| 10μg $O_3$ | | | 0.40 |

| 72h | $O_2$ | 10μg $O_3$ | 20μg $O_3$ |
|---|---|---|---|
| CT | 0.14 | 0.14 | 0.01 |
| $O_2$ | | 0.24 | 0.01 |
| 10μg $O_3$ | | | 0.01 |



**FIGURE 3** (a) Representative image at fluorescence microscopy of HMC3 cells stained for DNA with Hoechst 33342. Note the mitotic cells (arrows). Bar, 100 μm. (b) Mean values ± SD of percentage of mitotic cells at 48 h after the treatment in LPS-activated and LPS + DMF HMC3 cells. DMF, dimethyl fumarate; HMC3, human microglial clone 3; LPS, lipopolysaccharide

treated samples in both LPS-activated and LPS + DMF cells ($p = 0.06$ for both).

## 3.3 | Wound healing assay

The effect of gas exposure on the migration capability of LPS-activated and LPS + DMF cells was evaluated by the wound healing assay (representative images in Figure 5).

In comparison to non-activated cells (90.52 ± 3.81), LPS-activated CT cells showed no significant difference in migration rate at 6 h ($p = 0.06$); instead, LPS + DFM CT cells showed lower migration rates in comparison to both non-activated and LPS-activated CT cells ($p = 0.03$). At 24 h, LPS-activated CT cells showed a significant increase in migration rate in comparison to the non-activated ones (45.67 ± 10.45) ($p = 0.03$), whereas no statistical difference was found versus LPS + DMF cells ($p = 0.06$).

In LPS-activated cells (Figure 5c), no statistically significant difference was found in migration rate among CT and gas-treated samples

at 6 h post-treatment ($p = 0.79$), while at 24 h the migration rate of CT sample was significantly higher in comparison with $O_2$- and 10 μg $O_3$-treated samples ($p = 0.03$).

In LPS + DFM cells (Figure 5d), no statistical difference was found among CT and gas-treated samples at both 6 and 24 h.

After 48 h, the wound was completely healed in all samples (not shown).

## 3.4 | Cell morphology

The cell shape, surface protrusions, and organelle organization of HMC3 cells were observed by bright field microscopy, SEM, and TEM, respectively.

At inverted microscopy, HMC3 cells showed a flattened and spindle-like shape in all the conditions investigated, without evident modifications following gas treatments (Figure 6a). However, in LPS-activated and LPS + DMF samples large flat round-shaped cells were observed (Figure 6b,c).
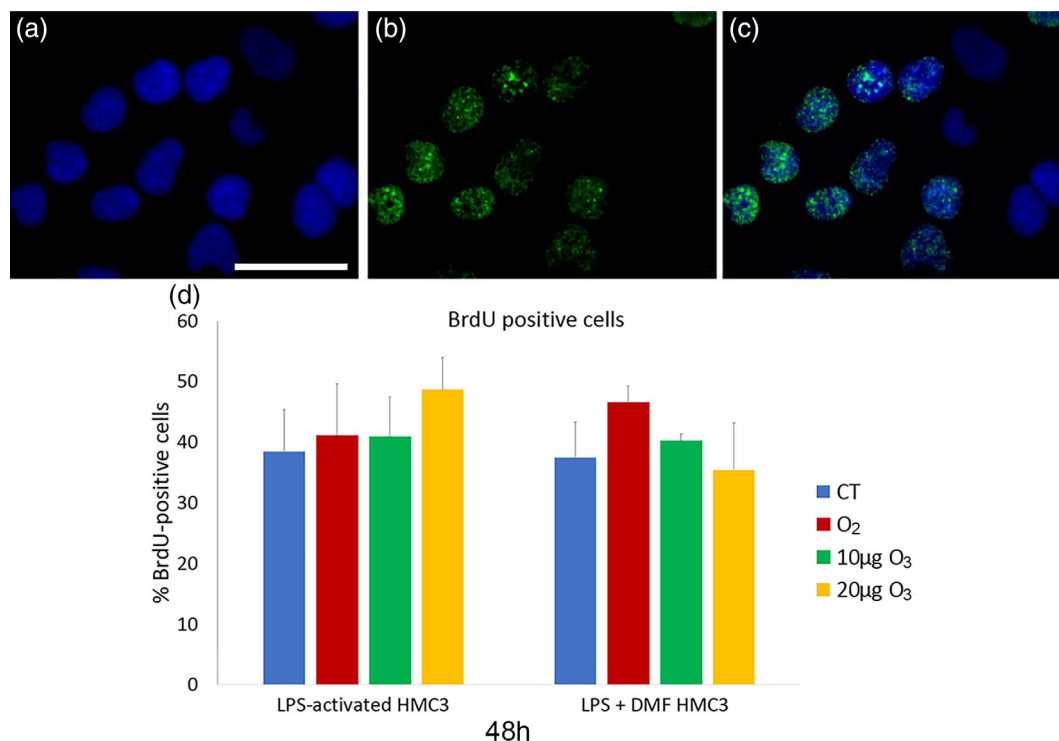
**FIGURE 4** Representative fluorescence microscopy images of HMC3 cells stained for DNA with Hoechst 33342 (blue) (a), immunolabeled for BrdU (green) (b), and merged (c). Bar, 100 μm. (d) Mean values ± SD of percentages of BrdU-positive cells 48 h after the treatment (one experiment in triplicate). BrdU, Bromodeoxyuridine; DMF, dimethyl fumarate; HMC3, human microglial clone 3; LPS, lipopolysaccharide

SEM observation showed many thin surface protrusions in all cell samples (Figure 7a–c), independently on activation, and gas treatment. The quantitative evaluation of the surface irregularity did not show significant differences between non-activated cells ($2.54 \pm 0.88$) and CT samples of LPS-activated and LPS + DFM cells ($p = 0.07$). Moreover, gas treatment did not induce significant change in cell surface irregularity in LPS-activated ($p = 0.18$) and LPS + DFM cells ($p = 0.73$) (Figure 7d).

TEM provided information on the fine structural organization of HMC3 cells (Figures 8 and 9). Non-activated cells showed one nucleus; the cytoplasm was characterized by well-preserved Golgi complex, abundant smooth endoplasmic reticulum, numerous free ribosomes, rare small lipid droplets, and glycogen granules (Figure 8a). Elongated mitochondria with developed lamellar cristae were distributed in the cytoplasm (Figure 8b).

Compared with the non-activated sample (Figure 8), in the CT samples of LPS-activated (Figure 9a) and LPS + DMF (Figure 9e) cells, the cytoplasm density decreased and many glycogen granule clusters were often associated with the numerous lipid droplets. In LPS-activated cells (Figure 9a–d) and in LPS + DMF cells (Figure 9e–h) gas-treated samples were similar with their respective CT.

## 3.5 | Nrf2 distribution

To assess whether the $O_3$ treatment might affect the nuclear distribution of the transcription factor Nrf2, we investigated the ultrastructural immunolabeling of HMC3 cell nuclei. In all samples, Nrf2 was distributed in the euchromatin space (Figure 10), especially on perichromatin fibrils where RNA transcription takes place (Niedojadlo et al., 2011).

Quantitative evaluation of the Nrf2 density revealed that LPS + DMF CT showed similar values to non-activated cells ($0.86 \pm 0.32$) ($p = 0.33$), whereas in LPS-activated CT was significantly lower ($p = 0.001$). LPS-activated CT also revealed lower values in comparison to LPS + DMF CT ($p = 0.02$).

As shown in Figure 11, in LPS-activated cells, both 10 and 20 μg $O_3$-treated cells showed an increase of the nucleoplasmic anti-Nrf2 labeling density in comparison with CT and $O_2$-treated cells. In LPS + DMF cells, no statistically significant difference was found among the samples ($p = 0.45$).

## 3.6 | Heme oxygenase 1

Heme oxygenase 1 (Hmox1) gene expression (Figure 12), assessed by Real-time quantitative polymerase chain reaction (RT-PCR), resulted significantly higher in both LPS-activated CT and LPS + DMF CT cells when compared with non-activated samples ($48.50 \pm 24.48$) ($p = 0.027$).

In both LPS-activated and LPS + DMF cells no significant difference was found in Hmox1 gene expression among CT and gas-treated samples, apart from a significant lowering in LPS + DMF cells treated with 20 μg $O_3$ (Figure 12).
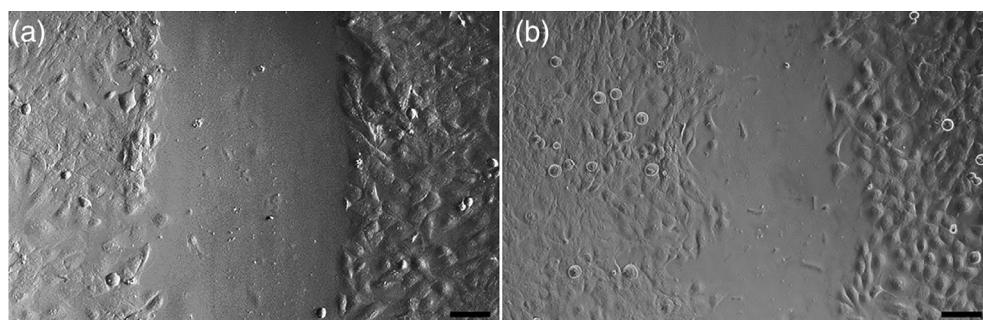
**FIGURE 5** Representative images at inverted microscopy of HMC3 cells at 6 h (a) and 24 h (b) of the wound healing assay. Bars, 100 μm. Means ± SD of percentages of cell-free areas of CT, $O_2$- and $O_3$-treated LPS-activated (c) and LPS + DFM (d) HMC3 cells at 6 h and 24 h of the wound healing assay. Asterisks (*) indicate the statistically significant difference from the corresponding CT samples ($p < 0.05$). DMF, dimethyl fumarate; HMC3, human microglial clone 3; LPS, lipopolysaccharide
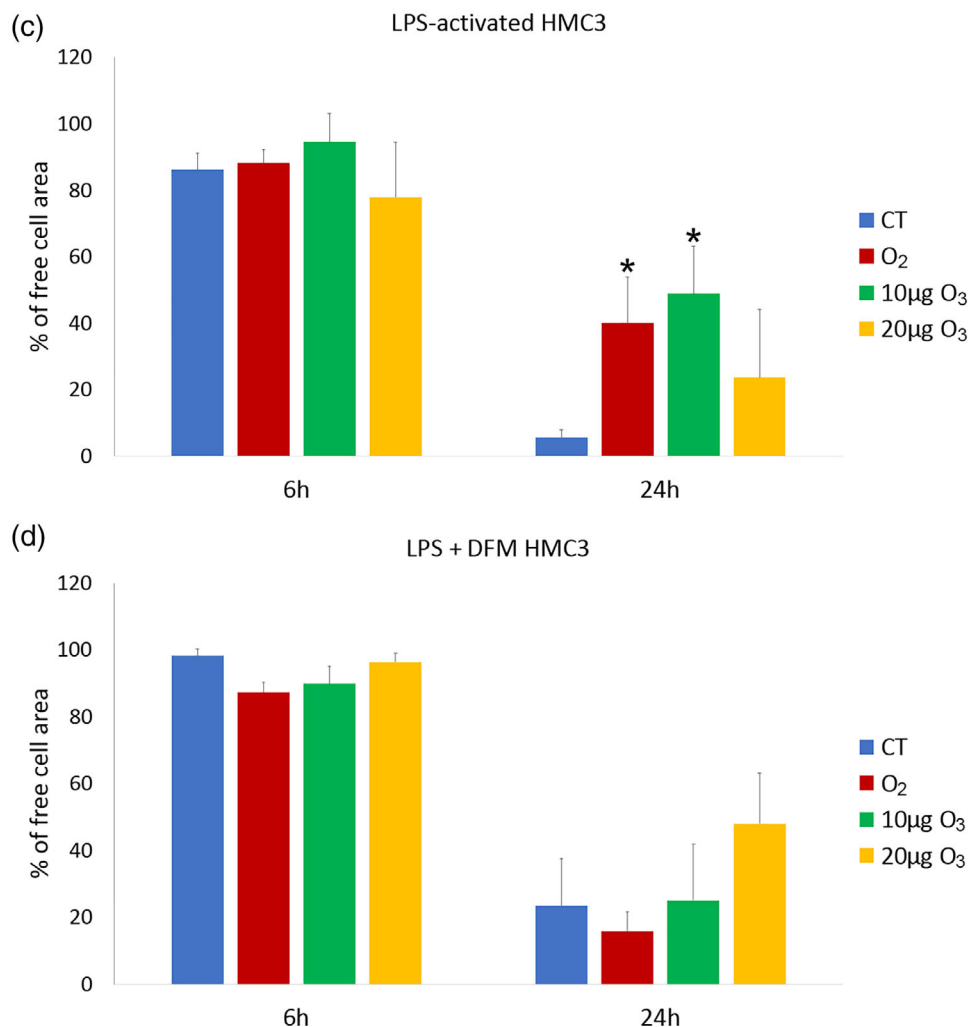
## 3.7 | IL-6, TNF-$\alpha$, and IL-13 secretion

The amount of IL-6 (Figure 13) and TNF-$\alpha$ (Figure 14) as pro-inflammatory cytokines, and IL-13 (Figure 15) as an anti-inflammatory cytokine was evaluated in the culture medium of LPS-activated and LPS + DMF HMC3 cells, in order to assess their secretory activity.

As for IL-6, LPS-activated CT cells showed significantly higher values in comparison to non-activated cells (695.45 ± 34.98) ($p = 0.005$). LPS + DMF CT cells showed values significantly higher than non-activated cells ($p = 0.004$) but significantly lower than CT of LPS-activated cells ($p = 0.004$). As shown in Figure 3, in LPS-activated

conditions and in LPS + DMF samples both 10 and 20 μg $O_3$-treated cells showed significantly lower values than CT and $O_2$-treated cells.

As for TNF-$\alpha$, CT samples of LPS-activated and LPS + DMF cells showed significantly higher values in comparison to non-activated cells (0.98 ± 0.29) ($p = 0.02$ and $p = 0.03$, respectively); moreover, CT sample of LPS + DMF cells showed significantly lower values than CT of LPS-activated cells ($p = 0.04$). In LPS-activated conditions (Figure 14), both 10 and 20 μg $O_3$-treated samples showed significantly lower values than CT and $O_2$-treated cells, while no significant difference was found among cell samples in LPS + DMF conditions ($p = 0.08$).
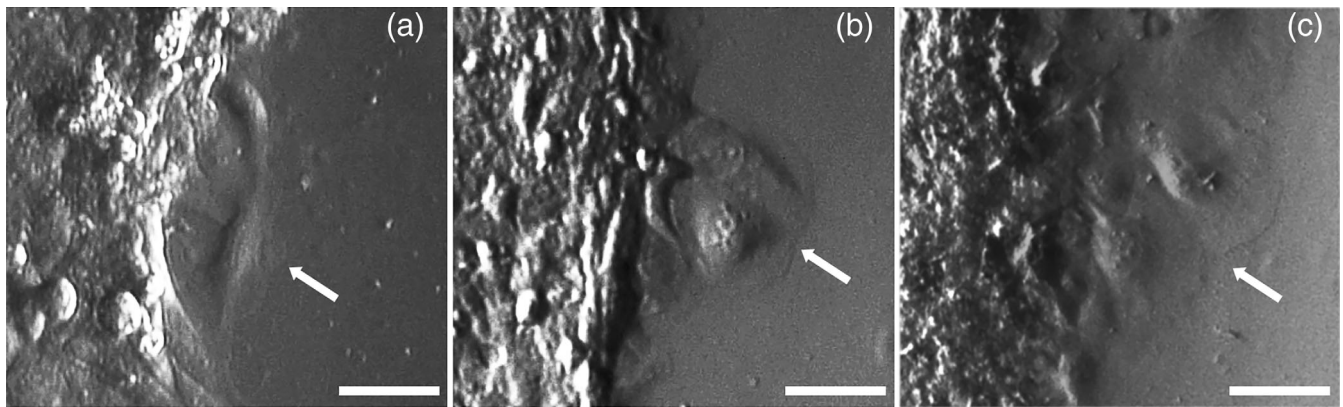
**FIGURE 6** Representative inverted microscope images of spindle-like non-activated HMC3 cells (a) and round-shaped cells in LPS-activated (b) and LPS + DMF (c) HMC3 cells (arrows). Bars, 50 μm. DMF, dimethyl fumarate; HMC3, human microglial clone 3; LPS, lipopolysaccharide
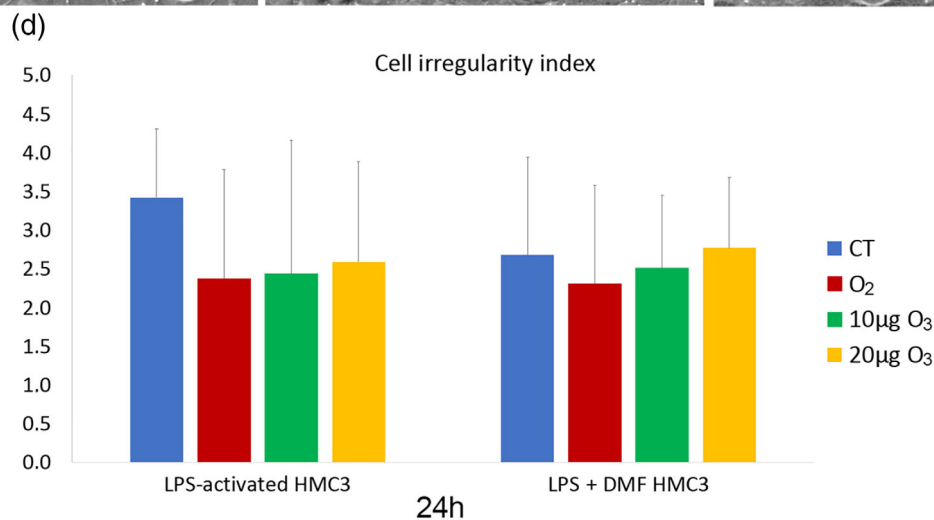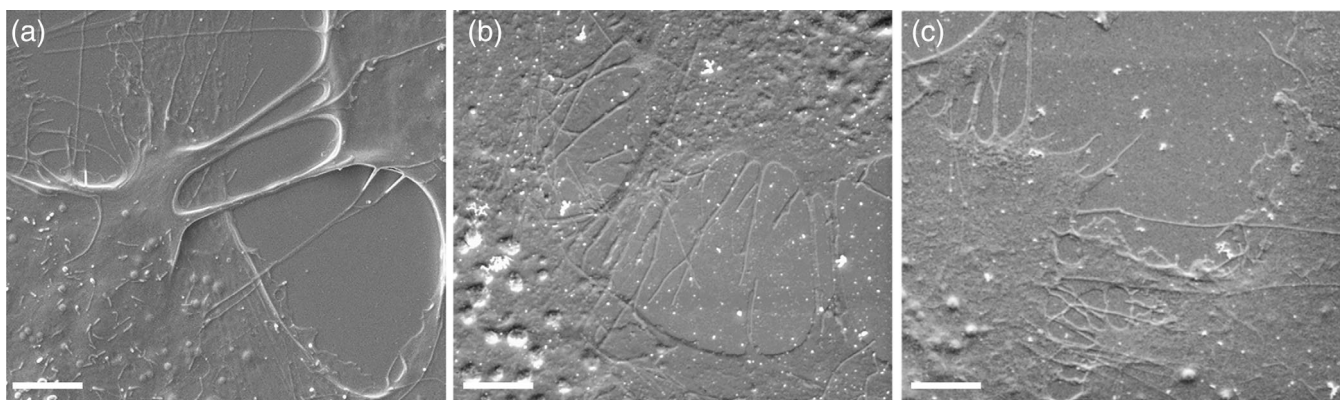


**FIGURE 7** Examples of SEM micrographs of non-activated cells (a), LPS-activated (b) and LPS + DMF CT cells. Bars, 5 μm. Means ± SD of the cell irregularity index at 24 h after the treatment (d). DMF, dimethyl fumarate; LPS, lipopolysaccharide; SEM, scanning electron microroscopy

As for IL-13 (Figure 15), CT samples of LPS-activated cells showed values below the detection limit, while CT samples of LPS + DMF cells showed values significantly lower that non-activated cells (31.08 ± 13.25) ($p = 0.03$). No significant difference was found among cell samples in LPS-activated and LPS + DMF conditions ($p = 0.66$ and $p = 0.06$, respectively).

## 4 | DISCUSSION

$O_2$-$O_3$ therapy proved to be beneficial in some neurodegenerative diseases characterized by high oxidative stress and inflammation (Delgado-Roche et al., 2017; Izadi et al., 2020; Lin et al., 2019; Lintas et al., 2013; Tahmasebi et al., 2021). These promising data require a
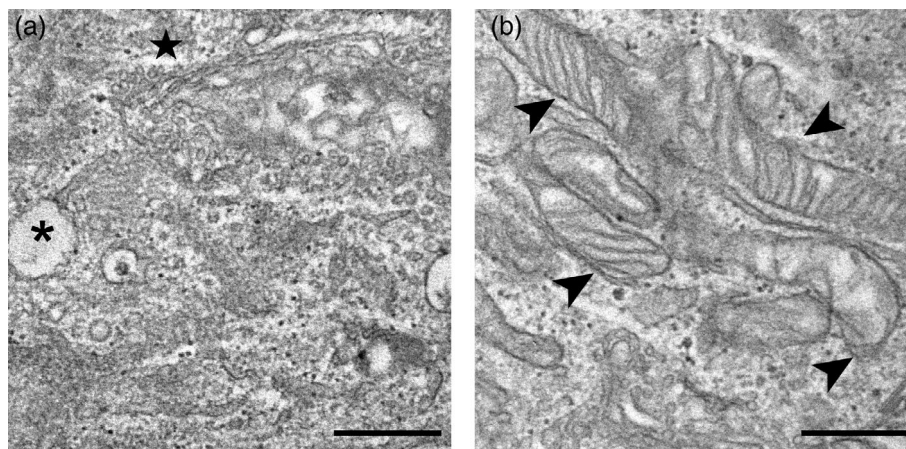
**FIGURE 8** TEM micrographs of non-activated cells (a–b). Note the cytoplasm rich in smooth endoplasmic reticulum and elongated mitochondria (arrowheads) with lamellar cristae. Asterisk (*) indicates a lipid droplet; star indicates Golgi complex. Bars, 500 nm. TEM, transmission electron microroscopy
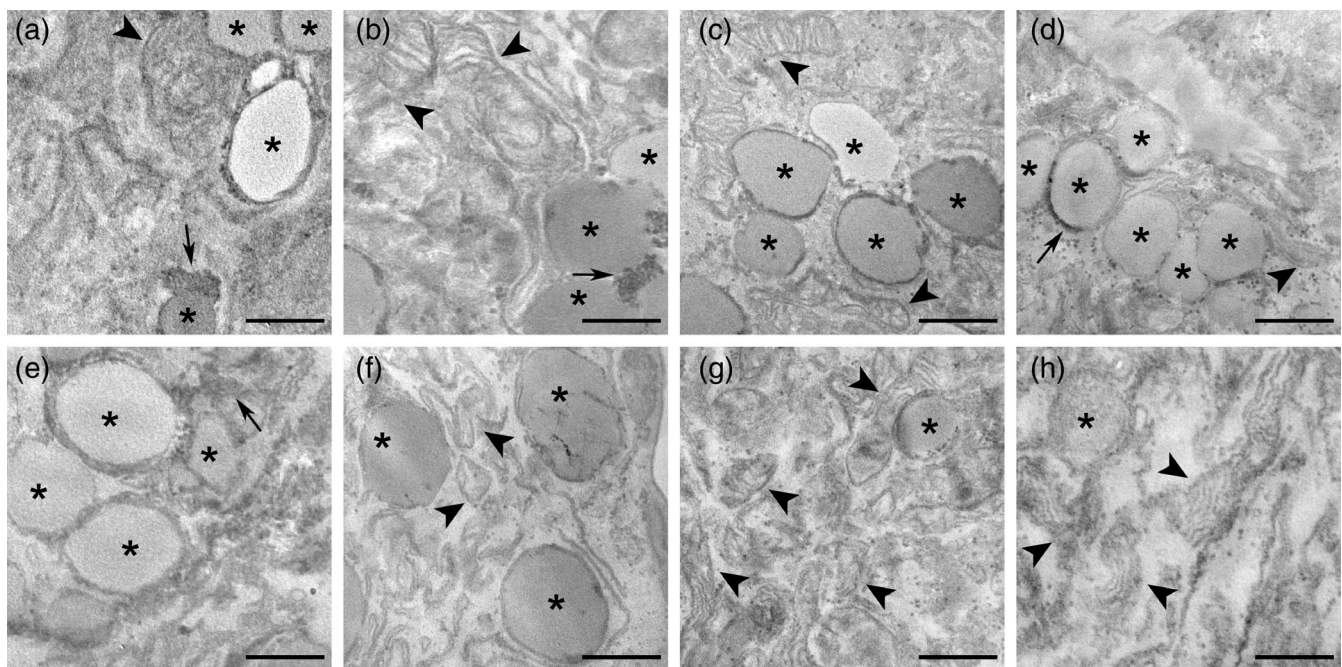


**FIGURE 9** TEM micrographs of LPS-activated (a–d) and LPS + DMF (e–h) HMC3 cells. CT cells (a, e); $O_2$-treated cells (b, f), 10 μg $O_3$-treated cells (c, g); 20 μg $O_3$-treated cells (d, h). Arrowheads indicate mitochondria. Note the accumulation of lipid droplets (asterisks) and glycogen (arrows) in LPS-activated and LPS + DMF cells. Bars, 500 nm. DMF, dimethyl fumarate; HMC3, human microglial clone 3; LPS, lipopolysaccharide; TEM, transmission electron microroscopy

deep knowledge of the $O_3$ action mechanisms on microglial cells, which play multiple roles for the maintenance of homeostasis in the CNS and are primarily involved in both neuroinflammatory and neuroprotective processes in many neurodegenerative diseases (Ho, 2019; Kwon & Koh, 2020; Leng & Edison, 2021; Voet et al., 2019).

First, our findings demonstrated that the in vitro experimental model used in the present study is reliable. In fact, consistent with previous findings on activated microglial cells, LPS-activated HMC3 cells showed increased migration rate (Dello Russo et al., 2018), morphological modifications from elongated/branched to larger roundish cells (Baek et al., 2021; Garcia-Contreras & Thakor, 2021), lipid accumulation in the cytoplasm (Khatchadourian et al., 2012), decreased cytoplasmic and mitochondrial electron density (Anderson

et al., 1995), decreased Nrf2 amounts, and increased Hmox1 gene expression and secretion of the pro-inflammatory cytokines IL-6 and TNF-$\alpha$ (Pallio et al., 2021). Treatment with DMF – a neuroprotective drug acting through Nrf2 (Scannevin et al., 2012) – proved to mitigate the alterations in LPS-activated cells, partially restoring some of the structural and functional features of non-activated HMC3 cells.

Gas treatment did not alter cell viability in both LPS-activated and LPS + DMF cells (apart from a lower vitality after 72 h from the treatment with 20 μg $O_3$ in LPS + DMF cells). These findings are in agreement with reports in the literature demonstrating that these low $O_3$ concentrations are safe for many cell types (Cisterna et al., 2021; Costanzo et al., 2018; Costanzo et al., 2015; Scassellati et al., 2017). However, HMC3 cells proved to be especially sensitive to oxidative

**FIGURE 10** Representative TEM micrographs of HMC3 cell nuclear details after immunolabeling of Nrf2: CT (a) and 20 µg $O_3$ (b) of LPS-activated cells; CT (c) and 20 µg $O_3$ (d) of LPS + DMF cells. Immunogold labeling (arrows) occurs on euchromatic regions, especially on perichromatin fibrils (thick arrows). C, cytoplasm. Bars, 200 nm. DMF, dimethyl fumarate; HMC3, human microglial clone 3; LPS, lipopolysaccharide; TEM, transmission electron microroscopy
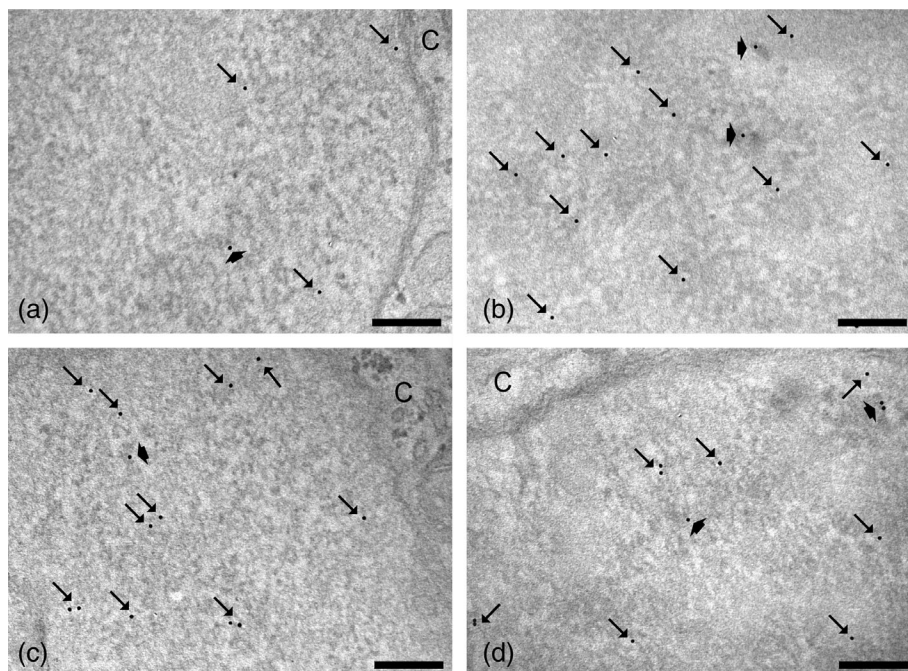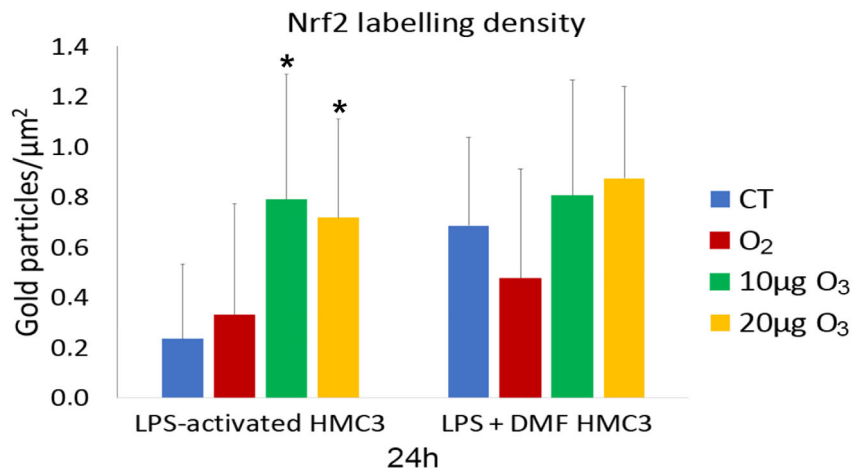


**FIGURE 11** Mean value ± SD of anti-Nrf2 labeling 24 h after treatment. The table reports the *p* values for all the comparisons made. Asterisks (*) indicate the statistically significant difference from the corresponding CT samples (*p* < 0.05). DMF, dimethyl fumarate; HMC3, human microglial clone 3; LPS, lipopolysaccharide; Nrf2, nuclear factor erythroid 2-related factor 2
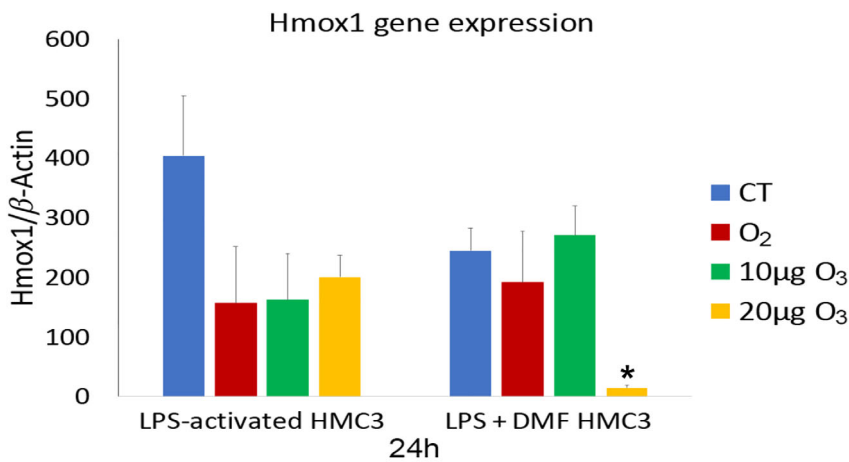


| LPS-act | $O_2$ | 10µg $O_3$ | 20µg $O_3$ |
|---|---|---|---|
| CT | 0.83 | 0.003 | 0.002 |
| $O_2$ | | 0.002 | 0.001 |
| 10µg $O_3$ | | | 0.63 |

stress since a concentration of 30 µg of $O_3$, which is tolerated by most cell types under similar experimental conditions, were lethal to them.
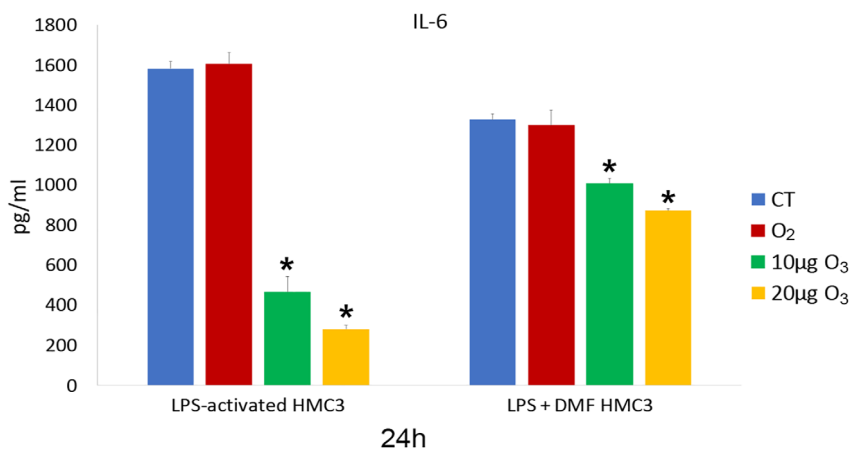
Similarly, gas exposure did not affect proliferation in both LPS-activated and LPS + DMF cells, as shown by the evaluation of both the mitotic index and BrdU-positivity, according to previous reports on other cell types in vitro (Costanzo et al., 2020; Costanzo et al., 2015; Scassellati et al., 2017).

The safety of 10 and 20 µg $O_3$ for HMC3 cells was unequivocally testified by the high-resolution analysis at TEM and SEM. In fact, while LPS treatment induced in microglial cells various morphological modifications in comparison to control (as highlighted above), gas exposure did not affect any feature in both LPS-activated and LPS + DMF cells.
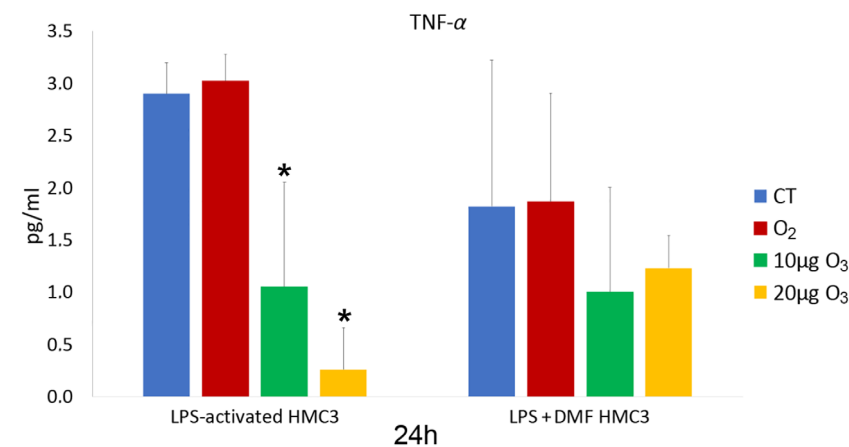
Cell motility represents a hallmark of microglial cell activation (Baek et al., 2021; Garcia-Contreras & Thakor, 2021; Zhang et al., 2016). Accordingly, after LPS treatment, some HMC3 cells showed a large roundish cell body, characteristic of activated microglia able to ameboid movement, while the wound healing test demonstrated that LPS-activated cells had a higher migration rate in comparison to non-activated cells. As for the effect of gas exposure, in LPS-activated cells both $O_2$ and 10 µg $O_3$ decreased significantly cell motility while cell surface protrusions, involved in cell migration (Fraley et al., 2010), showed a slight although not significant tendency to reduce. This pointed out the reduction of one typical feature of the inflammation phenotype. The reasons for such an effect remain unclear but it could be related to the influence of oxidant-antioxidant

**Hmox1 gene expression**

| LPS + DMF | O$_2$ | 10µg O$_3$ | 20µg O$_3$ |
|---|---|---|---|
| CT | 0.63 | 0.93 | 0.003 |
| O$_2$ | | 0.33 | 0.01 |
| 10µg O$_3$ | | | 0.001 |

**FIGURE 12** Mean value ± SD of Hmox1 expression at 24 h after treatment. Asterisk (*) indicates the statistically significant difference from the corresponding CT sample ($p < 0.05$). DMF, dimethyl fumarate; HMC3, human microglial clone 3; Hmox1, Heme oxygenase 1; LPS, lipopolysaccharide



**IL-6**

| LPS-act | O$_2$ | 10µg O$_3$ | 20µg O$_3$ | LPS+DMF | O$_2$ | 10µg O$_3$ | 20µg O$_3$ |
|---|---|---|---|---|---|---|---|
| CT | 0.47 | 0.005 | 0.005 | CT | 0.52 | 0.005 | 0.005 |
| O$_2$ | | 0.005 | 0.005 | O$_2$ | | 0.005 | 0.005 |
| 10µg O$_3$ | | | 0.005 | 10µg O$_3$ | | | 0.005 |

**FIGURE 13** IL-6 amounts (mean values ± SD) detected in the medium of LPS-activated and LPS + DMF HMC3 cell samples 24 h after gas treatment (two experiments in duplicate). The table reports the $p$ values for all the comparisons made. Asterisks (*) indicate the statistically significant difference from the corresponding CT samples ($p < 0.05$). DMF, dimethyl fumarate; HMC3, human microglial clone 3; IL-6, Interleukin-6; LPS, lipopolysaccharide



**TNF-α**

| LPS-act | O$_2$ | 10µg O$_3$ | 20µg O$_3$ |
|---|---|---|---|
| CT | 0.90 | 0.03 | 0.03 |
| O$_2$ | | 0.05 | 0.05 |
| 10µg O$_3$ | | | 0.19 |

**FIGURE 14** TNF-α amounts (mean values ± SD) detected in the medium of LPS-activated and LPS + DMF HMC3 cell samples 24 h after gas treatment (two experiments in duplicate). The table reports the $p$ values for all the comparisons made. Asterisks (*) indicate the statistically significant difference from the corresponding CT samples ($p < 0.05$). DMF, dimethyl fumarate; HMC3, human microglial clone 3; LPS, lipopolysaccharide; TNF-α, tumor necrosis factor-α

**FIGURE 15** IL-13 amounts (mean values ± SD) detected in the medium of LPS-activated and LPS + DMF HMC3 cell samples 24 h after gas treatment (two experiments in duplicate). DMF, dimethyl fumarate; HMC3, human microglial clone 3; IL-13, Interleukin-13; LPS, lipopolysaccharide
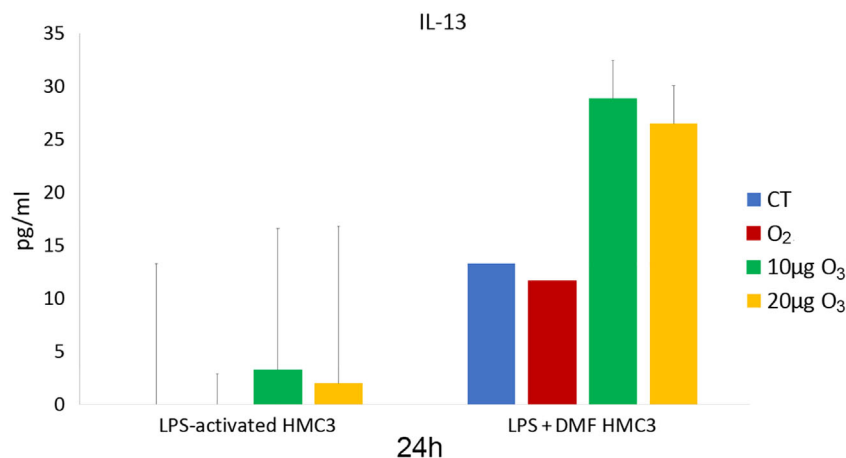


balance on cytoskeleton dynamics (Muliyil & Narasimha, 2014); studies on this topic are currently in progress in our laboratories.

Similarly to other cell types treated with low $O_3$ concentrations (Cappellozza et al., 2021; Galiè et al., 2018), in LPS-activated cells Nrf2 translocated to the nucleus following the mild oxidative stress due to 10 and 20 µg $O_3$ exposure. However, in HMC3 cells this translocation did not lead to an increase in the transcription of Hmox1 gene, the gene marker of the antioxidant response following $O_3$ treatment (Scassellati et al., 2017), thus revealing a lower responsiveness of these microglial cells to the antioxidant action of $O_3$ in comparison to other cell types submitted to the same gas treatment (Cappellozza et al., 2021; Cisterna et al., 2021; Scassellati et al., 2017). In LPS + DMF cells no difference in the amount of nuclear Nrf2 was induced by gas exposure. Since the quantity of nuclear Nrf2 found in LPS + DMF CT cells was higher than in LPS-activated CT cells, it can be hypothesized that $O_3$ has no additional effect to the nuclear translocation induced by the treatment with DMF (Scannevin et al., 2012). Consistently, no increase in Hmox1 expression was induced by the gas treatment in LPS + DMF cells. It is worth noting that Nrf2 has multiple direct and indirect effects on manifold pathways concerning not only the antioxidant response but also, for example, mitochondrial bioenergetics, unfolded protein response, proteasome activity, intermediary metabolism regulation, stem cell proliferation, and differentiation (Tonelli et al., 2018). This opens broad prospects for studies on the Nrf2-driven effects of $O_3$.

Cytokine secretion is another typical hallmark of microglia activation in vivo and in vitro (Prinz et al., 2019; Wolf et al., 2017; Woodburn et al., 2021). LPS is an inflammatory agent known to increase IL-6 and TNF-$\alpha$ secretion in HMC3 (Dello Russo et al., 2018; Garcia-Contreras & Thakor, 2021; Lu et al., 2021). IL-6 and TNF-$\alpha$ are pro-inflammatory cytokines: under physiological conditions, they are scarcely present, but in many CNS pathologies or injury they are produced in high amount by various immune cells including microglia, playing multiple roles in neurorepair (Rothaug et al., 2016; Schroeter & Jander, 2005; Welser-Alves & Milner, 2013). However, in the presence of chronic neuroinflammation, their excessive secretion becomes detrimental and may promote the development of neurodegenerative diseases (Kaur et al., 2019; Lyman et al., 2013; Shabab

et al., 2017; Smith et al., 2012). On the other hand, IL-13 is an anti-inflammatory cytokine mostly secreted by lymphocytes (Minty et al., 1993) and recently found to also be produced, although in small amount, by HMC3 (Caruso et al., 2021; Pallio et al., 2021).

In LPS-activated HMC3 cells, exposure to low $O_3$ concentrations induced a marked decrease in IL-6 secretion. Similar results were found for TNF-$\alpha$. On the other hand, pure $O_2$ seems to be ineffective in modulating both cytokines, demonstrating the direct involvement of $O_3$ in decreasing the secretion of pro-inflammatory cytokines in activated HMC3 cells. Such modulatory action of low $O_3$ concentration on cytokine secretion has been already documented both in vivo and in vitro (Cappellozza et al., 2021; Cisterna et al., 2021; Delgado-Roche et al., 2017; Güçlü et al., 2016; Tahmasebi et al., 2021; Tartari et al., 2020; Zeng et al., 2020).

Interestingly, the effect of low $O_3$ concentrations on pro-inflammatory cytokines is similar to that induced by the anti-inflammatory drug DMF. This could be because both $O_3$ and DMF act through Nrf2 (Scannevin et al., 2012), likely activating similar cytoprotective pathways. It is worth noting that, as reported in a previous work (Pallio et al., 2021), activated HMC3 reduced IL-6 and TNF-$\alpha$ secretion after treatment with Metaxalone, a drug that also induces Nrf2 increase. Low $O_3$ concentrations proved to significantly decrease IL-6 secretion even in LPS + DMF cells, thus suggesting an adjuvant role.

The secretion of IL-13 from non-activated HMC3 cells was quite scarce. LPS activation induced a drastic lowering of IL-13 secretion (that became undetectable in the medium), and the slight IL-13 increase after exposure to low $O_3$ concentrations was statistically insignificant. In LPS + DMF CT cells, the exposure to DMF restored the secretion of IL-13, similarly to what found by Pallio et al., 2021 after treating HMC3 cells with Metaxalone, but again the $O_3$ treatment did not change IL-13 secretion.

In conclusion, the combined application of refined microscopical and biomolecular techniques to activated microglial HMC3 cells confirmed that low-dose $O_3$ does not induce structural alterations while being able to decrease cell migration and the secretion of pro-inflammatory cytokines. Interestingly, these responses to $O_3$ treatment do not involve the upregulation of antioxidant genes such as

Hmox1, but anyway imply the activation of Nfr2, which is known to act through many pathways besides the antioxidant ones.

The results we obtained in this simplified system in vitro allowed elucidating a basic cell mechanism, suggesting that the modulation of microglia activity may contribute to the beneficial effects of the $O_2$-$O_3$ therapy in patients affected by neurodegenerative disorders characterized by chronic inflammation.

## ACKNOWLEDGMENTS

## CONFLICT OF INTEREST

The authors declare no conflicts of interest.

## DATA AVAILABILITY STATEMENT

The data that support the findings of this study are available from the corresponding author upon reasonable request.

## ORCID

*Barbara Cisterna* https://orcid.org/0000-0001-9314-4377
*Manuela Malatesta* https://orcid.org/0000-0001-8196-9232

## REFERENCES

Anderson, W. R., Martella, A., Drake, Z. M., Hu, S., Peterson, P. K., & Chao, C. C. (1995). Correlative transmission and scanning electron microscopy study of microglia activated by interferon-gamma and tumor necrosis factor-alpha in vitro. *Pathology - Research and Practice*, 191(10), 1016–1022. https://doi.org/10.1016/s0344-0338(11)80601-1

Baek, M., Yoo, E., Choi, H. I., An, G. Y., Chai, J. C., Lee, Y. S., Jung, K. H., & Chai, Y. G. (2021). The BET inhibitor attenuates the inflammatory response and cell migration in human microglial HMC3 cell line. *Scientific Reports*, 11, 8828. https://doi.org/10.1038/s41598-021-87828-1

Bocci, V. (2012). How a calculated oxidative stress can yield multiple therapeutic effects. *Free Radical Research*, 46(9), 1068–1075. https://doi.org/10.3109/10715762.2012.693609

Buendia, I., Michalska, P., Navarro, E., Gameiro, I., Javier Egea, J., & León, R. (2016). Nrf2-ARE pathway: An emerging target against oxidative stress and neuroinflammation in neurodegenerative diseases. *Pharmacology & Therapeutics*, 157, 84–104. https://doi.org/10.1016/j.pharmthera.2015.11.003

Cappellozza, E., Costanzo, M., Calderan, L., Galiè, M., Angelini, O., Tabaracci, G., & Malatesta, M. (2021). Low ozone concentrations affect the structural and functional features of Jurkat T cells. *Processes*, 9(6), 1030. https://doi.org/10.3390/pr9061030

Caruso, G. I., Spampinato, S. F., Costantino, G., Merlo, S., & Sortino, M. A. (2021). SIRT1-dependent upregulation of BDNF in human microglia challenged with Abeta: An early but transient response rescued by melatonin. *Biomedicines*, 9(5), 466. https://doi.org/10.3390/biomedicines9050466

Cisterna, B., Costanzo, M., Lacavalla, M. A., Galiè, M., Angelini, O., Tabaracci, G., & Malatesta, M. (2021). Low ozone concentrations differentially affect the structural and functional features of non-activated and activated fibroblasts in vitro. *International Journal of Molecular Sciences*, 22(18), 10133. https://doi.org/10.3390/ijms221810133

Cisterna, B., Costanzo, M., Nodari, A., Galiè, M., Zanzoni, S., Bernardi, P., Covi, V., Tabaracci, G., & Malatesta, M. (2020). Ozone activates the Nrf2 pathway and improves preservation of explanted adipose tissue in vitro. *Antioxidants (Basel)*, 9(10), 989. https://doi.org/10.3390/antiox9100989

Costanzo, M., Boschi, F., Carton, F., Conti, G., Covi, V., Tabaracci, G., Sbarbati, A., & Malatesta, M. (2018). Low ozone concentrations promote adipogenesis in human adipose-derived adult stem cells. *European Journal of Histochemistry*, 62(3), 2969. https://doi.org/10.4081/ejh.2018.2969

Costanzo, M., Cisterna, B., Covi, V., Tabaracci, G., & Malatesta, M. (2015). An easy and inexpensive method to expose adhering cultured cells to ozonization. *Microscopie*, 23, 46–52 https://www.pagepressjournals.org/index.php/microscopie/article/view/5164/4554

Costanzo, M., Cisterna, B., Vella, A., Cestari, T., Covi, V., Tabaracci, G., & Malatesta, M. (2015). Low ozone concentrations stimulate cytoskeletal organization, mitochondrial activity and nuclear transcription. *European Journal of Histochemistry*, 59(2), 2515. https://doi.org/10.4081/ejh.2015.2515

Costanzo, M., & Malatesta, M. (2019). Embedding cell monolayers to investigate nanoparticle-plasmalemma interactions at transmission electron microscopy. *European Journal of Histochemistry*, 63(1), 3026. https://doi.org/10.4081/ejh.2019.3026

Costanzo, M., Romeo, A., Cisterna, B., Calderan, L., Bernardi, P., Covi, V., Tabaracci, G., & Malatesta, M. (2020). Ozone at low concentrations does not affect motility and proliferation of cancer cells in vitro. *European Journal of Histochemistry*, 64(2), 3119. https://doi.org/10.4081/ejh.2020.3119

Delgado-Roche, L., Riera-Romo, M., Mesta, F., Hernández-Matos, Y., Barrios, J. M., Martínez-Sánchez, G., & Al-Dalaien, S. M. (2017). Medical ozone promotes Nrf2 phosphorylation reducing oxidative stress and pro-inflammatory cytokines in multiple sclerosis patients. *European Journal of Pharmacology*, 811, 148–154. https://doi.org/10.1016/j.ejphar.2017.06.017

Dello Russo, C., Cappoli, N., Coletta, I., Mezzogori, D., Paciello, F., Pozzoli, G., Navarra, P., & Battaglia, A. (2018). The human microglial HMC3 cell line: where do we stand? A systematic literature review. *Journal of Neuroinflammation*, 15(1), 259. https://doi.org/10.1186/s12974-018-1288-0

Dinkova-Kostova, A. T., Kostov, R. V., & Kazantsev, A. G. (2018). The role of Nrf2 signaling in counteracting neurodegenerative diseases. *FEBS Journal*, 285(7), 3576–3590. https://doi.org/10.1111/febs.14379

Elvis, A. M., & Ekta, J. S. (2011). Ozone therapy: A clinical review. *Journal of Natural Science, Biology and Medicine*, 2(1), 66–70. https://doi.org/10.4103/0976-9668.82319

Fraley, S. I., Feng, Y., Krishnamurthy, R., Kim, D. H., Celedon, A., Longmore, G. D., & Wirtz, D. (2010). A distinctive role for focal adhesion proteins in three-dimensional cell motility. *Nature Cell Biology*, 12(6), 598–604. https://doi.org/10.1038/ncb2062

Galiè, M., Costanzo, M., Nodari, A., Boschi, F., Calderan, L., Mannucci, S., Covi, V., Tabaracci, G., & Malatesta, M. (2018). Mild ozonisation activates antioxidant cell response by the Keap1/Nrf2 dependent pathway. *Free Radical Biology & Medicine*, 124, 114–121. https://doi.org/10.1016/j.freeradbiomed.2018.05.093

Galiè, M., Covi, V., Tabaracci, G., & Malatesta, M. (2019). The role of Nrf2 in the antioxidant cellular response to medical ozone exposure. *International Journal of Molecular Sciences*, 20(16), 4009. https://doi.org/10.3390/ijms20164009

Garcia-Contreras, M., & Thakor, A. S. (2021). Human adipose tissue-derived mesenchymal stem cells and their extracellular vesicles modulate lipopolysaccharide activated human microglia. *Cell Death Discovery*, 7(1), 98. https://doi.org/10.1038/s41420-021-00471-7

Güçlü, A., Erken, H. A., Erken, G., Dodurga, Y., Yay, A., Özçoban, Ö., Şimşek, H., Akçılar, A., & Koçak, F. E. (2016). The effects of ozone therapy on caspase pathways, TNF-alpha, and HIF-1alpha in diabetic nephropathy. *International Urology & Nephrology*, 48(3), 441–450. https://doi.org/10.1007/s11255-015-1169-8

—WILEY⎯

Ho, M. S. (2019). Microglia in Parkinson's disease. *Advances in Experimental Medicine and Biology*, *1175*, 335–353. https://doi.org/10.1007/978-981-13-9913-8_13

Izadi, M., Tahmasebi, S., Pustokhina, I., Yumashev, A. V., Lakzaei, T., Alvanegh, A. G., Roshangar, L., Dadashpour, M., Yousefi, M., & Ahmadi, M. (2020). Changes in Th17 cells frequency and function after ozone therapy used to treat multiple sclerosis patients. *Multiple Sclerosis and Related Disorders*, *46*, 102466. https://doi.org/10.1016/j.msard.2020.102466

Johnson, D. A., & Johnson, J. A. (2015). Nrf2-a therapeutic target for the treatment of neurodegenerative diseases. *Free Radical Biology & Medicine*, *88*, 253–267. https://doi.org/10.1016/j.freeradbiomed.2015.07.147

Kaur, D., Sharma, V., & Deshmukh, R. (2019). Activation of microglia and astrocytes: A roadway to neuroinflammation and Alzheimer's disease. *Inflammopharmacology*, *27*(4), 663–677. https://doi.org/10.1007/s10787-019-00580-x

Khatchadourian, A., Bourque, S. D., Richard, V. R., Titorenko, V. I., & Maysinger, D. (2012). Dynamics and regulation of lipid droplet formation in lipopolysaccharide (LPS)-stimulated microglia. *Biochimica et Biophysica Acta*, *1821*(4), 607–617. https://doi.org/10.1016/j.bbalip.2012.01.007

Kwon, H. S., & Koh, S. H. (2020). Neuroinflammation in neurodegenerative disorders: The roles of microglia and astrocytes. *Translational Neurodegeneration*, *9*(1), 42. https://doi.org/10.1186/s40035-020-00221-2

Larini, A., Bianchi, L., & Bocci, V. (2003). The ozone tolerance: (I) Enhancement of antioxidant enzymes is ozone dose-dependent in Jurkat cells. *Free Radical Research*, *37*(11), 1163–1168. https://doi.org/10.1080/10715760310001604170

Leng, F., & Edison, P. (2021). Neuroinflammation and microglial activation in Alzheimer disease: Where do we go from here? *Nature Reviews Neurology*, *17*(3), 157–172. https://doi.org/10.1038/s41582-020-00435-y

Lin, S. Y., Ma, J., An, J. X., Qian, X. Y., Wang, Y., Cope, D. K., & Williams, J. P. (2019). Ozone inhibits APP/Abeta production and improves cognition in an APP/PS1 transgenic mouse model. *Neuroscience*, *15*(418), 110–121. https://doi.org/10.1016/j.neuroscience.2019.07.027

Lintas, G., Molinari, F., Simonetti, V., Franzini, M., & Liboni, W. (2013). Time and time-frequency analysis of near-infrared signals for the assessment of ozone autohemotherapy long-term effects in multiple sclerosis. *Annual International Conference of the IEEE Engineering in Medicine and Biology Society*, *2013*, 6171–6174. https://doi.org/10.1109/EMBC.2013.6610962

Liu, Y., Lang, F., & Yang, C. (2021). NRF2 in human neoplasm: Cancer biology and potential therapeutic target. *Pharmacology & Therapeutics*, *217*, 107664. https://doi.org/10.1016/j.pharmthera.2020.107664

Lu, M.-C., Ji, J.-A., Jiang, Z.-Y., & You, K.-D. (2016). The Keap1–Nrf2–ARE pathway as a potential preventive and therapeutic target: An update. *Medicinal Research Reviews*, *36*(5), 924–963. https://doi.org/10.1002/med.21396

Lu, Z., Liu, S., Lopes-Virella, M. F., & Wang, Z. (2021). LPS and palmitic acid co-upregulate microglia activation and neuroinflammatory response. *Comprehensive Psychoneuroendocrinology*, *6*, 100048. https://doi.org/10.1016/j.cpnec.2021.100048

Lyman, M., Lloyd, D. G., Ji, X., Vizcaychipi, M. P., & Ma, D. (2013). Neuroinflammation: The role and consequences. *Neuroscience Research*, *79*, 1–12. https://doi.org/10.1016/j.neures.2013.10.004

Masan, J., Sramka, M., & Rabarova, D. (2021). The possibilities of using the effects of ozone therapy in neurology. *Neuro Endocrinology Letters*, *42*(1), 13–21.

McBean, G. J., López, M. G., & Wallner, F. K. (2017). Redox-based therapeutics in neurodegenerative disease. *British Journal of Pharmacology*, *174*(12), 1750–1770. https://doi.org/10.1111/bph.13551

Miller, E. D., Dziedzic, A., Saluk-Bijak, J., & Bijak, M. (2019). A review of various antioxidant compounds and their potential utility as

complementary therapy in multiple sclerosis. *Nutrients*, *11*(7), 1528. https://doi.org/10.3390/nu11071528

Minty, A., Chalon, P., Derocq, J. M., Dumont, X., Guillemot, J. C., Kaghad, M., Labit, C., Leplatois, P., Liauzun, P., Miloux, B., Minty, C., Casellas, P., Loison, G., Lupker, J., Shire, D., Ferrara, P., & Caput, D. (1993). Interleukin-13 is a new human lymphokine regulating inflammatory and immune responses. *Nature*, *362*(6417), 248–250. https://doi.org/10.1038/362248a0

Muliyil, S., & Narasimha, M. (2014). Mitochondrial ROS regulates cytoskeletal and mitochondrial remodeling to tune cell and tissue dynamics in a model for wound healing. *Developmental Cell*, *28*(3), 239–252. https://doi.org/10.1016/j.devcel.2013.12.019

Niedojadlo, J., Perret-Vivancos, C., Kalland, K. H., Cmarko, D., Cremer, T., van Driel, R., & Fakan, S. (2011). Transcribed DNA is preferentially located in the perichromatin region of mammalian cell nuclei. *Experimental Cell Research*, *317*(4), 433–444. https://doi.org/10.1016/j.yexcr.2010.10.026

Niki, E. (2016). Oxidative stress and antioxidants: Distress or eustress? *Archives of Biochemistry and Biophysics*, *595*, 19–24. https://doi.org/10.1016/j.abb.2015.11.017

Pallio, G., D'Ascola, A., Cardia, L., Mannino, F., Bitto, A., Minutoli, L., Picciolo, G., Squadrito, V., Irrera, N., Squadrito, F., & Altavilla, D. (2021). MAO-A inhibition by Metaxalone reverts IL-1beta-induced inflammatory phenotype in microglial cells. *International Journal of Molecualr Sciences*, *22*(16), 8425. https://doi.org/10.3390/ijms22168425

Prinz, M., Jung, S., & Priller, J. (2019). Microglia biology: One century of evolving concepts. *Cell*, *179*(2), 292–311. https://doi.org/10.1016/j.cell.2019.08.053

Re, L., Mawsouf, M. N., Menéndez, S., León, O. S., Sánchez, G. M., & Hernández, F. (2008). Ozone therapy: Clinical and basic evidence of its therapeutic potential. *Archives of Medical Research*, *39*(1), 17–26. https://doi.org/10.1016/j.arcmed.2007.07.005

Robledinos-Antón, N., Fernández-Ginés, R., Manda, G., & Cuadrado, A. (2019). Activators and inhibitors of NRF2: A review of their potential for clinical development. *Oxidative Medicine and Cellular Longevity*, *2019*, 9372182. https://doi.org/10.1155/2019/9372182

Rothaug, M., Becker-Pauly, C., & Rose-John, S. (2016). The role of interleukin-6 signaling in nervous tissue. *Biochimica et Biophysica Acta*, *1863*, 1218–1227. https://doi.org/10.1016/j.bbamcr.2016.03.018

Sagai, M., & Bocci, V. (2011). Mechanisms of action involved in ozone therapy: Is healing induced via a mild oxidative stress? *Medical Gas Research*, *1*, 29. https://doi.org/10.1186/2045-9912-1-29

Scannevin, R.-H., Chollate, S., Jung, M.-Y., Shackett, M., Patel, H., Bista, P., Zeng, W., Ryan, S., Yamamoto, M., Lukashev, M., & Rhodes, K. J. (2012). Fumarates promote cytoprotection of central nervous system cells against oxidative stress via the nuclear factor (erythroid-derived 2)-like 2 pathway. *Journal of Pharmacology and Experimental Therapeutics*, *341*(1), 274–284. https://doi.org/10.1124/jpet.111.190132

Scassellati, C., Costanzo, M., Cisterna, B., Nodari, A., Galiè, M., Cattaneo, A., Covi, V., Tabaracci, G., Bonvicini, C., & Malatesta, M. (2017). Effects of mild ozonisation on gene expression and nuclear domains organization in vitro. *Toxicology In Vitro*, *44*, 100–110. https://doi.org/10.1016/j.tiv.2017.06.021

Schroeter, M., & Jander, S. (2005). T-cell cytokines in injury-induced neural damage and repair. *Neuromolecular Medicine*, *7*(3), 183–195. https://doi.org/10.1385/NMM:7:3:183

Shabab, T., Khanabdali, R., Moghadamtousi, S. Z., Kadir, H. A., & Mohan, G. (2017). Neuroinflammation pathways: A general review. *International Journal of Neuroscience*, *127*(7), 624–633. https://doi.org/10.1080/00207454.2016.1212854

Shaw, P., & Chattopadhyay, A. (2020). Nrf2-ARE signaling in cellular protection: Mechanism of action and the regulatory mechanisms. *Journal of Cellular Physiology*, *235*(4), 3119–3130. https://doi.org/10.1002/jcp.29219

Smith, J. A., Das, A., Ray, S. K., & Banik, N. L. (2012). Role of pro-inflammatory cytokines released from microglia in neurodegenerative diseases. *Brain Research Bulletin*, *87*(1), 10–20. https://doi.org/10.1016/j.brainresbull.2011.10.004

Tahmasebi, S., Qasim, M. T., Krivenkova, M. V., Zekiy, A. O., Thangavelu, L., Aravindhan, S., Izadi, M., Jadidi-Niaragh, F., Ghaebi, M., Aslani, S., Aghebat-Maleki, L., Ahmadi, M., & Roshangar, L. (2021). The effects of oxygen-ozone therapy on regulatory T-cell responses in multiple sclerosis patients. *Cell Biology International*, *45*(7), 1498–1509. https://doi.org/10.1002/cbin.11589

Tartari, A. P. S., Moreira, F. F., Pereira, M. C. D. S., Carraro, E., Cidral-Filho, F. J., Salgado, A. I., & Kerppers, I. I. (2020). Anti-inflammatory effect of ozone therapy in an experimental model of rheumatoid arthritis. *Inflammation*, *43*(3), 985–993. https://doi.org/10.1007/s10753-020-01184-2

Tonelli, C., Chio, I. I. C., & Tuveson, D. A. (2018). Transcriptional regulation by Nrf2. *Antioxidants & Redox Signaling*, *29*(17), 1727–1745. https://doi.org/10.1089/ars.2017.7342

Viebahn-Haensler, R., & Fernández, O. S. L. (2021). Ozone in medicine. The low-dose ozone concept and its basic biochemical mechanisms of action in chronic inflammatory diseases. *International Journal of Molecular Sciences*, *22*(15), 7890. https://doi.org/10.3390/ijms22157890

Voet, S., Prinz, M., & van Loo, G. (2019). Microglia in central nervous system inflammation and multiple sclerosis pathology. *Trends in Molecular Medicine*, *25*(2), 112–123. https://doi.org/10.1016/j.molmed.2018.11.005

Welser-Alves, J. V., & Milner, R. (2013). Microglia are the major source of TNF-alpha and TGF-beta1 in postnatal glial cultures, regulation by cytokines, lipopolysaccharide, and vitronectin. *Neurochemistry International*, *63*(1), 47–53. https://doi.org/10.1016/j.neuint.2013.04.007

Wolf, S. A., Boddeke, H. W., & Kettenmann, H. (2017). Microglia in physiology and disease. *Annual Review of Physiology*, *79*, 619–643. https://doi.org/10.1146/annurev-physiol-022516-034406

Woodburn, S. C., Bollinger, J. L., & Wohleb, E. S. (2021). The semantics of microglia activation: Neuroinflammation, homeostasis, and stress. *Journal of Neuroinflammation*, *18*(1), 258. https://doi.org/10.1186/s12974-021-02309-6

Zeng, J., Lei, L., Zeng, Q., Yao, Y., Wu, Y., Li, Q., Gao, L., Du, H., Xie, Y., Huang, J., Tan, W., & Lu, J. (2020). Ozone therapy attenuates NF-kappaB-mediated local inflammatory response and activation of Th17 cells in treatment for psoriasis. *International Journal of Biological Sciences*, *16*(11), 1833–1845. https://doi.org/10.7150/ijbs.41940

Zhang, F., Nance, E., Alnasser, Y., Kannan, R., & Kannan, S. (2016). Microglial migration and interactions with dendrimer nanoparticles are altered in the presence of neuroinflammation. *Journal of Neuroinflammation*, *13*(1), 65. https://doi.org/10.1186/s12974-016-0529-3

*Article*

# L-Carnitine Functionalization to Increase Skeletal Muscle Tropism of PLGA Nanoparticles

Ilaria Andreana [1], Manuela Malatesta [2], Maria Assunta Lacavalla [2,3], Federico Boschi [4], Paola Milla [1], Valeria Bincoletto [1], Carlo Pellicciari [3,*], Silvia Arpicco [1] and Barbara Stella [1]

[1] Department of Drug Science and Technology, University of Torino, I-10125 Torino, Italy
[2] Department of Neurosciences, Biomedicine and Movement Sciences, University of Verona, I-37134 Verona, Italy
[3] Department of Biology and Biotechnology "Lazzaro Spallanzani", University of Pavia, I-27100 Pavia, Italy
[4] Department of Computer Science, University of Verona, I-37134 Verona, Italy
* Correspondence: carlo.pellicciari@unipv.it

**Abstract:** Muscular dystrophies are a group of rare genetic pathologies, encompassing a variety of clinical phenotypes and mechanisms of disease. Several compounds have been proposed to treat compromised muscles, but it is known that pharmacokinetics and pharmacodynamics problems could occur. To solve these issues, it has been suggested that nanocarriers could be used to allow controlled and targeted drug release. Therefore, the aim of this study was to prepare actively targeted poly(lactide-*co*-glycolide) (PLGA) nanoparticles (NPs) for the treatment of muscular pathologies. By taking advantage of the high affinity for carnitine of skeletal muscle cells due to the expression of $Na^+$-coupled carnitine transporter (OCTN), NPs have been actively targeted via association to an amphiphilic derivative of L-carnitine. Furthermore, pentamidine, an old drug repurposed for its positive effects on myotonic dystrophy type I, was incorporated into NPs. We obtained monodispersed targeted NPs, with a mean diameter of about 100 nm and a negative zeta potential. To assess the targeting ability of the NPs, cell uptake studies were performed on C2C12 myoblasts and myotubes using confocal and transmission electron microscopy. The results showed an increased uptake of carnitine-functionalized NPs compared to nontargeted carriers in myotubes, which was probably due to the interaction with OCTN receptors occurring in large amounts in these differentiated muscle cells.

**Keywords:** PLGA; L-carnitine; nanoparticles; active targeting; skeletal muscle cells; fluorescence microscopy; transmission electron microscopy

## 1. Introduction

For years, the enhanced permeation and retention (EPR) effect was the chosen strategy for passive targeting, being largely studied for nanocarrier accumulation in a tumor environment [1,2]. However, models used to study the EPR effect are often not sufficiently accurate to describe the nanocarrier behavior in the human body [3]. The active targeting approach is based on the identification of precise disease biomarkers, to which specific ligands on the nanocarrier surface are directed to promote accumulation into organs or tissues with consequent improved therapeutic effects. Furthermore, the high specificity of the ligands (e.g., antibodies, peptides) can facilitate nanocarrier internalization into cells with great affinity and precision [4].

Muscular dystrophies (MDs) are a group of chronic inherited genetic diseases which affect muscles, especially at the skeletal level. The most common MDs are represented by Duchenne muscular dystrophy and myotonic dystrophies, caused by different and specific gene mutations [5,6]. Currently, no therapies are available to counteract the pathogenic causes of MDs, and conventional treatments are based on glucocorticoids to mitigate symptoms [7]. Over the last years, various approaches have been proposed for the treatment

of localized mutations. For instance, gene therapy is considered the most recent strategy to target the pathogenic causes of MDs [8,9]. However, drawbacks related to the instability of the genetic materials or the unreached global distribution to all compromised tissues limit the therapeutical applicability of this strategy. Within this framework, drug delivery systems have been proposed for the treatment of MDs. However, in vivo delivery is challenging due to the presence of biological barriers: the complex architecture of skeletal muscle and the surrounding extracellular matrix (ECM) made of fibrous proteins are the main hurdles for drug delivery to muscle cells [10,11]. To restrict interactions with ECM, the intravenous administration of nanocarriers appeared to be a potential strategy to reach skeletal muscle fibers through their dense blood capillary network. However, the treatment of MDs requires long-term administration, which makes the biocompatibility and biodegradability of nanosystems important requirements.

In this context, surface-engineered nanosystems have been designed to actively promote muscle cell targeting thanks to peptides anchored on the nanocarrier surface [12,13]. In our work, we identified the $Na^+$-coupled organic cation/carnitine transporter (OCTN) as a potential target for drug delivery at the muscular level [14,15]. OCTN receptors constitute a subfamily of the solute carrier SLC22 family, whose differences in amino acid composition define the two main receptor classes, namely OCTN1 and OCTN2. Moreover, each member of SLC22 has differences in substrate affinity. In particular, OCTN2 has a high affinity for L-carnitine, which is a small zwitterion molecule endogenously synthetized by liver, kidney and brain [16].

L-Carnitine-associated polymer nanoparticles (NPs) have been shown to be effective in increasing drug delivery by oral administration: the insertion of an L-carnitine derivative, namely stearoyl-L-carnitine (SC), into the polymer matrix enhanced cellular uptake and intestinal absorption of drug molecules by OCTN2-mediated transport [17,18]. Furthermore, SC-conjugated PLGA NPs have been described as novel potential tools for colon cancer cell-targeted drug delivery. Indeed, cancer cells express high levels of OCTN2 and $ATB^{0,+}$ receptors, both having high affinity for L-carnitine [19]. The same approach can be exploited to target the respiratory epithelium of human trachea and bronchi, since the identification of OCTN transporters can play a significant role in the delivery of therapeutic molecules by a nanomedicine-based approach [20,21].

On these bases, in the present work we propose the formulation of drug-loaded SC-associated PLGA NPs to target the OCTN2 receptor expressed on skeletal muscle cells (Figure 1).
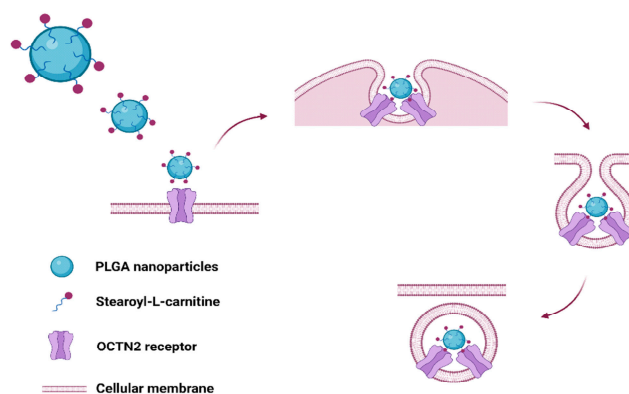


- PLGA nanoparticles
- Stearoyl-L-carnitine
- OCTN2 receptor
- Cellular membrane

**Figure 1.** Cellular uptake of SC-PLGA nanoparticles: functionalized nanoparticles bind to OCTN2 receptor on the cell membrane, forming a complex that is then internalized into the cell (created with BioRender.com).

We tested different percentages of SC to efficiently functionalize the NPs, which were then characterized. In vitro tests were carried out in an established non-tumor muscle cell line, with cells able to proliferate as myoblasts (mimicking activated satellite cells of skeletal muscle) and terminally differentiate into myotubes (mimicking the mature

myofiber) [22]. Cytotoxicity in the presence of targeted NPs was assessed, and cellular uptake was analyzed by confocal and transmission electron microscopy (TEM).

The recent understanding of the pathogenic mechanism of MDs has opened new possibilities for innovative strategies. As an example, a current approach for the treatment of myotonic dystrophy type I consists in drug repurposing, i.e., the identification of new therapeutic applications of existing drugs [23]. Within the frame of the repurposing approach, pentamidine (PTM), an aromatic diamine approved as an antiparasitic drug, has been investigated as an experimental MD treatment. Indeed, myotonic dystrophy type I results in the dystrophia myotonica protein kinase (DMPK) gene mutation, which leads to the amplification of the $(CTG)_n$ triplets. Furthermore, the transcription of expanded $(CUG)_n$ forms aggregates of hairpin structures in the nucleus, namely nuclear foci, responsible for the sequestration of the splicing factor muscle-blind-like (MBNL) protein family and the consequent myotonia and muscle weakness [24,25]. Recent in vitro and in vivo studies demonstrated that PTM associates with the expanded triplets, preventing MBNL1 sequestration, decreasing the formation of nuclear foci and reducing myotonia in experimental models [26,27]. However, its substantial toxicity at the potentially effective dose in vivo and its relevant side effects prevent its clinical applicability [28]. For these reasons and to improve drug efficacy, PTM has been encapsulated into targeted NPs for its proposed activity in the treatment of myotonic dystrophy type I [8,29–31].

## 2. Results

### 2.1. Preparation and Characterization of SC-Nanoparticles

Empty and drug-loaded SC-associated (5% and 10% *w/w*) PLGA NPs were prepared in a single step by nanoprecipitation [32], adding polyvinyl alcohol (PVA) in the aqueous phase as a stabilizer of the composite formulation. As reported in Table 1, all the NP samples showed a mean diameter of about 100 nm; in particular, the mean size value of empty NPs was lower than that of drug-loaded samples. Indeed, the incorporation of the free base form of PTM (PTM-B) increased the mean size until it grew to about 130 nm and the polydispersity index (PDI) value was greater than 0.2. Concerning the zeta potential, SC-associated and PTM-B-loaded NPs showed a less negative value than that of blank nanocarriers, thanks to the presence of positive charges on both SC and PTM-B.

**Table 1.** Physicochemical characteristics (mean diameter, PDI and zeta potential) of PLGA nanoparticles (n = 3).

| Nanoparticle Composition | Mean Diameter (nm $\pm$ S.D.) | PDI | Zeta Potential (mV $\pm$ S.D.) |
|---|---|---|---|
| PLGA | 94 $\pm$ 1 | 0.170 | −39.2 $\pm$ 1.8 |
| 5% SC-PLGA | 82 $\pm$ 1 | 0.198 | −23.7 $\pm$ 1.1 |
| 10% SC-PLGA | 73 $\pm$ 1 | 0.184 | −29.6 $\pm$ 1.0 |
| 5% SC-PTM-B-PLGA | 98 $\pm$ 11 | 0.399 | −18.4 $\pm$ 2.4 |
| 10% SC-PTM-B-PLGA | 128 $\pm$ 10 | 0.222 | −28.8 $\pm$ 3.3 |

The physical stability of the NP suspensions in the storage conditions was monitored for four weeks; in this period, no precipitation and/or aggregation occurred for 5% and 10% empty SC-NPs. On the contrary, for PTM-B-loaded nanosystems, the mean particle size, PDI and zeta potential values were stable only for 5% SC-NPs. On these bases, we selected the lower SC concentration for further characterization. In particular, 5% SC-PTM-B-PLGA NPs showed an encapsulation efficiency (EE) (calculated as the ratio between the amount of entrapped drug and the initial amount used in the preparation of nanocarriers $\times$ 100) of 65% and a drug loading (DL) (calculated as the ratio between the amount of entrapped PTM-B and the total nanocarrier weight $\times$ 100) of 1.9%. This EE was lower than that of untargeted NPs, which was about 90% [33]. HPLC analysis showed that 45% of the initially added SC was associated with 5% SC-PTM-B-PLGA NPs (corresponding to a final SC concentration of 22.5 μg/mL). To evaluate the PTM-B release from 5% SC-NPs, the

suspension was incubated for 24 h at 37 °C in phosphate-buffered saline (PBS) pH 7.4. In these conditions, the drug is stably associated to the polymer matrix thanks to electrostatic interactions, as previously reported [33]: indeed, after 24 h, only 60% of PTM-B is released (Figure 2).
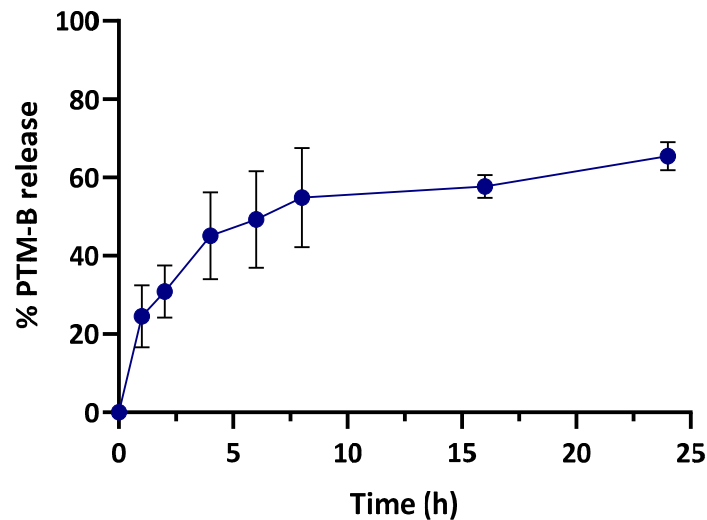


**Figure 2.** PTM-B release from 5% SC-nanoparticles as a function of time after incubation in PBS pH 7.4 at 37 °C.

### 2.2. Cytotoxicity Assay

C2C12 myoblasts were cultured and incubated for 2 h, 24 h and 24 h + 24 h of recovery in a culture medium without NPs, with increasing concentrations of 5% SC-NPs used to evaluate cell metabolic activity. As shown in Figure 3, metabolic activity was similar in control samples and in samples exposed to any nanocarrier concentration after 2 h of incubation. Conversely, metabolic activity decreased significantly after 24 h incubation in a dose-dependent manner (from 86% for the lowest concentration to 62% for the higher concentration), indicating a cytotoxic effect. After 24 h incubation with 5% SC-NPs followed by 24 h of recovery, metabolic activity showed similar values in control samples and in samples exposed to 5% SC-NPs. The exception was the highest concentration, which induced a significant decrease in 24%.
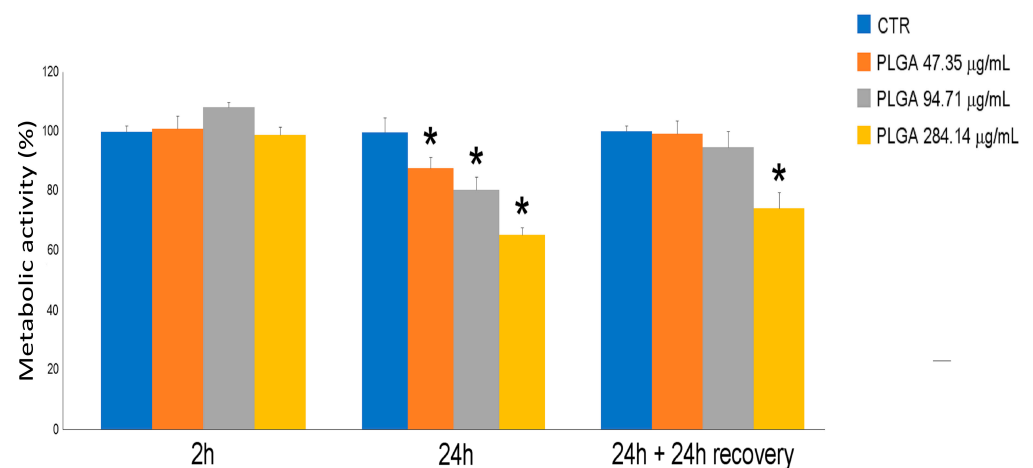


**Figure 3.** C2C12 myoblast metabolic activity, evaluated by MTT assay after 2 h, 24 h, 24 h + 24 h recovery treatment, in presence of 5% SC-nanoparticles. Data are given as mean values $\pm$ SEM, representative of three independent experiments. * $p < 0.03$ vs. control (CTR) sample.

### 2.3. Nanoparticle Distribution in Myoblasts and Myotubes

To compare the cell internalization of 5% SC-associated or untargeted NPs, C2C12 myoblasts and myotubes were incubated for 2 h and 24 h with fluorescent (Nile Red-loaded) NPs. Confocal microscopy (CFM) analysis showed that both NP types were already internalized after 2 h (not shown) and accumulated in the cytoplasm after 24 h without entering the cell nucleus (Figure 4A–D).
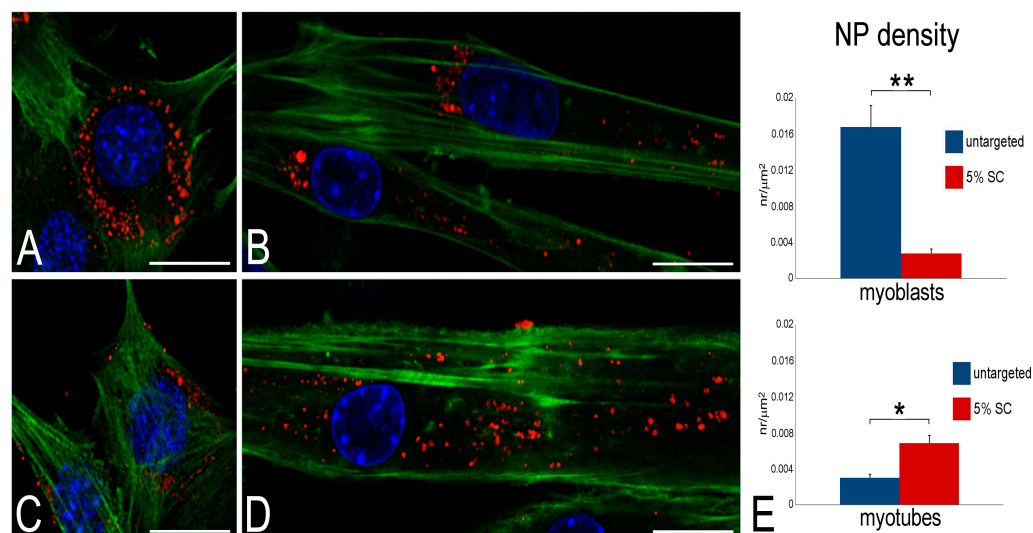


**Figure 4.** (**A**) CFM micrographs of myoblasts (**A**,**C**) and myotubes (**B**,**D**) incubated with untargeted nanoparticles (**A**,**B**) and 5% SC-associated nanoparticles (**C**,**D**). Nanoparticles are loaded with Nile Red (red), cells are stained with phalloidin (green) and nuclei with Hoechst 33,342 (blue). Bars, 20 μm. (**E**) Quantitative evaluation of internalized nanoparticles; data are given as mean values ± SEM. ** $p < 0.001$; * $p < 0.01$.

Morphometric analysis, performed to quantify the internalized NPs after 24 h incubation, demonstrated that untargeted NPs accumulated in myoblasts in significantly higher amounts than 5% SC-NPs. Conversely, in myotubes a higher number of 5% SC-NPs was internalized compared to the untargeted ones (Figure 4E).

TEM analysis confirmed the uptake of 5% SC-NPs within myoblasts and myotubes (Figure 5) after 2 h and 24 h incubation, allowing us to shed light on the NP interaction with the cellular components. At TEM, NPs showed a regular roundish shape and a moderate electron density, conditions which allowed their unequivocal visualization.

The intracellular fate of 5% SC-NPs was the same in myoblasts and myotubes. After 2 h of incubation, 5% SC-NPs were found to enter the cells by endocytosis (Figure 4A). Once in the cytoplasm, they underwent endosomal escape (Figure 4B). After 24 h incubation, most NPs were free in the cytosol (Figure 4C,D). However, some NPs were found to be partially surrounded by double membranes as a typical sign of the autophagic process (Figure 4E), while secondary lysosomes containing NP remnants accumulated in the cytoplasm (Figure 4F). NPs were never found inside the nucleus. Only several cells showed signs of stress, such as vacuolization or mitochondrial swelling, at 24 h incubation (not shown).
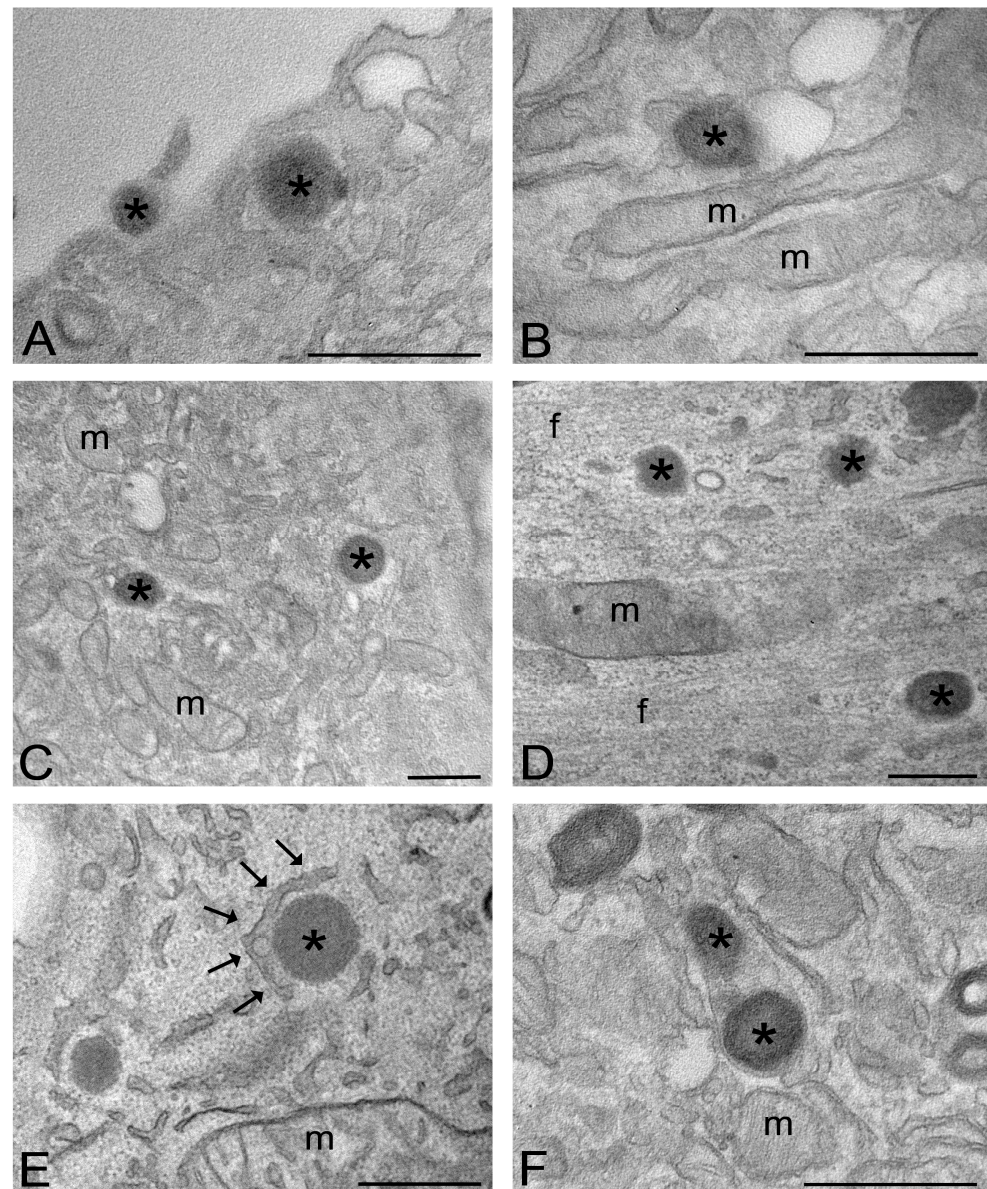
**Figure 5.** TEM micrographs of myoblasts (**A–C**,**F**) and myotubes (**D**,**E**) after 2 h (**A**,**B**) and 24 h (**C–F**) incubation with 5% SC-nanoparticles, respectively. (**A**) Two nanoparticles (asterisks) are entering the cell by endocytosis. (**B**) A nanoparticle (asterisk) is escaping an endosome. (**C**,**D**) Nanoparticles (asterisks) occur free in the cytosol. (**E**) A nanoparticle, occurring free in the cytosol (asterisk), is enclosed by double membranes (arrows) undergoing autophagocytosis. (**F**) Two nanoparticles (asterisks) inside a secondary lysosome. m, mitochondria; f, myofibril bundles. Bars, 200 nm.

### 2.4. Immunofluorescence Detection of OCTN2 Receptor

To detect the presence of OCTN2 receptors in myoblasts and myotubes in order to gain further insight into the possible role of the transporter, the cells were labeled with the anti-OCTN2 antibody and evaluated by immunofluorescence. The presence of OCTN2 receptors was observed in both myoblasts and myotubes, but in myotubes the number of receptors was significantly higher (Figure 6).
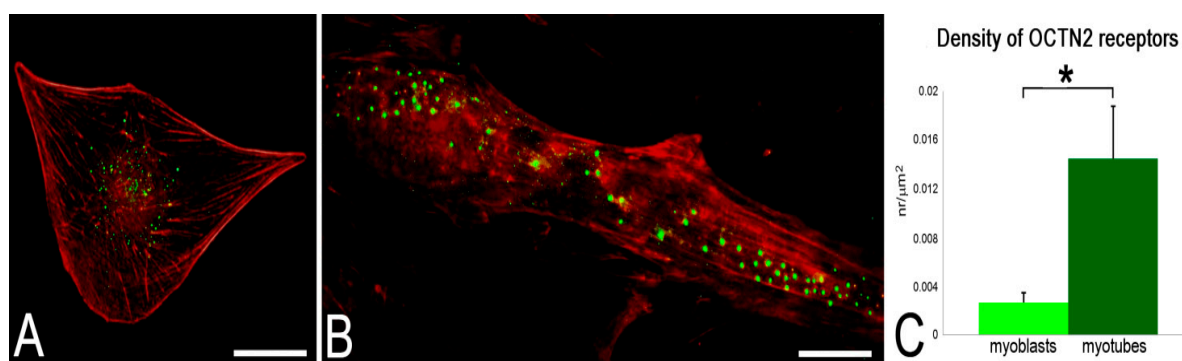
**Figure 6.** CFM micrographs of a myoblast (**A**) and a myotube (**B**), immunolabelled for OCTN2 (green); counterstaining with phalloidin (red). Bars, 20 μm. Note the higher density of receptors in the myotube (**C**); data are given as mean values ± SEM. * *p*< 0.001.

## 3. Discussion

In this work, L-carnitine was exploited as an active targeting agent to increase the muscle tropism of PLGA NPs and improve the therapeutical treatment of MDs. L-carnitine is a specific substrate for a plasma membrane transporter, namely OCTN2, a $Na^+$-coupled transporter that is characterized by high binding affinity for L-carnitine ($K_m$~10 μM) [34]. PLGA NPs themselves are poorly taken up by differentiated muscle cells [35,36], but chemical modification of the surface of these NPs with a specific targeting molecule would potentially enhance the efficiency of the uptake process and cell selectivity. The rationale of this study is that differentiated muscle cells preferentially express OCTN2 receptors, which recognize L-carnitine as substrate.

To promote the L-carnitine association to PLGA NPs, we have chosen a commercial derivative, i.e., SC, in which the hydroxyl group of L-carnitine was conjugated to a stearoyl moiety. In this way, during NP formation, the SC long fatty chain anchors to the PLGA matrix by hydrophobic interactions and exposes hydrophilic L-carnitine on the NP surface (Figure 1) [19]. According to this approach, the covalent linkage between PLGA and L-carnitine can be avoided. A similar strategy has been used to prepare L-carnitine-functionalized NPs by solvent extraction/evaporation to increase drug oral delivery by carnitine receptor-mediated uptake [18].

In this work, PTM, a drug repurposed for potential applications in MD treatment [26], was encapsulated in muscle-targeted NPs. We used the free base form of PTM to increase its hydrophobicity and, thus, the incorporation into the lipophilic inner core of the NPs. At the same time, the association of PTM-B to PLGA was promoted by the electrostatic interactions between the positively charged PTM-B amidinic groups and the negatively charged PLGA carboxyl functions, as previously reported [33].

All the NPs were prepared by nanoprecipitation, adding PVA as a surfactant to stabilize the nanosystems. In previous studies, different concentrations (from 0.1 to 1% *w/v*) of PVA were assessed to obtain stable NPs, limiting, at the same time, PVA toxicity in vitro. Finally, a nontoxic 0.2% PVA concentration was used [37].

NPs were formulated at 5% and 10% SC to investigate the effect of the ligand percentage on the NP characteristics. As reported in Table 1, the NP mean diameter tends to diminish with the increase in SC percentage during NP formation, probably as a consequence of the amphiphilic character of SC. On the contrary, the incorporation of PTM-B into functionalized NPs causes mean size and PDI to increase: this effect may be due to the more complex composition of the systems and the localization of PTM-B inside the NP matrix. Moreover, the zeta potential of targeted NPs was higher than that of untargeted ones, suggesting that SC is located on the NP surface. When PTM-B is added, the zeta potential value becomes even less negative due to the presence of the positively charged groups of the drug. Since the stability of the drug-loaded nanosystems was guaranteed only at 5% of SC, we evaluated the EE only for this sample, showing that the insertion of

SC in the polymer matrix reduced the incorporation of PTM-B from 90% of untargeted NPs to 65%. This result is probably caused by the interaction of the stearoyl chain of SC with the polymer matrix and the competition with PTM-B incorporation. However, the drug release profile demonstrated a stable association of PTM-B with the polymer matrix thanks to the electrostatic interactions, as previously reported [33].

When administered to myoblasts in vitro, 5% SC-NPs were proved to exert a slight toxicity in a dose-dependent manner. Since PLGA is a biodegradable and biocompatible polymer without toxic effects in vitro and in vivo [38], the increased cytotoxicity may be related to the presence of SC. Indeed, some studies demonstrated the potential toxicity of acylcarnitine derivatives. Accordingly, a high level of acylcarnitine derivatives is an indicator of compromised lipid metabolism [39]. Furthermore, in cardiomyocytes, acylcarnitine has been shown to disrupt the sarcolemmal integrity and electrophysiologic functions, possibly leading to the alteration of myocardial activity [40]. Taking into account that lipid metabolism occurs in mitochondria where the dehydrogenases responsible for tetrazolium salt MTT reduction are located, and that L-carnitine is a key element for mitochondrial homeostasis, we can assume that SC would interfere with mitochondrial activities, thus reducing myoblast metabolism. These effects seem to be transitory and reversible, as suggested by the resumption of cell metabolism after a 24 h-recovery.

The observations, made at CFM and especially at TEM, demonstrated that a low number of cells, treated with 5% SC-NPs at the PLGA concentration of 94.71 μg/mL, showed stress signs after 24 h incubation according to the MTT assay results. In this study, we selected this concentration for microscopy analyses due to technical reasons. In fact, the sample sections for TEM are very thin (70–90 nm), allowing the observation of a limited cell volume. Therefore, to be sure to have performed an adequate sampling of internalized NPs at the ultrastructural level, it was advisable to use a relatively high NP concentration while preserving the viability of most of the cell population. Of note, in view of future studies with targeted drug-loaded NPs, these PLGA concentrations correspond to a nontoxic amount of entrapped PTM-B. Under these experimental conditions, it was therefore possible to monitor the uptake and intracellular fate of 5% SC-NPs. Both CFM and TEM demonstrated that 5% SC-NPs rapidly enter myoblasts and myotubes and accumulate in the cytoplasm but never penetrate the cell nucleus, thus avoiding the unpredictable side-effects due to possible interactions between NPs, nucleic acids and nuclear factors confined inside the nuclear envelope. This finding should be therefore considered as a biocompatibility feature of 5% SC-NPs.

The experimental evidence at TEM indicates that 5% SC-NPs enter myoblasts and myotubes by the classical endocytic process [18,41]. Once inside the cell, 5% SC-NPs rapidly escape the endosomes and occur free in the cytosol, similarly to what was previously reported for untargeted PLGA NPs in muscle cells [36] as well as for other polymeric NPs [42,43]. However, the free NPs re-enter the endolytic pathway due to autophagic process, thus undergoing enzymatic degradation, as demonstrated by the large number of secondary lysosomes containing NP remnants at the longer incubation time. The degradation of 5% SC-NPs through a physiological pathway further supports the biocompatibility of this nanosystem.

Although 5% SC-NPs proved to enter both myoblasts and myotubes, morphometric analysis, which was performed at CFM to quantify the NP amounts, revealed that these nanocarriers were better internalized in myotubes than in myoblasts. In detail, untargeted NPs were internalized in large amounts in myoblasts and in lower amounts in myotubes, whereas L-carnitine-functionalized NPs were internalized in higher amounts in myotubes than in myoblasts. The more efficient uptake of untargeted PLGA NPs in myoblasts with respect to myotubes was already reported in both murine C2C12 cells and human primary muscle cell cultures [35,36], being ascribed to multiple factors affecting nanocarrier internalization [44]. These include: (i) the higher metabolic rate of cycling cells in comparison to terminally differentiated ones [45]; (ii) the differential expression in myoblasts and myotubes of many proteins involved in e.g., adhesion, transmembrane transport, cytoskeleton

dynamics [46–48], and in plasmalemma lipid composition [49]; (iii) the remarkable difference in cell size [50]; (iv) a different protein corona [51] due to the different composition of the culture media. It is likely that the enhanced uptake of targeted NPs in myotubes is due to the higher amount of OCTN2 receptors in comparison to myoblasts. In fact, OCTN2 is considered as the most important plasma membrane carnitine transporter [16,52]. Both myoblasts and myotubes are known to express OCTN2 receptors [53], but the functional activity induced by the differentiation process, such as spontaneous contractile activity, may induce in myotubes the translocation of OCTN2 receptors to the plasma membrane, similarly to what was observed in skeletal muscle in vivo [54]. Accordingly, in vitro studies on human primary cell cultures suggested that the carnitine transport system gradually develops during myogenesis before being fully expressed in the adult tissue [55].

## 4. Materials and Methods

### 4.1. Materials

PLGA 75:25 (Resomer® RG 752 H, Mw = 4–15 kDa) (analytical grade), SC, PVA (Mw = 31–50 kDa, 98–99% hydrolyzed), PTM isethionate (PTM-I), dimethyl sulfoxide (DMSO), phosphoric acid, sodium hydroxide and sodium 1-heptanesulfonate were purchased from Merck (Milan, Italy). All the solvents used were of analytical grade or HPLC grade and were purchased from Carlo Erba Reagenti (Milan, Italy). Ultrapure water used for the buffers was obtained from a Milli-Q® Plus Purification System (Merck Millipore, Vimodrone Milan, Italy). Solvent evaporation was carried out using a rotating evaporator (Heidolph Laborota 400, Heidolph Instruments, Schwabach, Germany) equipped with a vacuum pump (Diaphragm Vacuum Pump DC-4). Lyophilization was performed with a LyoQuest-85® freeze drier (Azbil Telstar Technologies, Barcelona, Spain). C2C12 myoblasts, an immortalized murine cell line, were purchased from ECACC 91031101. Dulbecco's modified Eagle medium (DMEM), fetal bovine serum (FBS), glutamine, amphotericin B and penicillin-streptomycin were purchased from Gibco, Thermo Fisher Scientific (Waltham, MA, USA). Thiazolyl Blue Tetrazolium Bromide (MTT solution), Phalloidin-Atto 488, Phalloidin-Atto 594 and Alexafluor 488 were obtained from Merck.

### 4.2. Preparation and Characterization of Free Base form of PTM

PTM-B was obtained by dissolving PTM-I in distilled water and adding a 25% *w/w* $NH_4OH$ solution at 4 °C. The obtained precipitate was filtered, washed with a 5% $NH_4OH$ solution and dried under vacuum conditions overnight. The conversion of PTM-I into PTM-B was confirmed by mass spectrometry analysis using electrospray ionization or by atmospheric pressure chemical ionization, in positive ion mode, on a Micromass ZQ spectrometer (Waters, Milan, Italy), as previously reported [56].

### 4.3. Preparation of Nanoparticles

SC-associated PLGA NPs were prepared by the nanoprecipitation technique [32]. Practically, for each preparation, an aliquot of a methanolic stock solution of SC (1 mg/mL), corresponding to SC 5% or 10% *w/w*, was added to 5 mg of PLGA 75:25 dissolved in acetone, until a total volume of 1 mL was reached. The organic solution was then dripped into 5 mL of a 0.2% *w/w* PVA solution in MilliQ® water under magnetic stirring. The formation of NPs occurred immediately. After solvent evaporation under reduced pressure, an aqueous NP suspension was obtained. PTM-B-loaded SC-associated NPs were prepared as well, adding an aliquot of a methanolic stock solution of PTM-B (2.5 mg/mL) to the organic solution containing PLGA and SC, for a maximum of 30 µg/mL PTM-B concentration in the final NP suspension. To purify the NPs from unincorporated drugs and SC, PTM-B-loaded SC-associated NPs were extensively dialyzed against MilliQ® water at 4 °C (Spectra/Por® 3500 MWCO dialysis membrane; Spectrum, Houston, TX, USA). Unloaded and untargeted NPs, i.e., without PTM and/or SC, were prepared as well. Fluorescent NPs were prepared by adding 1.4 µg of the fluorescent probe Nile Red/mg of PLGA. The suspensions were then stored at 4 °C until further use.

### 4.4. Characterization of Nanoparticles

The mean hydrodynamic diameter and the PDI of all the NP samples were analyzed by dynamic light scattering (DLS) using a nanosizer (Zetasizer Nano Z, Malvern Inst., Malvern, UK). The selected angle was 173°, and the measurements were carried out at 25 °C after dilution of the particulate suspensions in MilliQ® water. Each measurement was performed in triplicate.

The surface charge of the NPs was evaluated by zeta potential measurements at 25 °C after appropriate dilution in MilliQ® water of the suspensions, using the Smoluchowski equation and the Nanosizer Nano Z. Each reported value is the average of three measurements.

The physical colloidal stability of the NP suspensions in the storage conditions (4 °C) was monitored by evaluating mean diameter, PDI and zeta potential by DLS at different interval times for 4 weeks. Each measurement was carried out in triplicate.

The amount of incorporated PTM-B was determined spectrophotometrically (DU 730 UV-vis spectrophotometer, Beckman Coulter, Brea, CA) at 264 nm using a calibration curve. To this aim, each suspension was lyophilized for 24 h; then, the powder was dissolved in dichloromethane and methanol was added to precipitate PLGA. Then, the suspension was centrifugated (6000 rpm for 15 min) to separate the precipitated polymer. The supernatants were then measured at 264 nm [33]. The concentration of the polymer in the suspensions was based on dry weight analysis. Each sample was analyzed in triplicate. The results were expressed as EE and DL.

### 4.5. Determination of the Associated SC Percentage

The amount of SC associated with the NPs was determined by UV-HPLC on a Shimadzu LC-10ADvp pump equipped with a Shimadzu SPD-10Avp UV–Vis detector set at 215 nm. The analysis was performed on lyophilized NP samples, dissolved in the HPLC mobile phase. Chromatographic separations were performed at room temperature on a reverse phase Kinetex 5 μm C18 100 Å, 150 × 4.6 mm (Phenomenex, Castelmaggiore, Bologna, Italy), equipped with a C18 4.0 × 3.0 mm SecurityGuard cartridge. The volume of injection was 20 μL, and the mobile phase was a mixture of sodium phosphate buffer 50 mM pH 2.7 and methanol (98:2, *v/v*) containing sodium 1-heptanesulfonate 2.5 mM, delivered at a flow rate of 0.7 mL/min. Data acquisition and processing were carried out using Autochro 3000 software (Young Lin Instrument, Anyang, South Korea) running on a Windows XP-equipped computer, and the amount of SC was calculated from a calibration curve in the range of 50 to 400 μg/mL.

### 4.6. PTM-B Release from Nanoparticles

To evaluate the PTM-B release from 5% SC-NPs as a function of time, the suspensions were incubated at 37 °C in a 10 mM PBS buffer pH 7.4 in sink conditions. Aliquots (1 mL) were withdrawn at predetermined time intervals (0, 1, 2, 4, 6, 8, 16, and 24 h) and, after purification by dialysis, the drug content was measured as previously described and compared to the initial value.

### 4.7. Cell Culture and Treatment

C2C12 myoblasts were cultured in 75 cm$^2$-plastic flasks using DMEM, supplemented with 10% (*v/v*) FBS, 1% (*w/v*) glutamine, 0.5% (*v/v*) amphotericin B, 100 units/mL of penicillin-streptomycin and incubated at 37 °C with 5% $CO_2$. Cells were trypsinized in 0.05% EDTA in PBS and seeded in flat-bottom 96-well plates ($3 \times 10^3$ cells/well) for the MTT assay or onto glass coverslips (12-mm diameter) in 24-multiwell plates ($8 \times 10^3$ cells/well). For the differentiation into myotubes, myoblasts seeded on coverslips were grown at confluence and then a differentiation medium (containing 1% FBS) was added for 7 days. Twenty-four hours after seeding, the cells were treated with 5% SC-NPs for increasing times (see below) and analysis then processed.

*4.8. Cytotoxicity Assay*

The tetrazolium salt MTT (3-(4,5-dimethylthiazol-2-yl)-2,5-diphenyltetrazolium bromide) assay was used to assess the cytotoxicity of 5% SC-NPs on myoblasts. This colorimetric assay is based on the reduction of the MTT to purple formazan crystals by the mitochondrial NAD(P)H-dependent oxidoreductase enzymes: the darker the sample, the greater the number of metabolically active cells. This measurement of metabolic activity therefore represents an indicator of cell viability and cytotoxicity. The cells were treated with different nanocarrier concentrations, selected based on their PTM-B entrapment capacity (from 47.35 to 284.14 µg/mL of PLGA) for 2 h, 24 h and 24 h + 24 h of recovery (i.e., the medium containing the NPs was removed and replaced by a fresh one devoid of NPs). Untreated cells were used as the control. At the end of each incubation period, the medium was replaced by 100 µL of 0.5 mg/mL MTT solution (0.5 mg/mL in medium) and incubated for 4 h at 37 °C in a cell incubator. Then, the MTT solution was removed, and formazan crystals were dissolved in 100 µL of DMSO. The absorbance was measured at 570 nm using a ChroMate 4300 ELISA microplate reader (Awareness Technology Inc., Palm City, FL, USA). Experiments were performed in triplicate. Statistical comparisons between control and experimental conditions were made by the Mann–Whitney pairwise test and significant difference was set at $p \leq 0.05$.

*4.9. Fluorescence and Transmission Electron Microscopy Analysis*

For microscopy analyses of NP uptake and intracellular distribution, myoblasts and myotubes, adhering to glass coverslips, were incubated for 2 h and 24 h with NPs at the concentration of 94.71 µg/mL.

For CFM, the cells were incubated for 2 h and 24 h with Nile Red-labeled PLGA NPs (5% SC- and untargeted). At the end of each incubation time, cells were fixed with 4% ($v/v$) paraformaldehyde in PBS pH 7.4 for 30 min at room temperature. To visualize the intracellular distribution of fluorescent nanocarriers, the cells were washed in PBS, incubated with Phalloidin-Atto 488 diluted 1:20 in PBS, stained for DNA with Hoechst 33,342 (1 µg/mL in PBS), rinsed in PBS, and finally mounted in 1:1 mixture of glycerol:PBS.

For observations, a Leica TCS SP5 AOBS system (Leica Microsystems Srl, Milan, Italy) was used: for fluorescence excitation, a diode laser at 405 nm for Hoechst 33342, an Ar laser at 488 nm for Phalloidin-Atto 488 and Alexafluor 488, and a He/Ne laser at 543 nm for Nile Red and Phalloidin-Atto 594 were employed. Z-stack of 1 µm step-sized images (1024 × 1024 pixel format) were collected.

A morphometric analysis was performed to compare the amount of internalized 5% SC-NPs with untargeted NPs in both myoblasts and myotubes after 24 h incubation. The area of fifty cells per sample was measured by using Image J software (NIH), the number of fluorescent spots occurring in the cytoplasm was counted manually and their surface density (expressed as number/$\mu m^2$) was calculated. Statistical comparisons were made by the Mann–Whitney pairwise test (significant difference at $p \leq 0.05$).

For TEM, the cells were incubated for 2 and 24 h with the 5% SC-NPs at the same concentration used for CFM (94.71 µg/mL). Then, cells were fixed with 2.5% ($v/v$) glutaraldehyde and 2% ($v/v$) paraformaldehyde in 0.1 M PBS pH 7.4 at 4 °C for 2 h, post-fixed with 1% OsO$_4$ at room temperature for 1 h, dehydrated with acetone and embedded as a monolayer in Epon [57]. Ultrathin sections were observed, unstained or after weak staining with the uranyl acetate replacement stain (Electron Microscopy Sciences, Hatfield, PA, USA) (UAR-EMS). Observations were made in a Philips Morgagni TEM (FEI Company Italia Srl, Milan, Italy), operating at 80 kV and equipped with a Megaview II camera for digital image acquisition.

*4.10. Immunofluorescence Microscopy*

For immunofluorescence microscopy, the cells were fixed with 4% ($w/v$) paraformaldehyde in PBS pH 7.4 for 30 min at room temperature. Cells were then permeabilized in PBS containing 0.05% Tween 20 and 0.1% bovine serum albumin (BSA) and incubated with a

rabbit polyclonal antibody directed against the OCTN2 receptor (Abcam ab180757), diluted 1:200, for 1 h at room temperature. Cells were washed with PBS and incubated with the secondary antibody (Alexafluor 488), diluted 1:200 in PBS, for 1 h at room temperature. After washing, cells were incubated with Phalloidin-Atto 594, diluted 1:50 in PBS, for 1 h at room temperature. Finally, cells were washed and mounted in 1:1 mixture of glycerol:PBS. Observations were made with a Leica TCS SP5 AOBS system, as above. To quantify OCTN2 receptor signal, the area of thirty cells per sample was measured using Image J software (NIH), and the number of fluorescent spots occurring in the cell was counted manually and their surface density (expressed as number/$\mu m^2$) was calculated. Statistical comparisons were made by the Mann–Whitney pairwise test (significant difference at $p \leq 0.05$).

## 5. Conclusions

To our knowledge, our study demonstrates for the first time that the association of L-carnitine to PLGA NPs may allow skeletal muscle tropism. In fact, the uptake of L-carnitine-functionalized NPs was markedly increased in terminally differentiated muscle cells, where OCTN2 receptors are highly expressed, compared to myoblasts. Moreover, the developed nanosystem is characterized by a high biocompatibility with skeletal muscle cells, making the SC-NPs potential candidates for delivering therapeutic agents against muscular pathologies. However, the slight cytotoxicity of SC-NPs observed in myoblasts, although being transitory and reversible, deserves deeper study, as do the effects of these NPs on cell metabolism, specifically on mitochondrial activity, in both healthy and myotonic dystrophy type I-affected myotubes. The next steps will also concern the study of the targeting capability of SC-NPs inside the muscle organ, where muscle cells are surrounded by the connective tissue acting as a barrier. To this aim, a fluid dynamic system [58] will be used as an in vitro model to investigate the interactions between NPs and biological barriers [59]. Finally, the activity of PTM-B-loaded targeted NPs will be evaluated on the basis of a murine muscle cell line, transfected with human (CTG)n DNA, as an in vitro model expressing the myotonic dystrophy type I phenotype [29].

**Author Contributions:** Conceptualization, S.A. and B.S.; methodology, M.M.; investigation, I.A., M.M., M.A.L., F.B., P.M., V.B.; data curation, M.M.; writing—original draft preparation, I.A. and M.M.; writing—review and editing, B.S. and C.P.; supervision, C.P.; funding acquisition, B.S. All authors have read and agreed to the published version of the manuscript.

**Institutional Review Board Statement:** Not applicable.

**Informed Consent Statement:** Not applicable.

**Data Availability Statement:** Data are contained within the article. Additional data are available from the corresponding author, upon reasonable request.

**Conflicts of Interest:** The authors declare no conflict of interest.

## References

1. Ravi Kiran, A.V.V.V.; Kusuma Kumari, G.; Krishnamurthy, P.T.; Khaydarov, R.R. Tumor Microenvironment and Nanotherapeutics: Intruding the Tumor Fort. *Biomater. Sci.* **2021**, *9*, 7667–7704. [CrossRef]
2. Shi, Y.; van der Meel, R.; Chen, X.; Lammers, T. The EPR Effect and beyond: Strategies to Improve Tumor Targeting and Cancer Nanomedicine Treatment Efficacy. *Theranostics* **2020**, *10*, 7921–7924. [CrossRef] [PubMed]
3. Danhier, F. To Exploit the Tumor Microenvironment: Since the EPR Effect Fails in the Clinic, What Is the Future of Nanomedicine? *J. Control Release* **2016**, *244*, 108–121. [CrossRef] [PubMed]
4. Pearce, A.K.; O'Reilly, R.K. Insights into Active Targeting of Nanoparticles in Drug Delivery: Advances in Clinical Studies and Design Considerations for Cancer Nanomedicine. *Bioconjug. Chem.* **2019**, *30*, 2300–2311. [CrossRef]
5. Duan, D.; Goemans, N.; Takeda, S.; Mercuri, E.; Aartsma-Rus, A. Duchenne muscular dystrophy. *Nat. Rev. Dis. Primers* **2021**, *7*, 13. [CrossRef] [PubMed]
6. Lanni, S.; Pearson, C.E. Molecular genetics of congenital myotonic dystrophy. *Neurobiol. Dis.* **2019**, *132*, 104533. [CrossRef]
7. Mercuri, E.; Bönnemann, C.G.; Muntoni, F. Muscular Dystrophies. *Lancet* **2019**, *394*, 2025–2038. [CrossRef]

8. Andreana, I.; Repellin, M.; Carton, F.; Kryza, D.; Briançon, S.; Chazaud, B.; Mounier, R.; Arpicco, S.; Malatesta, M.; Stella, B.; et al. Nanomedicine for Gene Delivery and Drug Repurposing in the Treatment of Muscular Dystrophies. *Pharmaceutics* **2021**, *13*, 278. [CrossRef] [PubMed]

9. Ahmed, Z.; Qaisar, R. Nanomedicine for Treating Muscle Dystrophies: Opportunities, Challenges, and Future Perspectives. *Int. J. Mol. Sci.* **2022**, *23*, 12039. [CrossRef]

10. Sleboda, D.A.; Stover, K.K.; Roberts, T.J. Diversity of Extracellular Matrix Morphology in Vertebrate Skeletal Muscle. *J. Morphol.* **2020**, *281*, 160–169. [CrossRef]

11. Engin, A.B.; Nikitovic, D.; Neagu, M.; Henrich-Noack, P.; Docea, A.O.; Shtilman, M.I.; Golokhvast, K.; Tsatsakis, A.M. Mechanistic Understanding of Nanoparticles' Interactions with Extracellular Matrix: The Cell and Immune System. *Part Fibre. Toxicol.* **2017**, *14*, 22. [CrossRef] [PubMed]

12. Huang, D.; Yue, F.; Qiu, J.; Deng, M.; Kuang, S. Polymeric Nanoparticles Functionalized with Muscle-Homing Peptides for Targeted Delivery of Phosphatase and Tensin Homolog Inhibitor to Skeletal Muscle. *Acta Biomater.* **2020**, *118*, 196–206. [CrossRef] [PubMed]

13. Yu, C.-Y.; Yuan, Z.; Cao, Z.; Wang, B.; Qiao, C.; Li, J.; Xiao, X. A Muscle-Targeting Peptide Displayed on AAV2 Improves Muscle Tropism on Systemic Delivery. *Gene* **2009**, *16*, 953–962. [CrossRef]

14. Pochini, L.; Scalise, M.; Galluccio, M.; Indiveri, C. OCTN Cation Transporters in Health and Disease: Role as Drug Targets and Assay Development. *J. Biomol. Screen* **2013**, *18*, 851–867. [CrossRef] [PubMed]

15. Kou, L.; Sun, R.; Ganapathy, V.; Yao, Q.; Chen, R. Recent Advances in Drug Delivery via the Organic Cation/Carnitine Transporter 2 (OCTN2/SLC22A5). *Expert Opin. Targets* **2018**, *22*, 715–726. [CrossRef] [PubMed]

16. Juraszek, B.; Nałęcz, K.A. SLC22A5 (OCTN2) Carnitine Transporter-Indispensable for Cell Metabolism, a Jekyll and Hyde of Human Cancer. *Molecules* **2020**, *25*, 14. [CrossRef]

17. He, C.; Jin, Y.; Deng, Y.; Zou, Y.; Han, S.; Zhou, C.; Zhou, Y.; Liu, Y. Efficient Oral Delivery of Poorly Water-Soluble Drugs Using Carnitine/Organic Cation Transporter 2-Mediated Polymeric Micelles. *ACS Biomater. Sci. Eng.* **2020**, *6*, 2146–2158. [CrossRef]

18. Kou, L.; Yao, Q.; Sun, M.; Wu, C.; Wang, J.; Luo, Q.; Wang, G.; Du, Y.; Fu, Q.; Wang, J.; et al. Cotransporting Ion Is a Trigger for Cellular Endocytosis of Transporter-Targeting Nanoparticles: A Case Study of High-Efficiency SLC22A5 (OCTN2)-Mediated Carnitine-Conjugated Nanoparticles for Oral Delivery of Therapeutic Drugs. *Adv. Health Mater.* **2017**, *6*. [CrossRef]

19. Kou, L.; Yao, Q.; Sivaprakasam, S.; Luo, Q.; Sun, Y.; Fu, Q.; He, Z.; Sun, J.; Ganapathy, V. Dual Targeting of L-Carnitine-Conjugated Nanoparticles to OCTN2 and ATB$^{0,+}$ to Deliver Chemotherapeutic Agents for Colon Cancer Therapy. *Drug Deliv.* **2017**, *24*, 1338–1349. [CrossRef]

20. Ingoglia, F.; Visigalli, R.; Rotoli, B.M.; Barilli, A.; Riccardi, B.; Puccini, P.; Dall'Asta, V. Functional Activity of L-Carnitine Transporters in Human Airway Epithelial Cells. *Biochim. Biophys. Acta* **2016**, *1858*, 210–219. [CrossRef]

21. Rotoli, B.M.; Visigalli, R.; Barilli, A.; Ferrari, F.; Bianchi, M.G.; Di Lascia, M.; Riccardi, B.; Puccini, P.; Dall'Asta, V. Functional Analysis of OCTN2 and ATB$^{0,+}$ in Normal Human Airway Epithelial Cells. *PLoS ONE* **2020**, *15*, e0228568. [CrossRef]

22. Strohman, R.C.; Paterson, B.; Fluck, R.; Przybyla, A. Cell Fusion and Terminal Differentiation of Myogenic Cells in Culture. *J. Anim. Sci.* **1974**, *38*, 1103–1110. [CrossRef] [PubMed]

23. Pushpakom, S.; Iorio, F.; Eyers, P.A.; Escott, K.J.; Hopper, S.; Wells, A.; Doig, A.; Guilliams, T.; Latimer, J.; McNamee, C.; et al. Drug repurposing: Progress, challenges and recommendations. *Nat. Rev. Drug Discov.* **2019**, *18*, 41–58. [CrossRef] [PubMed]

24. López-Martínez, A.; Soblechero-Martín, P.; de-la-Puente-Ovejero, L.; Nogales-Gadea, G.; Arechavala-Gomeza, V. An Overview of Alternative Splicing Defects Implicated in Myotonic Dystrophy Type I. *Genes* **2020**, *11*, 1109. [CrossRef]

25. Mulders, S.A.; van den Broek, W.J.; Wheeler, T.M.; Croes, H.J.; van Kuik-Romeijn, P.; de Kimpe, S.J.; Furling, D.; Platenburg, G.J.; Gourdon, G.; Thornton, C.A.; et al. Triplet-repeat oligonucleotide-mediated reversal of RNA toxicity in myotonic dystrophy. *Proc. Natl. Acad. Sci. USA* **2009**, *106*, 13915–13920. [CrossRef]

26. Warf, M.B.; Nakamori, M.; Matthys, C.M.; Thornton, C.A.; Berglund, J.A. Pentamidine Reverses the Splicing Defects Associated with Myotonic Dystrophy. *Proc. Natl. Acad. Sci. USA* **2009**, *106*, 18551–18556. [CrossRef]

27. Coonrod, L.A.; Nakamori, M.; Wang, W.; Carrell, S.; Hilton, C.L.; Bodner, M.J.; Siboni, R.B.; Docter, A.G.; Haley, M.M.; Thornton, C.A.; et al. Reducing levels of toxic RNA with small molecules. *ACS Chem. Biol.* **2013**, *8*, 2528–2537. [CrossRef]

28. Andreana, I.; Bincoletto, V.; Milla, P.; Dosio, F.; Stella, B.; Arpicco, S. Nanotechnological approaches for pentamidine delivery. *Drug Deliv. Transl. Res.* **2022**, *12*, 1911–1927. [CrossRef]

29. Repellin, M.; Carton, F.; Boschi, F.; Galiè, M.; Perduca, M.; Calderan, L.; Jacquier, A.; Carras, J.; Schaeffer, L.; Briançon, S.; et al. Repurposing Pentamidine Using Hyaluronic Acid-Based Nanocarriers for Skeletal Muscle Treatment in Myotonic Dystrophy. *Nanomedicine* **2022**, *47*, 102623. [CrossRef]

30. Chakraborty, M.; Llamusi, B.; Artero, R. Modeling of Myotonic Dystrophy Cardiac Phenotypes in *Drosophila. Front. Neurol.* **2018**, *9*, 473. [CrossRef] [PubMed]

31. Baroni, A.; Neaga, I.; Delbosc, N.; Wells, M.; Verdy, L.; Ansseau, E.; Vanden Eynde, J.J.; Belayew, A.; Bodoki, E.; Oprean, R.; et al. Bioactive Aliphatic Polycarbonates Carrying Guanidinium Functions: An Innovative Approach for Myotonic Dystrophy Type 1 Therapy. *ACS Omega* **2019**, *4*, 18126–18135. [CrossRef] [PubMed]

32. Fessi, H.; Puisieux, F.; Devissaguet, J.P.; Ammoury, N.; Benita, S. Nanocapsule Formation by Interfacial Polymer Deposition Following Solvent Displacement. *Int. J. Pharm.* **1989**, *55*, R1–R4. [CrossRef]

33. Stella, B.; Andreana, I.; Zonari, D.; Arpicco, S. Pentamidine-Loaded Lipid and Polymer Nanocarriers as Tunable Anticancer Drug Delivery Systems. *J. Pharm. Sci.* **2020**, *109*, 1297–1302. [CrossRef]

34. Amat di San Filippo, C.; Wang, Y.; Longo, N. Functional Domains in the Carnitine Transporter OCTN2, Defective in Primary Carnitine Deficiency. *J. Biol. Chem.* **2003**, *278*, 47776–47784. [CrossRef]

35. Guglielmi, V.; Carton, F.; Vattemi, G.; Arpicco, S.; Stella, B.; Berlier, G.; Marengo, A.; Boschi, F.; Malatesta, M. Uptake and Intracellular Distribution of Different Types of Nanoparticles in Primary Human Myoblasts and Myotubes. *Int. J. Pharm.* **2019**, *560*, 347–356. [CrossRef] [PubMed]

36. Costanzo, M.; Vurro, F.; Cisterna, B.; Boschi, F.; Marengo, A.; Montanari, E.; Meo, C.D.; Matricardi, P.; Berlier, G.; Stella, B.; et al. Uptake and Intracellular Fate of Biocompatible Nanocarriers in Cycling and Noncycling Cells. *Nanomedicine* **2019**, *14*, 301–316. [CrossRef] [PubMed]

37. Menon, J.U.; Kona, S.; Wadajkar, A.S.; Desai, F.; Vadla, A.; Nguyen, K.T. Effects of Surfactants on the Properties of PLGA Nanoparticles. *J. Biomed. Mater. Res. A* **2012**, *100*, 1998–2005. [CrossRef] [PubMed]

38. Wang, Q.; Shen, M.; Li, W.; Li, W.; Zhang, F. Controlled-Release of Fluazinam from Biodegradable PLGA-Based Microspheres. *J. Env. Sci. Health B* **2019**, *54*, 810–816. [CrossRef]

39. Reuter, S.E.; Evans, A.M. Carnitine and Acylcarnitines. *Clin. Pharm.* **2012**, *51*, 553–572. [CrossRef]

40. Su, X.; Han, X.; Mancuso, D.J.; Abendschein, D.R.; Gross, R.W. Accumulation of Long-Chain Acylcarnitine and 3-Hydroxy Acylcarnitine Molecular Species in Diabetic Myocardium: Identification of Alterations in Mitochondrial Fatty Acid Processing in Diabetic Myocardium by Shotgun Lipidomics. *Biochemistry* **2005**, *44*, 5234–5245. [CrossRef]

41. Costanzo, M.; Carton, F.; Marengo, A.; Berlier, G.; Stella, B.; Arpicco, S.; Malatesta, M. Fluorescence and Electron Microscopy to Visualize the Intracellular Fate of Nanoparticles for Drug Delivery. *Eur. J. Histochem.* **2016**, *60*, 2640. [CrossRef] [PubMed]

42. Kulkarni, S.A.; Feng, S.-S. Effects of Particle Size and Surface Modification on Cellular Uptake and Biodistribution of Polymeric Nanoparticles for Drug Delivery. *Pharm. Res.* **2013**, *30*, 2512–2522. [CrossRef] [PubMed]

43. Sun, J.; Zhang, L.; Wang, J.; Feng, Q.; Liu, D.; Yin, Q.; Xu, D.; Wei, Y.; Ding, B.; Shi, X.; et al. Tunable Rigidity of (Polymeric Core)–(Lipid Shell) Nanoparticles for Regulated Cellular Uptake. *Adv. Mater.* **2015**, *27*, 1402–1407. [CrossRef] [PubMed]

44. Mahmoudi, M. Debugging Nano-Bio Interfaces: Systematic Strategies to Accelerate Clinical Translation of Nanotechnologies. *Trends Biotechnol.* **2018**, *36*, 755–769. [CrossRef] [PubMed]

45. Chang, J.-S.; Chang, K.L.B.; Hwang, D.-F.; Kong, Z.-L. In Vitro Cytotoxicitiy of Silica Nanoparticles at High Concentrations Strongly Depends on the Metabolic Activity Type of the Cell Line. *Env. Sci. Technol.* **2007**, *41*, 2064–2068. [CrossRef]

46. Kislinger, T.; Gramolini, A.O.; Pan, Y.; Rahman, K.; MacLennan, D.H.; Emili, A. Proteome Dynamics during C2C12 Myoblast Differentiation. *Mol. Cell Proteom.* **2005**, *4*, 887–901. [CrossRef]

47. Casadei, L.; Vallorani, L.; Gioacchini, A.M.; Guescini, M.; Burattini, S.; D'Emilio, A.; Biagiotti, L.; Falcieri, E.; Stocchi, V. Proteomics-Based Investigation in C2C12 Myoblast Differentiation. *Eur. J. Histochem.* **2009**, *53*, e31. [CrossRef]

48. Forterre, A.; Jalabert, A.; Berger, E.; Baudet, M.; Chikh, K.; Errazuriz, E.; De Larichaudy, J.; Chanon, S.; Weiss-Gayet, M.; Hesse, A.-M.; et al. Proteomic Analysis of C2C12 Myoblast and Myotube Exosome-like Vesicles: A New Paradigm for Myoblast-Myotube Cross Talk? *PLoS ONE* **2014**, *9*, e84153. [CrossRef]

49. Briolay, A.; Jaafar, R.; Nemoz, G.; Bessueille, L. Myogenic Differentiation and Lipid-Raft Composition of L6 Skeletal Muscle Cells Are Modulated by PUFAs. *Biochim. Biophys. Acta* **2013**, *1828*, 602–613. [CrossRef]

50. Fröhlich, E.; Meindl, C.; Roblegg, E.; Griesbacher, A.; Pieber, T.R. Cytotoxity of Nanoparticles Is Influenced by Size, Proliferation and Embryonic Origin of the Cells Used for Testing. *Nanotoxicology* **2012**, *6*, 424–439. [CrossRef]

51. Rahman, M.; Laurent, S.; Tawil, N.; Yahia, L.; Mahmoudi, M. Nanoparticle and Protein Corona. In *Protein-Nanoparticle Interactions: The Bio-Nano Interface*; Rahman, M., Laurent, S., Tawil, N., Yahia, L., Mahmoudi, M., Eds.; Springer Series in Biophysics; Springer: Berlin/Heidelberg, Germany, 2013; pp. 21–44. ISBN 978-3-642-37555-2.

52. Wu, X.; Huang, W.; Prasad, P.D.; Seth, P.; Rajan, D.P.; Leibach, F.H.; Chen, J.; Conway, S.J.; Ganapathy, V. Functional Characteristics and Tissue Distribution Pattern of Organic Cation Transporter 2 (OCTN2), an Organic Cation/Carnitine Transporter. *J. Pharm. Exp.* **1999**, *290*, 1482–1492.

53. Georges, B.; Le Borgne, F.; Galland, S.; Isoir, M.; Ecosse, D.; Grand-Jean, F.; Demarquoy, J. Carnitine Transport into Muscular Cells. Inhibition of Transport and Cell Growth by Mildronate. *Biochem. Pharm.* **2000**, *59*, 1357–1363. [CrossRef] [PubMed]

54. Furuichi, Y.; Sugiura, T.; Kato, Y.; Takakura, H.; Hanai, Y.; Hashimoto, T.; Masuda, K. Muscle Contraction Increases Carnitine Uptake via Translocation of OCTN2. *Biochem. Biophys. Res. Commun.* **2012**, *418*, 774–779. [CrossRef] [PubMed]

55. Martinuzzi, A.; Vergani, L.; Rosa, M.; Angelini, C. L-Carnitine Uptake in Differentiating Human Cultured Muscle. *Biochim. Biophys. Acta* **1991**, *1095*, 217–222. [CrossRef] [PubMed]

56. Peretti, E.; Miletto, I.; Stella, B.; Rocco, F.; Berlier, G.; Arpicco, S. Strategies to Obtain Encapsulation and Controlled Release of Pentamidine in Mesoporous Silica Nanoparticles. *Pharmaceutics* **2018**, *10*, 195. [CrossRef]

57. Costanzo, M.; Malatesta, M. Embedding Cell Monolayers to Investigate Nanoparticle-Plasmalemma Interactions at Transmission Electron Microscopy. *Eur. J. Histochem.* **2019**, *63*, 3026. [CrossRef]

58. Carton, F.; Calderan, L. Malatesta M. Incubation under fluid dynamic conditions markedly improves the structural preservation in vitro of explanted skeletal muscles. *Eur. J. Histochem.* **2017**, *61*, 2862. [CrossRef]

59. Carton, F.; Malatesta, M. In Vitro Models of Biological Barriers for Nanomedical Research. *Int. J. Mol. Sci.* **2022**, *23*, 8910. [CrossRef]